UNIVERSIDAD COMPLUTENSE DE MADRID

FACULTAD DE FARMACIA

TESIS DOCTORAL

Síntesis de nanopartículas de tierras raras y su uso en aplicaciones biomédicas

Synthesis of rare earth nanoparticles and their use in *in vivo* biomedical applications

MEMORIA PARA OPTAR AL GRADO DE DOCTORA

PRESENTADA POR

Vivian Andrea Torres Vera

DIRECTORES

Jorge Rubio Retama
Enrique López Cabarcos

UNIVERSIDAD COMPLUTENSE DE MADRID

FACULTAD DE FARMACIA

TESIS DOCTORAL

Síntesis de nanopartículas de tierras raras y su uso en aplicaciones biomédicas/ Synthesis of rare earth nanoparticles and their use in *in vivo* biomedical applications

MEMORIA PARA OPTAR AL GRADO DE DOCTOR

PRESENTADA POR

Vivian Andrea Torres Vera

Bajo la dirección de los doctores:

Jorge Rubio Retama

Enrique López Cabarcos

Madrid, España 2023

UNIVERSIDAD COMPLUTENSE DE MADRID

FACULTAD DE FARMACIA

TESIS DOCTORAL

Programa de Doctorado en Farmacia

Síntesis de nanopartículas de tierras raras y su uso en aplicaciones biomédicas/ Synthesis of rare earth nanoparticles and their use in *in vivo* biomedical applications

MEMORIA PARA OPTAR AL GRADO DE DOCTOR

PRESENTADA POR

Vivian Andrea Torres Vera

Bajo la dirección de los doctores:

Jorge Rubio Retama

Enrique López Cabarcos

A mis padres por enseñarme que los sueños se cumplen si luchas por ellos.

Todos mis logros son el producto de su dedicación, apoyo, esfuerzo y amor incondicional.

Vuela Alto…

AGRADECIMIENTOS

Luego de más de cuatro años trabajando en esta tesis por fin ha finalizado. Este proyecto me ha hecho crecer como profesional pero aún más importante me ha hecho crecer como persona y no habría sido posible sin todas las personas que me acompañaron durante el proceso. Primero quiero agradecerles a mis directores de Tesis el prof. Enrique López Cabarcos y el prof. Jorge Rubio Retama. A Enrique quiero agradecerte por ser la primera persona en darme la bienvenida al grupo, que sin haberme conocido anteriormente se arriesgó a ser mi director de tesis, también te agradezco por haberme acompañado en todo este camino y estar presente y disponible todas las veces que te necesité. A Jorge, creo que no tengo palabras para agradecerte todo lo que has hecho por mí, gracias por enseñarme, por la infinita paciencia que has tenido conmigo en estos cuatro años, por escucharme en mis momentos de crisis, por apoyarme en los momentos difíciles, he aprendido infinidad de cosas gracias a ti. Solo me queda decirte que como investigador eres grande, pero como persona aún más, esta tesis ha sido realizada gracias a tu esfuerzo también.

A mis compañeros del laboratorio. Irene el solecito del laboratorio, la persona que llega con su gran sonrisa a alegrarnos el día, te agradezco por ser mi amiga y cómplice en todas las travesuras, y realmente este tiempo no habría sido tan divertido sin tu presencia. Diego que has sido como mi papá pollito enseñándome el funcionamiento del laboratorio, como hacer las síntesis y muchas cosas más, gracias por todo lo que me enseñaste, por ser un excelente mentor y sobre todo gracias por ayudarme y aconsejarme cuando lo necesité. A Christoph, quiero agradecerte por siempre estar dispuesto a colaborar, por el buen ánimo con que siempre estabas en el laboratorio y por todas las charlas. A Alexis quiero agradecerte por ser un apoyo enorme durante los últimos años, por siempre traer la calma, muchos éxitos en tu doctorado, sé que lo harás genial. A Don Carlos quiero agradecerle por todos los buenos momentos y ser un gran apoyo en esta última etapa del doctorado. A las nuevas caras del grupo Idoya, Paula, Mohammed quiero desearles muchos éxitos en esta nueva etapa que están comenzando, han entrado a un grupo de investigación maravilloso donde tienen la oportunidad de aprender infinidad de cosas a nivel científico y desarrollarse como profesionales, también se que cuentan con una excelente red de apoyo en esta travesía y que van a hacer grandes cosas allí.

A Marco y Rafa quiero agradecerles por toda su ayuda en este proceso, por toda su buena disposición, de ustedes dos he aprendido muchas cosas. A Gonzalo, “parcerito” gracias por las tertulias académicas y no académicas, por ayudarme a definir un poco más el camino que quiero seguir de aquí en adelante. A Sonia y Óscar quiero expresarles todo mi agradecimiento no solo por ayudarme a realizar muchos de los experimentos mostrados en esta tesis, también por su calidad humana, por siempre estar dispuestos a enseñarme. Ustedes dos son la muestra viviente de lo que significa ser profesor y los admiro profundamente por eso. Quiero agradecer también a toda la unidad de Química-Física II de la Facultad de Farmacia por todo su apoyo y cariño, en especial quiero agradecerle a Piedad Yusta y Visi Sanchéz por toda su ayuda y haber sido tan lindas conmigo siempre. A todas las personas de los diferentes CAIs de la Universidad Complutense de Madrid que me han ayudado con muchos análisis presentados en esta tesis.

I would like to thank Dr. Serena Zacchigna and the Cardiovascular Biology Group at the International Center for Genetic Engineering and Biotechnology (ICGEB) for allowing me to spend six months in their laboratory. It was an unforgettable experience as I learned completely new techniques for me and made great friends. I would like to thank Dr. Serena Zacchigna for accepting me in her group and being always present during the development of the project. My special thanks also go to Nina Volf, Roman Vureich, Matteo Cauteruccio and Ricardo Correa for all their support and friendship. I would also like to thank Lucía, Luis, Pamela, Claudia, Matilde, Lubna, Felix, Guiliana and many others for the beautiful moments I spent with each and every one of you there.

Quiero agradecer a COLFUTURO en su programa crédito-beca 2018 por el apoyo económico recibido en los primeros años, así como (RENiM) por el contrato como investigadora de proyecto. También quiero agradecerle al Instituto Italo-Latinoamericano (IILA) por el apoyo que me permitió realizar la estancia de 6 meses en el ICGEB en Trieste, Italia.

A mis papás Paulo y Patricia quiero especialmente agradecerles y dedicarles esta tesis, ustedes junto a mi hermano son el motor de mi vida. Mami te quiero agradecer por todos tus esfuerzos y sacrificios, que no han sido pocos, porque yo soy lo que soy por ti, tú has sido mi apoyo incondicional en cada una de mis aventuras para llegar hasta aquí. Papito a ti te quiero agradecer por las grandes enseñanzas, en especial en estos últimos años, me has enseñado lo que es el optimismo, la fortaleza, la resiliencia, y las ganas de luchar por una meta, eres la persona que me inspira todos los días, me llena de orgullo y eres el referente que tengo para ser una profesional apasionada e intachable como lo fuiste tú. A mi hermano Paulo, chiqui gracias por ser tan noble, por siempre estar pendiente de mi así yo este lejos, siempre he admirado ese corazón tan grande que tienes. A mis hermanas, Mónica, María Paula y Miranda quiero agradecerles por estar en mi vida, por poderlas ver crecer y poderme sentir orgullosa de lo que son. Quiero agradecerles a mis abuelas, María O y Yolanda, por mimarme tanto, por cocinarme y cumplirme los antojos cada vez que fui a verlas para recargar baterías. A mis tíos Beto y Margarita gracias por escucharme, por quererme tanto y siempre estar pendientes de mí, a mis primas Jessica, Paola y Andrea y mi ahijada Paola Andrea, gracias por todas nuestras chocoaventuras en estos años.

Quiero agradecer también a la que fue mi segunda familia, mi familia en España, Alex, Encarni, la tía Chus, David y Luffy, no hay palabras para agradecerles todo lo que hicieron por mí, esta tesis es en gran parte gracias a ustedes. Gracias por abrirme las puertas de su casa y recibirme como un miembro más de su familia, por acompañarme en cada cumpleaños, navidad, año nuevo, reyes etc, que estuve lejos de casa. Gracias por cuidarme durante la pandemia y las veces que estuve enferma, gracias por todo el apoyo que recibí por su parte durante estos 4 años, gracias por darme un hogar mientras yo estuve lejos del mío, por enseñarme la cultura española y acompañarme a explorar este maravilloso país. A Alex muchas gracias por tu cariño, tus cuidados, por los buenos momentos, por ser el apoyo más importante en esta travesía.

A mis amigos Sandra, María Clara, Mónica, Julián, Joliet, Catalina, Carlitos y Ricardo, ustedes son una parte fundamental de mi vida y han estado presentes en todo este camino desde el inicio, gracias por las charlas, los consejos, los viajes, las copas, las risas y las innumerables anécdotas que tengo con cada uno de ustedes. Ricardo quiero agradecerte especialmente por siempre estar ahí para mí, por actuar como guía, consejero y sobre todo por leer y corregir esta tesis innumerables veces. Gracias a Humor Amarillo (Rosita, Mati, Antonio, Joseph, Andrea, Alexis, Enrique, Irene y Martina) por los buenos momentos que hemos compartido, por las cenas, los viajes, las fiestas, las bromas etc. Este último año ha sido especialmente divertido gracias a ustedes.

Finalmente quiero agradecerles al prof. Edgar Vargas Escamilla y al Dr. Wolfram Baumann por todas sus enseñanzas cuando estuve en Uniandes, es bien sabido que unos buenos cimientos son fundamentales para un edificio sólido, gracias a la formación recibida por ustedes dos durante mi pregrado, la maestría y los años que trabajé como profesora allí, se reflejan en lo que soy ahora. Siempre han sido un referente para mí en cuanto a lo que significa ser un buen investigador y sobre todo lo que es ser un excelente profesor y me han enseñado lo crucial que es el sentido social en esta profesión. Espero algún día llegar a ser como ustedes.

“En el fondo, los científicos somos gente con suerte, podemos jugar a lo que queramos durante toda la vida”.

Lee Smolin

INDEX

Abstract

ABSTRACT

Nanomaterials are an excellent alternative to conventional fluorescent probes (organic dyes and fluorescent proteins) because they overcome their main limitations. Thus, they increase resistance to photobleaching, photostability, enable multiplexing, extend lifetime, etc. Moreover, due to the versatility of nanomaterials and especially nanoparticles that can be modified on their surface, they increase biocompatibility in biological systems and specificity in targeting, which makes them an excellent option for *in vivo* and *in vitro* biomedical applications.

Rare earth nanoparticles are of great interest for biomedical applications due to their unique physical and chemical properties. Ln^{3+} ions have highly degenerate electronic states and strongly favored *f-f* orbital transitions, which translate into specific optical properties such as large Stokes shifts, long lifetimes, sharp and intense emission bands, and considerable resistance to photobleaching and photochemical degradation. It is worth noting that in this type of nanoparticles, depending on the transitions that occur after the excitation process, light emission can occur through an upconversion process, in which multiple photons with lower energy produce emission with higher energy, or through a downshifting process. In this process, a photon with higher energy produces a lower emission. Thanks to this type of emission, rare earth nanoparticles can emit light in a wide range of the electromagnetic spectrum, from UV-vis emissions to near-infrared emissions, making them excellent fluorescent probes. Combining the above properties with the versatility these nanoparticles to bound biological molecules such as DNA, RNA proteins, etc., they are ideal candidates for theracnostic applications (detection and treatment) and are also suitable for bioimaging, as sensors and as drug carriers.

This thesis is focused on the development of rare earth nanoparticles for in vivo and in vitro applications, focusing on the optimization of optical and physicochemical properties. The work begins by studying the effects of dopant concentration and excitation intensity on the emission of the "upconversion" and "downshifting" processes of β-$NaYF_4$:Yb^{3+},Er^{3+} nanoparticles. One of the most important strategies for optimizing the luminescence properties is select the right dopants and the optimal ratio that will give the highest possible brightness intensity. For this purpose, nanoparticles were synthesized from β-$NaYF_4$:Yb^{3+},Er^{3+} with different ratios (between 0 and 10) of Yb^{3+}/Er^{3+}, keeping the other properties such as size, crystalline phase, and total concentration of dopants in the matrix the same. Then, the effect of the ratio on the intensity of the emissions in the visible spectrum (upconversion) and on the emissions in the near infrared (downshifting) was observed. The results show that as the Yb^{3+}/Er^{3+} ratio increases, there is a sharp increase in luminescence that follows a power law. However, after ratio 2, it is observed that the exponential increase in intensity decreases and that the maximum light intensity occurs at ratio 4 for both types of emission. In order to explain the observed behavior, the results were theoretically reproduced using a "rate equation" model that allows describing the role of the different emission mechanisms as a function of the ratio of dopants. According to the results, the emissions generated in nanoparticles with a Yb^{3+}/Er^{3+} ratio between 0 and 2 are mainly excited state absorption (ESA), a process based on a multistep system in which a single ion absorbs photons successively. At ratios above 2, the main mechanism is energy transfer upconversion (ETU), a process in which the Yb^{3+}/Er^{3+} pair acts as sensitizer and activator, respectively. In this mechanism, Yb^{3+}, once excited, transfers its energy to Er^{3+}, which in turn is excited, leading to the emission of photons from an excited state of higher energy.

After studying and optimizing the luminescence of rare earth nanoparticles, the second proposed objective was to address one of the major challenges for these nanoparticles in

biomedical applications, namely their use in aqueous or biological media. Transfer of earth nanoparticles from an organic to an aqueous medium is usually accompanied by attenuation of luminescence, degradation and, at low concentrations, dissolution of the particles. To solve this problem, we followed the strategy of protecting β-$NaYF_4$:Yb^{3+},Er^{3+} nanoparticles by coating them with a hydrophobic polymer through the polymerization of styrene or a mixture of polystyrene and methyl methacrylate. In this way, we aim to reduce the direct interaction of water molecules with the nanoparticles leading to non-radiative relaxations of Yb^{3+}, and likewise reduce quenching and improve optical properties (luminescence and lifetime) in aqueous solutions. Our approach was to combine two strategies: First, we replaced the oleic acid ligands on the surface of the nanoparticles with 10-methacryloyldecyl phosphate to achieve surface passivation and colloidal stability in organic media and also to obtain a highly polymerizable end group. Second, microemulsion polymerization of the nanoparticles in styrene and/or methyl methacrylate was used to obtain a core@shell structure in which the polymer layer provides colloidal stability and protects the nanoparticles in aqueous media. After the optimization of the protective layer, its efficiency was studied under different conditions, i.e., at different concentrations of nanoparticles in solution, in media containing different concentrations of phosphates, and also as a function of temperature. The obtained results show that the polymer-coated β-$NaYF_4$:Yb^{3+},Er^{3+}nanoparticles exhibit a high level of protection against quenching, dissolution and degradation due to interactions with phosphates under normal conditions. This protective layer also shows very good performance under extreme conditions, such as low concentrations of β-$NaYF_4$:Yb^{3+},Er^{3+} ($\simeq$10μg/mL) in water and even at temperatures above 50°C. Moreover, the efficiency of this protective layer was compared with the most commonly used layer in aqueous environment, polyacrylic acid layer. The results show that styrene-coated β-$NaYF_4$:Yb^{3+},Er^{3+} nanoparticles are much more resistant to biological applications and show less decrease in luminescence and lifetime than polyacrylic acid-coated β-$NaYF_4$:Yb^{3+},Er^{3+} nanoparticles.

The efficiency of rare earth nanoparticle emission is related to the chemical composition and interaction with the solvation spheres of the medium, as established in the previous work of this thesis. Moreover, the emission is closely related to the structural architecture of the nanoparticle. For this reason, the role of the structural architecture on the emission and thermal sensitivity of $NaYF_4$@$NaYF_4$:Nd_{60},Yb_{20}@CaF_2 nanoparticles was investigated in the third part of the work. These nanoparticles are among the most efficient near-infrared nanothermometers and are characterized by a sandwich-like structure in which the active layer (@$NaYF_4$:Nd_{60},Yb_{20}) is located between a $NaYF_4$ core and a CaF_2 protective layer. In this work, we focused on studying the effects of the thickness of the active layer, the presence of a protective layer, and the influence of an active or inactive core on the spectroscopic properties. Therefore, we have synthesized a series of core, core@shell, and core@shell@shell nanoparticles and studied the emission intensity, lifetime curves, quantum yield, and thermal sensitivity as a function of the aforementioned properties. The results show that increasing the thickness of the active layer is essential to improve the efficiency of the nanoparticles. The best lifetime and the highest quantum yield were obtained with nanoparticles with a thickness of 2 nm. After evaluating the lifetime of the different sets of nanoparticles as a function of temperature, we also found that there is a linear relationship between the absolute quantum yield and the thermal sensitivity. The growth of the protective layer of CaF_2 significantly increases the lifetime, quantum yield, and thermal sensitivity of the nanoparticles by preventing contact between the rare earth ions and the medium. Finally, comparing the quantum yield between nanoparticles with an active core and an inactive core, we find that it is more efficient for the Nd^{3+} and Yb^{3+} ions to be confined in a layer surrounding an inactive core because the quantum yield is higher. All the experimentally obtained information was used to develop a theoretical model that explains the different pathways of deexcitation of the emitting ions and provides an understanding of the thermal sensitivity and quantum efficiency

in this type of nanostructure. The model describes the radiative and non-radiative dynamics of the Yb^{3+} ions as a function of their position within the matrix and the architecture of the nanoparticles. It has been observed that the reduction of matrix and/or surface defects leads to an increase in thermal sensitivity and quantum efficiency, since they favor the non-radiative emissions typical of a "back energy transfer (BET)" process as a function of temperature.

In this work, the photoluminescent properties of rare earth nanoparticles were optimized from various aspects. However, for their use in biomedical applications, it is also necessary to study their behavior in in vitro and in vivo models and to explore not only their advantages as fluorescent probes but also their applicability as theracnostic systems. The final work of this thesis focused on the development of a nanosystem that promotes endothelial cell proliferation in vitro and in mouse models. To this purpose, $NaYF_4@NaYF_4:Nd_{60},Yb_{20}@CaF_2$ nanoparticles were used with a signaling protein (the endothelial growth factor VEGF) bound to their surface, which plays a fundamental role in the process of cellular angiogenesis. Although VEGF is an important target in treatments to regenerate new tissue after cardiovascular accidents, its effects have been found to be short-lived because it has a limited lifetime within the body. To extend the lifetime of VEGF, a nanosystem of rare-earth nanoparticles was developed to serve as a platform, increasing the stability of the protein and thus enhancing its lifetime and effect on biological systems. Subsequently, the $NaYF_4@NaYF_4:Nd_{60},Yb_{20}@CaF_2$ nanoparticles were synthesized and characterized, VEGF was anchored to the surface, and the effect of this nanosystem on the proliferation of HUVEC cells was studied. The results show that thanks to the VEGF- $NaYF_4@NaYF_4:Nd_{60},Yb_{20}@CaF_2$ nanosystem, cell survival increases by 40-60% compared to free VEGF and cell proliferation increases by 30% thanks to the stability of the nanosystem. In vivo results in a mouse model show that 7 days after injection of the nanosystem, cell proliferation increases by 37% compared to free VEGF, making this strategy an excellent candidate for angiogenic therapy.

Resumen

RESUMEN

Los nanomateriales son una excelente alternativa a las sondas fluorescentes tradicionales (colorantes orgánicos y proteínas fluorescentes) ya que solucionan las principales limitaciones estas. Aumentando así, la resistencia al fotoblanqueo, la fotoestabilidad, permitiendo la multiplexación, mejorando los tiempos de vida, etc. Adicionalmente debido a la versatilidad que poseen los nanomateriales y más concretamente las nanopartículas para ser modificadas en su superficie, aumentan la biocompatibilidad en sistemas biológicos y la especificidad en la detección del objetivo, haciéndolas una excelente opción para aplicaciones biomédicas *in vivo* e *in vitro*.

Las nanopartículas de tierras rara son de gran interés en aplicaciones biomédicas debido a sus propiedades físicas y químicas únicas. Los iones Ln^{3+} poseen estados electrónicos altamente degenerados y transiciones entre orbitales *f-f* altamente favorecidas, lo que se traduce en propiedades ópticas especificas como grandes desplazamientos de Stokes, largos tiempos de vida, bandas de emisiones intensas y nítidas, una resistencia considerable al fotoblanqueo y a la degradación fotoquímica. Cabe mencionar que en este tipo de nanopartículas dependiendo de las transiciones involucradas, luego del proceso de excitación, la emisión de luz puede darse siguiendo los procesos “upconversion”, donde múltiples fotones de baja energía producen una emisión de mayor energía o procesos de “downshifting” donde un fotón de mayor energía produce una emisión menor. Gracias a este tipo de emisiones las nanopartículas de tierras raras pueden generar luz en un amplio rango dentro del espectro electromagnético, que va desde emisiones en el UV-Vis hasta emisiones en el infrarrojo cercano, convirtiéndolas así en excelentes sondas fluorescentes. Combinando las propiedades ya mencionadas con la versatilidad que poseen estas nanopartículas para anclar moléculas biológicas como proteínas DNA, RNA, etc, son candidatos ideales para aplicaciones teracnósticas (de detección y tratamiento), así mismo son útiles en bioimagen, como sensores y como transportadores de medicamentos.

Este trabajo de tesis está orientado en el desarrollo de nanopartículas de tierras raras para aplicaciones *in vivo e in vitro*, enfocándose principalmente en la optimización de las propiedades ópticas y fisicoquímicas. El trabajo de Tesis comienza estudiando el efecto de la concentración de los dopantes y de la intensidad de la excitación en la emisión de los procesos de “upconversion” y “downshifting” de nanopartículas de β-$NaYF_4$:Yb^{3+},Er^{3+}. Esto se realiza debido a que una de las estrategias claves para optimizar las propiedades lumínicas es elegir los dopantes correctos y el ratio óptima que den la máxima intensidad de brillo posible. Para ello se sintetizaron nanopartículas de β-$NaYF_4$:Yb^{3+},Er^{3+} con diferentes ratios (entre 0 y 10) de Yb^{3+}/Er^{3+} manteniendo iguales las demás propiedades como el tamaño, la fase cristalina y la concentración total de dopantes dentro de la matriz. Posteriormente, se observó el efecto del ratio sobre la intensidad de las emisiones en el espectro visible (“upconversion”) y en las emisiones en el infrarrojo cercano (“downshifting”). Los resultados muestran que se produce un gran aumento de la luminiscencia a medida que aumenta la relación Yb^{3+}/Er^{3+} siguiendo un comportamiento de acuerdo con la ley de la potencia. Sin embargo, al incrementar el ratio por encima de 2 se observa que el aumento exponencial de la intensidad disminuye y que la máxima intensidad lumínica se produce en el ratio 4 para los dos tipos de emisiones. Para explicar los comportamientos observados, se reprodujeron teóricamente los resultados mediante un modelo de “ecuaciones cinéticas” que permitió describir el papel de los diferentes mecanismos de emisión presentes en relación con el ratio de los dopantes. De acuerdo con los resultados, en

el proceso “upconversion” las emisiones producidas en nanopartículas con ratios de Yb^{3+}/Er^{3+} entre 0 y 2, el mecanismo de emisión principal es la absorción en estado excitado (ESA) que es un proceso basado en un sistema multinivel donde se produce una absorción sucesiva de fotones por un solo ion. En ratios superiores a 2 el mecanismo principal es el mediante transferencia de energía de conversión ascendente (ETU), proceso por el cual la pareja Yb^{3+}/Er^{3+} funcionan como sensibilizador/activador respectivamente. En este mecanismo el Yb^{3+} tras ser excitado transfiere su energía al Er^{3+} que a su vez se excita produciendo una emisión de fotones desde un estado excitado de energía mayor.

Después de estudiar y optimizar la luminiscencia de nanopartículas de tierras raras, como segundo objetivo, se planteó enfrentar uno de los principales desafíos de estas nanopartículas en las aplicaciones biomédicas y es su uso en medios acuosos o biológicos. La transferencia de nanopartículas de tierras del medio orgánico al acuoso suele ir acompañada por una extinción de la luminiscencia, una degradación y a bajas concentraciones, una disolución de ellas. Para solucionar este problema se planteó una estrategia para proteger nanopartículas β-$NaYF_4$:Yb^{3+},Er^{3+} mediante el recubrimiento con un polímero hidrofóbico a través de la polimerización del estireno o de una mezcla poliestireno y metilmetacrilato, de esta forma se pretende disminuir la interacción directa de las moléculas de agua con las nanopartículas, que causen relajaciones no radiativas del Yb^{3+} y así mismo se pretende disminuir el quencheo y mejorar las propiedades ópticas (luminiscencia y tiempo de vida) en soluciones acuosas. Nuestro enfoque fue combinar dos estrategias conjuntas, la primera fue reemplazar los ligandos de ácido oleico presentes en la superficie de las nanopartículas, por 10-metacriloildecil fosfato (MPD) para lograr la pasivación de la superficie y la estabilidad coloidal en medios orgánicos y también para obtener un grupo terminar altamente polimerizable. En segundo lugar, se utilizó la polimerización por microemulsión de las nanopartículas en estireno y/o metilmetacrilato para así conferir una estructura core@shell donde la capa del polímero aporte estabilidad coloidal y proteja la nanopartícula en medios acuosos. Luego de optimizar la capa protectora, se estudió su eficiencia bajo diferentes condiciones, es decir a diferentes concentraciones de nanopartículas en solución, en medios con diferentes concentraciones de fosfatos y también en función de la temperatura. Los resultados obtenidos muestran que las nanopartículas de β-$NaYF_4$:Yb^{3+},Er^{3+} recubiertas con polímero poseen una alto nivel de protección en contra del quencheo, la disolución y la degradación por interacción con fosfatos en condiciones normales. También fue posible demostrar que esta capa protectora funciona muy bien bajo condiciones extremas como lo son a bajas concentraciones de β-$NaYF_4$:Yb^{3+},Er^{3+} ($\simeq 10 \mu g/mL$) en agua, e incluso a temperaturas mayores a los 50°C. Adicionalmente, se comparó la eficiencia de está capa protectora con la capa comúnmente más utilizada en ambientes acuosos, es decir la capa de ácido poliacrílico; los resultados muestran que las nanopartículas de β-$NaYF_4$:Yb^{3+},Er^{3+} cubiertas con estireno son mucho más resistentes para aplicaciones biológicas y que tienen una menor disminución en la luminiscencia y en los tiempos de vida que las nanopartículas β-$NaYF_4$:Yb^{3+},Er^{3+} cubiertas con ácido poliacrílico.

La eficiencia en la emisión de las nanopartículas de tierras raras, como se ha observado en los trabajos anteriores de esta tesis, está relacionada con la composición química y la interacción con las esferas solvatación del medio. Adicionalmente, la emisión está estrechamente relacionada con la arquitectura estructural propia de la nanopartícula; Por esta razón, en la tercera parte del trabajo de tesis, se ha estudiado el papel que tiene la arquitectura estructural en la emisión y en la sensibilidad térmica de nanopartículas $NaYF_4$@$NaYF_4$:Nd_{60},Yb_{20}@CaF_2. Estas nanopartículas son uno de los nanotermómetros más eficientes en la región del infrarrojo cercano, y se caracterizan por poseer una estructura tipo sándwich donde la capa activa (@$NaYF_4$:Nd_{60},Yb_{20}) se encuentra entre un núcleo de $NaYF_4$ y una capa protectora de CaF_2. En este trabajo en particular, nos hemos centrado en el estudio del efecto del grosor de la capa activa, la presencia de una capa protectora y la influencia de poseer un núcleo activo o inactivo en las propiedades espectroscópicas. Por lo tanto, hemos sintetizado un conjunto de nanopartículas core, core@shell y core@shell@shell y se ha evaluado la intensidad de la emisión, las curvas del tiempo de vida, el rendimiento cuántico y la sensibilidad térmica en función de las características ya mencionadas. Los resultados muestran que el aumento del grosor de la capa activa es primordial para mejorar la eficiencia de las nanopartículas obteniendo el mejor tiempo de vida y el mayor rendimiento cuántico con nanopartículas con 2 nm de grosor. Además, luego de evaluar el tiempo de vida de los diferentes conjuntos de nanopartículas en función de la temperatura, observamos que existe una relación lineal entre el rendimiento cuántico absoluto con la sensibilidad térmica. En cuanto al crecimiento de la capa protectora de CaF_2 se observa que aumenta de manera significativa el tiempo de vida, el rendimiento cuántico y la sensibilidad térmica de las nanopartículas al evitar el contacto entre los iones de tierras raras y el medio. Finalmente, al comparar el rendimiento cuántico de nanopartículas con un núcleo activo y un núcleo inactivo observamos que es más eficiente que los iones de Nd^{3+} y de Yb^{3+} se encuentren encerrados en una capa que rodee un núcleo inactivo ya que el rendimiento cuántico es mayor. Toda la información obtenida experimentalmente se utilizó para desarrollar un modelo teórico que explique las diferentes vías de desexcitación de los iones emisivos y que permita una comprensión de la de la sensibilidad térmica y la eficiencia cuántica en este tipo de nanoestructuras. El modelo describe la dinámica radiativa y no radiativa de los iones Yb^{3+} en función de su localización dentro de la matriz y la arquitectura de las nanopartículas. Se observó que la disminución de los defectos de la matriz y/o de la superficie logran un aumento en la sensibilidad térmica y en el rendimiento cuántico debido a que favorecen las emisiones no radiativas propias de un proceso de devolución de energía (BET) térmicamente dependiente.

A través de este trabajo de tesis se han optimizado las propiedades fotoluminiscentes de las nanopartículas de tierras raras desde diferentes puntos de vista, sin embargo, para ser utilizadas en aplicaciones biomédicas es necesario estudiar también su comportamiento en modelos *in vitro* e *in vivo* y estudiar no solo las ventajas que tienen en cuanto a sondas fluorescentes, sino también en cuanto a su aplicabilidad como sistemas teracnósticos. El último trabajo de esta tesis fue enfocado en desarrollar un nanosistema que participe en el aumento de la proliferación de células endoteliales *in vitro* y en modelos de ratón. Para ello se utilizaron nanopartículas de $NaYF_4@NaYF_4:Nd_{60},Yb_{20}@CaF_2$ a las cuales se les ancló en su superficie una proteína señalizadora (el factor de crecimiento endotelial VEGF), que juega un papel primordial en el proceso de angiogénesis celular. Pese a que la VEGF es una diana importante en los nuevos tratamientos de regeneración de tejidos luego de accidentes cardiovasculares, se ha observado que su efecto es de corta duración debido a que posee un tiempo de vida limitado dentro del organismo. Como estrategia para aumentar el tiempo de vida de la VEGF, se diseñó un nanosistema compuesto de nanopartículas de tierras raras que sirva de soporte y por lo tanto genere estabilidad a la proteína aumentando así el tiempo de vida y su efecto en sistemas biológicos. Luego se ser sintetizadas y caracterizadas las nanopartículas de $NaYF_4@NaYF_4:Nd_{60},Yb_{20}@CaF_2$ se ancló la VEGF a la superficie, posteriormente se estudió el efecto de este nanosistema en la proliferación de células HUVEC. Los resultados muestran que gracias al nanosistema VEGF-$NaYF_4@NaYF_4:Nd_{60},Yb_{20}@CaF_2$ hay un incremento en la supervivencia celular entre el 40-60% comparada con la VEGF libre y que la proliferación celular aumenta un 30% gracias a la estabilidad proporcionada por el nanosistema. Los resultados *in vivo* en un modelo de ratón, muestran que luego 7 días de ser inyectado el nanosistema la proliferación celular aumenta en un 37% comparada con la VEGF libre haciendo esta estrategia una excelente candidata para la terapia angiogénica.

1. Introduction

INTRODUCTION

> *"May it be a light to you in dark places,*
> *when all other lights go out"*
>
> J.R.R. Tolkien

1.1 Luminescence

Luminescence is the property associated with the emission of light as a product of a physical or chemical reaction. This property has always been of great interest to humanity, as the Chinese in the 8th or 9th century were fascinated by the brightness of fireflies and wrote many texts about it, unknowingly describing luminescence for the first time.[1] Aristotle described in his writings the emission of light from a fish in the process of decomposition, and sailors of the 13th century spoke in their logbooks about the bioluminescent effect caused by algae in the sea. Scientists of the 14th and 15th centuries studied the effect of luminescence in nature, such as Nicolas Monarde, who described the intense blue color that came out of the aqueous part of wood, and that it only glowed when the solution came into contact with white light.[1] In 1603, Vicenzo Cascariolo described the luminous effect of barite ($BaSO_4$), which was known to the Greeks as sunstone. After he mixed it with charcoal and heated it, the mixture glowed in moonlight (see Figure 1). He called this effect phosphorescence, a term used for many centuries to describe substances that have the property of glowing for an extended period after being illuminated by an external source. in 1888, Eilhard Wiedamann defined this effect as **luminescence**, referring to any phenomenon of light emission in which there is no increase in temperature.[1]

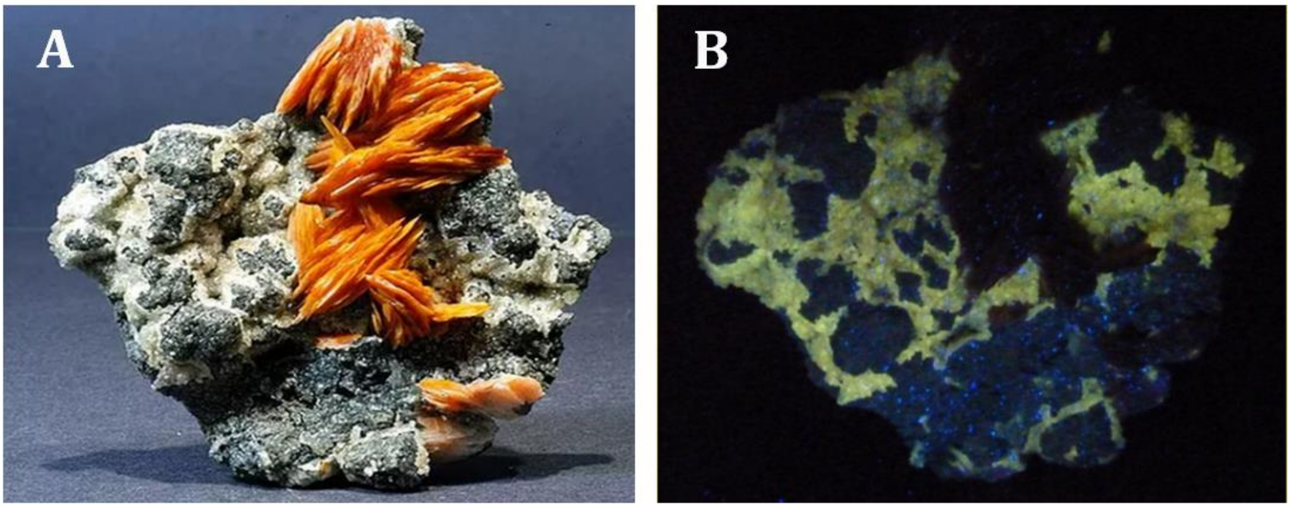

Figure 1. Barite ($BaSO_4$) and cerussite ($PbCO_3$) **A.** Rock in daylight. **B.** Rock is illuminated by ultraviolet light. The yellow color corresponds to cerussite and the blue color to barite.

Today we know that luminescence is an emission of energy caused by chemical reactions, electrical energy, or subatomic motion,[2] and several types of luminescence are known: Chemiluminescence, the emission of light caused by a chemical reaction. Bioluminescence, living things produce the emission of light through biochemical reactions. Electroluminescence, the result of an electric current flowing through a substance. And photoluminescence by the absorption and emission of photons.[2] Figure 2 shows an example of the different types of luminescence.

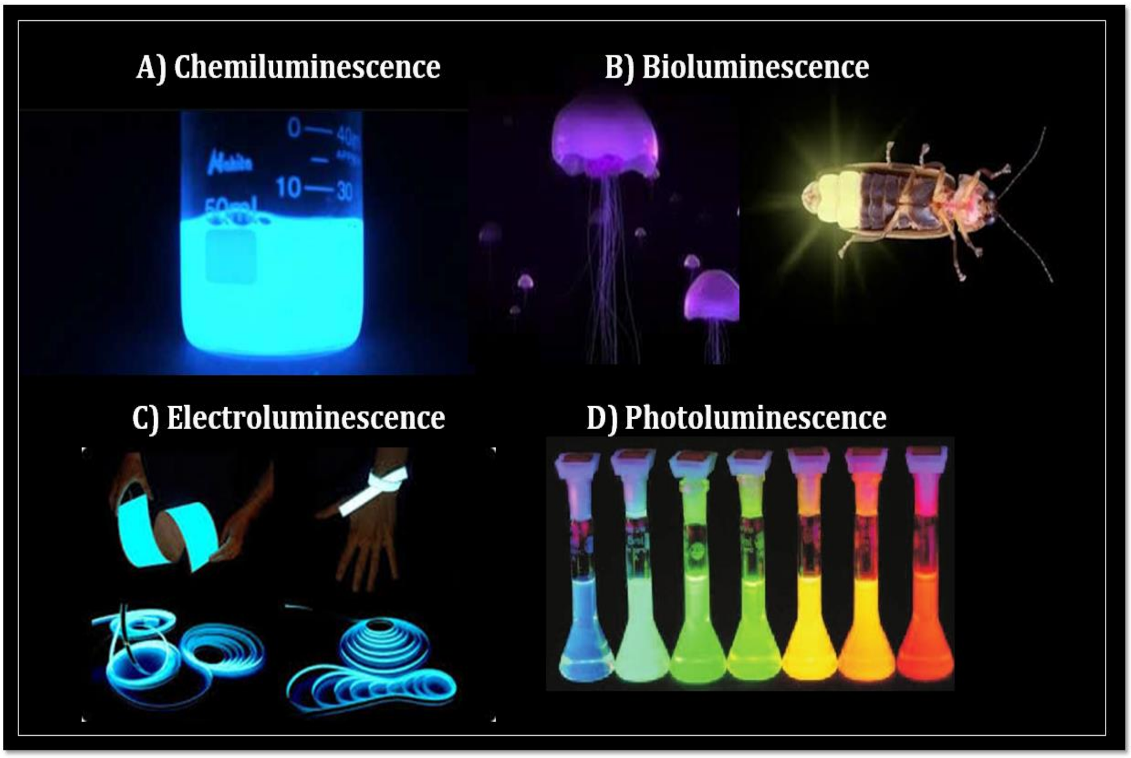

Figure 2. The principal types of luminescence. **A)** Luminescence due to a chemical reaction of luminol. **B)** Bioluminescence of *Pelagia noctiluca* (jellyfish) & *Lamprey's noctiluca* (common firefly). **C)** Thulium doped phosphorus oxynitride-based electroluminescent material for led applications. **D)** Lanthanide-based nanoparticles in solution after being excited with a laser.

In the last century, interest in **photoluminescence** has grown exponentially as its study has enabled the development of new technologies that have improved the quality of people's lives. Applications range from the simplest, such as neon signs, to many others more complex, such as the development of new quantitative analysis techniques that are used daily in many areas of science. For example, it is used to detect oil spills or illegal dumping of crude oil, or to identify pathogens in food using biosensors with photoluminescent materials, etc.[3] However, the fields in which photoluminescence has been most explored are medicine and biology with the development of fluorescence microscopy.[4] In recent decades, the focus has been on the development of new photoluminescent materials as contrast agents,[5] in nanothermometry,[6], and the development of new biosensors to detect various diseases.[7]

1.1.1 *Photoluminescence*

Photoluminescence, as mentioned above, is the emission of light from a material that emits it from excited electronic states. After excitation, various relaxation processes take place in which other photons are re-emitted to produce light. The time that elapses between the absorption of energy and the emission of light can vary from femtoseconds to milliseconds, and in exceptional cases the delay in emission can be minutes or hours. Depending on the relaxation type of the atoms and the duration of the relaxation process, photoluminescence is divided into **Phosphorescence** (long lifetimes) and **Fluorescence** (short lifetimes).[8]

Phosphorescence has a 1,000-year-old history and is described in a note in a Chinese text called "Xiāng Shán Yě Lù" written by Y. Wen and published in the ancient Song production (960-1279 AD). In it, the artistic work of the painter Z. Xu, which had the property of being visible at night thanks to the "magic" ink with which it was painted, is described. This ink came from Japan and was possibly made from the calcium of pearl oysters.[9] Later, the first scientific reports on the synthesis of phosphorescent materials are attributed to the aforementioned Vicente Cascariolo with his studies on sunstone. Curiously, the mystery of sunstone was finally solved in 2012 by J. Hölsä and M. Bettinelli *et al.* Using modern experimental techniques, they demonstrated that the luminescence of the stone was due to the $3d^94s^1 \rightarrow 3d^{10}$ transition of monovalent copper impurities (Cu^+) in the reduced product of the mineral barite, BaS.[9] From then on, and especially in the 20th century, phosphorescent materials were developed, mainly based on the ZnS type doped with Cu^+ or Co^{2+}. These materials, which emit in the green region of the electromagnetic spectrum, were used primarily as luminous paint in the armies of World War I and World War II. However, they have also found friendlier applications, such as in glow-in-the-dark toys.[9]

Phosphorescence occurs when, after electron excitation, the photon is emitted from a triplet energy state (T). Thus, it is a process forbidden by the spin selection rule (i.e., that the spin of the excited state is the same as that of the ground state). As a result, the emission has a long lifetime. In this case, the absorption of photons is part of a phenomenon called crossover between systems (see Figure 3), in which the excited electron changes spin and ceases to be paired with the electron in the ground state, becoming a transition forbidden by the Pauli exclusion principle. When an excited molecule transitions to the triplet state, it continues to release potential energy to the environment, although it now descends the vibrational scale of the triplet and is trapped in the lower electronic level of the triplet, which always has a lower energy than the singlet, Figure 3. This energy cannot be absorbed, and the electron cannot return to its ground state. However, due to spin-complexing of the orbitals, the selection law is broken, and the molecule can return to its ground state and emit light for an extended period until the energy is dissipated. This process is typical when atoms of high atomic weight, such as iodine (Y) or bromine (Br), are involved.[10,11]

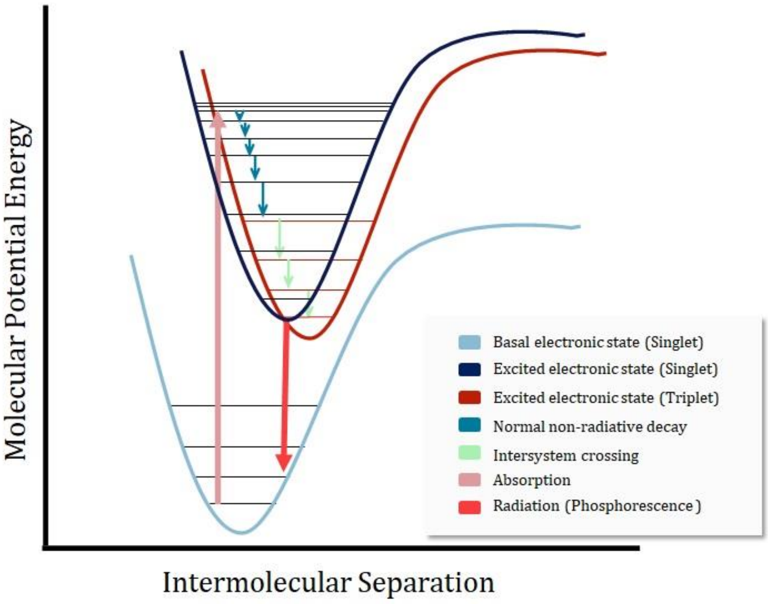

Figure 3. The mechanism that explains the phosphorescence process

On the other hand, we have fluorescence, an emission with a shorter lifetime than phosphorescence. The first observation of the phenomenon of fluorescence was made by Sir Jhon Williams Herschel in 1845, he observed that quinine tonic water, when it was excited with ultraviolet light (from the sun), emitted light with a wavelength of 450 nm. He described the glow as a "beautiful sky blue" At the time, this phenomenon was unusual and could not be explained by the scientific knowledge, today it is known to be a typical effect of fluorescence.[11] Over time, fluorescence became a very sensitive detection method, in 1877, for example, it was used to prove that the Danube and Rhine rivers were connected by underground currents. In this case, fluorescein was introduced into the Danube and after 60 hours the characteristic green color of fluorescein appeared in a small river that flowed into the Rhine.[11] in 1950, during World War II, the United States War Department became interested in monitoring antimalarials drugs with quinine. The results obtained led to the National Institutes of Health program, which developed the first functional spectrophotometer.[11] This new analytical technique was completely revolutionary and led to the study of photoluminescence and enabled the development of numerous fluorescent materials.

Fluorescence is the emission from the excited electron is in a singlet energy level (S). This process follows the spin selection rule (i.e., the excited state and ground state have opposite spins). This makes it a more frequent process with a shorter lifetime. [8,10] the excited molecule collides with other molecules in the environment, releasing energy in a non-radiative manner and descending the scale of vibrational levels until it returns to its ground state. The molecules in the environment may not absorb most of the energy difference. The energy is stored long enough and the surplus of energy is realized spontaneously by radiation.[10] Figure 4.

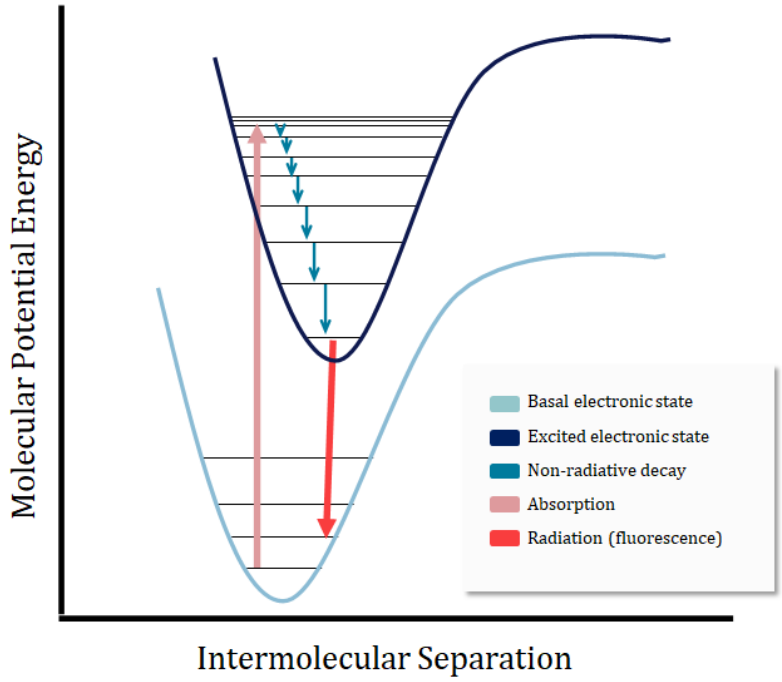

Figure 4. The mechanism that explains the fluorescence process.

A molecule that can absorb energy from electromagnetic radiation and has multiple ways to return to the electronic ground state. Alexander Jablonski, known as the father of fluorescence spectroscopy, after studying the behavior of numerous luminescent substances, developed a simple diagram that explains step by step the general mechanism of light emission, and is called the Jablonski diagram Figure 5.[11] It shows the electronic states within the molecule and the transitions that can occur between them. Within the diagram, the electronic states are grouped vertically by their relative energy and horizontally by the frequency of their spins. Nonradiative transitions are indicated by dotted arrows and radiative transitions by solid arrows. The fundamental vibrational states for each electronic level are represented by thicker lines and the other vibrational states by thinner lines. The energy levels shown in the Jablonski diagram were calculated based on the wave-particle duality of photons and the Bohr model combined with the Plank-Einstein relation. [10] From the equation shown below:

$$E = hv = \frac{hc}{\lambda}$$

Equation 1

Where E is the photon's energy (energy level), h is the Planck constant, v is the frequency, c is the light speed, and λ is the wavelength.

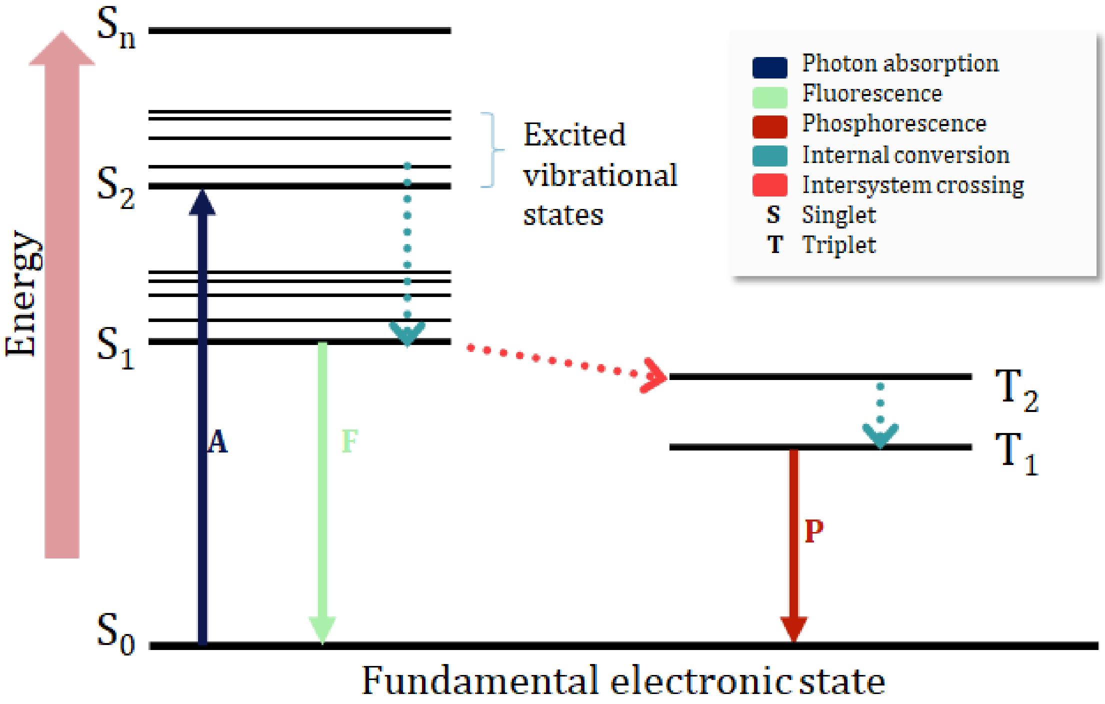

Figure 5. The Jablonski diagram summarizes all the processes that occur in fluorescence and phosphorescence.

The Jablonski diagram excludes relaxation pathways that do not involve photons. Examples of these mechanisms include quenching, energy transfer, solvent-solvent interactions, and solute-solvent interactions.[8]

From the analysis of the Jablonski diagram, we can deduce that the energy of emission is lower than that of absorption. Fluorescence normally occurs at lower energies and longer wavelengths (*Equation 1*), this phenomenon is known as Stokes' law. Sir G.G. Stokes observed this property in 1852 with a relatively simple experiment. He used sunlight as the source of ultraviolet excitation and a blue glass filter that was part of a stained-glass window. This filter selectively transmitted light below 400 nm that was absorbed by quinine. The incident light was prevented from reaching the eye (the detector) by a yellow glass filter (of wine) filter. The fluorescence of quinine occurs at 450 nm and is therefore clearly visible.[11]

A Stokes shift is when the emission from a fluorescent molecule has a lower energy and a longer wavelength, as in his experiment, (Figure 6. Scheme it represents. A. For the Stokes shift. B. The anti-Stokes shift. this is the usual phenomenon for most fluorophores. Conversely, there are cases where the emitted photon has a higher energy than the absorbed photon, the emission occurs at shorter wavelengths than the excitation; this is called an anti-Stokes shift (Figure 6B) an example of this phenomenon is the **upconversion of nanoparticles**.

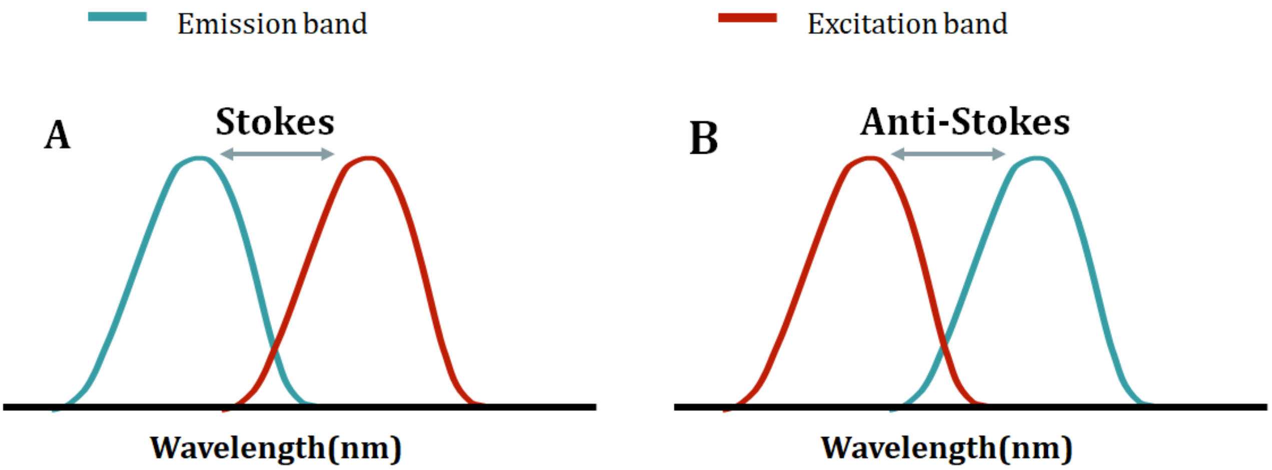

Figure 6. Scheme it represents. **A.** For the Stokes shift. **B.** The anti-Stokes shift.

Another general property of fluorescence is that the emission spectrum is usually a mirror image of the absorption spectrum, which is known as Kasha's rule.[8] In some exceptions, the emission spectrum is not a mirror image of the absorption, which means that the vibrational levels involved in the molecules are different in emission and absorption. In addition, the emission spectrum is independent of the excitation wavelength if the excitation frequency is within the absorption range of the molecule.[11]

Finally, one special characteristic of the photoluminescence spectra (both fluorescence and phosphorescence) is it provides information only about the immediate environment because these processes are very fast, and the nuclei do not have enough time to move. Before absorption, the molecule is in the lowest vibrational state of its basal electronic level; later, when a transition occurs, the molecule is excited, but the nuclear environment remains constant. Therefore, this transition occurs without a change in the geometry of the molecular core. Electronic transitions that occur vertically pass through different vibrational levels of the higher or excited electronic state. This transition usually occurs at the level that represents the distance between the nuclei as the one with the lowest vibrational level of the ground state. [10]. This is referred to as the **Frank-Condon principle**.

1.1.2 Relaxation mechanisms of excited states within a molecule and their influence in the fluorescence

Once the energy of the molecule is absorbed, the mechanisms by which the remaining energy can be released and the electron returned to the ground state (the state that is statistically most probable at room temperature) can be radiative, as emitted light, or nonradiative, with the energy being released primarily as heat.[10,11] Figure 7 shows a diagram of the most common relaxation mechanisms.

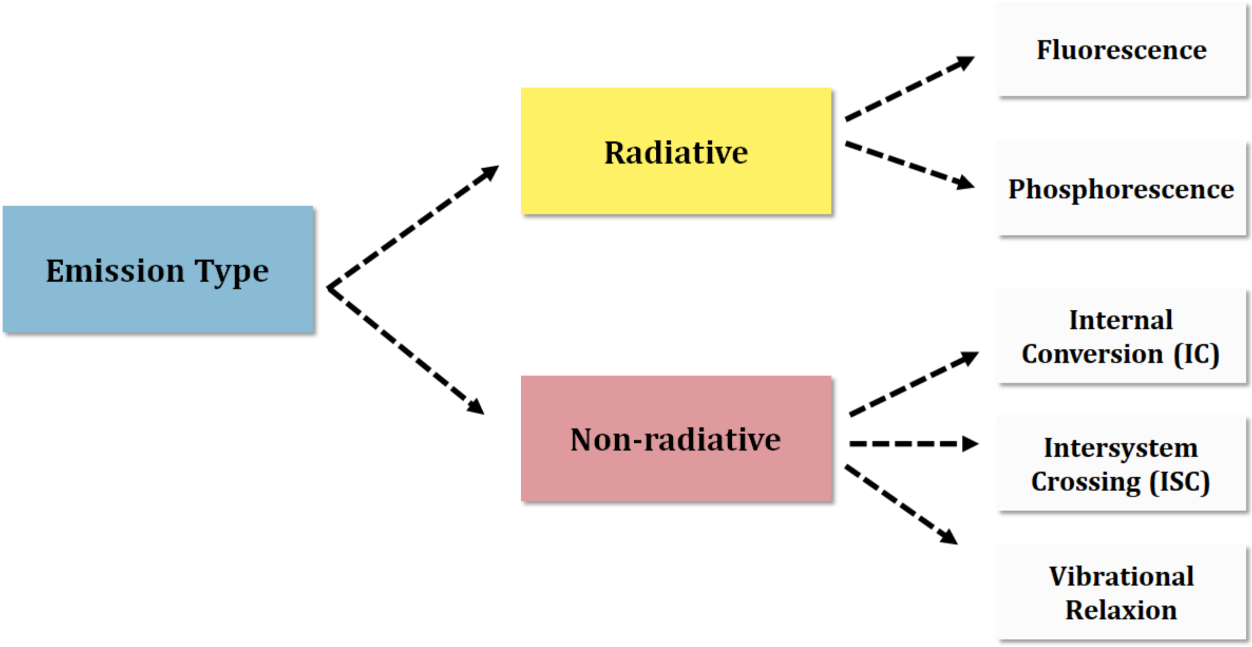

Figure 7. Diagram shows the most common relaxation mechanisms and the type of emission they belong.

Non-radiative emissions can be generated in three different ways: Internal conversion, a transition without radiation between energy states of the same rotational state. Intersystem crossing, defined by the transition of an electron from a singlet state to a triplet state in a nonradiative manner by reversing the spin of the excited electron, is normal when the vibrational levels of two excited states overlap and the energy exchange during the transition is consequently small. Finally, vibrational relaxation, the most common emission, occurs in collisions between excited molecules and solvent molecules. In these collisions, the excess vibrational energy is transferred to the solvent molecules. The vibrational energy gain of the solvent is reflected in a slight increase in the temperature of the medium. Vibrational relaxation is such an efficient process that the average lifetime of an excited vibrational state is approximately 10-15 s.[10]

There are certain variables that can affect radiative emissions, i.e., photoluminescence, convert these emissions to non-radiative. Variables that significantly affect fluorescence include the molecular structure of the fluorophore, temperature, solvent, pH, and the influence of concentration. The fluorophore is the component of a molecule that makes it fluorescent. It is usually a functional group of molecules that absorbs the energy of a particular wavelength and emits it at another wavelength. Temperature, in turn, affects the quantum efficiency of fluorescence. It decreases with increasing temperature because the frequency of collisions increases, increasing the probability of non-radiative emission. Decreasing the viscosity of the solvent also decreases the fluorescence because the probability of non-radiative decays also increases. Changing the polarity of the solvent, in turn, leads to bathochromic or hypsochromic effects, which cause a shift in the maximum absorption peak to longer or shorter wavelengths, respectively. The pH has a significant effect on aromatic compounds with acidic or basic functional groups. Therefore, the wavelength and emission intensity may be different for the ionized and non-ionized forms of the same compound.[12]

A disadvantage of fluorescence is that its intensity can be affected by various processes. This is referred to as quenching. These processes include excited-state reactions, energy transfer, complex formation, and molecular collisions. Collisional quenching occurs when the excited-state fluorophore is deactivated upon contact with some other molecules in solution, which call quenchers. A wide variety of small molecules or ions can act as quenchers of the fluorescence, such as iodine (I^-), oxygen or acrylamide. In collisional quenching the fluorophore returns to the ground state during a diffusive encounter with the quencher, but the molecules are not chemically altered in this process. For the collisional quenching the decrease in the intensity is described by the Stern-Volmer equation:

$$\frac{F_0}{F} = 1 + K[Q] = 1 + k_q \tau_0 [Q]$$

Equation 2

Where the $\frac{F_0}{F}$ is given by the ratio of the decay rate, K is the Stern-Volmer quenching constant, k_q is the bimolecular quenching constant, τ_0 is the unquenched lifetime and $[Q]$ is the quencher concentration. The Stern-Volmer quenching constant indicates the sensitivity of the fluorophore to a quencher. A fluorophore inaccessible to water soluble quenchers, the value is low, free fluorophores in solution or on the biomolecules surface have a high , K.[12] The phenomenon of quenching can also provide a valuable context to understand the role of the excited-sate lifetime in allowing fluorescence measurements to detect dynamic processes in solution.

1.1.3 Fluorescence Lifetimes and Quantum Yields

The lifetime and quantum yield of fluorescence are two properties that, along with light intensity, are perhaps the most important in fluorescent materials. Fluorescence lifetime is defined as the average time required for a fluorophore to return to its ground state after excitation. This process is mainly considered as first-order kinetic decay and is expressed as:

$$\tau_{1/2} = \frac{1}{\Gamma_r + K_{nr}}$$

Equation 3

Here Γ_r is the rate coefficient of the decay of the fluorescence of the fluorophore and K_{nr} represents the sum of the decay rates of the non-radiative emissions. The lifetimes is important because it determines the time available for the fluorophore to interact with or diffuse in its environment, and hence the information is available for its emission.

Quantum yield is the way to interpret the efficiency of fluorescence. By definition, it is the ratio between the number of photons emitted and the number of photons absorbed (*Equation 4*) and can be expressed in the mathematical terms defined earlier as follows (**Equation 5**)[13]

$$\Phi = \frac{Num.\, of\ photons\ emitted}{Num.\, of\ photons\ absorbed}$$

Equation 4

$$\Phi = \frac{\Gamma_r}{\Gamma_r + K_{nr}}$$

Equation 5

The maximum quantum yield of quantum fluorescence is 1, which means that for every photon absorbed, one photon is emitted. However, compounds with a quantum yield of 0.10 are considered quite fluorescent.[13] Comparison of the lifetimes and the quantum yield is very informative to understand all the processes behind the fluorescence

1.2 Fluorescent probes

Fluorescence probes represent the most important field of fluorescence spectroscopy. Thousands of these compounds are known, since the discovery of fluorescence, several types of fluorescent molecules have been synthesized. The first fluorescent molecule was synthesized in 1871 by Adolf von Baeye when he heated phthalic anhydride and resorcinol over a zinc catalyst and obtained a deep red powder that emitted intense greenish-yellow fluorescence in the presence of alkaline solutions. Baeyer named this compound "resorcinphthalein" Today it is known as fluorescein (Figure 8A) and serves as a scaffold for xanthene-based fluorophores.[14] In 1887, Ceresole succeeded in finding a new class of red fluorescent molecules, which he named rhodamine (Figure 8B). An interesting property of rhodamines is the effect of solvent polarity on their color and fluorescence emission. In nonpolar solvents, they are colorless; in polar solvents, they fluoresce.[14] This property and the ease of synthesis make rhodamines ideal scaffolds for the construction of photoactivatable dyes. In the 1970s, Alan Waggoner began his search for photostable, water-soluble, non-cytotoxic dyes. Inspired by the family of cyanine dyes then used to create color in photographic film, he began to systematically modify the structure of cyanine dyes to make them suitable for use in living cells. His work gave rise to the cyanine dye (Cy) family, which includes Cy3 (Figure 8C) and Cy5, which are among the most used fluorochromes in biomedical research.[15] In the 1990s, Roger Y. Tsien changed the structure of GFP (green fluorescent protein), which is responsible for bioluminescence in the jellyfish *Aequorea Victoria* (Figure 8D) and created a new family of fluorescent probes that emit light at different wavelengths.[16] These types of fluorophores are very important in fields such as biochemistry, microbiology, genetic engineering, and physiology.[11]

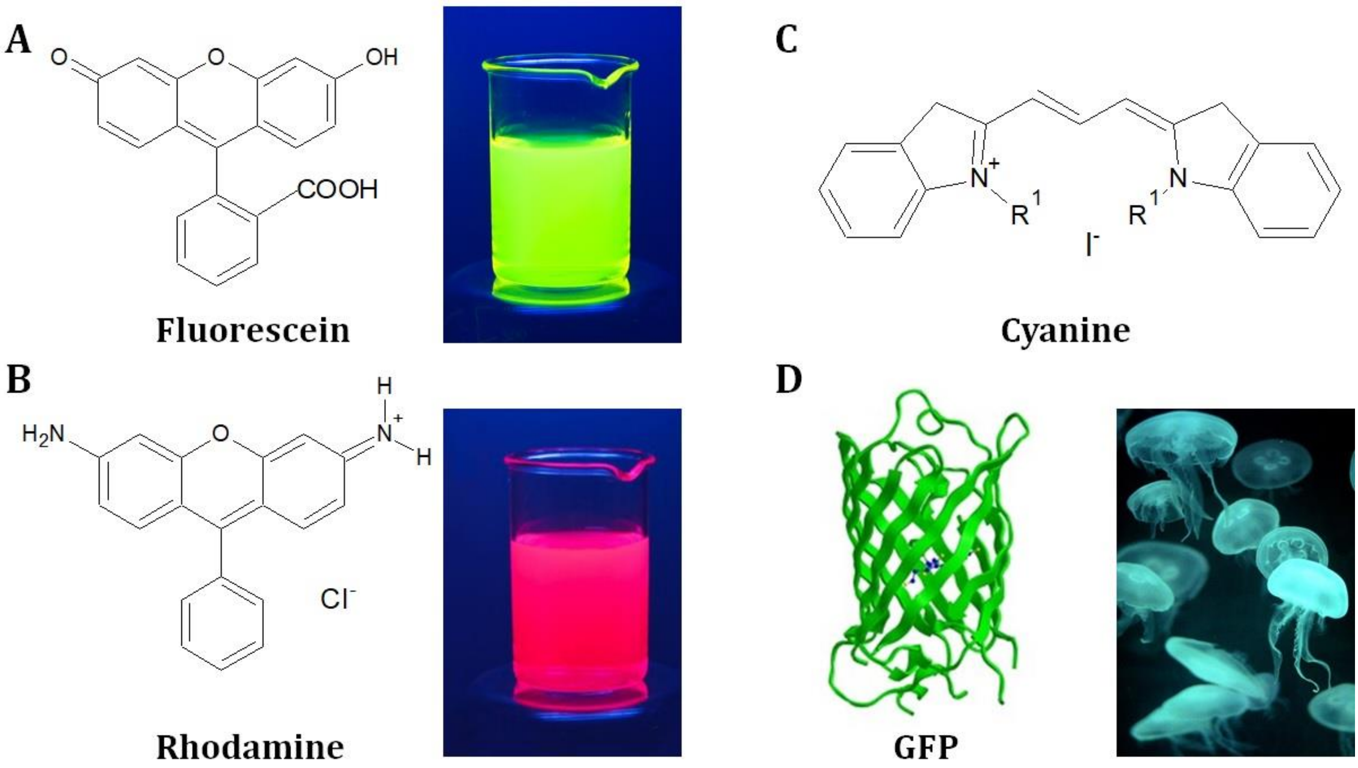

Figure 8. Schematic illustrating the first synthetically produced fluorophores. **A)** Chemical structure and emission of fluorescein. **B)** Chemical structure and emission of rhodamine **C)** Chemical structure of Cy3. **D)** Structure of green fluorescent protein (GFP), Natural GFP emission in jellyfish *Aequorea Victoria.*

Fluorescence measurements, however, are limited by factors that directly affect fluorophores, for example organic dyes are limited by factors such as "photobleaching," in which light intensity disappears when the fluorophore is degraded due to bond breaks in the chemical structure or nonspecific reactions with the medium,[17] or fluorescence intermittency, a phenomenon characterized by a random change between brightness "on" and darkness "off" while the fluorophore is continuously excited, which affects the reproducibility of experiments.[18] Another problem is the natural emission of light by biological or organic structures (autofluorescence) because it interferes with the specific fluorescence signals, especially if the signal is very weak.[19] Moreover, some organic dyes are sensitive to the cellular environment, which causes changes in their photophysical and photochemical behavior and hence their spectral properties.

One solution is fluorescence imaging with nanoparticles in biological systems. This idea has attracted much attention in recent years because it has several advantages. First, each nanoparticle can carry many fluorescent centers. In this way, many dye molecules are combined into a single particulate entity that integrates the fluorescence of each dye molecule, greatly improving the sensitivity of the overall detection system.[20] Second, the dye molecules are encapsulated in the particle matrix, which protects them from photobleaching. Third, nanoparticles are much smaller (about two to three orders of magnitude) than cells, which makes them suitable for cellular applications. Finally, the fluorescent centers in nanoparticle systems are protected from the external environment, which could make them suitable for both *in vitro* and *in vivo* applications without changing the fluorescence intensity or emission wavelength.[21]

1.2.1 Nanoparticles as fluorescent probes

A variety of fluorescent nanoparticles (NPs) have been described in the literature. They can be divided into three main types: Dye-doped fluorescent NPs, crystalline semiconductor NPs (e.g., QDs), and metal NPs. Dye-doped NPs are usually silica nanoparticles that are colored by the introduction of dyes after synthesis.[22] Silica is particularly attractive due to its predictable and adaptable chemistry and has led to derivatives of a number of commonly used organic dyes such as fluorescein,[23,24] rhodamine,[25] and cyanine,[26] which can be covalently bound inside the particle core or on the particle surface. This type of nanoparticles has several advantages: The functional groups on the surface NP are available for coupling reactions, the dye molecules are protected by the polymer matrix, which increases their photostability, and a variety of dye molecules can be entrapped. The excellent photostability makes these NPs suitable for applications where high intensity or long-lasting excitations are required, such as intracellular optical imaging.[20] In addition, the ability to modify their surface can create a nanosystem available for bioconjugation and provide useful results in immunoassays. Rusling *et. al.* used Ru(bpy)-doped silica NPs as markers in an electro-chemiluminescent sensor for detection of prostate-specific antigen.[27] Their system was improved and used to detect 4 biomarkers for prostate cancer.[28] In addition, Li and Xu used FITC-doped silica NPs in a sandwich assay format to detect *Shigella flexneri*, a bacterial dysentery endemic in Asia,[29] to name a few examples. However, although this type of nanoparticle is useful and versatile, its optical properties lag behind compared with the other types of nanoparticles (QDs and metal nanoparticles).[20]

Quantum dots (QDs) are ultrasmall, bright, and extremely photostable nanometer-scale semiconductor crystallites with a broad excitation band but a narrow emission band.[20] The fluorescence of QDs is due to the radiative recombination of an excited electron-hole pair.[30] They absorb photons when the excitation energy exceeds the band gap. During this process, electrons are promoted from the valence band to the conduction band. The light emission results from the recombination of the charge carriers.[30] The band gap of QDs is size dependent, varying the size of QDs tunes the emission wavelength from the blue to the near-infrared region, with QDs, it is possible to image biological samples in multiple colors.[31] These nanometer-sized conjugates can be made water-soluble and biocompatible and could offer important advantages over organic dyes. In addition, high-quality dots are very stable to photobleaching and have narrow, symmetric emission spectra.[20] This type of nanoparticles has been extensively studied for applications in biomedicine, for molecule targeting, whole-body imaging, tumor imaging, drug delivery and drug screening. Figure 9 is an example of the potential of QDs for bioimaging. The figure shows an optical+infrared fluorescence fusion image of a mouse taken 5 minutes after nanoparticle injection.[32]

On the other hand, metal nanoparticles have been a strong focus on developing new biosensors and other technologies for the high-throughput and ultrasensitive detection, identification, and quantification of biomolecules.[20] As nonradioactive labels, a variety of metal NPs such as gold, silver, europium, and rare-earth have shown promise for bioimaging. Nanosized gold and silver do not fluoresce but scatter light very efficiently. Light scattering by nanometer-sized particles is mainly due to the collective oscillation of conduction electrons triggered by the incident light, this phenomenon is known as surface plasmon resonance.[33] The frequency band (color) of the scattered light depends on the size, shape, and material properties of the particle. Silver or gold NP in the 30-120 nm size range efficiently scatter light in the visible spectrum and are not subject to photobleaching.[33] A 100-nm plasmon resonant particle can have a brightness equivalent to that of about 100,000 fluorescein molecules.[20] Gold NPs have been extensively studied for the treatment of oncological diseases using photodynamic therapy (PDT)[34] because gold conjugation facilitates intracellular penetration. In addition, they are excellent nanocarriers that can transport drugs such as peptides,[35] proteins,[36,37] plasmid DNAs (pDNAs), small interfering RNAs (siRNAs), and chemotherapeutic agents.[38] Also, Au NPs have been used as efficient sensors for the detection of different analytes such as metal ions, anions, and molecules like, saccharides, nucleotides,[39] proteins[40,41] and toxins.[42]

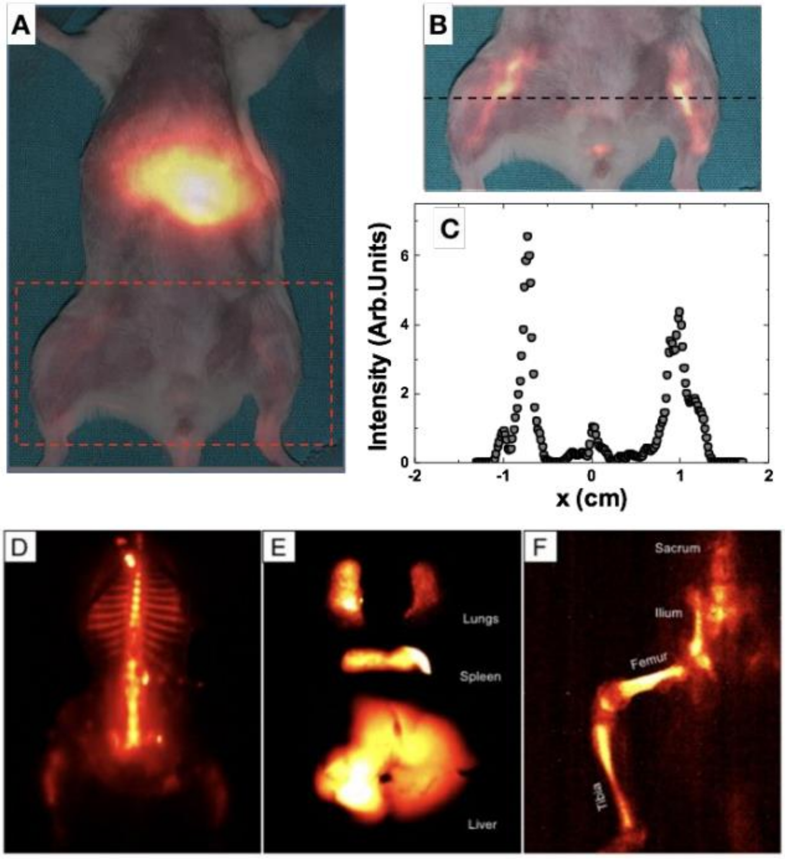

Figure 9. **A)** In vivo imaging of an anesthetized mouse 5 min after intravenous injection of the Ag_2S nanoparticles optimized here. The animal was optically excited with an 800 nm laser diode with a power density of 45 mW/cm^2 and luminescence (1000-1400 nm) was recorded with an infrared camera. **B)** Magnification of the lower extremities where the femoral vessels can be seen. **C)** A cross-section of the intensity profile measured along the black dashed line in (B). **D)** Ex vivo NIR-II images of a dissected mouse skeleton **E)** lungs, spleen, and liver; and **F)** detailed image of mouse femur, tibia, ilium, and sacrum.[32]

Finally, rare earth (RE) based NPs have some advantages compared to other available materials for biomedical applications. In general, RE -based NPs show low toxicity and high thermal and chemical stability. Compared to other luminescent NPs, such as nanostructures functionalized with dyes and quantum dots (QDs), RE -based NPs also exhibit high photostability, high luminescence quantum yield, and sharp emission band, the latter offering higher selectivity for bioassays.[20] Due to these properties, rare earth nanoparticles have been used in this work to develop biomedical applications *in vitro* and *in vivo* and to improve their optical properties. This type of NPs will be discussed in more detail in the next section.

1.3 Rare-earth based nanoparticles

Rare earths (RE), which include yttrium, scandium, and the 14 elements of the lanthanide series (Ln), have attracted considerable interest in recent decades in both academic research and industry due to their unique physical and chemical properties.[43] This is reflected in the exponential increase in the number of publications over the last two decades. Figure 10 shows the number of publications on rare earth nanoparticles on the last 20 years, with most studies focusing on biphotonics (42%) and nanomedicine (28%) for ultrasensitive biosensors, light-guided cancer therapies (e.g., photothermal therapies), diagnostics, and drug delivery.[44]

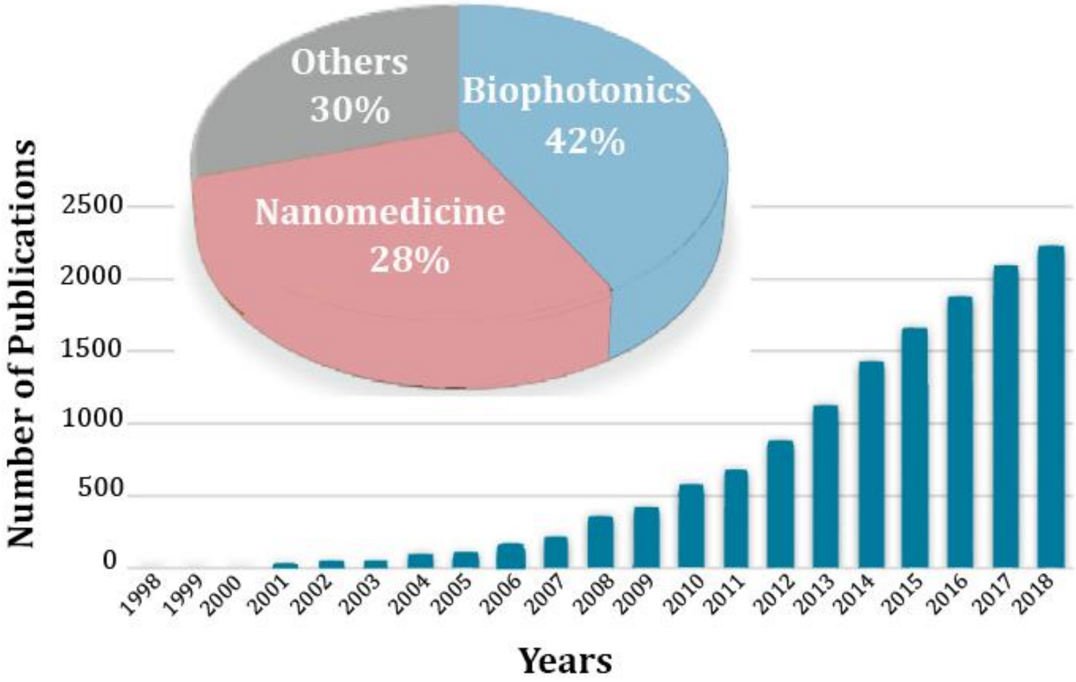

Figure 10. Number of publications presenting studies that explore UCNPs and DCNPs in biophotonics, nanomedicine, and other fields. UCNP and DCNP research has gained increasing attention, as shown by Clarivate Analytics' Web of Science (WoS) (version 5.32) scientific citation search platform. The pie chart shows the percentage of published research in biophotonics, nanomedicine, and other areas.[44]

The history of the luminescent materials compound by rare earth began in 1960 when, thanks to breakthrough advances in purification technology, rare earth phosphors were successfully used in lamps and cathode ray tubes.[45] Since then, research into rare earth luminescent materials has made continuous and significant progress, and the range of applications has been constantly expanded. Today, rare earth luminescent materials are used in almost all areas of photonics and optoelectronics, i.e., in lighting,[46,47] displays,[48,49] sensor technology,[50] and biomedicine[51] as others.

Rare earths (especially lanthanides) have unique optical, electronic, magnetic, and catalytic properties. When a lanthanide ion is present in complexes, the outer electron shell, which includes the 5d and 6s electron orbitals, has a large atomic radius that is susceptible to ligand field and shielding effects. This type of ion has a relatively low ionization energy, so the three outer electrons can be easily removed. The most common and stable electron configuration of the lanthanide series Ln^{3+}, i.e., $[Xe]4f^{n}$ ($0<n<14$).[52] Within this configuration, the arrangement of electrons varies greatly, and due to Coulomb interactions and orbital-spin complexes between the *f* electrons, the electron distributions result in highly degenerate energy levels.[53] When Ln^{3+} cations are incorporated into a crystalline matrix, its energy levels are easily affected by the outer 5p and 5s orbitals by the ln^{3+} because they form a shield. However, the crystalline field surrounding the cation can circumvent the parity selection rule and promote intraconfigurational transitions between *f*-*f* orbitals, leading to unique properties such as large Stokes shifts, long excited state lifetimes, sharp and intense luminescence with very narrow emission bands, and high resistance to the blinking effect of fluorescence.[54] Rare earth doped phosphors exhibit considerable resistance to photobleaching and photochemical degradation because 4*f* electrons play an essential role in chemical bonds that cannot be broken in photochemical processes.[55] Therefore, Ln^{3+} are considered as promising luminescent supporters for applications including bioimaging,[56] sensing,[57] therapy,[58–60] lighting and displays, [61] and photovoltaic devices.[62,63]

Depending on the electronic transitions involved within the complex, the energy levels of Ln^{3+} can emit light upon irradiation, with ultraviolet (UV) or infrared (IR) light, by various optical processes such as downshifting (DF), downconversion (DC), and upconversion (UC). Figure 11 DFL is a photoluminescence process in which a high-energy excited photon is converted into a lower-energy emitting photon. DC is similar to the DF process, except that one high-energy excitation photon leads to several lower-energy emitting photons, with a higher quantum yield than in DF. UC is an inverse process to DC and represents the combination of multiple low-energy excitation photons producing a photon with higher emission energy.[64] The DF and DC processes are Stokes shift processes, and UC is an anti-Stokes shift process.

The magnetic moments, magnetic susceptibilities, and electronic relaxation times of Ln^{3+} are determined by their 4*f* electron configurations and differ dramatically along the series.[51] The symmetric electron ground state of Gd^{3+} leads to weak spin-orbit coupling and consequently a long electronic relaxation time, while the asymmetric electron ground states of Tb^{3+}, Dy^{3+}, Ho^{3+}, and Er^{3+} give them a short electronic relaxation time but larger magnetic moments and magnetic susceptibilities.[65] These have been used to accelerate nuclear relaxation and shift the resonance frequency. For example, some Gd^{3+}-containing complexes are widely used as contrast agents in magnetic resonance imaging (MRI) to shorten the relaxation time of protons and increase image contrast.[66–68]

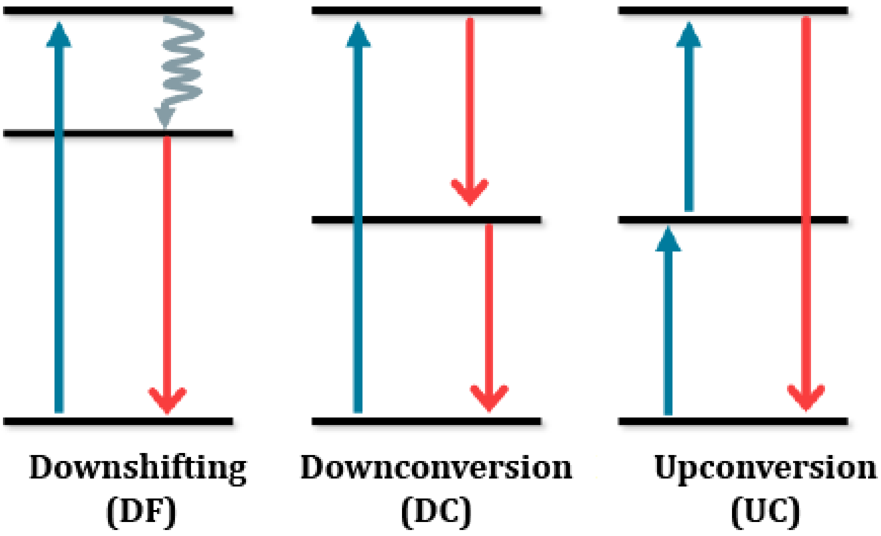

Figure 11. Simplified energy level diagrams describing the basic principle of DF, DC, and UC processes using the 4*f* energy levels of lanthanide ions. The blue lines represent the excitation process, the red lines the emission processes, and the gray line the relaxation of the multiphoton.

With advances in the field of nanotechnology, a new generation of fluorophores has emerged from the development of nanostructured materials containing rare-earth ions either as dopants or as the main component of the nanosystem. The incorporation of these ions opens the possibility of new applications, especially in the use of nanoparticles with size between 1-100 nm, where most biomolecular interactions take place.[56] Thus, the incorporation of RE into NPs enables their use in many different biomedical applications, including bioimaging, biosensing, targeting, drug delivery, and other therapies.

Some desirable requirements that NPs intended for biomedical applications should meet. For example, uniform size, shape, composition, and surface chemistry are important, as these parameters can have a strong influence on their physicochemical properties.[69] In particular, particle geometry has been reported to play an important role in cell-material interactions, affecting cellular uptake and cellular functions.[70] *In vivo* and *in vitro* assays usually require controlled particle size to improve permeation and retention efficiency,[71] as well as high colloidal stability and low toxicity. As mentioned earlier, rare earth nanoparticles have low toxicity and high thermal and chemical stability, compared to other materials. They also exhibit high photostability, high luminescence quantum yield, and sharp emission bands, which also provide higher selectivity for bioassays.[70]

The use of RE -based NPs for luminescent imaging is based on the luminescent properties of Ln cations contained as dopants in a variety of inorganic matrices such as oxides, fluorides, phosphates, vanadates, molybdates, and tungstates, inorganic matrices not necessarily based on RE. Although RE compounds usually facilitate the doping process by favoring the incorporation of the doping Ln cations with the same charge and very similar size.[72] Depending on the doping cations chosen, two main groups of RE -based luminescent NPs can be formed. First, there are up-conversion nanoparticles (UCNPs), which are capable of emitting light of shorter wavelength after being excited by long-wavelength radiation (i.e., anti-Stokes luminescence), and down-conversion nanoparticles (DCNPs), which convert higher-energy photons into lower-energy photons (i.e., conventional Stokes luminescence). Both UCNPs and DCNPs have attracted considerable research interest because they are excited by NIR radiation, which avoids photodestruction and background fluorescence of biological systems and allows greater penetration depth into biological tissues.[73]

1.3.1 Upconversion Nanoparticles (UCNPs)

The upconversion of photons involves the absorption of two or more photons of lower energy and the emission of one photon of higher energy. For example, the absorption of several photons in the near-infrared (NIR) and the emission of a smaller number of photons in the UV-visible.[74] This is not a common process typically associated with materials containing transition metals, lanthanide ions, or actinides, as a variety of degenerate electronic states are possible in this type of transition. To date, there are five different mechanisms for upconversion photoluminescence in Ln^{3+}-doped nanoparticles. These are sequential photon absorption (ESA), energy transfer upconversion (ETU), photon avalanche (PA), cross-relaxation (CR), and cooperative upconversion (CSU).[74] Figure 12 shows a schematic representation of the most common UCL processes.

The ESA mechanism is based on the successive absorption of two or more photons by a single ion due to the ladder-like structure, Figure 12A. This mechanism assumes that the distances between the ground state (G), the first energy level E_1, and the second energy level E_2 are equal. When an ion is excited, the photon transitions from the ground state to the E_1 level. Then another photon is absorbed by the laser, causing the E_1 photon to rise to a higher energy state E_2. Thus, a sequential absorption of photons takes place, which eventually leads to emission from the E_2 level. The efficiency of the process is independent of the concentration of the dopant. The Ln^{3+} that achieve a highly efficient process are Er^{3+}, Ho^{3+}, Tm^{3+}, and Nd^{3+}.[75]

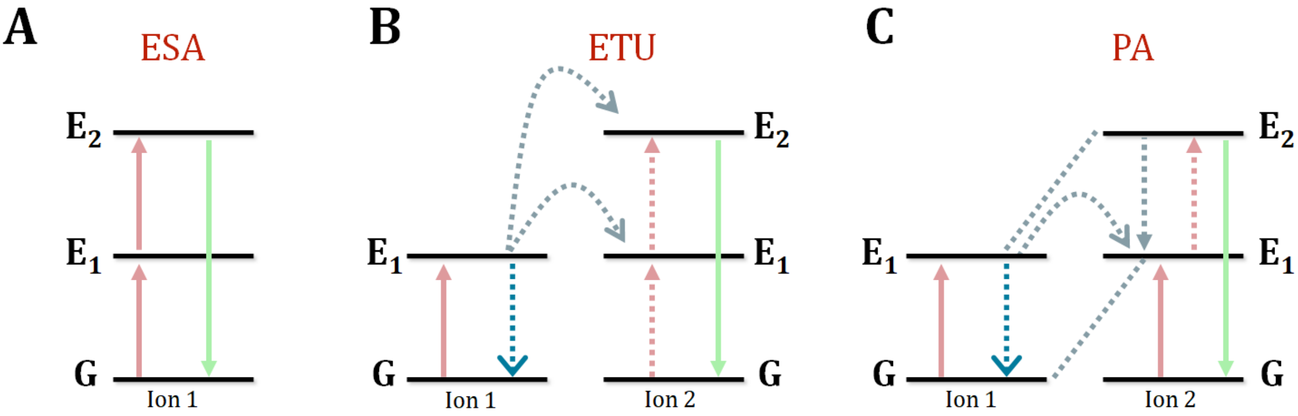

Figure 12. Simplified diagram of the most common upconversion photoluminescence processes. **A** sequential photon absorption (ESA). **B** up-conversion energy transfer (ETU). **C** photon avalanche (PA). The pink arrows indicate the absorption of photons, the gray dotted arrows represent the energy transfer, the blue dotted arrows illustrate the spontaneous emissions, and finally, the green arrows represent the emission of photons by the upconversion process.

The PA process is the less common mechanisms and usually happen inside the laser. The PA mechanism starts similarly to the ESA process. It uses the cross-relaxation mechanism to increase the population of the excited state and produce a photon avalanche effect leading to emission (Figure 12C). An excited-state ion transfers energy to a ground-state ion in cross-relaxation, creating two exciting ions with intermediate energy.[76] Finally, the most efficient process, the ETU mechanism (Figure 12B), involves two adjacent ions. Ion 1, also known as the sensitizer, is first excited by the absorption of a photon from the ground state to the metastable state E_1. Later, it transfers the energy to the E_1 and G states of the activator (ion 2). As a result, ion 2 is excited to the higher state E_2 and energy emission arises. The efficiency of an upconversion process by the ETU mechanism is related to the average distance between neighboring sensitizer-activator ions, which is determined by the doping concentrations.[76] The most commonly activator/sensitizer pairs are Yb^{3+}/Tm^{3+} and Yb^{3+}/Er^{3+}. The Yb^{3+} ion is a particular sensitizer because its emission, around 980nm, are located in a region where biological tissues exhibit very low scattering (biological window I).[74]

For lanthanide-doped nanoparticles, the mechanism of upconversion is essentially the same as for bulk materials. However, the effects associated with surface area and size have important implications for the emission spectrum and quantum yield of UCNPs. Remember that in fluorescence, the mechanisms of radiative and nonradiative relaxation compete and that radiative relaxation decreases the lifetime of excited states, while the presence of phonons increases the probability of energy transfer. Surface-related effects can also significantly affect the color and luminescence efficiency.[73] The surface ligands of nanomaterials can possess a high level of vibrational energy, which contributes significantly to phonon-assisted effects.

To obtain an efficient nanoparticle for the upconversion process, it is important to make a good choice of crystal lattice matrix. Fluoride materials have long excited-state lifetimes, which are often observed due to the low phonon energies (about 350 cm^{-1})[77] of the crystal lattice (Table 1). However, lattice impurities can increase multiphonon relaxation rates between metastable states, thereby reducing the overall intensity of visible emission.[73] Low nonradiative losses are also observed in lattices containing heavy halogenides, but these materials suffer from low chemical stability. Metal oxides provide the desired chemical stability, but conventional oxygen-based systems often have large phonon energies above 500 cm^{-1} (Table 1).[78]

Table 1. Highest phonon lattice energy commonly used matrices for rare-earths ions.[73]

Material	Highest Phonon Energy (cm^{-1})
Phosphate Glass	1200
Silica Glass	1100
Fluoride Glass	550
Chalcogenide Glass	400
$LaPO_4$	1050
Yttrium Aluminum Garnet (YAG)	860
YVO_4	600
LaF_3	300
$LaCl_3$	240

Host lattices based on cations such as Na^+, Ca^{2+}, and Y^{3+} with ionic radii close to those of lanthanide dopant ions prevent the formation of crystal defects and lattice stresses. Therefore, Na^+ and Ca^{2+} fluorides are generally superior host materials for upconversion phosphors.[73,75,79] One of the most efficient nanocrystals in upconversion luminescence is the $NaYF_4$: Yb^{3+}, Er^{3+} nanoparticles which is 20 times higher than that of La_2O_3:Yb^{3+},Er^{3+} and 6 times higher than $La_2(MoO_4)_3$:Yb^{3+},Er^{3+}. Another crucial aspect is the crystalline structure, photoluminescence is highly affected by nonharmonic couplings of phonons within the matrix. The non-harmonic phononic effect is more pronounced in the cubic phase (α) than in the hexagonal phase (β) because the substitution of Na^+ and lanthanide cations in the cubic phase is random compared to the distribution of highly ordered cations in the hexagonal lattice,[80] Figure 13. In fact, The UC efficiency of the green emission in hexagonal-phase $NaYF_4$:Yb^{3+}/Er^{3+} is approximately 10 times stronger than that in cubic $NaYF_4$:Yb^{3+}/Er^{3+}.

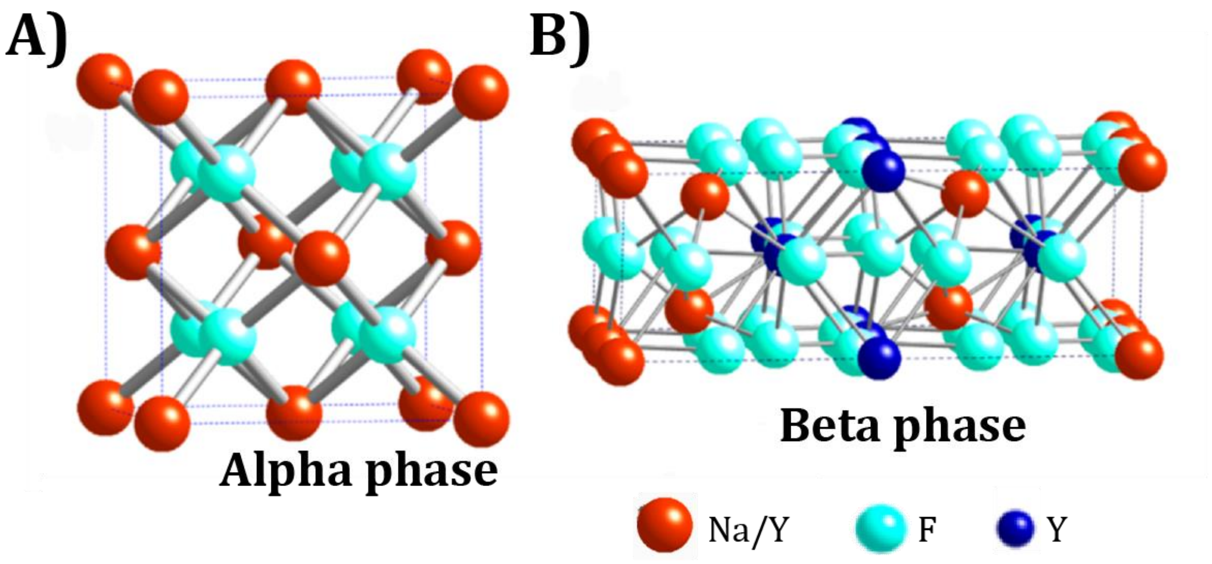

Figure 13. $NaYF_4$ crystal structure **A)** Alpha phase **B)** Beta phase.

It is possible to control the formation of one or the other crystalline phase by the different synthesis methods or the parameters used, e.g. strategies at low temperatures 290°C-295°C promote the formation of polymorphisms with a dominance of the cubic phase, while at a high reaction temperature of 310°C the nanoparticles obtained have a hexagonal phase.[81]

1.3.2 Downconversion nanoparticles (DCNPs)

Photoluminescence bioimaging is an in vivo technique that, by collecting light in the bodies of animals (rather than in anatomical tissues or cell cultures), allows visualization of biological structures, processes, and functions with a high degree of precision and spatial resolution, surpassing other imaging techniques such as X-rays or nuclear magnetic resonance.[82] For decades, bioimaging has used techniques that detect light in the visible (400-700 nm) and infrared (NIR I 700-900 nm) regions of the spectrum. These regions of the electromagnetic spectrum present many challenges because living tissue in this range exhibits autofluorescence and a high scattering coefficient, resulting in a diffuse image with reduced contrast.[83] In the last decade, alternatives have emerged to address these problems. One of these is the development of luminescent or fluorescent probes that emit in regions of the near infrared where tissue and water have no emission. These regions are also known as biological windows. A variety of materials that serve this purpose have been investigated, including small molecules,[84,85] polymer-encapsulated dyes,[86,87] "quatum dots" (QDs),[88,89] and nanoparticles.[90,91]

Materials that emit in the NIR range include nanoparticles doped with rare earths. Taking advantage of the unique properties of UCNPs and their potential bioapplications, numerous studies have been conducted to optimize the optical properties of these nanomaterials. Despite these efforts, challenges remain related to their low up-conversion efficiency, limited hosts, and limited wavelength. [92] Recently, strategies have been developed using other types of p-lanthanide ions such as Nd^{3+} because their excitation wavelength provides an alternative to UCL. As mentioned in the previous section, downconversion is a Stokes-shifted emission. It occurs when a lanthanide ion is excited from the ground state G to the excited state E_2 (Figure 11). Later, the photon relaxes non-radiatively to the metastable level E_1, from which light emission occurs. It is important to note that the nonradiative relaxation process from the E_2 to E_1 state is governed by the dynamics of the phonons within the nanophosphor.[93] This phenomenon is also known as **quantum cutting** or "quantum splitting" because one high-energy photon is absorbed and two low-energy photons are produced, with emission generally occurring in the NIR spectrum.[83]

Fifteen lanthanides show down-conversion luminescence. The ions of Pr^{3+}, Nd^{3+}, Ho^{3+}, Er^{3+}, and Tm^{3+} are the most promising for applications in the NIR because their spectral lines lie in the 1000 to 1700 nm region of the electromagnetic spectrum.[94] The main resonant energy levels are $^1G_4$ for the Pr^{3+} ion (98.80 cm^{-1}), $^4F_{3/2}$ for the Nd^{3+} ion (11260 cm^{-1}), $^5I_6$ for the Ho^{3+} ion (8610 cm^{-1}), and $^4I_{13/2}$ for the Er^{3+} ion (6610 cm^{-1}).[83] There are processes that compete with the DCL and reduce the intensity of emission in the NIR, the upconversion process, the luminescence quenching effect caused by nonradiative cross-relaxation processes between neighboring ER ions or by the transfer/migration of excitation energy to a point where electrons are trapped, such as defects or impurities in the host lattice. This quenching problem becomes more important when lanthanide-doped probes are used in biological applications because the energy transfer from ER ions to the OH groups of the aqueous solution is significant.[95] Apart from this, the efficiency of luminescence is determined by: **(1)** the population of the resonance level by direct excitation or sensitization; **(2)** competing processes, including but not limited to upconversion luminescence, nonradiative cross-relaxation, and the aqueous quenching effect; **(3)** the intrinsic efficiency of the 4*f*-4*f* transitions of the electric dipole of the RE ions themselves. The most studied emitter ions to date are Er^{3+} and Nd^{3+} due to their luminescence emission in the NIR-II window, which is at 1550 and 1050 nm, respectively. Lanthanide-doped ions have been synthesized with a variety of inorganic hosts, including: $LaPO_4$, LaF_3, $NaYF_4$, and $CePO_4$.[96]

DCNPS were initially focused on applications in solar energy[63] or telecommunications.[97] The first attempts to use DCNP as biomedical imaging agents (NIR I or NIR II) were made in the last two decades. In 2002, Veggel et al. reported Nd^{3+}-doped LaF_3 nanoparticles that exhibited emissions in NIR I and NIR II when excited with a laser at 514 nm. These materials initially attracted attention because they were in the second "telecommunication window" (where silica fibers exhibited improved efficiency and enhanced long-range transmissions) and were considered promising for polymer-based optical components.[98] In 2006, inspired by Veggel's work, Wang et al. developed a simple method to synthesize $LaF_3:Nd^{3+}$ in aqueous solution at low temperature and indicated that this type of DCNP would have potential application in biomedical imaging. Since then, research has been conducted on the development of various biosensors, with applications *in-vivo* and *ex-vivo*, making DCNP nanoparticles a new branch of nanophosphors.

In vivo fluorescence and luminescence based molecular imaging in the biological NIR window makes it possible to obtain higher-resolution images at tissue depths of less than a centimeter, taking advantage of the reduced light scattering and autofluorescence of tissue in the spectral range of 1,000-1,700 nm.[99,100] Currently, there are few probes in the literature that exhibit emission, including CNTs,[100] QDs such as lead sulfide (PbS),[101] from indium arsenide[88] and more recently the QDs from silver sulfide,[32] down-converting nanoparticles doped with rare earths can also be found.[69,102] DNPs have attracted great interest for in vivo biological imaging applications due to their unique properties such as millisecond lifetime, stable, superior photochemistry, low toxicity, and good biodistribution.[83] A recent work that combines all these properties is that of Hao et al, who synthesized luminescent nanorods of $NaLuF_4$: Gd/Yb/Er/Ce that emit an intense signal at 1525 nm, which was used to diagnose small tumors and metastatic formations in the brains of mice in a noninvasive manner and provided images with excellent resolution.[103] The impressive quality and clarity of in vivo images produced by detecting light emitted by DCNPs in the NIR have generated tremendous interest in research and activities in this field in recent years.[104] Bioimaging techniques have the prospect of becoming indispensable and helping us in the future to understand biological processes in vivo through images with spatial and temporal resolution never before seen in mammals. Furthermore, in theranostic systems may allow us not only to detect disease, but also to treat it *in situ*. The future development and applicability of in vivo bioimaging depend on the optical properties of the probes. Therefore, it is necessary to continue working on improving these optical properties, increasing the colloidal stability of nanoparticles in aqueous systems, and building highly specific biosensors.

1.4 Application of RE based nanoparticles in biomedicine

The use of novel RE nanoparticles for biological and therapeutic applications is an emerging area of research. Several research groups worldwide are investigating biomedical applications for these types of NPs. Their unique physicochemical properties help to significantly improve conventional approaches to disease diagnosis and therapies for human health. Most important applications of rare earth nanoparticles are discussed below.

1.4.1 Bioimaging

Magnetic resonance imaging (MRI) has become a powerful imaging tool because it provides high spatial and temporal resolution of the anatomical and physiological systems of the organism.[105] It is a non-invasive technique with a high penetrating capability. The application of RE nanoparticles for MRI has focused primarily on their use as contrast agents. In 2003, Donald *et al*. evaluated the physicochemical properties and magnetic resonance properties of gadolinium oxide nanoparticles. They concluded that Gd^{3+} is an excellent positive contrast agent for MRI because of the seven unpaired electrons in gadolinium, high paramagnetic stability, and slow electron relaxation.[106] In 2013, Mignot *et al*. injected rodents with gadolinium nanoparticles and followed their excretion by MRI. This showed that excretion of these nanoparticles from the body occurs exclusively through the kidneys.[107] in 2014, thanks to ICP analysis, *Sancey et al*. confirmed that excretion of the nanoparticles occurs via the kidneys (Figure 14).[108]

One of the most studied applications in this field is the use of ultrasmall gadolinium nanoparticles to detect primary tumors, as it is a noninvasive technique that does not require ionizing radiation. Since the surface of rare-earth nanoparticles can be easily modified and seeded with different molecules, this enables the development of theracnostic systems, i.e., dual systems suitable for both in situ detection and treatment. Li *et al.* demonstrated this theracnostic approach by combining gemcitabine, an anticancer drug, with gadolinium nanoparticles used in MRI. In this study, the nanosystem was shown to be able to increase the retention time and contrast of the signal in a mouse model with inhibition. MDA-MB-231 tumors in vivo very effectively.[109] Systems combining the properties of gadolinium nanoparticles (suitable for T1) with magnetic nanoparticles (suitable for T2) have also been developed to create dual contrast agents for T1 and T2 that improve the quality of MRI images.[110,111]

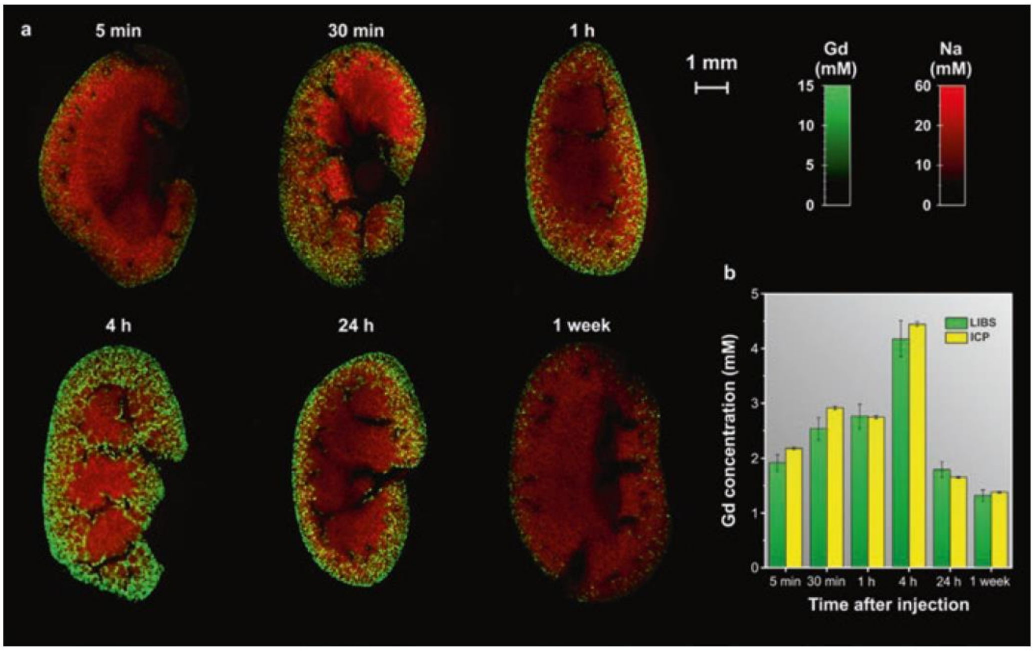

Figure 14. Distribution of gadolinium-based nanoparticles in the kidney as a function of the time elapsed since administration. (**a**), Quantitative imaging of Gd and Na in kidney coronal sections. The images were recorded at a 40-mm resolution and represent 30,000 pixels. (**b**), Agreement between the Gd concentrations measured via LIBS (green) and ICP (yellow). [108]

1.4.2 Biosensing

Biosensing is usually the detection of biologically active molecules or parameters that are critical for biomedical and environmental applications. In the last decades, various researchers have thoroughly investigated the potential of RE -nanoparticles for biosensing applications. In the case of RE -NPs, the luminescence lifetime is independent of concentration and excitation power, and variation in lifetimes may indicate interactions with the environment. In addition, RE -NPs can be used for simultaneous detection of multiple substances due to the multiple and sharp emission bands.[112] Many substances, from inorganic ions to cells, have been detected using this type of nanoparticle. Normally, biosensing with RE -NPs is based on direct detection of luminescence, luminescence resonance transfer signal or using their lifetime.[113]

In 2015, Stipic *et al*. showed that luminescence resonance energy transfer of rare earth-based nanoparticles can be used to detect immune responses triggered by biotoxins.[114] Tan *et al.* prepared coordination polymer nanoparticles (CPNPs) based on terbium (Tb^{3+}) and demonstrated detection of the drug ciprofloxacin in urine samples at low. Jin *et al.* prepared $NaYF_4$:$Yb_{(20\%)}$,$Tm_{(1\%)}$ nanoparticles with a lifetime of 160 µs and detected single *Giardia lamblia*, a parasite that causes the diarrheal disease known as giardiasis, using a time-gated orthogonal scanning automated microscopy platform.[115] Zhang *et. al.* prepared $NaGdF_4$:Yb,Ln^{3+}@$NaYF_4$:Yb@$NaNdF_4$:Yb@$NaYF_4$ nanoparticles with a core-shell-shell structure with Yb^{3+}/Ln^{3+}-doped activation core, a Yb^{3+}-doped energy relay layer, a Nd^{3+}/Yb^{3+}-doped energy absorption layer, and an inert outer layer. [112] The doped Ln^{3+} in the activation core conferred different emission colors and lifetimes when illuminated by an 808-nm laser. These nanoparticles were incorporated into porous polystyrene microspheres, and the composites were used for simultaneous detection of human papillomavirus (HPV) subtypes in patient samples using a time-resolved imaging system.[112] In our research group, Mendez Gonzalez et al. have developed a biosensor based on $NaYF_4$:Yb,Er@SiO_2 nanoparticles functionalized with ssDNA to detect small oligonucleotides with high specificity.[116]

Regarding in vivo and in vitro applications of RE -NPs as biosensors, there is work such as that of Ren *et al.* who developed an Er-based lanthanide nanoparticle of $NaErF_{4:2.5\%}$Ce@$NaYbF_4$ coupled with a dye-brush polymer (Dye- BP) with an emission wavelength of 1525 nm, which is close to the infrared II biological imaging window. They also conjugated a tumor-targeting angiopep-2 peptide that could target gliomas in a mouse model. Using this luminescent probe (IR), they successfully removed the glioma from the mouse brain.[117]

1.4.3 Therapeutic Applications

Due to the characteristic properties of rare earth nanoparticles, they can be used in various biomedical applications as part of a treatment and not only for diagnostic and imaging applications. Their main therapeutic properties include antimicrobial, anticancer, angiogenic, and radioprotective agents, etc.[118] The combination of all these properties explains their role in the diagnosis and treatment of cardiovascular, diabetic, vascular, inflammatory, and immunological diseases, where they act as theracnostic systems.[112]

1.4.3.1 Drug Delivery

RE -NPs are considered promising for drug delivery compared to conventional therapeutics. This is because therapeutic moieties at bulk scale possess certain limitations, such as minimal selectivity, low specificity, and poor solubility.[119] Therefore, RE-NPs nanoparticles have successfully demonstrated that they can overcome the major challenges of bulk therapeutic materials by showing therapeutic efficacy at lower dosages with minimal toxicities and higher precision. Moreover, the target specificity of the ligands is an advantage for their use as drug carriers. *Rajendiran et al.* synthesized lanthanum fluoride-doped terbium nanoparticles functionalized with chitosan and used as carriers for methotrexate. This facilitated targeted delivery of the drug to cancer cells and showed a greater extent of cytotoxicity (MCF -7) than the free drug.[120] *Yang et al.* synthesized $NaREF_4$ nanoparticles (RE including neodymium, lutetium, and ytterbium). Their results demonstrated the biocompatibility of the complex with certain in vitro assays and confirmed its application for the delivery of the anticancer drug doxorubicin (DOXO) to HeLa cells.[121] Li *et al*. synthesized gadolinium-based nanoparticles loaded with gemcitabine monophosphate, an anticancer drug. They observed significant in vivo tumor inhibition in mouse model with higher retention time and better diagnosis with improved MRI contrast.[109] Wu et al. synthesized a β-$NaYF_4$:$Ce^{3+}Tb^{3+}$ complex and encapsulated it in mesoporous silica nanocomposites. They used it as a drug carrier for the controlled release of DOX and confirmed significant cytotoxicity (toward A549 cells) by in vitro assays.[122]

1.4.3.2 Imaged-Guide Therapy

In theranostics, the luminescent property of lanthanide nanoparticles helps determine the precise location of therapeutic needs, which is referred to as "image-guided therapy." The luminescent or fluorescent properties of lanthanide nanoparticles are induced by 4f-4f transitions and contribute to numerous applications in therapy.[123] Lanthanide nanoparticles act as multimodal platforms that serve as systems for imaging and also for treatment. Hagan et al. reported that the use of rare earth nanoparticles in the form of chelate markers in immunoassays increased sensitivity and overcame the problem of autofluorescence. The sustained luminescence of rare earth nanoparticles with very minimal interference is the most important factor for their use in therapeutic techniques.[124] Victor *et al*. synthesized a complex of hydroxyapatite and conjugated alginic acid as a carrier of the drug 4-acetylsalicylic acid for the treatment of colon cancer. When the complex was doped with neodymium, it achieved the ability to fluoresce in the near IR, making it a good choice for early detection and targeted treatment of tumors.[125] In 2014 Rocha *et al.* reported that neodymium ions, when doped with lanthanum fluoride nanoparticles, show promise as probes for bioimaging of target areas because of their high penetrating power (up to 1 cm), high image contrast, and lower autofluorescence.[126] Singh *et al.* synthesized a nanohybrid with SnO_2 nanoparticles doped with Tb^{3+} ions incorporated into a polyvinyl alcohol matrix, the nanohybrid exhibits biocompatibility toward HeLa cells at higher concentrations and possesses luminescent properties, thereby supporting optical imaging of the target area both *in vitro* and *in vivo*.[127] In 2021, Liu et al. reported imaging and therapy of glioblastoma using dye-sensitized core-shell $NaYF_4$:Yb/Tm@$NaYF_4$:Nd nanoparticles with strong upconversion/downconversion luminescence. Their UV upconverting emission was used to monitor the release of SO_2 from the 5-amino-1,3-dihydrobenzo[c]thiophene-2,2-dioxide prodrug for gas therapy, and the NIR-II downconverting emission at 1340 nm was used for imaging.[128]

1.4.3.3 Angiogenesis/Anti-angiogenesis Activity

Angiogenesis is the process of growth and development of new blood vessels from pre-existing vessels, which is tightly regulated in various pathophysiological processes. Under physiological conditions, it is controlled by growth factors, such as VEGF (vascular endothelial growth factor), etc. Under certain disease conditions, when the endogenous production or activity of growth factors is disturbed, exogenous delivery of growth factors/molecules is required to restore the process of angiogenesis. Recently, several research groups have thoroughly investigated the design, development, and therapeutic application of various pro-angiogenic rare earth lanthanide nanoparticles.

Augustine *et al* (2017) have demonstrated the pro-angiogenic properties of europium hydroxide nanorods (EHNs) *in vitro* using different in endothelial cells and *in vivo* using chick embryo and zebrafish test systems. EHNs have been shown to promote endothelial cell proliferation, cell migration, and vessel formation, which are hallmarks of angiogenesis. EHNs have been reported to induce blood vessel formation in vivo in chick embryos and transgenic zebrafish.[129] In 2016, Zhao *et al.* investigated rare earth nanoparticles such as europium hydroxide/terbium hydroxide nanoparticles in transgenic zebrafish model. The results showed that these nanoparticles trigger angiogenesis through redox signalling.[130] Other nanoparticles, such as cerium oxide nanoparticles, were extensively studied for their angiogenesis/anti-angiogenesis properties. Das et al. reported the stimulation of angiogenesis by cerium oxide nanoparticles.[131] The nanoparticles promote the formation of endothelial tubes and support the growth of blood vessels in the chicken embryo by activating HIF-1α and VEGF via modulation of intracellular oxygen content.[131]

1.4.3.4 Anticancer Therapy

Cancer is one of the most important health problems worldwide, causing about one million deaths in the world every year. It is a disease that has accompanied mankind for thousands of years, and over time various approaches have been studied. Currently, it is treated mainly by surgery, chemotherapy, radiotherapy, and targeted therapies. Rare earth nanoparticles are a more recent approach because, as mentioned earlier, they have luminescent properties that are suitable for signaling the location of a tumor. They also have an easily modifiable surface that allows them to bind anticancer drugs. In addition, they themselves have anticancer properties that improve the effectiveness of therapy. Lai *et al*. synthesized lanthanum hexaboride nanoparticles coated with carbon doped silica (LaB_6@C-SiO_2) and studied them on Hela cell lines, showing significant cytotoxicity upon near-infrared irradiation. They found that LaB_6@C-SiO2 provides an alternative source for the use of gold nanoparticles as a cost-effective photothermal treatment in cancer therapy.[132] Bakht *et al.* experimented on non-small cell type lung cancer insensitive to chemotherapy and observed dual therapeutic significances of nano Pr_2O_3, nano Nd_2O_3 particles in cancer treatment since nano Pr_2O_3 holds radiotherapeutic property and this when decays to nano Nd_2O_3 attains autophagy-inducing property to cancer cells.[133] In 2019, Panda *et al.* synthesized CeO_2 nanoparticles to investigate their efficacy as anticancer agents. Their results showed that the nanoparticles exhibited remarkable differential cytotoxicity against healthy (BHK121, baby hamster kidney cells) and human colon cancer cells (HCT116). Nuclear fragmentation assay showed significant DNA fragmentation in HCT116 cells, while an intact nucleus was observed in normal cells, suggesting that cerium induces apoptotic cell death in colon cancer cells.[134]

Intensively researched for various applications in medicine. Therefore, it is important to optimize the synthesis patterns, make them more stable in biological media, increase their quantum efficiency, improve their biodistribution, avoid quenching improve the optical properties, etc., to get more out of this tool. For this reason, the aim of this PhD thesis is to perform a comprehensive study on lanthanide-based nanoparticles. It starts with optimizing the optical properties of $NaYF_4$:Yb^{3+}/Er^{3+} nanoparticles in UCL and DCL by varying the ratio between the dopants. Subsequently, the stability and luminescence of the same nanoparticles in water were improved by coating with different polymers, we also studied the increase in fluorescence and thermal sensitivity of $NaYF_4$@Nd^{3+},Yb^{3+}@CaF_2 downconversion nanoparticles and how the thickness of the active shell affects these properties. Finally, these same particles were used as a platform to stabilize VEGF protein to enhance endothelial cell proliferation in vitro and in vivo.

2. Objetivos

OBJETIVOS

Esta tesis doctoral está orientada a cuatro objetivos generales donde cada uno constituye un proyecto en si, por lo que cada objetivo general representa un capítulo de este escrito.

1) Realizar un estudio básico sistemático de nanopartículas de conversión ascendente de $NaYF_4$ dopadas con Yb^{3+} y Er^{3+} variando la ratio entre los dopantes (entre el 0 y el 22% en total) y la densidad de potencia con el fin de observar qué ocurre con las propiedades ópticas de las nanopartículas y sus emisiones de fluorescencia de conversión ascendente y descendente.

2) Recubrir las nanopartículas $NaYF_4:Yb^{3+}/Er^{3+}$ con distintas capas de polímeros hidrofóbicos e hidrofílicos, volviendo así las nanopartículas más estables en agua, medios biológicos, resistentes a aumentos de temperatura y evitando el quencheo de la luminiscencia.

3) Estudiar las propiedades ópticas y la sensibilidad térmica de nanopartículas basadas en lantánidos de $NaYF_4@Nd^{3+},Yb^{3+}@CaF_2$ en función del grosor del Shell activo.

4) Incrementar la proliferación celular en el proceso de angiogénesis de células endoteliales, utilizando un complejo compuesto por nanopartículas downconversion $NaYF_4@Nd^{3+},Yb^{3+}@CaF_2@VEGF\text{-}A$.

3. *Objectives*

OBJECTIVES

This dissertation is guided by four general objectives, each of which is a project, so that each general objective constitutes a chapter of this writing.

1) To perform a basic systematic study of $NaYF_4$ nanoparticles for upconversion doped with Yb^{3+} and Er^{3+}, varying the ratio between the dopants (between 0 and 22% total) and the power density to observe what happens to the nanoparticles. Optical properties of the nanoparticles and their fluorescence emissions upon upconversion and downconversion.

2) Coat the $NaYF_4$:Yb^{3+}/Er^{3+} nanoparticles with different layers of hydrophobic and hydrophilic polymers to make the nanoparticles more stable in water and biological media, more resistant to temperature increases, and prevent quenching of luminescence.

3) Investigate the optical properties and thermal sensitivity of nanoparticles based on $NaYF_4$@Nd^{3+},Yb^{3+}@CaF_2 lanthanides as a function of active shell thickness.

4) Enhancement of cell proliferation in the process of angiogenesis of endothelial cells by a complex of $NaYF_4$@Nd^{3+},Yb^{3+}@CaF_2@VEGF-A downconversion nanoparticles.

4. *Materials & Methods*

Materials and Methods

4.1 Chemicals

4.1.1 Chemicals using in synthesis

The following products were bought from Sigma-Aldrich Inc (Saint Louis MO, USA) and used without further purification: ytterbium(III) chloride hexahydrate (99.9%)($YbCl_3·6H_2O$), yttrium(III) chloride hexahydrate (99.9%) ($YCl_3·6H_2O$), erbium(III) chloride hexahydrate (99.9%) ($ErCl_3·6H_2O$), Neodymium (III) chloride hexahydrate (99.9%) ($NdCl_3·6H_2O$), sodium hydroxide (NaOH) (≥98%), calcium chloride ($CaCl_2$) (≥99%), ammonium fluoride (NH_4F) (≥98%), oleic acid (OA) (≥90% GC), 1-octadecene (ODE) (technical grade 90%), oleylamine (OA) (technical grade 70%), methanol (MeOH) (≥99.9% HPLC), absolute ethanol (EtOH), n-hexane (≥97% GC), dimethyl sulfoxide (DMSO) (≥99.9%), Toluene (>90%), chloroform ($CHCl_3$)(≥99.8%), N,N-dimethylformamide (DMF) (>99%), nitrosyl tetrafluoroborate ($NOBF_4$) (95%), styrene (>99%), methyl methacrylate (99%), hexadecane (HD) (99%), sodium dodecyl sulfate (SDS) (>99%), potassium persulfate (KPS) (≥99.9%), 10-methacryloyldecylphosphate (MDP, 99%) poly-acrylic acid (PAA) (Concentration=50wt% in water; Mw~5000g/mol) potassium phosphate dibasic trihydrate (≥99%, Reagent Plus), Cyclohexane (≥ 97% GC), Hydrochloric acid (HCl) (37%), Trifluoroacetic acid (99%) (TFA), sodium trifluoroacetate (NaTFA), N-(3-Dimethylaminopropyl)-N′-ethylcarbodiimide hydrochloride (99%) (EDC·HCl), N-hydroxysulfosuccinimide sodium (Sulfo-NHS) (≥96%), 2-(N-Morpholino)ethanesulfonic acid (MES) (≥99%), Sodium chloride anhydro (NaCl) (≥99%), 4-(2-Hydroxyethyl)piperazine-1-ethanesulfonic acid (HEPES) (99.5%), was purchased from LGC Group, Spain. Cooper TEM grids were brought from Structure probe Inc (west Chester, PA, USA), Formvar solution was obtained from SIGMA.

4.1.2 in-vivo and in-vitro experiments

Dulbecco's Modified Eagle Medium (DMEM low glucose, GlutaMAX Supplement #10567014 Life Technologies), Endothelial Growth medium serum free (EGM-SFM, CellBiologics), Fetal Bovine Serum (FBS, #10270-106 Life Technologies), Penicillin (Sigma Aldrich), Streptomycin (Sigma Aldrich), Trypsin Protease (Ms Grade, Thermo Fisher), Gelatin Solution from porcine skin and Fibronectin solution from bovine plasma (Sigma Aldrich), Phosphate buffered saline solution (PBS, Thermo Fisher), Bovine Serum Albumin (BSA, Sigma Aldrich), Paraformaldehyde Solution (PFA, Boster Solutions), Tween 20 (Sigma Aldrich), Triton™ X-100 (Sigma Aldrich), Human monoclonal antibody anti CD31/PECAM-1 (eBioscience™, Thermo Fisher), Click-iT™ EdU Imaging Cell Proliferation Kit, Alexa Fluor™ 647 Dye (Invitrogen, Thermo Fisher), Hoechst 33342, trihydrochloride, trihydrate-10 mg/ml solution in water(Invitrogen, Thermo Fisher), StemPro™ Accutase™ Cell Dissociation Reagent (Thermo Fisher).

4.2 Methods and instrumentation Used

4.2.1 *Transmission Electron Microscopy (TEM), High Resolution Transmission Electron Microscopy (HR-TEM) & High-angle Annular Dark-field Imaging (HAADF)*

The transmission electron microscope (TEM) takes advantage of the physical-atomic phenomena that occur when an electron beam strikes an ultrathin sample. Depending on the thickness and type of atoms that make up the sample, the collided electrons are selectively scattered. Some of the electrons bounce off or are absorbed by the object, while others penetrate it and produce a magnified image of the sample. The image is focused by a fluorescent screen or sensor, such as a charge coupled device (CCD) camera. The electron gun, the source of emission of the beam, which may be a tungsten filament, is connected to a voltage source that is in the range of 80-300 kV. The electron beam is manipulated by combining several sets of lenses. The condenser lenses are responsible for the initial formation of the beam after the emission of electrons, the objective lenses focus the beam onto the sample, and the projection lenses are responsible for expanding the reflected beam onto the screen.

High-resolution transmission electron microscopy (HRTEM) uses both transmitted and scattered beams to produce an interference image. It is a phase-contrast image and can be as small as the crystal's unit cell. Here, the outgoing modulated electron waves interfere with themselves at minimal angles as they propagate through the objective. All the outgoing electrons from the sample are merged into one point in the image plane. HRTEM has been used extensively and successfully to analyze crystal structures and lattice defects in various types of advanced materials at atomic resolution. It can characterize point defects, faults, dislocations, precipitates, grain boundaries, and surface structures.

HAADF is a technique that produces an annular dark field image formed by the scattering of electrons at very high angles. The images are created based on the atomic number (Z) of the atoms present in the sample. When the electron beam interacts with the nucleus of the atom, many electrostatic interactions occur when the analyzed element has a high Z number, resulting in more scattered electrons at high angles. Consequently, the HAADF detector detects a larger signal, making these elements appear brighter on the resulting image. This strong dependence on Z makes HAADF a useful method to easily identify small regions of high Z element in a matrix of lower Z material. An extremely important application for HAADF is the determination of the size and distribution of metal particles.

The chemical and morphological characterization of RE-NPs was carried out using a JEOL JEM 1010 electron transmission microscope (TEM) working at a voltage of 80 kV. High-resolution images were taken (HR-TEM) using a microscope JEOL JEM 2100 at a working voltage of 200 kV. High-angle annular dark-field (HAADF) scanning TEM and EDX mappings have been realized using an FEI Talos F200X (FEI, USA, 80 kV) coupled to an EDX detector. All samples were prepared by adding 10 mL of the UCNPs solution (ca. 3mg/mL) on a Cu or Cu/C grid and allowing the solvent to evaporate at room temperature.

4.2.2 Fluorescence Microscopy

Fluorescence microscopy, as the name implies, is a microscopic technique that uses fluorescence and phosphorescence instead of the usual phenomena of light reflection and absorption. In this technique, the sample is illuminated with a much higher intensity of light. This light excites fluorescent species in the sample, which then emit light. The image produced is based on the second light source or emission wavelength of the fluorescent species rather than the light originally used to illuminate and excite the sample. Light of the excitation wavelength is focused on the sample through the objective lens. The fluorescence emitted from the sample is focused through the objective lens onto the detector. Since most of the excitation light is transmitted through the sample, only the reflected excitation light reaches the objective lens along with the emitted light.

Fluorescence images were acquired with Leica inverted fluorescent microscope equipped with Leica DFC450 C camera using LAS V4.4 software (Leica Microsystems), Nikon Eclipse Ti-E inverted fluorescent microscope equipped with DC-152Q-C00-FI using NIS V4.30 software (Nikon) and Zeiss Laser Scanning microscope. Images were acquired at 4x or 20x magnification. Individual 4x magnification fields were stitched together using Image Composite Editor software (Microsoft Research).

4.2.3 Fourier transform Infrared (FT-IR) spectroscopy

Infrared spectroscopy (IR) is based on the molecular absorption of electromagnetic radiation in the infrared region, which promotes transitions in the ground states (lowest energy) of the molecule's rotational and vibrational energy levels. This absorption is characteristic of the type of chemical bond present in the sample. A spectrometer is used to measure this absorption as a function of wavelength (in terms of wavenumber, usually 4000-600 cm^{-1}). The result is a spectrum that serves as a characteristic "molecular fingerprint" and allows identification of functional groups in organic and inorganic samples.[135]

Previously, samples were analyzed stepwise by irradiation. Diffract samples with different lengths of the individual (scattered) waves. In Fourier transform infrared spectroscopy (FTIR), on the other hand, spectral data at all wavelengths are obtained in a single transmission. Here, a continuous IR source generates light at a broad infrared wavelength. The infrared light passes through the interferometer and is then shone directly onto the sample. Unlike scattered light measurements, an interference program is first generated, which must be converted to a IR spectrum. This interference (a raw signal) represents the light intensity not as a function of wavelength, but as a function of the position of the moving mirror in the interferometer. Therefore, the signal is first subjected to a Fourier transform (FT) to obtain an IR representation of intensity as a function of wavenumber. The acquisition of the FTIR spectrum is not only faster than conventional instruments. In addition, these spectrometers have a much better signal-to-noise ratio, and because the laser-calibrated wavelength scale is so precise, the wavelength accuracy is much higher.[135]

To characterize the nanoparticles, in particular to confirm that the different functionalization performed were successful, a Thermo Nicolet 200IR spectrometer was used to obtain FT-IR spectra. The samples were prepared by grinding the dried nanoparticles with potassium bromide (KBr) until a thin powder was obtained. The powder was then processed into a pellet using a mechanical press (at 10 tons). While air and moisture were removed using a vacuum pump. Background and sample spectra were recorded in absorption mode with a resolution of 4 cm^{-1} and 128 scans. The spectra were H_2O and CO_2 corrected.

4.2.4 Thermogravimetric analysis (TGA)

The thermogravimetric analysis is a characterization technique that allow to determinate the decomposition temperature of organic compounds. TGA measures weight changes in a material as a function of temperature (or time) under a controlled atmosphere (Nitrogen and air). When the material is hybrid between organic an organic part (e.g., the lanthanide-based nanoparticles) is possible to determinate the ratio between them, also is possible to characterize and quantify the ligands linking in the nanoparticles surface.

TGA analyses were performed using a TGA/DSC 1 STAR system (Mettler Toledo). In a typical experiment, concentrated samples (~6 mg of nanoparticles) were deposited and dried at 82° C in a 70 µL alumina crucible, which was weighed before and after sample addition and drying by using both the TGA/DSC internal microbalance and an external microbalance (AT261 DeltaRange, Mettler Toledo), for comparison. The samples were then introduced into the TGA/DSC and after stabilization, the experiment was started. The heating program consisted in i) heating to 120°C at a heating rate of 5 °C/min; ii) holding the temperature at 120 °C for 30 min to evaporate traces of adsorbed water; iii) increasing the temperature to 530 °C at a rate of 10 °C/min; iv) maintaining the temperature at 530 °C for 10 min; v) returning to the starting temperature. The gas flows used during the experiments were 20 cm^3/min for O_2 and N_2, respectively.

4.2.5 Dynamic light scattering (DLS)

Dynamic light scattering (DLS) is photon correlation spectroscopy or semi-elastic scattering of light. It is a physicochemical technique for determining the size distribution of suspended particles or macromolecules in solution, such as nanoparticles, proteins, or microgels.

DLS is based on the Brownian motion of the scattered particles. The principle of Brownian motion is based on the fact that particles constantly collide with solvent molecules. When particles are dispersed in a solution, they move randomly in all directions. During these collisions, a certain amount of energy is transferred, which triggers the movement of the particles. The energy transfer is constant and therefore affects smaller particles more. As a result, smaller particles move at higher speeds than larger particles. If all other parameters affecting the motion of the particles are known, the hydrodynamic diameter can be determined by measuring the velocity of the particles.[136]

The relationship between the velocity of the particles and the size of the particles is given by the Stokes-Einsteins equation (Equation 6). The velocity of the particles is determined by the translational diffusion coefficient D. In addition, the viscosity of the dispersant and the temperature are included in the equation since these parameters directly affect the movement of the particles. The basic requirement for the Stokes-Einstein equation is that the motion of the particles is based solely on Brownian motion. Once deposition begins, there is no more random motion, which would lead to inaccurate results. Thus, the onset of deposition creates an upper size limit for DLS measurements. In contrast, the lower size limit is determined by the signal-to-noise ratio. Small particles do not scatter much light, resulting in an inadequate measurement signal.[136]

$$D = \frac{k_B T}{6\pi\eta R_H}$$

Equation 6

Where D is the translational diffusion coefficient “speed of the particles”, k_B is the Boltzmann constant, η is the viscosity, and R_H is hydrodynamic radius.

In this project, the samples' hydrodynamic diameter (Dh) was determined using a ZetaSizer Nano ZS (Malvern Instruments). The accumulation time was determined automatically for each sample. The multimodal analysis method was selected in the DLS software provided by Malvern using the Stokes-Einstein equation. For DLS experiments, samples were diluted to ~50 µg/mL.

4.2.6 X-ray powder diffraction crystallography

The physical and chemical properties of nanoparticles are strongly influenced by the size, shape and structural strain of the particles, including: rheology, surface area, cation exchange capacity, solubility, reflectivity, etc. The crystallite size is determined by measuring the magnification of a particular in-plane X-ray reflectance within the crystal cell unit. The magnification is inversely related to a single peak's width at half height (FWHM): the narrower the peak, the larger the crystallite. This is due to the periodicity of the in-phase crystallite domains, which enhance the X-ray diffraction and result in a tall and narrow peak. If the crystals are free of defects and periodically arranged, the X-rays will be diffracted at the same angle, even though the different layers of the sample. If the crystals are randomly arranged or have a shallow degree of periodicity, the peaks will be wider.

To determine the crystalline phase, X-ray diffraction (XRD) patterns of the dried UCNP powders were recorded using a PANalytical Model XPPert PRO MPD Multi-Purpose Diffractometer from 10° to 70 °.

4.2.7 Z-Potential

The Z-potential is the capacitance describing the intensity of the static electric field of the Double layes (DL) at the boundary between the nano and the liquid. Colloids have a surface charge caused by the particles and their environment.[137] This leads to colloidal stability due to Van der Waals interaction forces and repulsive forces of the DL. This stability can be affected by pH, concentration, and conductivity. For the Z-potential, values close to 0 indicate low colloidal stability because the repulsive forces are low, leading to aggregates of the nanoparticles. In addition, the Z-potential measures the charge on the surface of the nanoparticles, which helps to verify whether the surface of the nanoparticles is properly functionalized.[137]

Z-potential measurements were performed using a Malvern Nano- ZS instrument. Samples for Z-potential experiments were freshly prepared prior to measurements by diluting them to a final concentration of ~50 µg/mL. Measurements were performed at 25°C using the automatic mode (10 minimum runs - 100 maximum runs), with an equilibration time of 120 seconds and the Smoluchowski fit model. At least 3 independent measurements were performed for each sample.

4.2.8 *Steady-state photoluminescence measurements*

The luminescence spectra of the emission from the Lanthanide-Based nanoparticles were measured using a fluorescence system built by Professors Dr. Óscar Calderón Dr. Sonia Melle at the Faculty of Optics of the UCM in collaboration with Dr. Jorge Rubio-Retama at Pharmacy Faculty of UCM.[138] Figure 15 shows schematically the operation of the apparatus used to perform the photoluminescence measurements. The excitation beam comes from a 10 W CW twisted laser (JDSU, L4-9897603) operating at a wavelength of 976 nm and equipped with a current and temperature controller (ILX Lightwave, LDX-36025-12 and LDT -5525B, respectively). The laser beam is passed through a dichroic short-pass filter (Semrock, FF01-775 / SP) and then focused with a 10x objective on a Hellma 101.015- QS microcuvette, 3X3 mm^2 slice thickness. The luminescence of the sample is reflected by the dichroic mirror onto the short pass filter, which blocks the reflected radiation between 770 and 1050 nm.

The beam is then focused onto an optical fiber connected to a monochromator (Horiba Jobin Yvon IHR320). The monochromator uses an 1800 gram per millimeter grating fired at a wavelength of 500 nm and a photomultiplier tube (Hamamatsu, R928). To measure the upconversion luminescence in the emission required for each project, IR downconversion spectra were measured using a solid-state InGaAs detector (Horiba Jobin Yvon, DSS-IGA020TC) and a 900 gram per millimeter grating fired on at 1.5 µm. Three spectra were recorded for each sample. Intensity was calculated by integrating the area of the spectra within the emission bands and taking the maximum deviation as the error. The results shown without error bars correspond to a single representative measurement.

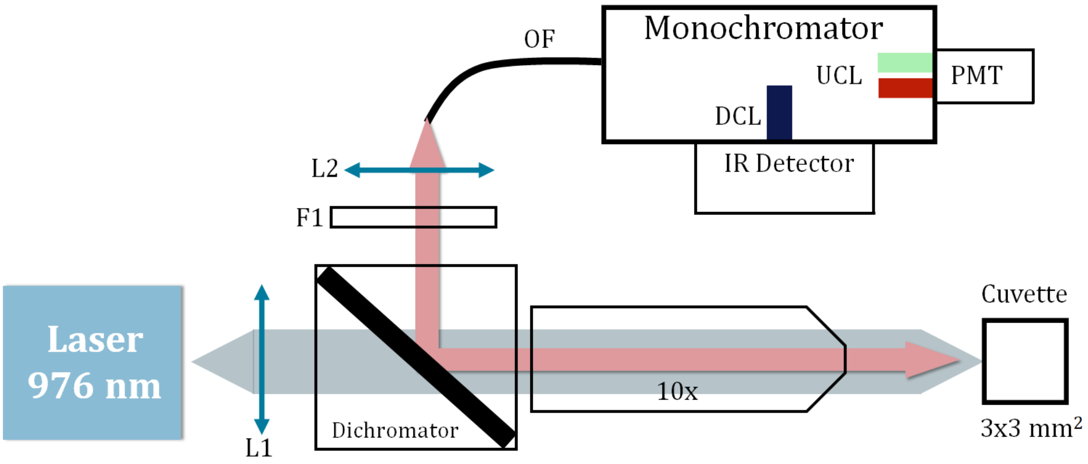

Figure 15. Schematic representation of the system for measuring upconversion and downconversion of luminescence.

4.2.9 *Photoluminescence lifetime measurements*

The time-resolved photon counting method was used to determine the luminescence lifetime of the different samples. Excitation pulses of 40 µs duration (with 125 Hz repetition rate) were generated using the laser current controller (LDX-36025-12, from ILX Lightwave). Luminescence emissions were detected by the photomultiplier tube connected directly (without using a preamplifier stage) to a 50 Ω input of a digital oscilloscope (Agilent, DSO9104A). The oscilloscope is triggered by a signal from the laser current control. Our in-house developed Matlab program was used to analyze each recorded signal in real time directly in the oscilloscope. This code simulates the discriminator and the multichannel counter. After analyzing more than 5000 trigger signals, a luminescence decay curve was generated. The luminescence lifetime was determined by fitting the decay curves to a double exponential function. The fit was made from the time when the luminescence reached 60% of its maximum value to the last recorded time (2 ms, long enough to ensure complete decay of the luminescence).

4.2.10 Ultrasonication

The ultrasonication step was performed with an ultrasonication tip (Branson 250 Sonifier, analog cell resolver; 200 W max output power) operating at 70% duty cycle with the output power in the "1" position (which sets the amplitude of the power supply output voltage to 10% of the nominal amplitude of the converter).

4.2.11 Western Blot

Western blot is generally used to separate and identify proteins. In this technique, a mixture of proteins is separated by gel electrophoresis according to their molecular weight and thus their type. These results are then transferred to a membrane, creating a band for each protein. The membrane is then incubated with labelled antibodies specific for the protein of interest. Figure 16 outlines the basic steps of the Western blot. The unbound antibody is washed off, leaving only the antibody bound to the protein of interest. The bound antibodies are then detected by developing the film. Since the antibodies bind only to the protein of interest, only one band should be visible. The thickness of the band corresponds to the amount of protein present. Thus, a standard can indicate the amount of protein present.

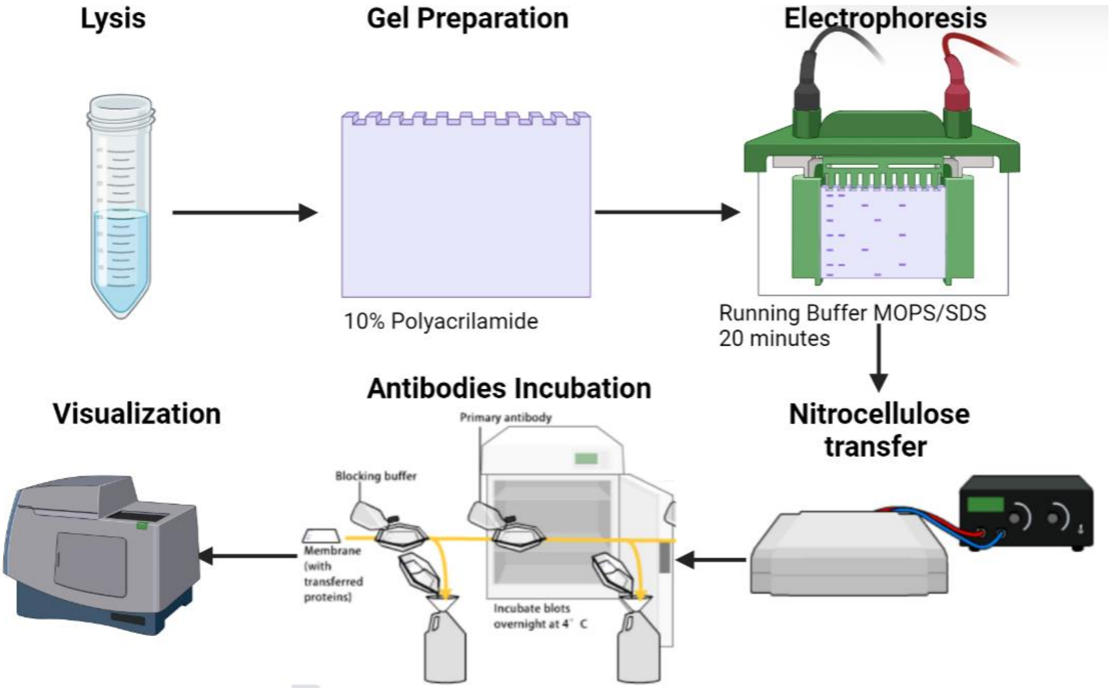

Figure 16. Scheme illustrating the basic steps in Western blotting. **1)** Cell lysis, **2)** Gel preparation, **3)** Electrophoresis 20 minutes, 180 V, **4)** Gel transfer to nitrocellulose. **5)** Incubation of antibodies and **6)** visualization by chemiluminescence.

4.3 Synthesis

4.3.1 Synthesis of $NaYF_4$: Yb^{3+}/Er^{3+} Upconversion Nanoparticles

Monodisperse β-$NaYF_4$:Yb_x,Er_y nanoparticles were synthesized following the thermal co-precipitation method.[139] First, appropriate amount of yttrium(III) chloride hexahydrate (236.63 mg, 0.78 mmol), ytterbium(III) chloride hexahydrate, and erbium(III) chloride hexahydrate were dissolved in 1 mL of MeOH. Afterward, the rare earth methanol solution was mixed with 1-octadecene (15 mL, 46.9 mmol) and oleic acid (6 mL, 19 mmol) in a three-neck round bottom flask by moderate stirring. The resultant mixture was heated to 140°C under a nitrogen flow at a heating rate of 5°C min^{-1} with a heating mantle (Nahita Blue, Serie 656) coupled to a temperature controller (JP selecta). At this point, HCl traces and solvents were removed by using a vacuum pump over 20 min. The next step was to add 10 mL of a methanol solution containing NaOH (100 mg, 2.5 mmol) and NH_4F (148.16 mg, 4.0 mmol), allowing the reaction to incubate for 30 minutes. The temperature was increased again to 110°C with a heating rate of 1°C min^{-1} under an N_2 flow. Again, a vacuum pump was used over 20 min. Finally, the solution was heated until it reached a temperature of 316°C and refluxed for 1 h. After the solution was cooled down to room temperature, nanoparticles were purified by splitting the product into four centrifuge tubes and vigorously mixing them with 4 mL of MeOH. Subsequently, the phases were separated, and the methanol phase was removed. Then, the sample was centrifuged at 8500 rpm for 20 minutes. The pellet was washed twice with 1 mL of EtOH without redispersing it. The pellet was finally dried and dispersed in 4 mL of hexane for storage. Figure 17 outlines the basic steps in synthesizing the UCNPS of β-$NaYF_4$: Yb^{3+}/ Er^{3+}.

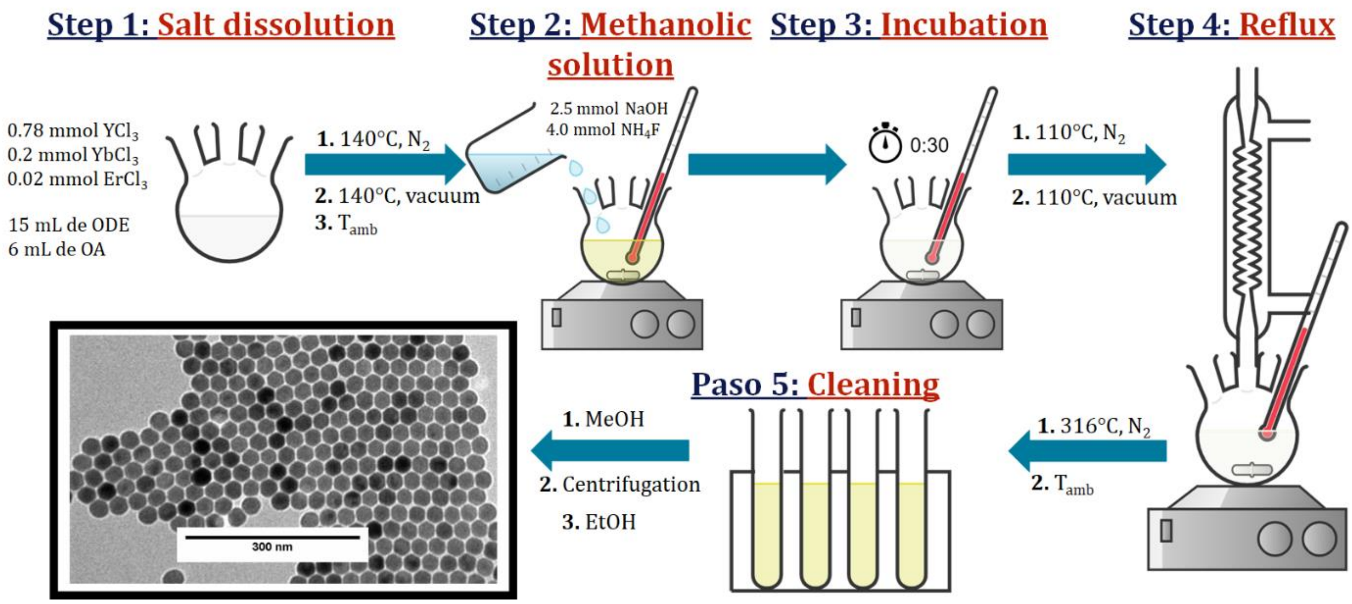

Figure 17. General scheme illustrating the steps in synthesizing UCNPs nanoparticles by thermal co-precipitation.

4.3.2 Removal of $NaYF_4$: Yb^{3+}/Er^{3+} Nanoparticles capping agent.

Removal of oleate (capping agent) from the surface of $NaYF_4$: Yb^{3+}/Er^{3+} nanoparticles synthesized in section 4.3.1 was performed using a slightly modified method.[140,141] Briefly, 8 mL of DMF was added to a 50 mL round bottom flask with a magnetic stir bar. Then, 100 mg of NPs in hexane were sonicated for 5 min and carefully added onto the DMF phase without stirring. Then, 100 mg of $NOBF_4$ was added to the flask and the two phases were mixed for 10 minutes with vigorous stirring. The removal of most of the oleate molecules from the surface of UCNPs was confirmed by their phase transfer from hexane to DMF. Previous reports indicated that 15-20% of the oleate could still adhere to the surface after this treatment.[140] The DMF phase was then extracted and divided into two Teflon centrifuge tubes, which were completed by adding $CHCl_3$ and centrifuged at 10,000×g for 10 min. Then, each pellet was redispersed in 1 mL of DMF, and the centrifuge tubes were refilled with 7 mL of $CHCl_3$ and centrifuged again. This procedure was repeated two more times. Finally, the $NaYF_4$: Yb^{3+}/Er^{3+} nanopaticles were redispersed in 2 mL DMF and stored.

4.3.3 Surface Functionalization with MDP of $NaYF_4$: Yb^{3+}/Er^{3+} Nanoparticles

First, 53 mg of MDP (0.17 mmol) was added to a glass vial with a magnetic stir bar. Then, 10 mL of $CHCl_3$ was added and the mixture was stirred vigorously until the MDP was completely dissolved. The amount of MDP was always adjusted to achieve a theoretical surface coating excess of ≈25 MDP molecules per nm2 of UCNPs. At this point, 2 mL of uncapped UCNPs (50 mg mL^{-1}) in DMF (4.3.2) was added to the vial, ultrasonicated for 2 minutes, and incubated for 1 hour with moderate agitation. Then, the resulting UCNPs-MDP dispersion was divided into two Teflon centrifuge tubes, 600 µL of hexane was added to each, and centrifuged at 13.300×g for 12 minutes. The supernatant was then carefully discarded, the pellets were redispersed in 7 mL of $CHCl_3$, 600 µL of hexane was added, and the tubes were centrifuged again. This washing procedure was repeated a total of three times. Finally, the pellets were redispersed in 3 mL of $CHCl_3$ again and stored at 4°C in a sealed vial.

4.3.4 Polymerization of UCNPs-MDP to Obtain Protective Hydrophobic Polymer Shells

In a typical synthesis, 11 mg of UCNPs-MDP (4.3.3) was centrifuged in $CHCl_3$ at 21 000 × g for 10 min. The supernatant was discarded, and the $CHCl_3$ traces were removed from the pellet with a gentle stream of air. The resulting pellet was ultrasonically redispersed in 600µL St and centrifuged again. The pellet was then redispersed in 600µL St by ultrasonication (2 minutes) again, 7.2 µL hexadecane was added, and the dispersion was vortexed and ultrasonicated for 2 minutes more. The dispersion was then added dropwise to a 10 mL round bottom flask containing 4.5 mL SDS (40 mm) and $NaHCO_3$ (1.2 mm) with vigorous stirring. The flask was sealed with a septum, and the mixture was homogenized for 1 hour. The mixture was placed in an ice bath for 10 minutes with moderate stirring. After this time, the chilled flask was opened, a sonication tip was inserted, and the solution was ultrasonicated for 3 minutes (Branson 250 Sonifier, analog cell resolver, 200 W maximum output power; duty cycle 70%, output power control set to position 1). After sonication, the flask sealed with a septum was stirred for 10 minutes at RT. It was then purged with N_2 for 10 minutes. The flask was then immersed in an oil bath (which had previously been heated to 70°C), and polymerization was initiated after 4 minutes by adding 225µL of the KPS initiator (7.5 mg mL ^{1}). The mixture was gently stirred at 70 °C for 2 hours, then the flask was removed from the oil bath and cooled to RT. The product was divided among five Eppendorf tubes and centrifuged at 21 000×g for 10 minutes. The supernatant was discarded, and the pellets were redispersed in 200µL SDS (40 mm), diluted by adding 1 mL deionized water (DI-H_2O), homogenized by vortexing, and centrifuged again. This purification process was repeated once more. For final washing, the pellets were redispersed in 1.2 mL DI-H_2O, centrifuged again, and redispersed in a final volume of 1 mL (DI-H_2O) and stored.

4.3.5 *Coating nanoparticles $NaYF_4$: Yb^{3+}/Er^{3+} with polyacrylic acid PAA*

We followed the metod described by *Sirkka et al.*[142] 10 mg UCNPs in hexane (4.3.1) were divided between two Eppendorf tubes and pelleted by centrifugation at 21000×g for 10 min. The resulting pellets were then carefully dried to remove traces of hexane. Subsequently, 1 mL of HCl (0.1 m) was added to each Eppendorf tube, and the pellets were redispersed by ultrasonication (5 min). The dispersed UCNPs were then incubated for 5 h with vigorous shaking at RT to remove the oleate molecules that acted as capping agents. The UCNPs were then recovered by centrifugation, and the supernatant was discarded. Then, the UCNPs were again dispersed in 1 mL of DI-H_2O and centrifuged again. After the supernatant was discarded, 1 mL of a 2.5% by weight aqueous PAA solution (pH = 9) was added to each UCNP pellet, which was dispersed by sonication and vortexing. The reaction was incubated for 16 h with vigorous shaking at RT, resulting in the formation of a thin PAA layer on the UCNP surface. UCNPs-PAA were obtained by centrifugation (21000×g, 10min). After the supernatant was discarded, the nanoparticles were dispersed in 1 mL DI-H_2O, and this step was repeated twice. Finally, the resulting pellet was redispersed in 250 µL DI-H_2O.

4.3.6 *Synthesis of α-$NaYF_4$ core nanoparticles*

The inert core of α-$NaYF_4$ nanoparticles was synthesized by thermal decomposition at high temperature from sodium and yttrium trifluoroacetates. The first step was the preparation of the precursors, in which YCl_3 (1.0 mmol, 303.3 mg) was dissolved in 10 ml of TFA at 90°C under reflux overnight in a three-neck flask. The mixture was then evaporated at 70°C under a flow of nitrogen until the $Y(TFA)_3$ powder was completely dry and white in color. $Y(TFA)_3$ was then dissolved in OA (3.2 mL, 10 mmol), OM (3.2 mL, 10 mmol), and ODE (6.4 mL, 20 mmol); NaFTA (136 mg, 1.0 mmol) was also added to the mixture.). Using a nitrogen atmosphere and a heating jacket (Nahita Blue, 656 series) connected to a temperature controller (JP selecta), the mixture was heated to 110°C with a temperature ramp of 1°C/min. Once this temperature was reached, vacuum was maintained for 30 minutes. Finally, the temperature was raised to 310°C under reflux for 30 minutes. For purification, after the solution cooled naturally, 20 mL of ETOH was added and centrifuged at 8500 RPM for 10 minutes. After removing the supernatant, the pellet was dispersed three more times in 20 mL of ETOH. Finally, the nanoparticles were redispersed and stored in 10 mL of hexane for further use.

4.3.7 Synthesis of α-$NaYF_4$@$NaYF_4$:$Yb^{3+}_{20\%}$ $Nd^{3+}_{60\%}$ Core/Shell Nanoparticles

The core/shell nanoparticles were prepared by a seed-mediated epitaxial growth method using the previously prepared α-$NaYF_4$ as the core nanoparticle. Briefly, the $Re(TFA)_3$ shell precursors were first synthesized by the same procedure as the $Y(TFA)_3$ precursors (Section 4.3.6), except that $YbCl_3 \cdot 6H_2O$ (77.8 mg, 0.20 mmol) $NdCl_3 \cdot 6H_2O$ (215.8 mg, 0.60 mmol), and $YCl_3 \cdot 6H_2O$ (61.0 mg, 0.20 mmol) were used. Then, the $Re(TFA)_3$ shell precursors were mixed with OA (10 mL, 32 mmol), ODE (10 mL, 31 mmol), NaTFA (136.1 mg, 1 mmol), and 0.5 mmol core nanoparticles in a three-neck flask. The solution was then heated to 110°C under a nitrogen atmosphere using a heating mantle (Nahita Blue, 656 series) connected to a temperature controller (JP selecta) with a temperature ramp of 1°C/min. Once this temperature was reached, vacuum was maintained for 30 minutes. Finally, the temperature was raised to 300°C under reflux for 30 minutes before cooling naturally to room temperature. The resulting core/shell nanoparticles were collected by the same procedure as the α-$NaYF_4$ core nanoparticles (Section 4.3.6) and dispersed in 10 mL of hexane for further use.

4.3.8 Synthesis of α-$NaYF_4$@$NaYF_4$:$Yb^{3+}_{20\%}$,$Nd^{3+}_{60\%}$@CaF_2 Core/Shell/Shell Nanoparticles

The procedure for preparing the core/shell/shell nanoparticles is similar to that for preparing the α-$NaYF_4$@$NaYF_4$:$Yb^{3+}_{20\%}$,$Nd^{3+}_{60\%}$ core/shell nanoparticles (see 4.3.7). For this purpose, the previously synthesized α-$NaYF_4$@$NaYF_4$:$Yb^{3+}_{20\%}$,$Nd^{3+}_{60\%}$ core/shell nanoparticles were used as cores for the seed-mediated growth of a CaF_2 shell. A mixture of α-$NaYF_4$@$NaYF_4$:$Yb^{3+}_{20\%}$,$Nd^{3+}_{60\%}$ core/shell nanoparticles (5 mL dispersion), OA (7 mL, 22.0 mmol), and ODE (7 mL, 21.0 mmol) was first heated to 110°C under nitrogen gas. After 30 min under vacuum, the temperature was further increased to 310°C. Then, 1.6 mL of $Ca(TFA)_2$ dissolved in OA (0.5 mmol mL^{-1}) was injected into the solution eight times at an interval of about 10 minutes. The resulting core/shell/shell nanoparticles were precipitated, washed with ethanol (see 4.3.7), and finally dispersed in 10 mL of hexane.

4.3.9 Coating α-$NaYF_4$@$NaYF_4$:$Yb^{3+}_{20\%}$, $Nd^{3+}_{60\%}$@CaF_2 nanoparticles with PAA

5 mg of α-$NaYF_4$@$NaYF_4$:$Yb^{3+}_{20\%}$, $Nd^{3+}_{60\%}$@CaF_2 nanoparticles synthesized in the previous section 4.3.8 were taken. Then 2 mL abs EtOH was added, and the solution was mixed with a vortex. The solution was then centrifuged at 14,000 rpm for one hour and the supernatant was removed. 1 mL of 0.1 M HCl was added and shaken at room temperature for 5 hours. After this time, the solution was centrifuged at 14800 rpm for one hour. The supernatant was removed again, and the pellet was washed with Milli-Q water and redispersed in 1 mL of a 2.5% PAA solution adjusted to pH 9 and incubated for 16 hours. Finally, the pellet was washed twice with Milli-Q water and centrifuged at 14800 rpm for one hour and redispersed in 250 µL of MES 20mM (pH 5.6).

4.3.10 Coupling reaction between α-$NaYF_4$@$NaYF_4$:$Yb^{3+}_{20\%}$, $Nd^{3+}_{60\%}$@CaF_2@PAA with VEGF-A 165 protein

To 1 mg of the PAA-functionalized nanoparticles described in the previous section 4.3.9, 1 mg of EDC·HCl in 5 µL of 20 mM MES (pH 5.6), and 3 mg of sulfo-NHS in 10 µL of MES were added. The solution was incubated for 2 hours and a half at room temperature in a shaker. After this time, it was centrifuged at 13.3 rpm for 10 minutes. After two more washes, the pellet was redispersed in 10 mM HEPES (pH 7.2). Then the solution and 10 µg of VEGF-A were incubated at 4ºC and stirred for 12 hours. Then the mixture was centrifuged again at 13.3 rpm for 10 min and washed 3 times to remove excess VEGF-A. Finally, the pellet was redispersed in 1 mL of HEPES for use in subsequent experiments.

4.4 In vitro and in vivo Experiments

Cell cultures were performed using primary human umbilical vein endothelial cells (HUVEC). These cells were isolated in the Cardiovascular Biology Research Group at the International Centre for Genetic Engineering and Biotechnology (ICGEB) in Trieste, Italy. Newborn umbilical cords were donated from the maternity ward of Cattinara Hospital in Trieste, Italy.

4.4.1 In vitro experiments using HUVEC cells

HUVEC cells were cultured in EGM-SFM medium supplemented with 10% FBS and 100µg/ml streptomycin. First, thawed HUVEC cells were seeded in a Petri dish previously coated with 0.2 mg/mL fibronectin/gelatin and incubated at 37ºC for three days. After detachment of the cells (1% StemPro™ in PBS), 4000 cells per well were seeded into a 96-well plate previously coated with fibronectin/gelatin and left in the incubator for another 24 hours. Finally, different concentrations of VEGF-α-$NaYF_4$@$NaYF_4$:$Yb^{3+}_{20\%}$, $Nd^{3+}_{60\%}$@CaF_2@PAA nanoparticles were added to the wells and the cells were incubated for another time lapse depending to the experiment.

4.4.2 Immunofluorescence analysis

Cells were washed twice with 1X PBS and fixed in 4% PFA for 15 minutes at room temperature. The cells were again washed twice with PBS. To permeabilize the cells, Triton X-100 0.5% v/v solution was added and incubated for 5 minutes at room temperature. We then blocked the solution with 5% w/v BSA in PBS 1X for 1 hour at room temperature. Incubation with the primary antibodies (CD -31, EdU kit) was performed at a ratio of 1:100 v/v with the blocking solution overnight at 4°C. The cells were washed again 3 times with PBS 1X. Finally, we stained the nuclei with Hoechst (1:5000) and washed them twice with PBS 1X and left them in PBS at 4°C in foil paper.

4.4.3 Western Blot

To determine the concentration of VEGF present on the surface of the nanoparticles, a Western blot was performed (see section 4.3.10). To lyse the protein, 100 µL Laemmli's 6X buffer (375 mM Tris-HCl pH 6.8, 6% SDS, 4.8% glycerol, 9% 2-mercaptoethanol, 0.03% bromophenol blue) was added to 30 mg of the nanocomplex. A shaker was used for mechanical dissociation and the solution was heated to 95ºC for five minutes. Electrophoresis was performed in 10% polyacrylamide gels with a SDS/MOPS 10X running buffer at 180 V for 20 minutes. The nitrocellulose membrane was probed with the VEGFR2 antibody dissolved in Immobilion® solution.

4.4.4 In vivo experiments

All animal experiments were performed in accordance with the guidelines of the European Parliament Directive 2010/63/UE on animal experimentation in compliance with European directives and international laws and policies (EC Council Directive 86/609, OJL 34, 12 December 1987) and were approved by the ICGEB Animal Welfare Board, the Ethics Committee, and the Italian Ministry of Health. Adult AplnCreER mice were used for the experiments. They came from the Bin Zhou laboratory and were crossed with mT/mG reporter mice (The Jackson Laboratory, stock number 007576) to obtain the "AplnCreER:mT/mG" lineage. All animals were maintained under optimal environmental conditions. They were kept in the bioexperimental facility of ICGEB at controlled temperature and a light/dark cycle of 12/12 hours.

4.4.5 Immunofluorescence of Tissues

Skeletal muscle was collected in PBS and fixed overnight in 2% PFA at 4°C. Tissues were then equilibrated in 30% sucrose overnight at 4°C before embedding in OCT (Bio-Optica) and cryosectioning. Three 100 µm sections were transferred to Superfrost glass microslides, permeabilized in 0.5% Triton X-100 for 15 minutes, blocked in 5% BSA for 30 minutes, and incubated overnight at 4°C with primary antibodies diluted in blocking solution. The following primary antibodies were used: Anti-CD31, 1:200. Alexa Fluor-conjugated secondary antibodies were used to detect the primary antibodies, while the nuclei were counterstained with Hoechst. Visualization of EdU incorporation into proliferating cells was performed using the EdU Click-iT assay (Invitrogen) according to the manufacturer's instructions.

5. Results & Discussion

RESULTS AND DISCUSSION

5.1 The effects of dopant concentration and excitation intensity on the upconversion and downconversion emission processes of β-$NaYF_4$:Yb^{3+}, Er^{3+} nanoparticles.

> *"Let us step into the night and pursue that*
> *flighty temptress, adventure."*
>
> `J.K. Rowling`

5.1.1 Abstract

The dopant concentration of lanthanide ions in photon upconversion nanoparticles (UCNPs) remains one of the key points to boost the brightness of these nanomaterials and, therefore, their application developments. Here, we analyzed the effect of Er^{3+} and Yb^{3+} dopant concentrations of β-$NaYF_4$:Yb^{3+},Er^{3+} nanoparticles on the visible upconversion and near-infrared downconversion luminescence intensities. Our approach carefully excluded all other factors whose variation affects luminescence properties such as the size, morphology, crystal structure, ion distribution, ligand, and surrounding medium, allowing us to exactly infer the influence of the ratio of Yb^{3+} to Er^{3+} ions on the nanoparticle luminescence. To maintain the size and morphological properties of nanoparticles, we used a total dopant concentration of 22% while varying the ratio of Yb^{3+} to Er^{3+} ions from 0 to 10. A huge increase in luminescence takes place as the Yb/Er ratio increases following a power-law behavior, and this luminescence enhancement is greater at low excitation intensities. Above a Yb/Er ratio of around two, saturation occurs with a slight peak when this ratio is around four. Simulations using a rate equation model showed that upconversion luminescence (UCL) is mainly produced by the energy transfer between neighboring Er^{3+} ions at low Yb/Er ratios, while at high ratios, the energy transfer from Yb^{3+} to Er^{3+} ions dominate. However, downconversion luminescence (DCL) is produced at all analyzed ratios, except 0, by the previous mechanism.

Keywords: *Up-conversion luminescence, doping ratio, down-conversion luminescence, resonance energy transfer, excited-state absorption, time-of-flight luminescence.*

5.1.2 Resumen

La concentración de dopantes de iones lantánidos Ln^{3+} en nanopartículas UCNPs, sigue siendo uno de los puntos clave para potenciar la intensidad del brillo de estos nanomateriales y, por tanto, su desarrollo de aplicaciones. En este trabajo, se analizará el efecto de las concentraciones de los dopantes Yb^{3+} y Er^{3+} sobre la intensidad de la conversión ascendente en el espectro visible y la conversión descendente en el NIR. Para mantener las propiedades de las UCNPs, como el tamaño y la fase cristalina, utilizamos una concentración total de dopante del 22% mientras variamos la proporción entre los iones de Yb^{3+} y Er^{3+} de 0 a 10. En los resultados se observa que se produce un gran aumento de la luminiscencia a medida que aumenta la relación Yb/Er siguiendo un comportamiento de acuerdo con la ley de potencia. Se observa que luego de la ratio 2 la magnitud del aumento de la intensidad disminuye levemente y que la mayor intensidad de la luminiscencia se observa en una ratio de 4. Se reprodujeron

teóricamente los principales hallazgos experimentales mediante un modelo “*rate equations*” que nos permitió describir el papel de los diferentes mecanismos de conversión ascendente de la relación Yb/Er de los dopantes.

Palabras Clave: *luminiscencia por conversión ascendente, relación entre los dopantes, luminiscencia por conversión descendente, transferencia de energía de resonancia, absorción en el estado excitado, luminiscencia en el tiempo de vuelo*.

5.1.3 Introduction

Nanocrystals doped with trivalent rare earths have become one of the most intriguing systems in photoluminescence because of their intriguing ability to produce photon upconversion.[74] Other upconversion systems, such as those based on two-photon absorption or second-harmonic generation, can also be used for upconversion emission. However, there are significant limitations associated with the need to use expensive pulsed lasers with high excitation intensity or nonlinear optical materials with a non-center-symmetric atomic or molecular organization, which has made rare earth nanoparticles an ideal candidate for these types of applications.[143]

As mentioned in section 1.3, rare earth nanoparticles exhibit high chemical and photochemical stability, large Stokes shifts, lower photobleaching, no flicker, long fluorescence lifetimes, sharp emission bandwidths, and high emission matching capability, making them attractive materials that have opened a variety of applications, such as. e.g., probes in optical imaging,[103] the labeling of biological molecules,[76] biosensors,[144] in the fight against counterfeiting,[145] solar energy,[146] drug delivery systems,[147] and nanothermometry, giving an idea of the enormous scientific and technological potential.

One of the most studied systems is based on $NaYF_4:Yb^{3+}/Er^{3+}$ nanoparticles due to its high efficiency in upconversion, which, together with other factors, is related to the low phonon energy of the host crystal lattice (about 320cm-1).[148] After excitation with a CW laser at 980 nm, these nanoparticles show three prominent upconversion bands in the blue (410 nm), green (520 and 540 nm), and red (650 nm) regions. Their intensities are the result of radiative and nonradiative decay events that affect the population of different energy levels involved in the general process and are very sensitive to variations in the surface-to-volume ratio,[149] crystalline structure,[150] and concentration of ions involved in doping the nanoparticles, as well as to the ligand and medium in which they are located.[151,152] All these factors determine the intensity of the emission bands and the efficiency of the upconversion and downconversion. For this reason, it would be desirable for rational design of UCNPs to understand the role of these factors in the overall process.[153]

One of the most important factors is the concentration of lanthanide doping within the nanoparticle. Most $NaYF_4$ UCNPs are doped with 2% Er^{3+} and 20% Yb^{3+} and to date show the most efficient photoluminescence in the green region of the electromagnetic spectrum, but this is only true for microcrystals.[77] Other work has examined the influence of the concentration of Er^{3+} and Yb^{3+} in the matrix. In general, it has been suggested that the optimal concentration of Yb^{3+} is between 17-20%, while the Er^{3+} concentration is usually 2 to 4%. It is important that the doping be relatively low to ensure spacing between dopants and avoid parasitic interactions.[154] Examples of concentration studies include the work of Cao et al.[155] where they used powder samples of $NaYF_4$ nanoparticles doped with 2% Er^{3+} and a wide range of Yb^{3+} concentrations. They found that the strongest luminescence emission occurred at 20% Yb^{3+}, which was due to a transition from a hexagonal phase to a cubic phase of the nanophosphor. Kaiser et al.[153] found maximum luminescence at low power densities when exciting nanoparticles doped with 14% Yb^{3+} and 3% Er^{3+}. On the other hand, core/shell UCNPs have shown the ability to enhance their luminescence by upconversion, increasing the amount of Yb^{3+} doping to very high percentages.[156,157]

$NaYF_4$: Yb^{3+}, Er^{3+} nanoparticles exhibit not only up-conversion luminescence (UCL) but also very efficient down-conversion luminescence (DCL) in the near infrared. In both cases, the emission depends on the size of the UCNPs. For UCL, the intensity increases with increasing nanoparticle size, while for DCL, the strongest emission occurs at diameters between 15 and 40 nm.[158] There is little published work on the effects of variations in the ratio of dopant concentrations on upconversion and downconversion emission, and even less analyzes the emission properties above and below the saturation excitation power density. For these reasons, we synthesized a series of UCNPs with identical size (30 nm) and the same morphological properties, using a $NaYF_4$ matrix as host and varying the ratio between dopants. To achieve this, we set a percentage of 22% for the Y^{3+} ions and codoping with Yb^{3+} and Er^{3+} and used different ratios of Yb^{3+}/Er^{3+} between 0 and 10. According to our review of the literature, there is no previous work that evaluates the composition and the influence of excitation power density on the upconversion and downconversion processes in these doping ratios.

5.1.4 Objectives

5.1.4.1 Overall Objective

Perform a systematic fundamental study of upconverting $NaYF_4$ nanoparticles doped with Yb^{3+} and Er^{3+} by varying the ratio between dopants (between 0 and 22% total) and the power density to observe the variation into the optical properties of the nanoparticles and their upconverting and downconverting fluorescence emissions.

5.1.4.2 Specific Objectives

- Synthesize β-$NaYF_4$:Yb^{3+}/Er^{3+} upconverting nanoparticles with Yb^{3+}/Er^{3+} ratios between 0 and 10.
- Morphological characterization of the UCNPs from $NaYF_4$:Yb^{3+}/Er^{3+} obtained in the previous objective by TEM and HRTEM scanning electron microscopy.
- Morphological characterization of the UCNPs of $NaYF_4$:Yb^{3+}/Er^{3+} by EDX and HAADF.
- Determine the crystalline phase of the $NaYF_4$:Yb^{3+}/Er^{3+} UCNPs by X-ray powder diffraction.
- Measure and analyze the luminescence emission spectra obtained from each of the $NaYF_4$:Yb^{3+}/Er^{3+} ratios.
- Determine the effect of power density in each of the ratios of $NaYF_4$:Yb^{3+}/Er^{3+} UCNPs
- Measure and analyze the half-life in each of the ratios of the $NaYF_4$:Yb^{3+}/Er^{3+}
- Perform a theoretical study to determine the predominant relaxation mechanism in each of the ratios of $NaYF_4$:Yb^{3+}/Er^{3+}

5.1.5 Experimental section

5.1.5.1 Synthesis of $NaYF_4$:Yb^{3+},Er^{3+} UCNPs

Monodisperse β-$NaYF_4$:Yb_x,Er_y nanoparticles with different doping ratios were synthesized by the thermal co-precipitation method described in Section 4.3.1 of Materials and Methods. Table X shows the different Yb^{3+}/Er^{3+} dopant ratios synthesized in this work. Three exact syntheses were performed for each dopant ratio.

Table 2. Relation between the number of moles of dopants used. In all cases, the number of moles of Y^{3+} remained constant at 0.78 mmol where 100% corresponds to the sum of the moles of Y^{3+}, Yb^{3+}, and Er^{3+} ions.

Ratio Yb^{3+}/Er^{3+}	**Yb^{3+} (mmol)**	**Yb^{3+} (%)**	**Er^{3+} (mmol)**	**Er^{3+} (%)**
10	0.200	20.0	0.020	2.0
8	0.196	19.6	0.024	2.4
4	0.176	17.6	0.044	4.4
1	0.110	11.00	0.110	11.0
0.25	0.044	4.4	0.176	17.6
0.12	0.024	2.4	0.196	19.6
0.1	0.020	2.0	0.200	20.0
0	0	0	0.220	22.0

5.1.5.2 Characterization

Morphological Characterization: The chemical and morphological characterization of UCNPs was carried out using a JEOL JEM 1010 electron transmission microscope (TEM) working at a voltage of 80 kV. High-resolution images were taken (HR-TEM) using a microscope JEOL JEM 2100 at a working voltage of 200 kV. High-angle annular dark-field (HAADF) scanning TEM and EDX mappings have been realized using an FEI Talos F200X (FEI, USA, 80 kV) coupled to an EDX detector. All samples were prepared by adding 10 mL of the UCNPs solution (ca. 3 mg/mL) on a Cu grid and allowing the solvent to evaporate at room temperature. To determine the crystalline phase, X-ray diffraction (XRD) patterns of the dried UCNP powders were recorded using a PANalytical Model XPPert PRO MPD Multi-Purpose Diffractometer.

Optical Characterization: The luminescent emission spectra of UCNPs were measured using a fluorescence home-built system described previously in section 4.2.8 (see the scheme in Figure 15). Different samples were synthesized for each Yb/Er ratio. At least three spectra were collected for each sample. Then, we computed the average intensity of the spectra integrated area within the green, red, or IR emission bands for each ratio and we took the maximum deviation as the error. Results presented without error bars correspond to a single representative measurement. Luminescence lifetimes were measured using the time-resolved photon counting method described in section 4.2.9 for each synthesis.

5.1.6 Results and discussion.

5.1.6.1 Morphological and structural studies

The emission properties of NaYF4:Yb,Er nanoparticles depend largely on their size, crystalline phase, dopant ion distribution, surface ligand and surrounding medium, and dopant ion composition. To properly isolate the effect of dopant concentration, we need to hold constant other factors that affect luminescence. Therefore, we synthesized monodisperse β-$NaYF_4$:Yb_x,Er_y nanoparticles with a total dopant concentration of 22% (x+y=0.22) and varied the ratio between Yb^{3+} ions and Er^{3+} (y/x) from 0 to 10 (see Table 2). Some representative ratios were confirmed by EDS measurements and are shown in Figure 18 and Table 3.

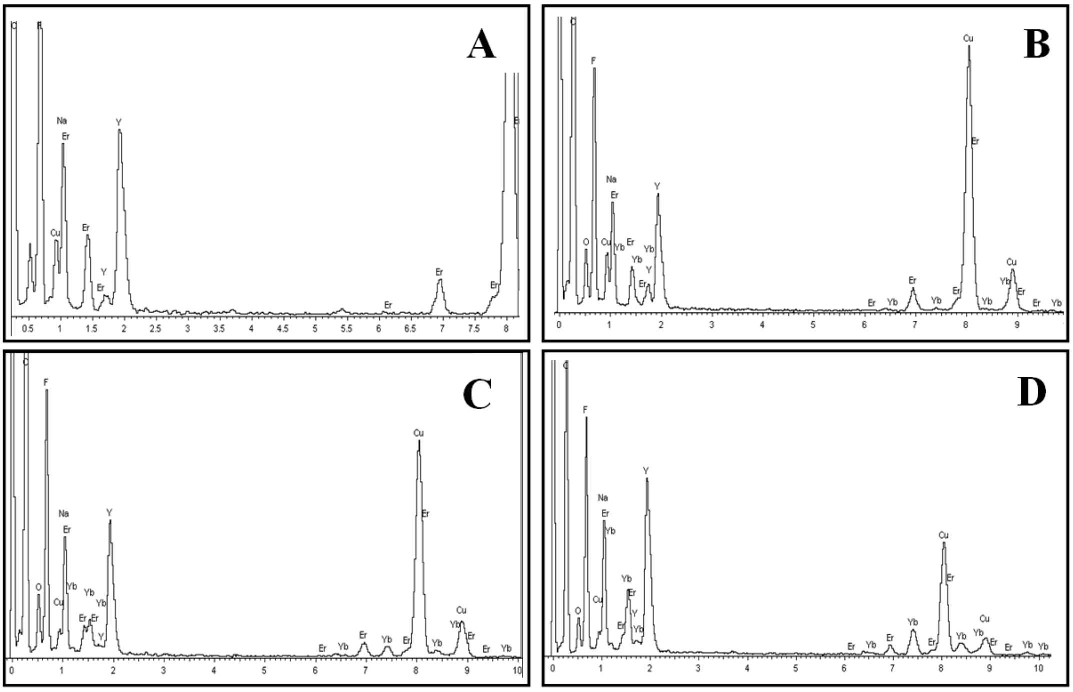

Figure 18. (A-D) EDS spectrum for $NaYF_4$:Er^{3+},Yb^{3+} nanoparticles with representative Yb^{3+}/Er^{3+} dopant ratios: (A) Ratio 0. (B) Ratio 0.1. (C) Ratio 0.25 (D) Ratio 1.

Table 3. Table including the atomic percent of lanthanides present into the nanoparticle unit cell obtained from EDS analysis.

Nominal Yb^{3+}/Er^{3+}	**at % Y^{3+}**	**at % Yb^{3+}**	**at% Er^{3+}**	**Yb^{3+}/Er^{3+} From EDS**
0	80.23	0.00	19.77	0
0.1	76.65	1.71	21.64	0.08
0.25	77.25	4.55	18.20	0.25
1	80.14	10.77	9.09	1.2

The nanoparticles have an average diameter of 30±2 nm regardless of the doping concentration, as shown in Figure 19 A,B, and C respectively. The HR-TEM images we obtained of the nanoparticles show their high crystallinity. Indeed, in Figure 19 D, E and F, can observe the edge of the crystal lattice with a value of 0.524 nm, which corresponds to the crystalline phases (100) of β-$NaYF_4$.

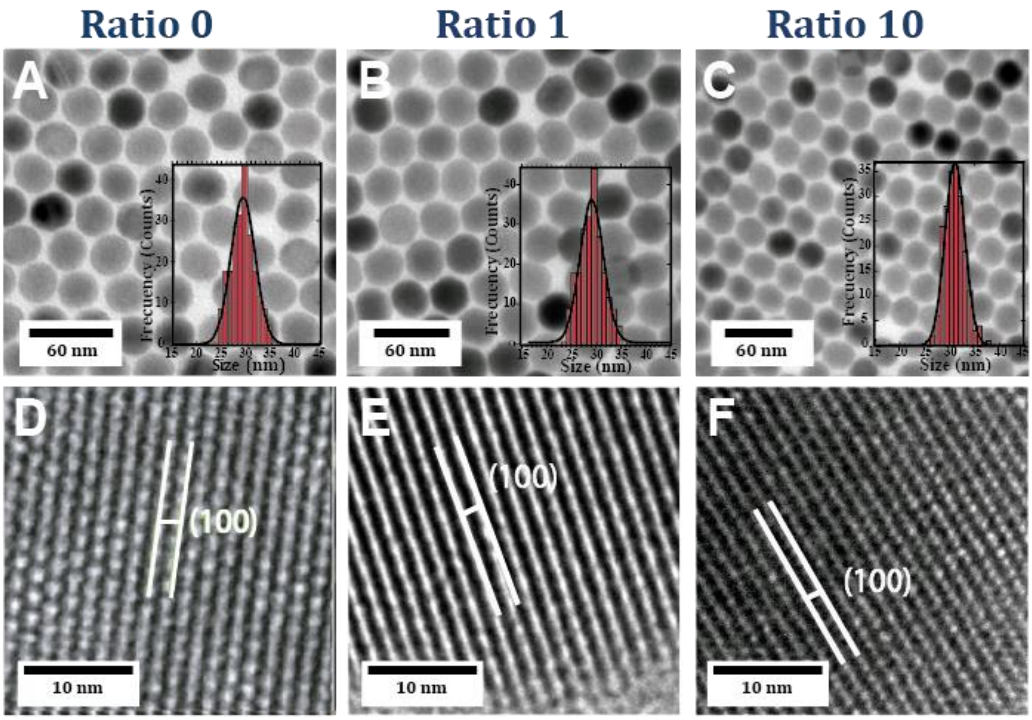

Figure 19. Images from TEM of the synthesized nanoparticles (A, B, and C). The inset in each figure shows the size distribution of the nanoparticles. A detailed study of the crystalline structure of the nanoparticles was performed using HR-TEM and is shown in panels D, E, and F. Figures A and D correspond to the nanoparticles doped with Er^{3+} only (Yb/Er ratio 0), Figures B and E correspond to nanoparticles doped with Yb^{3+} and Er^{3+} with a ratio of 1, and figures C and F correspond to nanoparticles doped with Yb^{3+} and Er^{3+} with a ratio of 10.

As mentioned earlier 1.2, the photoluminescence of the upconverting nanoparticles is strongly dependent on the phase of the matrix. Figure 20 shows the results obtained from the analysis of the crystalline phase by powder X-ray diffraction. Comparing the X-ray diffraction results with the pattern given in the "International Center for diffraction data" database for the hexagonal β-phase of the $NaYF_4$ crystal structure.[159] We find that the peaks agree with the spectra obtained for all the ratios, thus confirming that the crystalline phase is beta in each of the ratios.

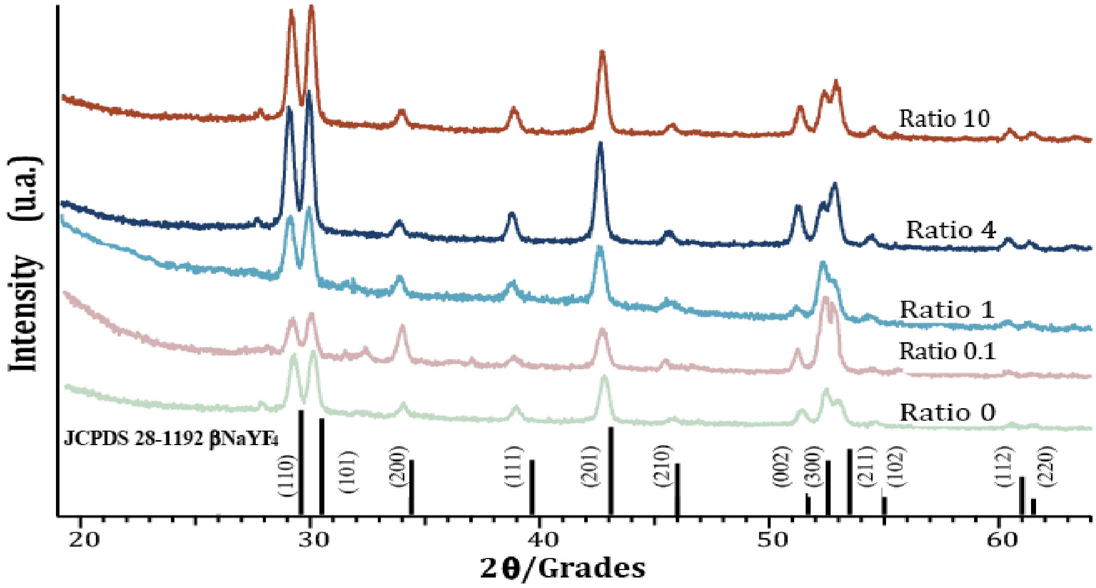

Figure 20. X-ray powder diffraction of NaYF4:Yb^{3+}/Er^{3+} UCNPs at different doping ratios. The black lines correspond to the pattern reported in the literature for the β-$NaYF_4$ nanoparticles.

Another important effect to be considered is related to the distribution of ions. Under certain synthesis conditions, the difference in ionic reactivity can lead to an anisotropic distribution of ions, as has been published previously.[160] This result prompts us to investigate the distribution of dopants in the nanoparticles using element mapping analysis. Figure 21 panels A, B, and C show an isotropic distribution of ions within the particles and the elemental profile analysis is shown in Figure 21, panels D, E, and F, respectively. This morphological characterization shows that there are no structural differences between the different synthesized nanoparticles with different doping ratios, so it is possible to attribute the photoluminescent differences solely to the presence of a different concentration of doping ions.

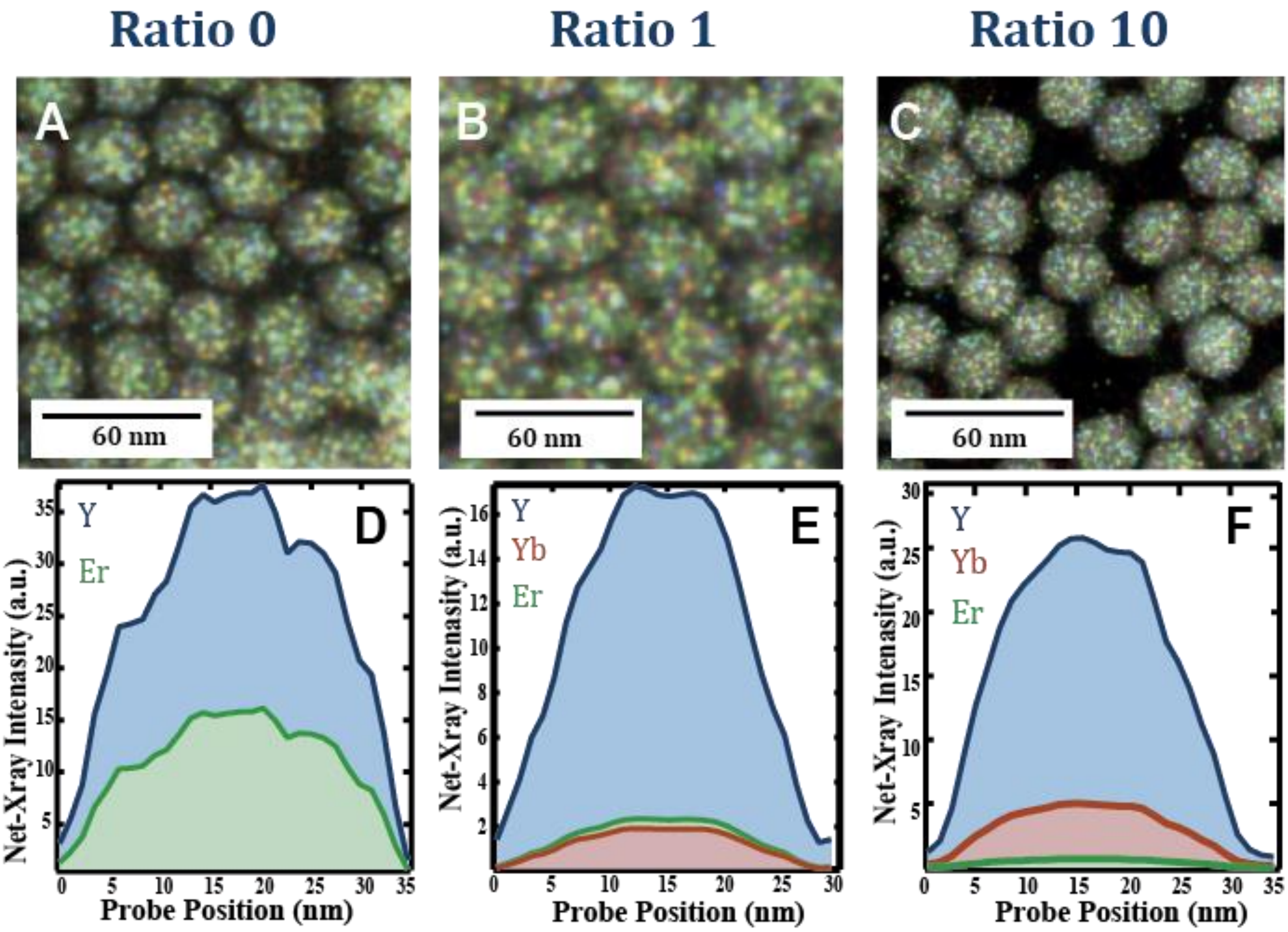

Figure 21. HAADF results. Elemental mapping of the obtained nanoparticles (A, B, C). Distribution profile of doping elements within each nanoparticle (D, E, F). Figures A and D correspond to nanoparticles doped with Er^{3+} only (Yb^{3+}/Er^{3+} ratio 0), figures B and E correspond to ratio 1, and figures C and F correspond to ratio 10.

5.1.6.2 Luminescence variation with Yb/Er ratio

To analyze the role of Yb/Er ratio on the luminescence properties of UCNPs, we measured, simultaneously, their UCL and DCL spectra under a NIR excitation CW laser at 976 nm. Results presented in Figure 22A show the spectra obtained from a 1 mg/mL hexane solution of UCNPs with different Yb/Er ratios excited with an intensity of 5.3 kW cm^{-2}, above the typical saturation value of transition ${}^2F_{5/2}\rightarrow{}^2F_{5/2}$ of the Yb^{3+} ions, which is I_{sat}^{Y} = 3 kW cm^{-2}. Different emission peaks are observed: two green emission peaks near 525 nm and 540 nm corresponding to ${}^2H_{11/2}$

$\rightarrow {}^4I_{15/2}$ and ${}^4S_{3/2} \rightarrow {}^4I_{15/2}$ transitions of the Er^{3+} ions, respectively; and a red emission peak around 655 nm corresponding to the ${}^4F_{9/2} \rightarrow {}^4I_{15/2}$ transition of Er^{3+} ions (see Figure 22A). Figure 22A also shows the downconversion luminescence of the NIR peak near 1.55 μm corresponding to the transition from the metastable level of Er^{3+} ions to their ground state, that is, ${}^4I_{13/2} \rightarrow {}^4I_{15/2}$. In both cases, upconversion and downconversion luminescence emission strongly increases with the Yb/Er ratio. However, above a ratio of 4, no further increase is observed. It should be noted that the range of Er^{3+} and Yb^{3+} concentrations investigated here varies from an Er^{3+} dopant concentration of 22% (ratio 0) where only Er^{3+} ions are present to a well-known standard ratio of 20% of Yb^{3+} and 2% of Er^{3+} (ratio 10). Thus, within this broad dopant range, different photon upconversion mechanisms are expected to occur. Figure 22B shows different population pathways of UCL emission bands. In the standard case of 20% of Yb^{3+} and 2% of Er^{3+} (ratio 10), the energy transfer from Yb^{3+} ions to Er^{3+} ions should dominate. However, when only Er^{3+} ions are present, the excited-state absorption from the ${}^4I_{11/2}$ level or the energy transfer between neighboring Er^{3+} ions should be responsible for the UCL emission process. On the other hand, the DCL can be achieved by the ground-state absorption (GSA) of laser photons by both Er^{3+} and Yb^{3+} ions.

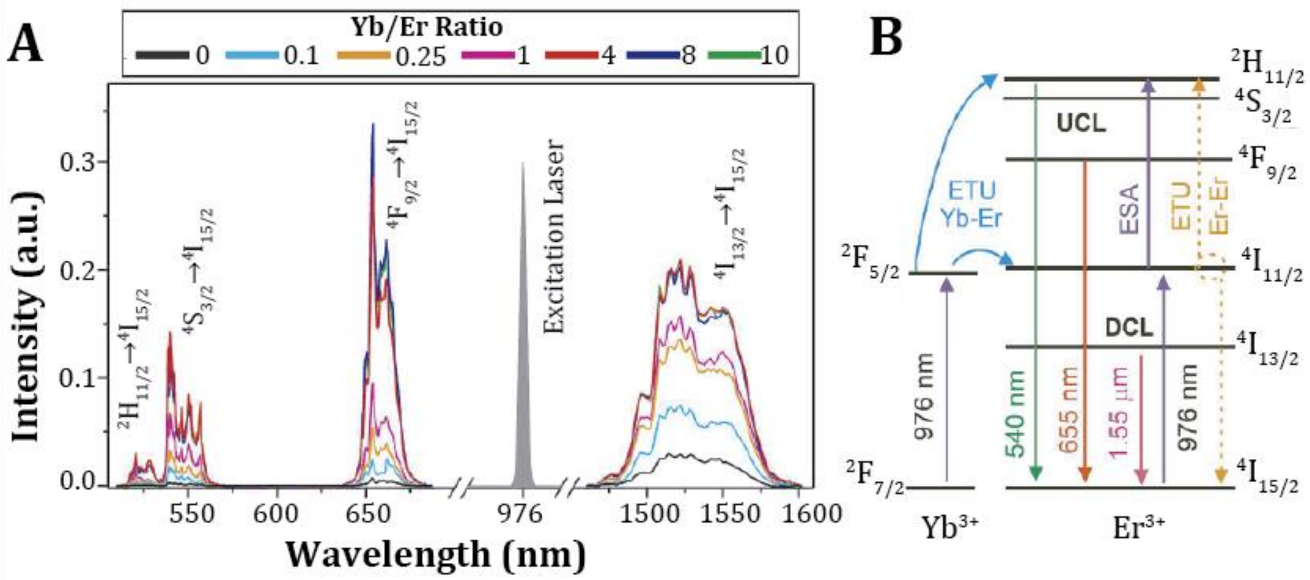

Figure 22. **A** upconversion and downconversion luminescence spectra for the different ratios of Yb/Er doping. Excitation wavelength 976 nm and a power density of 5.3 kW/cm². **B** Energy level diagram summarizing the pathways by which emission levels in the 520/540 nm (green) and 655 nm (red) region can be biphotonically populated by Er^{3+} ions.

To develop a more quantitative analysis, we show in Figure 23A and B the integrated spectra of the green and red bands as a function of the Yb/Er ratio for two different excitation intensities, 475 W/cm² below the Yb^{3+} saturation intensity and 5.3 kW/cm² above saturation. Both emission bands show similar behavior, namely a huge increase in luminescence intensity up to a saturation value reached for Yb/Er ratios above 1 (see the semi-logarithmic plot in Figure 23A). A wider range of variation (three orders of magnitude difference in luminescence) is observed at low excitation intensities (475 W/cm²) than at high excitation intensities (5.3 kW/cm²), where a twofold range of variation is obtained. This phenomenon can be better illustrated in the log-log plot in Figure 23B. We found that the UCL intensity increases with the Yb/Er ratio at ratios below 1 according to a power law. The exponent of the power law depends on the excitation intensity. A larger exponent is obtained for the linear absorption region (below saturation intensity), which produces the largest variation in luminescence intensity mentioned above. Figure 23C and D also show the integrated downconversion spectra. We observed similar behavior to upconversion luminescence (see the semilog plot in Figure 23C). Again, the variation in luminescence intensity is larger at low laser irradiances, as shown in the log-log plot in Figure 23D. It should be noted that the exponents of the power laws, which are smaller for the DCL are smaller than those for the UCL. Therefore, the upconversion phenomenon is more affected by variations in the Yb/Er ratio than the downconversion luminescence.

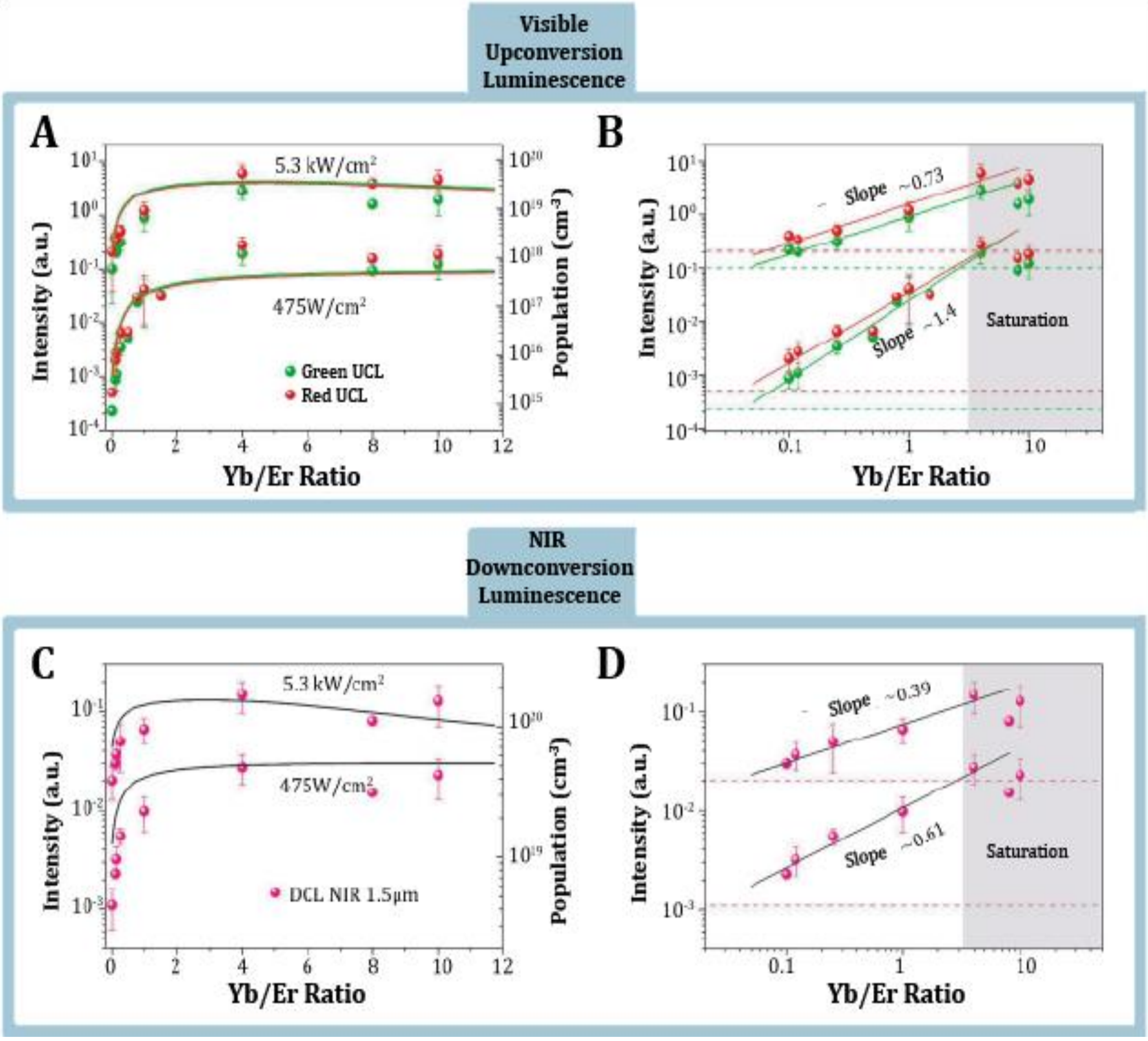

Figure 23. Upconversion (A and B) and downconversion (C and D) integrated luminescence as a function of the Yb/Er ratio for two different excitation intensities, 475 W/cm² below saturation intensity and 5.3 kW/cm² above saturation. Left panels (A and C) show the experimental data in the semi-log plot and the simulated intensity (solid line) from the rate equation model (Equation 7). Right panels (B and D) show a power-law behavior in a log–log plot and a saturation regime for Yb/Er ratios above 1. Ratio 0 has also been included in the log–log plot. Shadow areas show the ratios at which the luminescence intensity is saturated.

In summary, contrary to common belief, there is no critical Yb/Er ratio that maximizes luminescence intensity (usually set as a ratio of 10), but rather a wider range of ratios from about 2 to 10 that result in approximately the same value of luminescence intensity. In addition, the intensity decreases very slightly above ratio 4, which corresponds to a proportion of doped ions of 17.6% Yb^{3+} and 4.4% Er^{3+}.

As mentioned earlier, the variation of luminescence with excitation power is larger at low Yb/Er ratios, which could indicate saturation of luminescence at high Yb/Er ratios. To confirm this, we analyzed the dependence of green and red luminescence on excitation intensity for the two extreme Yb/Er ratios 10 and 0 (see Figure 24). For the ratio 10 (see circles), a biphotonic process (power law exponent close to 2) is obtained at excitation intensities below the saturation value of the Yb^{3+} transition. This quadratic behavior indicates the nature of the underlying upconversion mechanism: Two laser photons are required to obtain one visibly emitted photon. However, at excitation intensities above the saturation value, the quadratic behavior saturates due to absorption saturation of the Yb^{3+} transition, leading to an exponent closer to one. For the Yb/Er ratio 0 (see squares), the quadratic behavior (biphotonic process) persists for all excitation strengths. In this case, the first step of the UCL emission process occurs through the ground state absorption of the $^4I_{15/2} \rightarrow {}^4I_{11/2}$ transition from Er^{3+}. This transition has a larger saturation intensity, which is not reached by the laser power used in the experiments, and therefore continues to proceed in the linear absorption region.

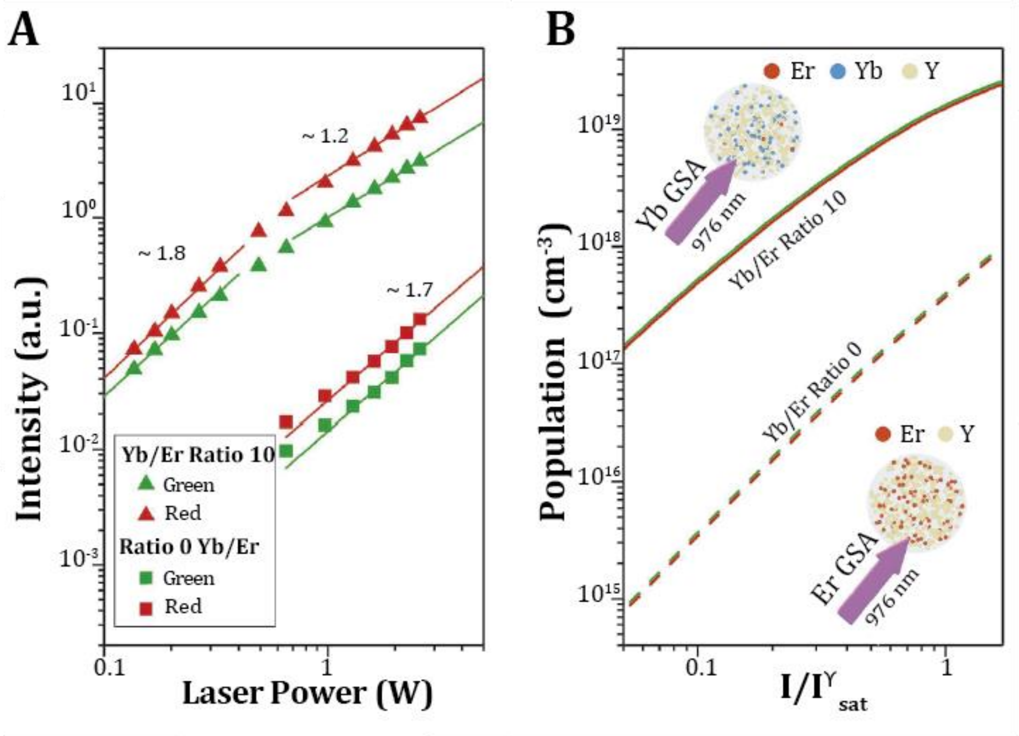

Figure 24. **(A)** Green and red integrated upconversion luminescence as a function of laser power for two extreme Yb/Er ratios: 0 (squares) and 10 (circles). Solid lines are linear fits to the data. **(B)** Simulated curves: Steady-state population of green and red emission levels as a function of normalized excitation intensity for Yb/Er ratio 10 (solid lines) and ratio 0 (dashed lines). The UCNP show the fraction of ions for these two Yb/Er ratios and indicate the ion responsible for the excitation absorption in each case: Yb^{3+} GSA for ratio 10 and Er^{3+} GSA for ratio 0.

5.1.6.3 Time-resolved luminescence Analysis

Let us now analyze the time resolved UCL for UCNPs with different Yb/Er ratios. Figure 25 shows the luminescence decay curves at both UCL bands: the green band at 539 nm and the red band at 654 nm. The luminescence signals generated by UCNPs with different ratios are approximately in agreement, indicating in principle a negligible influence of the Yb/Er ratio. We obtained a lifetime of about 127 ms for the green UCL and about 227 ms for the red UCL. Therefore, the Yb/Er ratio has no significant effect on the decay dynamics of the UCL emission process. The results support the idea that the UCL intensity depends on how efficient the green and red emitting levels are with respect to the total number of sensitizers (Yb^{3+} ions) and emitters (Er^{3+} ions) depends and excludes a possible variation of the surface luminescence quenching effect with the Yb/Er ratio. The decay curves in Figure 25 show an initial slope that is a signature of the upconversion process due to the energy transfer from Yb^{3+} to Er^{3+} ions. Interestingly, this initial luminescence increase also occurs when the Yb/Er ratio is decreased, even at a ratio of 0 where only Er^{3+} ions are present. This result suggests that there is an energy transfer process between neighboring Er^{3+} ions that competes with the excited state absorption process.

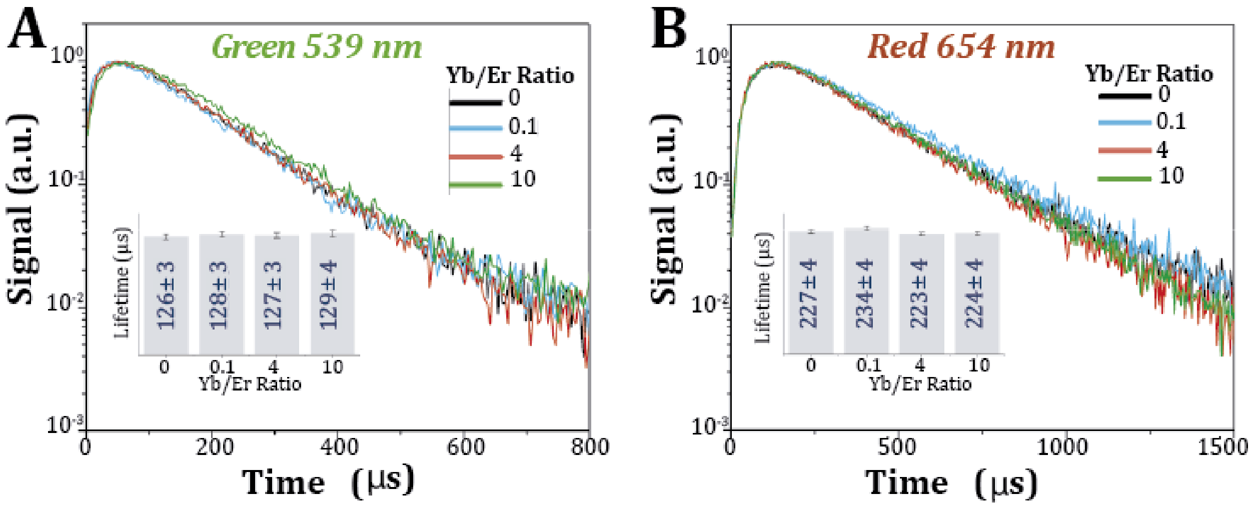

Figure 25. **(A)** Green and **(B)** red upconversion luminescence decay signals for UCNPs with different Yb/Er ratios. (inset) Lifetime values obtained by exponential fitting of the decay curves.

5.1.6.4 Rate Equation Analysis

To theoretically interpret the steady-state luminescence experiments by performing a rate equation analysis. We used the following rate equation model, which describes the main physical mechanism of our system (see details in Figure 26):

$$\frac{dN_1}{dt} = -W_1N_1 + W_{21}N_2 - K_3N_1N_1^Y - \frac{\sigma_{13}}{\sigma_{02}}\frac{W_1I}{I_{sat}}(N_1 - N_3) - 2C_1N_1^2,$$

$$\frac{dN_2}{dt} = -W_2N_2 + W_{32}N_3 + K_2N_0N_1^Y - K_{B2}N_2N_0^Y - K_4N_2N_1^Y + \frac{W_1I}{I_{sat}}(N_0 - N_2) - \frac{\sigma_{24}}{\sigma_{02}}\frac{W_1I}{I_{sat}}N_2 + C_1N_1^2 - 2C_2N_2^2,$$

$$\frac{dN_3}{dt} = -W_3N_3 + W_{43}N_4 + K_3N_1N_1^Y + \frac{\sigma_{13}}{\sigma_{02}}\frac{W_1I}{I_{sat}}(N_1 - N_3),$$

$$\frac{dN_4}{dt} = -W_4N_4 + K_4N_2N_1^Y + \frac{\sigma_{24}}{\sigma_{02}}\frac{W_1I}{I_{sat}}N_2 + C_2N_2^2,$$

$$\frac{dN_1^Y}{dt} = -W_1^YN_1^Y + \frac{W_1^YI}{2I_{sat}^Y}(N_0^Y - N_1^Y) - K_2N_0N_1^Y + K_{B2}N_2N_0^Y - K_3N_1N_1^Y - K_4N_2N_1^Y$$

Equation 7

Here N_j is the density of Er^{3+} ions in the energy level j, where the subscripts j = 0, 1, 2, 3, and 4 represent the $^4I_{15/2}$, $^4I_{13/2}$, $^4I_{11/2}$, $^4F_{9/2}$, and $^4S_{3/2}$ energy levels of Er^{3+} ions respectively (see Figure 26). The population of fast-decaying levels as $^4F_{7/2}$ and $^4I_{9/2}$ were neglected and the populations of energy levels $^2H_{11/2}$ and $^4S_{3/2}$ in thermal equilibrium. N_0^Y and N_1^Y are the Yb^{3+} ion density in the $^4F_{7/2}$, and $^4F_{5/2}$ energy levels. W_{jl} is the decay rate from level j to level l, whereas W_j (W_j^Y for Yb^{3+} ions) is the total decay rate of the energy level j. The decay rates from the excited-level to the ground state were considered as radiative decay rates (in the millisecond range) and corresponding to the next lower level as a faster nonradiative decay (microsecond range) through multi-phonon relaxation. On the other hand, K_2, K_3, and K_4 are the coefficients of the resonant energy transfer from Yb^{3+} ions (sensitizers) to levels *2*, *3*, and *4* of Er^{3+} ions (activators), respectively. K_{B2} is the coefficient of the back energy transfer from Er^{3+} ions in level *2* to Yb^{3+} ions. C_1 and C_2 are the coefficients of energy transfer between neighboring Er^{3+} ions. C_1 represents a quenching mechanism for erbium-doped amplifiers ($^4I_{13/2}$, $^4I_{13/2}$) → $^4I_{15/2}$, $^4I_{9/2}$, and C_2 represents an upconversion energy transfer to the green-emitting level ($^4I_{11/2}$, $^4I_{11/2}$) → $^4I_{15/2}$, $^4F_{7/2}$. σ_{jl} is the absorption ($\simeq$ emission) cross-section at the laser frequency for transition from level j to level l of Er^{3+} ions. The absorption cross-section of the Yb^{3+} transition is σ^Y. The laser intensity is denoted as I (in units of W/cm^2) and is normalized to the saturation intensity $I_{sat}^Y = \hbar\omega W_1^Y/(2\sigma^Y)$ for the Yb^{3+} transition and to $I_{sat} = \hbar\omega W_1/\sigma_{02}$ for the Er^{3+} transitions resonant with the excitation laser wavelength at 976 nm, where $\hbar\omega$ is the photon excitation energy.

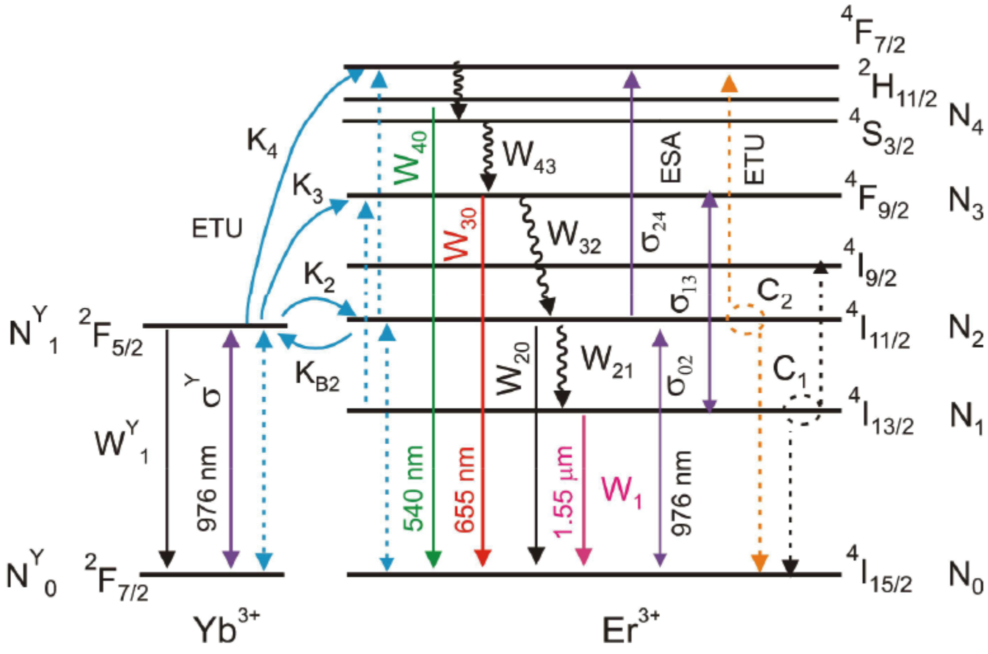

Figure 26. Energy level diagram for Yb^{3+} and Er^{3+} ions describing the physical processes used in our rate equation model. Blue lines represent the Yb–Er ETU mechanism (K_2, K_{B2}, K_3, and K_4), whereas orange and black dashed lines represent different Er–Er ETU mechanisms (C_1 and C_2). Purple lines represent the ground state absorption of Yb^{3+} (σ^Y) and Er^{3+} (σ_{02}) ions and the excited-state absorption of Er^{3+} ions (σ_{13} and σ_{24}). Solid lines represent radiative decay rates from different levels (W_1^Y for Yb^{3+} and W_1, W_{20}, W_{30}, W_{40} for Er^{3+}), whereas faster nonradiative decay rates are represented by wavy lines (W_{43}, W_{32} and W_{21}).

In our simulations, we have given the values for the decay, the energy transfer coefficient, and the absorption cross section in the same order of magnitude as in the literature.[153,161-163] We used them as control parameters to correctly reproduce the experimental results. Er^{3+} ions in the metastable level 1 , $^4I_{13/2}$ (see Figure 26) radiatively decay to the ground state $^4I_{15/2}$ with a decay time of $1/W_1$=4 ms while Yb^{3+} ions in level 1 (see Figure 26) decay to the ground state with a decay time of $1/W_1^Y$=2 ms. The other energy levels of Er^{3+} ions present two contributions, a radiative decay rate to the ground state in the millisecond range ($1/W_{20}$=2 ms, $1/W_{30}$=1 ms, and $1/W_{40}$ =1 ms) and a faster nonradiative decay rate to the next lower level (partially due to multi-phonon relaxation) which is within the microsecond range. Here, we used an intrinsic quantum yield for the green level 4 (see Figure 26), η0 = $W_{40}/(W_{40} + W_{43}) \simeq 0.06$, which leads to W_{43} = 1.6×10^4 s^{-1} . For simplicity, we took the same value for the rest of nonradiative decay rates, W_{32} = W_{21} = W_{43} (see Figure 26). Furthermore, the following values for the resonant energy transfer parameters are considered. Concerning the energy transfer from Yb^{3+} to Er^{3+} ion (see Figure 26), we set K_2 = 5×10^{-17} cm^3s^{-1} , a similar value for the back energy transfer K_{B2}=K_2, and a lower value for K_4 =0.5K_2. Considering our experimental results that indicate that both UCL emission bands have the same behavior with the Yb/Er ratio, we assume that the main population pathway for the red-emitting level is through the green-emitting level. Therefore, we neglected in the simulations the energy transfer from level $^4I_{13/2}$ (K_3= 0) and the excited state absorption from this level (σ_{13} = 0) (see Figure 26). The energy transfer coefficients between neighbors Er^{3+} ions were taken C_1=1.2×10^{-17} cm^3s^{-1} and C_2 =1.8×10^{-17} cm^3s^{-1}. The absorption cross-section of the Yb^{3+} transition σ^Y= 1.7×10^{-20} cm^2 is much larger than the corresponding to the Er^{3+} transition σ_{02} = 0.68×$10^{-21}$$cm^2$. The excited state transition from level $^4I_{11/2}$ to the green-emitting level is similar to the previous one, i.e, σ_{24} = σ_{02}. With these values, we obtained a saturation intensity of I^Y_{sat}= 3 kW/cm^2 for the Yb^{3+} transition and a much larger saturation value for the corresponding Er^{3+} transition I_{sat}=75 kW/cm^2. For the range of excitation laser powers used in our experiments, we operate below and above the saturation value of Yb^{3+} transition but very far away from the saturation value of Er^{3+} transition. Therefore, the behavior of the luminescence with the laser power is expected to be different for very low Yb/Er ratios (absorption of Er^{3+} ions without saturation) than for high ones (absorption of Yb^{3+} ions with possible saturation). To numerically study the effect of the Yb/Er ratio in the luminescence of the UCNPs, we varied the concentration of Er^{3+} and Yb^{3+} dopants accordingly with the Yb/Er ratios. To estimate the concentration of Er^{3+} (N_{Er}) and Yb^{3+} (N_{Yb}) ions, we followed the molecular weight calculation of UCNPs by Mackenzie et al.[164] We used the hexagonal crystal lattice parameters a_h=0.596 nm and c_h=0.353 nm to calculate the volume of a unit cell in the UCNP ($u_v \simeq$0.1086 nm^3). Then, we considered the fractional percentage of RE dopants f_{RE}(RE = Yb and Er) to compute the RE ion concentration N_{RE}= 1.5 f_{RE}/u_v .

The Equation 7 was solved using an explicit Runge-Kutta method in MatLab[165] considering that all population is initially in the ground states ($N_0 = N_{Er}$ and $N^Y_0 = N_{Yb}$).After an initial transient, the system reached the steady-state, and the final populations allowed us to compute the luminescence intensity. By numerically solving Equation 7 we obtained the steady-state populations for green (N_4), red (N_3), and IR (N_1) emission levels which are proportional to their luminescence emission intensities. We plotted the simulated populations (see lines in Figure 23A and C) as a function of the Yb/Er ratio for a laser intensity below (I/I^Y_{sat}=0.1) and above (I/I^Y_{sat}=1.2) the saturation intensity of the Yb^{3+} transition.

These simulated curves showed very good agreement with the experimental results. In addition, we theoretically analyzed the biphotonic behavior of the upconversion mechanism for the Yb/Er ratios used in Figure 24A. Then, we computed the population of green ($^4S_{3/2}$) N_4 and red ($^4I_{9/2}$) N_3 emission levels as a function of the excitation intensity. The results, shown in Figure 24B, showed the same behavior as the one reported in the experiments. For the Yb/Er ratio 0, the laser always operates in the linear absorption regime since the excitation intensity is below the saturation value of the ground state absorption of the Er^{3+} transition ($^4I_{15/2} \rightarrow {}^4I_{11/2}$). Therefore, the quadratic behavior remains. However, for the Yb/Er ratio 10, the laser absorption is due to the ground state absorption of the Yb^{3+} transition ($^2F_{7/2} \rightarrow {}^2F_{5/2}$). This transition exhibits a lower saturation value so that it can be reached with the excitation laser intensity used in the experiments, and therefore, a saturation of the quadratic behavior occurs.

We used our theoretical model to analyze the contribution of different mechanisms leading to upconversion and downconversion emission processes as a function of the Yb/Er ratio referred to as r hereafter. To produce both UCL and DCL, Er^{3+} ions need first to be excited into the intermediate level $^4I_{11/2}$. The population of the intermediate level is directly responsible for the DC emission processs since $^4I_{13/2}$ is populated through the $^4I_{11/2}$ level. Two possible mechanisms populate the intermediate level: **(1)** direct excitation by the laser, i.e., GSA of Er^{3+} ions (see Figure 27C)and **(2)** GSA of Yb^{3+} ions and energy transfer (ET) from the $^2F_{5/2}$ level of Yb^{3+} ions to the $^4I_{11/2}$ level of Er^{3+} ions (see Figure 27C). We analyzed the steady-state population N_1 of the $^4I_{13/2}$ level of Er^{3+} ions (see Figure 27B) with and without considering ET between Yb^{3+} and Er^{3+} ions. Figure 27B shows that the NIR emission at 1.55 mm was mainly achieved by way of the ET from Yb^{3+} ions to Er^{3+} ions even for very low values of the Yb/Er ratio. In the extreme case of Yb/Er ratios smaller than 0.01, the only mechanism leading to DCL is the GSA of Er^{3+} ions since the small number of Yb^{3+} ions in UCNPs is not able to efficiently populate the $^4I_{11/2}$ level of Er^{3+} ions.

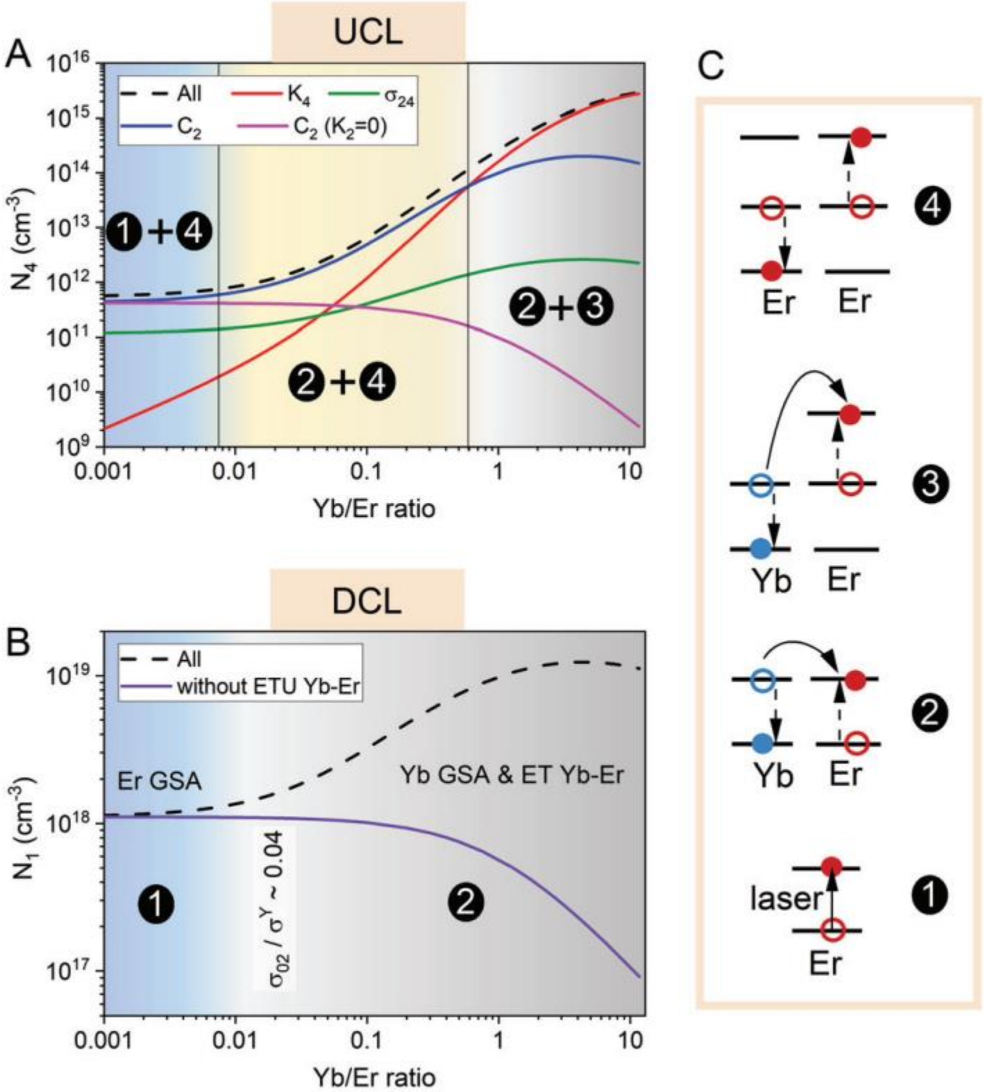

Figure 27. **(A)** Steady-state population of the green emission level ($^4S_{3/2}$) N_4 of Er^{3+} ions as a function of the Yb/Er ratio for a laser intensity I/I_{sat}^{Y}=0.01. Different curves were computed using different that populate the green and red emission levels. **(B)** Steady-state population of the NIR emission level ($^4I_{13/2}$) N_1 of Er^{3+} ions as a function of the Yb/Er ratio for a laser intensity I/I_{sat}^{Y}=0.01. Curves were computed with and without accounting for ET between Yb^{3+} and Er^{3+} ions. **(C)** A schematic of the main mechanisms involved in DCL and UCL.

To get a deeper insight, we have obtained an analytical expression for the population of the NIR emission level $^4I_{13/2}$ in the low excitation regime. We analytically solved the rate equation model (Equation 7 in section 5.1.6.4) in the steady state (time derivatives set to zero) by considering the small excitation signal regime, i.e., $I/I^Y_{sat} \ll 1$. In the case, most of the population remains in the ground state ($N_1 \simeq N_{Er}$ and $N^Y_0 \simeq N_{Yb}$) and the population of the excited states are obtained linearizing the Equation 7 as follows:

$$0 = -W_1N_1 + W_{21}N_2,$$

$$0 = -W_2N_2 + K_2N_{Er}N^Y_1 - K_{B2}N_{Yb}N_2 + \frac{W_1 I}{I_{sat}}N_{Er},$$

$$0 = -W_3N_3 + W_{43}N_4,$$

$$0 = -W_4N_4 + K_4N_2N^Y_1 + C_2N_2^2,$$

$$0 = -W^Y_1N^Y_1 + \frac{W^Y_1 I}{2I^I_{sat}}N_{Yb} - K_2N_{Er}N^Y_1 + K_{B2}N_{Yb}N_2,$$

Equation 8

Where N^Y_1, N_1 and N_2 are first-order perturbations, and N_3 and N_4 are second-order perturbations in the excitation intensity respectively. We have not included the processes neglected in our simulations ($K_3 = 0$ and σ_{13}=0) and the contribution of ESA (σ_{24}=0) which has been found to be negligible in comparison with Er-Er-ETU (see Figure 27A). From the above linear system of equations (Equation 8) we obtained the analytical steady state populations:

$$N^Y_1 = \frac{\dfrac{W^Y_1N_{Yb}}{W^Y_1 + K_2N_{Er}}\dfrac{I}{2I^Y_{sat}} + \dfrac{W_1K_{B2}N_{Yb}N_{Er}}{(W^Y_1 + K_2N_{Er})(W_2 + K_{B2}N_{Yb})}\dfrac{I}{I_{sat}}}{1 - \dfrac{K_2K_{B2}N_{Yb}N_{Er}}{(W^Y_1 + K_2N_{Er})(W_2 + K_{B2}N_{Yb})}},$$

$$N_2 = \frac{K_2N_{Er}}{W_2 + K_{B2}N_{Yb}}\,N^Y_1 + \frac{W_1N_{Er}}{W_2 + K_{B2}N_{Yb}}\,\frac{I}{I_{sat}},$$

$$N_1 = \frac{W_{21}}{W_1}N_2,$$

$$N_4 = \frac{K_4}{W_4}N_2N^Y_1 + \frac{C_2}{W_4}\,N_2^2,$$

$$N_3 = \frac{W_{43}}{W_3}N_4.$$

Equation 9

These analytical expressions (Equation 9) allow us to theoretically analyze the UCL and DCL emission intensity. In **¡Error! No se encuentra el origen de la referencia.** we compare the a nalytical populations given by Equation 9 (colored solid lines) with the result obtained by numerically solving Equation 8 (colored open circles) in the case of low excitation intensities (I/I_{sat}= 0.001). A perfect agreement is observed. Furthermore, we also plotted (black solid lines) the experimental power law obtained for the DCL and UCL intensities with the Yb/Er ratio (exponent 0.6 for DCL and 1.4 for UCL from Figure 24C and Figure 24D). Both, the numerical simulations and the analytical result from Equation 9, nicely match with the experimental behavior.

On the other hand, with the aim of obtaining a very simple and direct expression for the populations N_1 and N_4 as a function of the Yb/Er ratio we further simplified Equation 9. We first simplified the population of the Yb^{3+} excited state $^2F_{5/2}$, N_1^Y in Equation 9, by taking into account that $W_1^Y + K_2N_{Er} \simeq K_2N_{Er}$ and that the second term of the right hand side of N_1^Y is smaller than the first term since $(W_2 + K_{B2}N_{Yb})/\ K_{B2}N_{Er} > \sigma_{02}/\sigma^Y$. Then, we simplified N_2 in Equation 9 by keeping only the first term of the right hand side, which is larger than the second one while $N_{Yb}/N_{Er} > (\sigma_{02}/\sigma^Y\ )W_2/(W_2 + K_{B2}N_{Yb})$, which takes place in most of the analyzed ratios. Therefore, the population equations remain:

$$N_1^Y = \frac{W_1^Y(W_2 + K_{B2}N_{Yb})N_{Yb}}{W_2K_2N_{Er}} \frac{I}{2I_{sat}^Y},$$

$$N_2 = \frac{W_1^Y N_{Yb}}{W_2} \frac{I}{2I_{sat}^Y},$$

$$N_1 = \frac{W_{21}}{W_1} N_2,$$

$$N_4 = \frac{1}{W_4}\left(\frac{W_1^Y}{W_2}\right)^2 N_{Yb}^2 \left[\frac{K_4}{K_2} \frac{W_2 + K_{B2}N_{Yb}}{N_{Er}} + C_2\right] \left(\frac{I}{2I_{sat}^Y}\right)^2,$$

$$N_3 = \frac{W_{43}}{W_3} N_4.$$

Equation 10

We also plotted in **¡Error! No se encuentra el origen de la referencia.** the analytical populations given by Equation 10 (colored dashed lines), which still show a good agreement with the numerical simulations. More interestingly, these analytical population equations allowed us to nicely reproduce the enhancement of the DCL and UCL intensity found in the experiments. In particular, the best agreement between Equation 10 and the experimental power law behavior is found for ratios within the intermediate range [0.2−1.0].

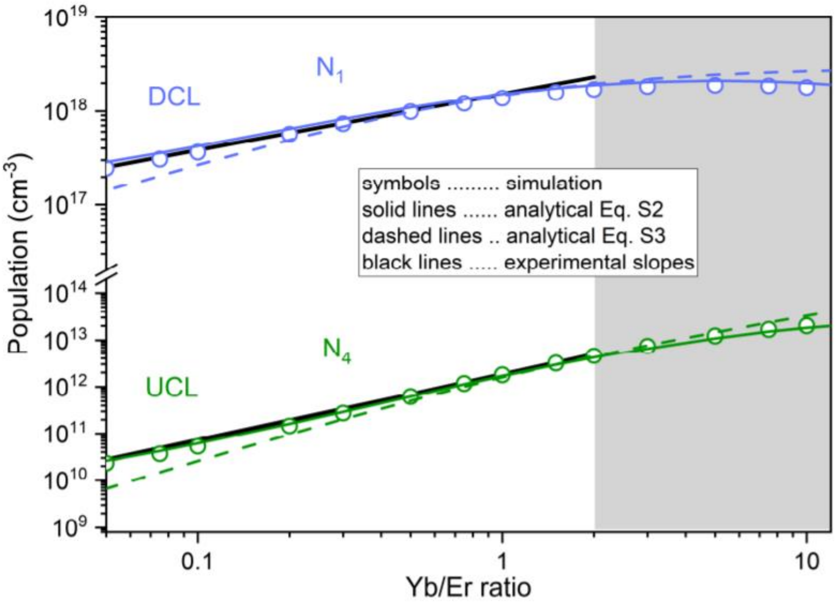

Figure 28. Steady-state populations for the green (N_4) and NIR (N_1) emission levels as a function of Yb/Er ratio. Analytical results using Equation 9 (colored solid lines) and Equation 10 (colored dashed lines). The numerical simulated result using equation Equation 8 (symbols). The black solid lines are power laws corresponding to the fit fitting of the experimental data: Exponent 0.6 for DCL and 1.4 for UCL

After that, we obtained an analytical expression for the population of the NIR emission level $^4I_{13/2}$ in the low excitation regime using N_2 from Equation 9 and N_1^Y from Equation 10.

$$N_1 \approx \frac{W_{21}W_1^Y N_{Yb}}{W_1 W_2}\frac{I}{2I_{sat}^Y} + \frac{W_{21}N_{Er}}{W_2 + K_{B2}N_{Yb}}\frac{I}{I_{sat}}$$

Equation 11

Where the first term of the right-hand side comes from Yb GSA and Yb–Er ET and the second one from Er GSA. The combination of both the ground state absorption cross sections and the concentrations of activators and sensitizers decides which ion absorbs NIR radiation more efficiently. A similar contribution of both terms takes place for $\frac{N_{Yb}}{N_{Er}} \approx \frac{\sigma_{02}}{\sigma^Y} = 0.04$. As the ground state absorption cross section of Yb^{3+} ions is more than one order of magnitude larger than the corresponding Er^{3+} ions, even at very low Yb/Er ratios, the global absorption can be ascribed to Yb^{3+} ions. Thus, the dependence of the population N_1 on the Yb/Er ratio can be mainly described as proportional to the concentration of Yb^{3+} ions (Equation 11) which can be written as a function of the Yb/Er ratio, r, as $N_1 \sim \frac{r}{(1+r)}$. The behavior given by this simple expression well matches with the power law of the DCL intensity found in the experiments with exponent 0.6. We can analytically write simple dependencies for the populations N_1 and N_4 on the Yb/Er ratio (referred as to r) valid within this range, see Equation 12 and **¡Error! No se encuentra el origen de la referencia.** show the results.

$$N_1 = \frac{W_{21}W_1^Y}{W_1 W_2} N_{Yb}\frac{I}{2I_{sat}^Y} \sim N_{Yb} \sim \frac{r}{1+r},$$

$$N_4 = \frac{C_2}{W_4}\left(\frac{W_1^Y}{W_2}\right)^2 N_{Yb}^2 \left(\frac{I}{2I_{sat}^Y}\right)^2 \sim N_{Yb}^2 \sim \left(\frac{r}{1+r}\right)^2$$

Equation 12

On the other hand, to produce UCL once the Er^{3+} ions are excited in the $^4I_{11/2}$ level, three different pathways can populate the green and red emission levels: **(1)** ETU from the Yb^{3+} ion to the excited Er^{3+} ion (Yb–Er ETU) (see Scheme 3 in Figure 27C); **(2)** ESA from this level; **(3)** ETU from the neighboring excited Er^{3+} ion (Er–Er ETU) (see Scheme 4 in Figure 27C). Equation 8 was solved by allowing independently only one of the three possible pathways: **(1)** Yb–Er ETU controlled by K_4; **(2)** ESA controlled by σ_{24}; and **(3)** Er–Er ETU controlled by C_2. Figure 27A shows the population of the green emission level N_4 as a function of the Yb/Er ratio when only one of the mechanisms is present at a time. For example, the red curve corresponds to Yb–Er ETU and was obtained by setting σ_{24}=0 and C_2=0 in the simulations. We also plotted in the same figure the result obtained when all processes were present (black dashed lines).

We observed how the dominant mechanism of upconversion changes as the Yb/Er ratio varies. At large values of the Yb/Er ratio (above 1), Yb–Er ETU was the dominant mechanism as expected. ET from Yb^{3+} ions to Er^{3+} ions dominates at both steps, first, to populate the intermediate level $^4I_{11/2}$ and then to populate the green emission level (mechanisms 2 and 3 in Figure 27, respectively). For lower Yb/Er ratios, Yb–Er ETU seems to be negligible since there are very few Yb^{3+} ions to transfer their energy to the excited Er^{3+} ions. Therefore, for Yb/Er ratios below 1, the primary mechanism for obtaining upconversion was the energy transfer between Er^{3+} ions, instead of the ESA process (see Figure 27A). As we showed in Figure 27B, the excitation of the intermediate level $^4I_{11/2}$ was due to the ET from Yb^{3+} ions even at values of the Yb/Er ratio as low as 0.01. This means that the population of the green emission level is due to a combination of two types of ET mechanisms: The Yb–Er ET to populate the intermediate level $^4I_{11/2}$ and Er–Er ETU to finally populate the green emission levels (mechanisms 2 and 4 in

Figure 27). We corroborated this by numerically solving Equation 8 considering only Er–Er ETU (using K_4= 0 and σ_{24} =0 as we did to obtain the blue line in Figure 27A) and removing ET processes between Yb^{3+} and Er^{3+} ions that populate the intermediate level (K_2= K_{B2}= 0). In this case (magenta line in Figure 27A), UCL is produced by GSA of Er^{3+} ions and Er–Er ETU (mechanisms 1 and 4 in Figure 27). These mechanisms are only relevant for very low values of the Yb/Er ratio when there are virtually no Yb^{3+} ions. In summary, as the Yb/Er ratio was varied, three different mechanisms were found to explain the whole UCL emission process, corresponding to the three different coloured regions shown in Figure 27A.

We have also obtained an analytical expression for the population of the green emission level valid in the low excitation regime (see Equation 13):

$$N_4 \approx \frac{1}{W_4}\left(\frac{W_1^Y}{W_2}\right)^2 N_{Yb}^2\left[\frac{K_4}{K_2}\,\frac{W_2 + K_{B2}N_{Yb}}{N_{Er}} + C_2\right]\left(\frac{I}{2I_{sat}^Y}\right)^2$$

Equation 13

The first term of the right-hand side comes from Yb–Er ETU, which dominates at large Yb/Er ratios. At lower Yb/Er ratios, the second term of Equation 13 which comes from Er–Er ETU, dominates so the population N_4 (and therefore N_3) follows roughly a quadratic dependence on the concentration of Yb^{3+} ions and can be described in terms of the Yb/Er ratio as: $N_4 {\sim} N_{Yb}^2 {\sim} r^2(1+r)^2$. This simple expression gives us the behavior of the UCL intensity with the Yb/Er ratio, being in good agreement with the power-law behavior found in the experiments with exponent 1.4. For comparison, **¡Error! No se encuentra el origen de la referencia.** s hows the simulated result from Equation 8, the analytical results, and the fit to the experimental data.

5.1.7 Conclusion

We investigated experimentally and theoretically the influence of dopant ion concentration on the UCL and DCL properties of $NaYF_4$:Yb^{3+},Er^{3+} nanoparticles at different excitation intensities. Our approach carefully excluded all other factors whose variation affects the luminescence properties, such as size, morphology, crystal structure, ion distribution, ligand, and surrounding medium, which allowed us to accurately determine the influence of the ratio of Yb^{3+} to Er^{3+} ions on NP luminescence. In particular, we studied the luminescence emission from 30 nm monodisperse β-$NaYF_4$:Yb^{3+},Er^{3+} nanoparticles with a fixed total amount of dopants in the matrix of 22% by replacing this 22% Y^{3+} ions with a variable ratio of Yb^{3+} ions to Er^{3+} ions between 0 and 10. In both cases (UCL and DCL), the luminescence emission increased significantly with increasing Yb/Er ratio. However, no additional increase was observed at ratios greater than four. Larger variations in UCL and DCL were observed when the excitation intensity was decreased. Time-resolved luminescence analyzed in UCL did not show any appreciable change with dopant ratio, indicating a negligible effect of dopant ratio on the decay dynamics of the UCL emission process.

Finally, a theoretical model was used to analyze the contribution of the different mechanisms involved in UCL and DCL involved when the doping ratio is varied. The results confirm that the dominant mechanism of UCL varies with the Yb/Er ratio. At very low Yb/Er ratios, the Yb-Er ETU was negligible, and the Er-Er ETU process even took precedence over ESA. Above the ratio of 1, the predominant mechanism was the Yb-Er ETU, as expected. In the middle range of dopant ratios, both energy transfer mechanisms contribute simultaneously to luminescence in a cooperative manner: Yb-Er ET, to occupy the intermediate level of Er^{3+} ions, and Er-Er ETU to occupy the green and red emitting levels. The DCL emission process in the NIR region at 1550 nm was mainly achieved by the energy transfer from Yb^{3+} ions to Er^{3+} ions. It can be concluded that there was a competition between the GSAs of both types of ions and their concentrations. However, since the GSA of Yb^{3+} ions was an order of magnitude larger than that of Er^{3+} ions, the total absorption was attributed to Yb^{3+} ions, even for the lowest analyzed Yb/Er ratio of 0.1 (except 0).

5.2 Upconverting Nanoparticles in Aqueous Media: Not a Dead-End Road. Avoiding Degradation by Using Hydrophobic Polymer Shells

> "Well, I feel that we should always put a little art into what we do. It's better that way."
>
> Jules Verne

5.2.1 Abstract

One of the major challenges in using UCNPS in biomedical applications is that their transfer into aqueous media is often accompanied by severe luminescence quenching, partial dissolution by water, and even complete degradation by molecules such as phosphates. These are currently the main problems hindering the use of UCNPs in the clinic. In this work, a strategy is developed to coat and protect β-NaYF$_4$ UCNPs from these effects by forming a hydrophobic polymer shell (HPS) by miniemulsion polymerization of styrene (St) or St and methyl methacrylate mixtures. This allows one to obtain single core@shell UCNPs@HPS with a final diameter of ≈60-70 nm. Stability studies reveal that these HPSs serve as a very effective barrier, impeding polar molecules to affect UCNPs optical properties. Even more, it allows UCNPs to withstand aggressive conditions such as high dilutions (5 µg/mL), high phosphate concentrations (100 mM), and high temperatures (70°C). The physicochemical characterizations prove the potential of HPSs to overcome the current limitations of UCNPs. This strategy, which can be applied to other nanomaterials with similar limitations, paves the way toward more stable and reliable UCNPs with applications in life sciences.

Keywords: *Upconversion nanoparticles, polymers shells, dissolution, degradation, phosphate protection.*

5.2.2 Resumen

Uno de los principales desafíos en el uso de UCNPS en aplicaciones biomédicas es que su transferencia a medios acuosos suele ir acompañada de una severa extinción de la luminiscencia, una disolución parcial en agua e incluso una degradación por la interacción con moléculas como los fosfatos. Estos son actualmente los principales problemas que dificultan el uso de UCNP en la clínica. En este trabajo, se desarrolló una estrategia para recubrir y proteger los UCNP β-NaYF$_4$ de estos efectos mediante el recubrimiento con un polímero hidrofóbico (HPS) a través de la polimerización de estireno (St) o una mezcla de St y metacrilato de metilo. Esto permite obtener nanopartículas de forma core@shell recubiertas con el polímero, con un diámetro final de ≈60-70 nm. Los estudios de estabilidad revelan que estos HPS sirven como una barrera muy eficaz, impidiendo que las moléculas polares afecten las propiedades ópticas de las UCNPs. También permite que las UCNPs resistan condiciones agresivas como: altas diluciones (5 µg/mL), concentraciones altas de fosfato (100 mM) y temperaturas altas (70 °C). Las caracterizaciones fisicoquímicas demuestran el potencial de las HPS para superar las limitaciones actuales de las UCNPs. Esta estrategia, que se puede aplicar a otros nanomateriales con limitaciones similares, allana el camino hacia UCNPs más estables y confiables con aplicaciones en ciencias de la vida.

Palabras Clave: *Nanopartículas de conversión-ascendente, cubierta de polímeros hidrofóbicos, prevención de la degradación, protección de fosfatos.*

5.2.3 Introduction

The transfer step of the UCNPs to water is highly detrimental to their luminescent properties, and for their bio-applications due to several reasons.[6,166–168] First, the aqueous transfer of UCNPs is usually accompanied by a strong decrease in the lifetime and luminescence of the lanthanides forming them.[168,169] This is due in part to surface damping resulting from the vibrational modes of the hydrophilic molecules used to render the UCNPs water-dispersible, but mainly to a combination of the strong nonradiative relaxation of Yb^{3+} when coupled to the vibrational modes of water and the relatively high absorption by water (λ_{exc} = 976 nm) at the wavelength used to excite the Yb^{3+}-sensitised UCNPs.[168,169] Second, the solubility product of UCNPs matrices such as β-$NaYF_4$, one of the most efficient and widely used hosts, is quite low (1.6×10^{-26}).[170] However, the high specific surface area of UCNPs (≈46.4 m^2/g for UNCPs of Ø= 30 nm), together with the low concentrations normally required in bioapplications, are in such ranges that UCNPs often suffer time-dependent structural degradation due to dissolution and precipitation of their host matrices in aqueous media.[171,172] Indeed, this effect on the structural integrity of UCNPs has been reported for concentrations of less than 50 µg/mL in nanoparticles with diameters of 25-31 nm.[170] In this regard, it is reasonable to assume that this phenomenon will be even more detrimental in the new generations of UCNPs, considering the current trend toward the synthesis of ultrasmall UCNPs for biological applications or the development of core-and-shell UCNPs, where the dissolution of the shells used to enhance or modify their optical properties will lead to a significant decrease in their luminescence and a change in their optical characteristics.[173–177] Moreover, increasing the temperature of the medium shifts the solubility equilibrium toward the dissolution of UCNPs. For this reason, the application of UCNPs in fields such as nanothermometry or platforms that require thermal cycling, such as polymerase chain reaction (PCR), is currently very difficult when low concentrations of UCNPs are required. Third, the fact that fluoride (F^-) and lanthanide ions (Ln^{3+}) are released into the aqueous medium until solubility equilibrium is reached has important implications. On the one hand, the presence of chemical species (e.g., phosphates) that can trap free Ln^{3+} and form more stable compounds can shift the solubility equilibrium of the host matrices until the UCNPs dissolve completely.[178,179]

On the other hand, the presence of F^- and Ln^{3+} ions in solution raises some questions and concerns about the biocompatibility and bioaccumulation of these ions when UCNPs are used in biological fluids. For example, several toxicity issues have already been attributed to F^- and Ln^{3+}.[180–182] In addition, the high phosphate content may make certain sites in at specific locations within the body, such as the mineral matrix of bone, be susceptible to bioaccumulation of Ln^{3+}.[183,184]

These drawbacks urge the development of a strategy that satisfactorily resolves these limitations and takes a step forward to ensure realistic prospects for these promising materials in the life sciences while expanding their range of current applications. In this direction, several approaches have been explored to alleviate some of these problems. For example, Lahtinen et al. used the so-called common ion effect (addition of KF to aqueous solutions) to hinder the dissolution of UCNPs when used at low concentrations and room temperature (RT)[170]. In a later work, Palo et al. developed a strategy based on coating UCNPs with oppositely charged polyelectrolyte bilayers to delay the disintegration of UCNPs, especially during the first 5 hours.[185] A similar layer-by-layer strategy was later used to mitigate quenching caused by water molecules.[186] Other work has also shown that ligand replacement of the UCNP capping agent with an appropriate molecule can prevent luminescence quenching in some cases.[187] Interestingly, the resulting UCNPs appear to exhibit increased resistance to chemically deleterious molecules such as phosphate buffers and acidic media when some phosphate/phosphonate-containing molecules are used in this type of ligand replacement strategy.[183,186,188] This is due to the high binding affinity between the phosphonate groups and the Ln^{3+} on the surface of the UCNPs, which hinders the release of the ions from the host matrix and partially shields them from other ligands and water molecules. However, not all phosphonates effectively passivate the surface of UCNPs.[189] Indeed, the literature seems to indicate that passivation is often enhanced by capping agents that simultaneously contain one or more phosphonate/phosphonic groups on one side that Design a protective layerstrongly coordinates with the surface of UCNPs and a less polar moiety (e.g., aliphatic chains) on the other side to provide shielding from water and other ligands.[183,190–192] Interestingly, using capping agents containing carboxyl or sulfonate groups instead of phosphonate groups or keeping the original capping agents of UCNPs (e.g., oleic acid) seems to be a viable strategy to partially shield UCNPs from the aqueous environment as long as they are coated with amphipathic molecules containing long aliphatic chains or polymer chains with low polarity.[192–195] This highlights the importance of creating a relatively robust and effective shielding layer around the UCNPs, as this appears to partially limit the diffusion of water and other possible ligands that may adversely affect the optical properties and structural integrity of the UCNPs. Indeed, the use of an interlayer with hydrophobic properties may be one of the best possible approaches, as it not only helps to prevent polar and deleterious molecules from diffusing to the surface of the UCNPs, but also partially maintains a local environment similar to the original postsynthetic hydrophobic conditions (e.g., chloroform or hexane dispersions) in which the UCNPs show their best performance.

We present a simple design of the UCNPs surface that ensures their protection in aqueous media under various harsh conditions. Our approach is based on the combination of two synergistic strategies: first, the oleic acid ligands on the surface of UCNPs are replaced by 10-methacryloyldecyl phosphate (MDP) in nonpolar solvents to achieve surface passivation, colloidal stability in organic media, and a terminal polymerizable group. Second, dispersion and radical miniemulsion polymerization of these UCNPs in styrene (St) or a mixture of St and methyl methacrylate (MMA) is aimed at forming a robust hydrophobic shell with controlled thickness that isolates and protects the UCNPs from the aqueous environment. This method is also expected to confer them colloidal stability in aqueous media, as polar groups are incorporated during the polymerization process. The resulting polymer coated UCNPs were extensively characterised optically, morphologically, and chemically, and their resistance to various harsh conditions such as phosphate buffer, very high dilutions, and high temperatures was studied. An amazing improvement in the chemical resistance of the UCNPs was demonstrated, suggesting that this type of strategy could pave the way to safer UCNPs with more reliable optical properties and expanded applications in life sciences.

5.2.4 *Objectives*

5.2.4.1 General Objective

Develop a protective coating for the $NaYF_4$: Yb^{3+}/Er^{3+} upconverting nanoparticles that can protect them from degradation in aqueous media and harsh conditions such as high temperatures, high solutions, and phosphate buffers, avoiding quenching and preserving the optical properties of the nanoparticles.

5.2.4.2 Specific Objectives

- Synthesis and Characterization of $NaYF_4:Yb^{3+},Er^{3+}$ Nanoparticles.
- Cover the $NaYF_4:Yb^{3+},Er^{3+}$ nanoparticles with an hydrophobic polymer (polystyrene).
- Optimize the coverage of the $NaYF_4:Yb^{3+},Er^{3+}$ nanoparticles by modifying the synthesis conditions.
- Optical and morphological characterization of the the $NaYF_4:Yb^{3+},Er^{3+}$@Ps nanoparticles.
- Perform resistance studies under conditions of low dilution, temperature and phosphate buffer of $NaYF_4:Yb^{3+},Er^{3+}$@Ps nanoparticles and compare the results with $NaYF_4:Yb^{3+},Er^{3+}$ covered with polyacrylic acid (PAA).

5.2.5 Experimental Section

5.2.5.1 Synthesis of UCNPs and Functionalization with MPD

First Monodisperse β-$NaYF_4:Yb^{3},{}^{+}Er^{3+}$ nanoparticles were synthesized by the thermal co-precipitation method described in Section 4.3.1 of Materials and Methods. Subsequently, the functionalization of the surface of the NPs was carried out according to the procedure described in sections 4.3.2 and 4.3.4 varying the conditions such as the amount of monomer, sonication time, nanoparticle concentration, reaction time, and protective shell composition, The different conditions are listed in Table 4.

Table 4. List of different conditions tested during miniemulsion polymerization

Sample name	UCNPs (mass)	Composition (% vol)	Monomer (vol)	Reaction time	Ultrasonication
P1	44 mg	St(100%)	1.2 mL	60 min	No
P2	44 mg	St(100%)	1.2 mL	60 min	Yes (tip)
P3	11 mg	St(100%)	1.2 mL	60 min	Yes (tip)
P4	11 mg	St(100%)	1.2 mL	60 min	Yes (tip)
P5	11 mg	St(100%)	0.6 mL	60 min	Yes (tip)
P6	11 mg	St(100%)	0.3 mL	60 min	Yes (tip)
$P7_{15}$	11 mg	St(100%)	0.6 mL	15 min	Yes (tip)
$P7_{30}$	11 mg	St(100%)	0.6 mL	30 min	Yes (tip)
P100%	11 mg	St(100%)	0.6 mL	60 min	Yes (tip)
P75%	11 mg	St/MMA (75/25%)	0.45 mL/0.15 mL	60 min	Yes (tip)
P50%	11 mg	St/MMA (50/50%)	0.45 mL/0.45 mL	60 min	Yes (tip)
P25%	11 mg	St/MMA (25/75%)	0.15 mL/0.45 mL	60 min	Yes (tip)
P8	11 mg	St/MMA (50/50%)	0.45 mL/0.45 mL	60 min	Yes (Bath)

During these experiments the aqueous phase (4.5 mL; SDS 40 mM, $NaHCO_3$, 1.2mM), hexadecane (24.6 µmoles), initiator (KPS; 225µL, 7.5 mg/mL) and polymerization temperature (70°C) were kept constant.

To compare the spectroscopic and chemical properties of the polymer-coated β-$NaYF_4:Yb^{3},{}^{+}Er^{3+}$ nanoparticles, the surface of the same set of nanoparticles was modified to obtain a polyacrylic acid shell using the method described in section 4.3.5.

5.2.5.2 Characterization

TEM images were acquired by using a JEOL JEM 1010 working at 80 kV and a GATAN Megaview II digital camera. High resolution TEM (HR-TEM) images were obtained using a JEOL JEM 2100 working at 200 kV and coupled to a GATAN Orius SC1000 digital camera. Samples were prepared by depositing a drop of UCNPs dispersion onto Formvar-coated copper grids and dried at RT. High-angle annular dark-field (HAADF) scanning TEM (STEM) and energy-dispersive X-ray (EDX) mappings were conducted by using a FEI Talos F200X (ThermoFisher Scientific, USA) coupled to an EDX detector. For the FT-IR analysis A Thermo Nicolet 200IR spectrometer was used to obtain FT-IR spectra. Samples were prepared by grinding the dried nanoparticles with potassium bromide (KBr) until a thin powder was obtained. Then, the powder was transformed into a pellet by using a mechanical press while air and moisture were removed using a vacuum pump. Background and sample spectra were acquired working in absorbance mode with a resolution of 4 cm^{-1} and 128 scans. Spectra were H_2O and CO_2 corrected. For the thermogravimetric analysis we used a TGA/DSC 1 STAR system (Mettler Toledo. Following the procedure describe in section 4.2.4. The gas flows used during the experiments were 20 cm^3/min for O_2 and N_2, respectively. The Z-potential measurements were carried out with a Malvern Nano-ZS instrument using the method described in section 4.2.7. The Steady-state photoluminescence measurements were obtained using the procedure of the section 4.2.8.

5.2.5.3 Long-Term Stability Assays at High Dilution and Room Temperature (DI-H_2O and Phosphate Buffer)

Long-term stability studies of very diluted UCNPs samples (5 µg/mL of UCNPs) were carried out in both DI-H_2O and 100 mm potassium phosphate buffer (K^+PB). We analyzed the aging for the UCNPs with different polymer shells and their results were compared with UCNPs-PAA, used as a control sample. For each sample, as soon as it was diluted to 5 µg/mL and transferred to the cuvette, it was placed inside the temperature controller cell holder (Jasco, ETC-273T), set at 25°C. After 5 min (considered from here on as time zero), before any significant degradation occurred, the luminescence spectra were measured. Then, the luminescence spectra were measured several times during the next 72 h. For the analysis, all integrated luminescence intensities were normalized to the intensity obtained at time zero. Once the samples aged for 72 h, we also analyzed their decay time at RT and compared it with the decay times obtained for the corresponding not aged samples at a concentration of 100 µg/mL, when chemical degradation was negligible. For TEM characterization after the 72 h stability study in DI-H_2O, samples were concentrated by centrifuging at 21 000 × g during 30 min. To prepare the samples for HR-TEM characterization after the 72h K^+PB stability study, samples were centrifuged five times with DI-H_2O in order to remove excess buffer, and finally concentrated in DI-H_2O after the fifth centrifugation step.

5.2.5.4 Stability Assay at High Dilution and High Temperature (70°C) in DI-H_2O

A long-term stability study of very diluted UCNPs-P75% samples in water at 5 µg/mL was also carried out at high temperature (70°C) to analyze the protective role of the HPS in comparison with that provided by the PAA layer. All spectra were taken at 25°C to account only for the luminescence decrease due to degradation and not to thermometric properties of the UCNPs luminescence. The protocol was the following: right after diluting the samples at 5 µg/mL, the cuvette was introduced in the temperature controller cell holder at 25°C, waited for sample temperature stabilization (5 min), and measured the time zero luminescence spectra. Then, temperature was increased up to 70°C, waited for sample temperature stabilization (10 min), and left the samples at 70°C for 1h to permit the disintegration of the UCNPs. After 1h at 70°C, the temperature was decreased again to 25°C, waited for sample temperature stabilization (20 min), and then measured the spectra again. The temperature cycle was repeated six more times up to 7h. Once the experiments were finished, the authors also analyzed the luminescence decay time at RT of the samples and compared it with the decay times obtained for the corresponding not aged samples at a concentration of 100 µg/mL, when chemical degradation was negligible.

5.2.6 Results and Discussion

5.2.6.1 Results of synthesis of UCNPs and Functionalization with MPD

The synthesis of monodisperse β-$NaY_{0.78}F_4$:$Yb_{0.20}$,$Er_{0.02}$ nanoparticles was performed according to a previously reported thermal coprecipitation method presented at section 4.3.1. The mean diameter of the synthesized UCNPs used in this work was 36±1 nm. A representative TEM picture of the resulting β-$NaY_{0.78}F_4$:$Yb_{0.20}$,$Er_{0.02}$ UCNPs is depicted in Figure 29A, HR-TEM analyses Figure 29B shows the crystalline structure of the synthesized UCNPs, with a characteristic lattice distance of 0.52 nm that can be assigned to (100) lattice plane of the hexagonal β-$NaYF_4$.[196] SAED analysis further confirmed that NaY0.78F_4:$Yb_{0.20}$,$Er_{0.02}$ UCNPs were in their β-phase according to the JCPDS 16-0334 diffraction card. Figure 29C

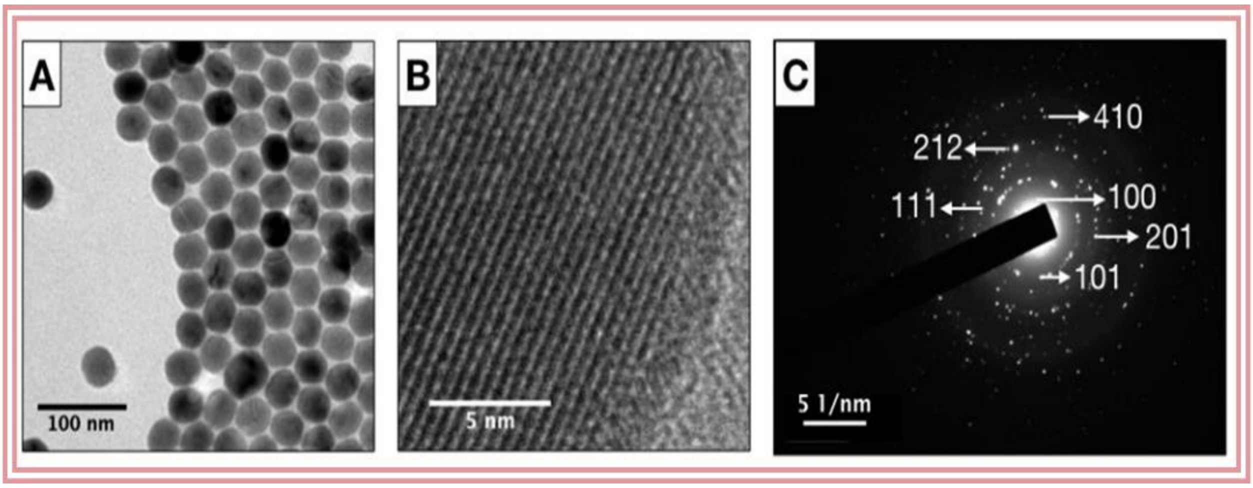

Figure 29. **A)** TEM image of oleate-capped UCNPs showing their monodisperse, quasi-spherical morphology. **B)** HR-TEM magnification of an oleate-capped UCNP showing the 100-lattice plane of the hexagonal NaYF4 phase. **C)** Selected area electron diffraction (SAED) pattern of oleate-capped UCNPs. The *100* (d=0.515 nm), *101* (d= 0.290 nm), *111* (d=0.227 nm), *201* (d=0.207 nm), *212* (d=0.130 nm), and *410* (d=0.112 nm) planes from the hexagonal phase of $NaYF_4$ are easily seen, confirming that $NaYF_4$ is in its hexagonal phase according to the JCPDS 16-0334 diffraction map.

The subsequent treatment of the UCNPs with $NOBF_4$ removed the oleate molecules from their surface (Figure 30A[i]) and allowed phase transfer of the resulting UCNPs from hexane to N,N-Dimethylformamide (DMF). Their later incubation with MDP in DMF/$CHCl_3$ led to their surface functionalization with MDP (Figure 30A[ii]), as shown by FT-IR analyses (see Figure 30B). FTIR analyses of the initial oleate-capped UCNPs yielded the characteristic peaks of the asymmetric and symmetric stretching vibrations of the COO^- group at 1463 and 1552 cm^{-1}, respectively.[197,198] The additional peaks at 2852 and 2936 cm^{-1} correspond to the symmetric and asymmetric stretching vibrations of the aliphatic oleate chain, respectively.[198] Interestingly, after completion of the ligand exchange with MDP, significant changes can be observed in the FTIR spectra of the UCNPs: **1)** new peaks appear at 1085 and 1164 cm^{-1} corresponding to the $P{=}O$ stretching vibration, when substituted with —O, and the in-phase stretching vibration of the $P{-}O^-$, **2)** the peaks at 1648 and 1723 cm^{-1} prove the presence of the methacryloyl group in the MDP, as they correspond to the stretching vibration of $C{=}C$ conjugated with carbonyl groups and of conjugated $C{=}O$ groups, respectively, **3)** the peaks at 2852, 2936 and 2952 cm^{-1} are assigned to the symmetric and asymmetric CH_2 stretching and the asymmetric $CH_2{-}O$ stretching of the ether in MDP, respectively.[198]

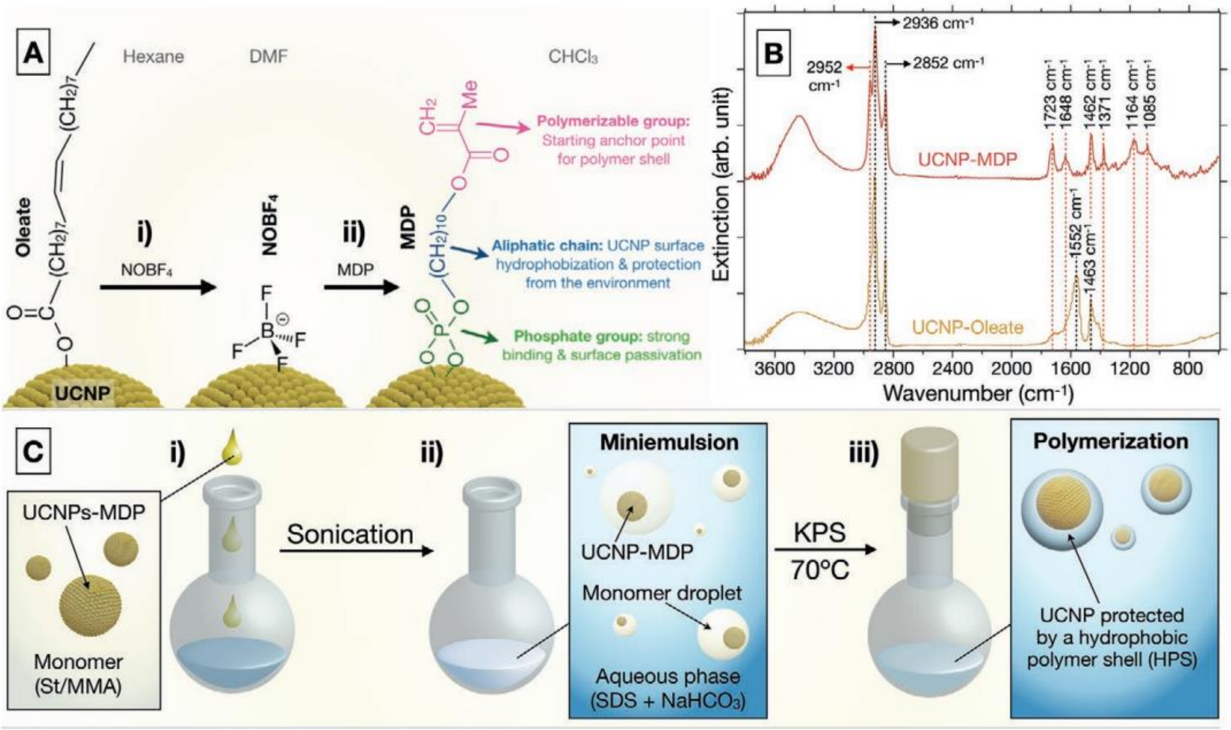

Figure 30. **(A)** Process of surface functionalization of UCNPs involving *(i)* removal of oleate capping agent with $NOBF_4$ and *(ii)* functionalization of UCNPs with MDP in $CHCl_3$. **B)** FT-IR spectra of the UCNPs coated with oleate and MDP. **C)** The main steps required to coat UCNPs-MDP with the HPS by miniemulsion polymerization. Namely, *(i)* dropwise addition of UCNPs-MDP dispersed in the monomer (St or St/MMA mixtures) into the aqueous phase containing SDS and $NaHCO_3$; *(ii)* ultrasonication of the mixture to generate the nanodroplets (i.e., the miniemulsion); *(iii)* addition of the radical initiator (KPS) and initiation of polymerization by heating to 70 °C.

The ligand exchange with MDP provides the resulting UCNPs with several advantages, see Figure 30A. First, the phosphate group within MDP has a strong binding affinity toward the surface of UCNPs,[188] ensuring that the ligand does not detach easily, while providing surface passivation. Second, the MDP aliphatic chain provides hydrophobicity to the surface, which allows UCNPs to be dispersed in the hydrophobic monomer precursors (i.e., St and MMA) that will be polymerized to yield the protective polymer shell in later steps. The MDP aliphatic chains also hamper the adsorption of polar molecules onto the UCNPs' surface, minimizing the luminescence quenching produced by water. Third, the MDP methacryloyl moiety will provide a starting point to initiate, propagate, or terminate the growth of polymer chains during the formation of the protective polymer shell. Finally, MDP can also improve the wetting of UCNPs with polystyrene (PS) and other hydrophobic polymers, favoring a more homogeneous growth of the polymer shell barrier around them and a complete coating of their surface.

5.2.6.2 Coating of UCNPs with HPS by Miniemulsion Polymerization

Miniemulsion polymerization was used to the resulting UCNPs-MDP with a protective hydrophobic polymer shell (HPS). In this method, St or a mixture of St and MMA formed the dispersed oily phase; sodium dodecyl sulfate (SDS) was used as a surfactant; hexadecane was used as hydrophobe or droplet costabilizer; and potassium persulfate (KPS) was used as a radical initiator.[199,200] Miniemulsion polymerization was chosen as a coating method because it offers several advantages over other polymerization approaches, such as fast polymerization kinetics, high St conversion, the possibility of encapsulating single or multiple nanoparticles (NPs) thanks to their isolation in monomer nanodroplets (i.e., nanoreactors) and relatively easy control of the composition, thickness, and morphology of the polymer shell.[199–204]

Interestingly, if oleate-capped UCNPs are directly used in this polymerization process, uncoated snowman-like Janus structures are obtained because of the partial phase separation between the polymer shell and the nanoparticles during polymerization (see Figure 31). This was one of the reasons for replacing oleate with a potentially more suitable component such as MDP.

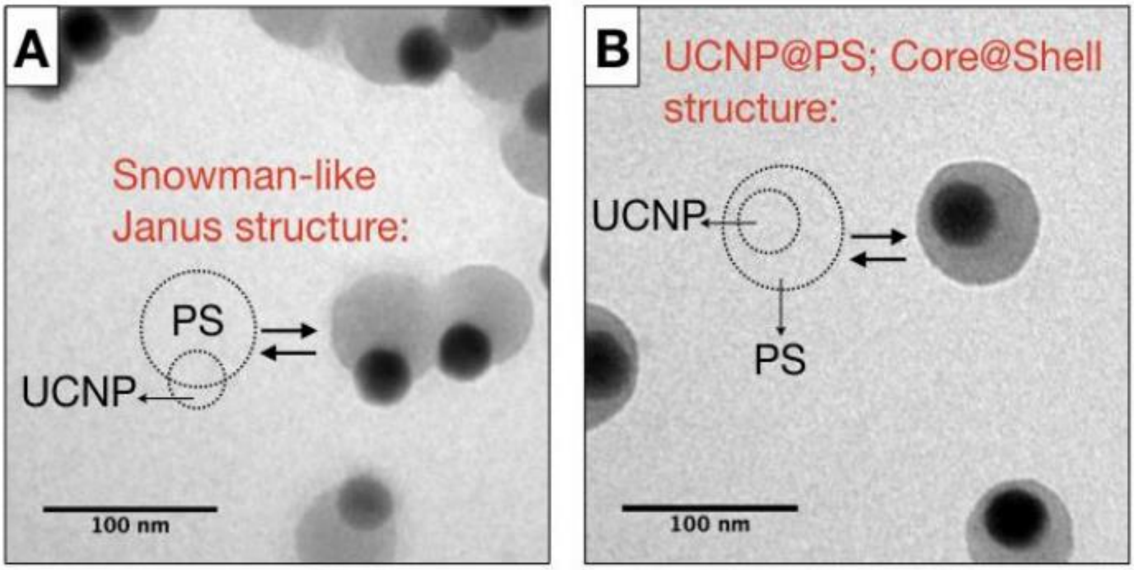

Figure 31. A) TEM image of UCNPs-oleate coated with polystyrene shells. Reduced wetting between the oleate-coated UCNPs and the polystyrene shell results in NP/shell phase separation leading to snowman-like Janus structures where the UCNPs are exposed to the environment. B) TEM image of polystyrene shell coated UCNPs-MDP. The improved wetting allows the formation of Core@Shell structures where the UCNPs (cores) are protected from the environment.

The coating of UCNPs-MDP by miniemulsion polymerization is summarized in Figure 30C. First, UCNPs-MDP were dispersed in St or St/MMA mixtures and added dropwise to a vigorously stirred aqueous solution of 40 mm SDS and 1.2 mm $NaHCO_3$, see Figure 30C[i]. After stirring for 1 h, the resulting emulsion was ultrasonicated to reduce the size of the monomer droplets down to the nanometric range, see Figure 30C[ii]. This allows to create independent nanoreactors containing the UCNPs-MDP, where the polymerization can start in parallel to encapsulate the UCNPs contained thereof.[201] After heating the solution to 70°C, KPS was added to start the radical polymerization of the monomer droplets, yielding the PS or polystyrene-co-poly-methyl methacrylate (PS/PMMA) HPS, see Figure 30C[iii].

5.2.6.2.1. ***Ultrasonication:*** by studying the miniemulsion polymerization process and optimize the coating of the UCNPs-MDP, we first tested the effect of ultrasonic treatment (see Section 4.2.10). In Figure 32P1, it can be seen that without sonication, large submicrometric aggregates of nanoparticles are formed and their morphology is poorly controlled. In contrast, the high energy introduced into the system with an ultrasonic tip (Figure 30C[ii]) can break and enlarge the specific surface area of the dispersed phase (i.e., monomer+UCNPs-MDP) in the initial emulsion, resulting in homogeneous monomer nanodroplets.[199,201] These were effectively stabilized by hexadecane and SDS molecules,[199] allowing polymerization to proceed in these nanoreactors and producing well-defined nanometric HPS, see Figure 32P2. We confirmed that ultrasonic treatment is essential for the formation of the monomer nanodroplets in which the UCNPs-MDP are encapsulated.

We have additionally tested whether it is possible that ultrasonication baths can provide similarly excellent results, making this method more accessible with commonly available laboratory equipment. The results shown in Figure 33 describing a polymer-coated nanoparticle very similar to the others, demonstrate that it is possible to use commonly available laboratory equipment (ultrasonic baths) to produce high-quality UCNPs coated with protective polymer shells and having a simple morphology with a featuring single- core@shell morphology.

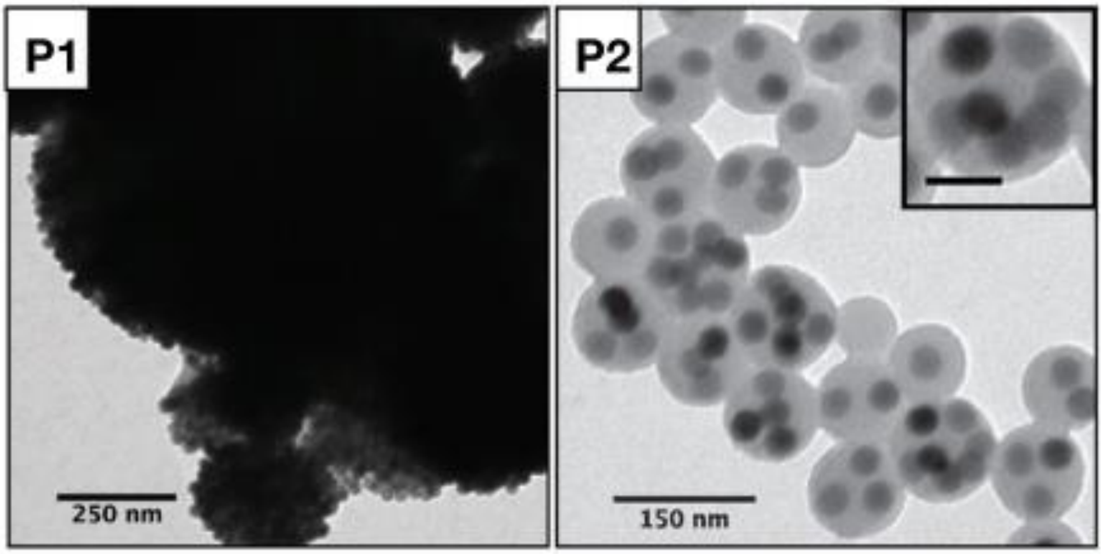

Figure 32. TEM Images of: **P1)** UCNPs@PS aggregates produced when not ultrasonication step; **P2)** Multi-core@shell UCNPs@PS with multiple cores and shells when the ultrasonic step is integrated into the process. All scale bars of the inserts = 50 nm.

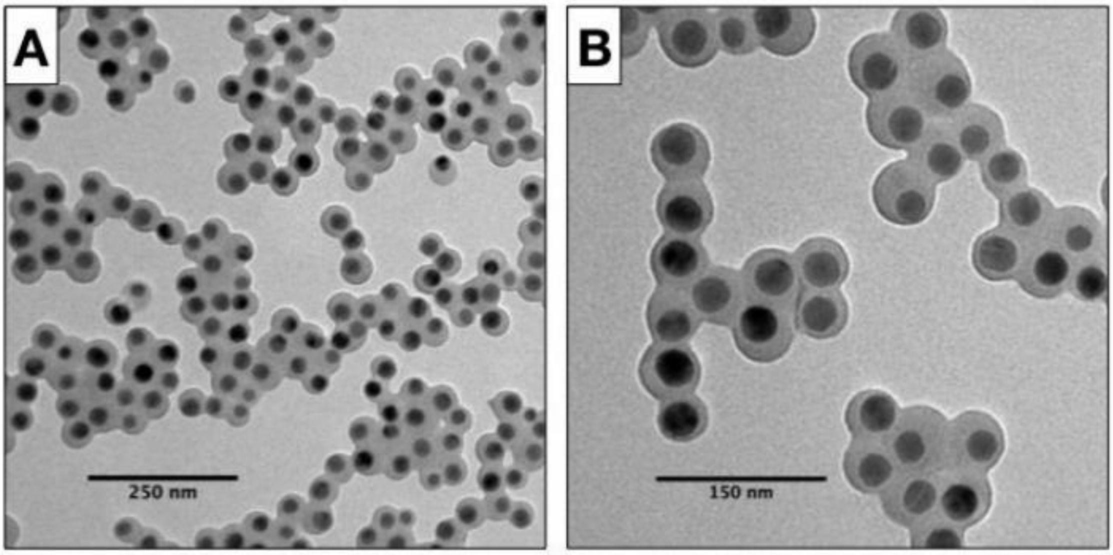

Figure 33. TEM images of UCNPs@PS/PMMA resulting from using an ultrasonication bath. A) TEM image of synthesis P8 (50%/50% St/MMA). B) TEM image magnification of synthesis P8.

5.2.6.2.2. ***UCNPs-MDP concentration & monomer volume:*** Adjustment of the UCNPs-MDP concentration in the dispersed phase using a fixed amount of SDS and monomer allowed control of the number of encapsulated UCNPs. Thus, a 4-fold reduction in the amount of NPs used in miniemulsion polymerization allowed a transition from nanoparticles with multiple cores inside the shell to those with a shell containing a single nanoparticle (see Figure 34P2. and Figure 34P3). The partial eccentric position of the core relative to the shell is attributed to the interfacial tension between the surface of the UCNPs-MDP, the monomer/growth polymer shell, and the aqueous phase.[204–206] The resulting UCNPs-MDP coated with PS, or "**UCNPs@PS**" from now on, were monodisperse in size, featuring 88 ± 4 nm in diameter.

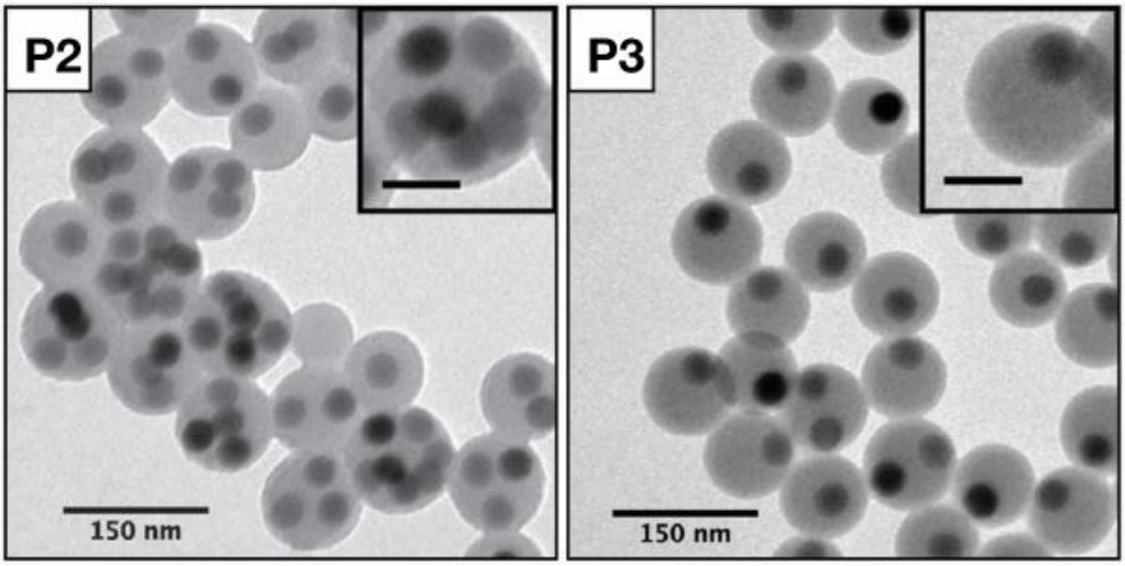

Figure 34. **P2)** Multi-core@shell UCNPs@PS with multiple cores and shells when the ultrasonic step is integrated into the process; **P3)** Single-core@shell UCNPs@ PS prepared after adjusting the initial amount of UCNPs-MDP from 44 to 11 mg. All scale bars of the inserts = 50 nm.

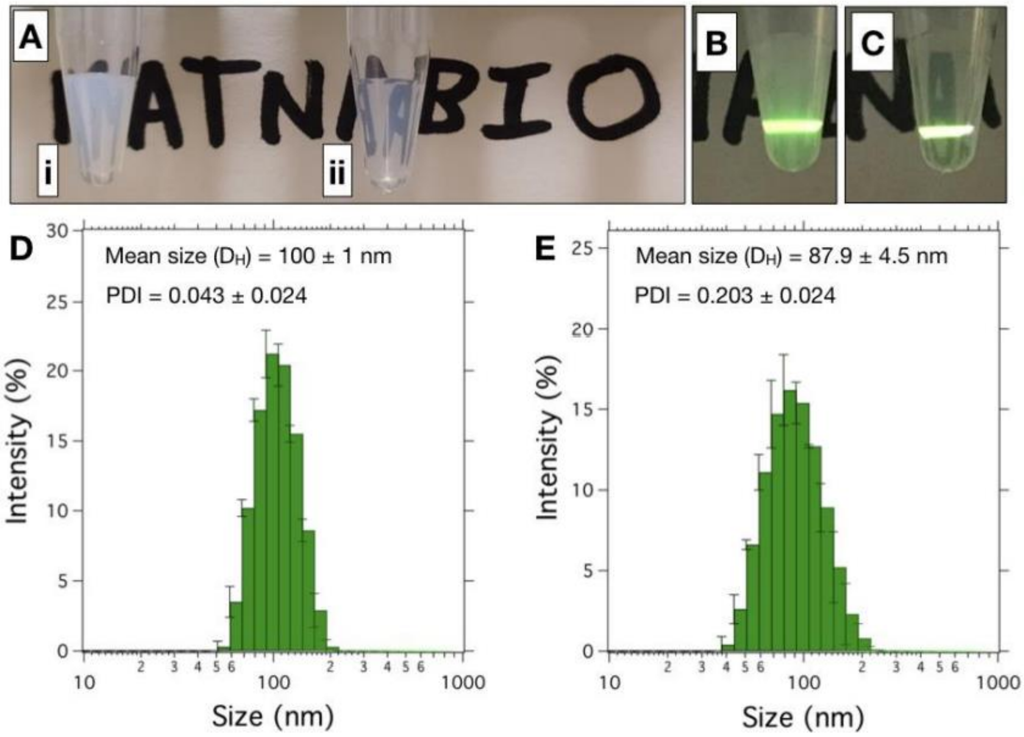

Figure 35. **A)** Photograph of 1 mg/mL dispersions of UCNPS@PS for particles with different TEM diameters: **i)** ⦸ = 88 nm and **ii)** ⦸ = 70 nm. **B & C)** Emission from the dispersion shown in **A.i)** & **A.ii)**, respectively, both under CW excitation with a 976 nm laser (~250 W/cm^2). **D) & E)** DLS Intensity size distributions of the previous UCNPs@PS. These analyses yielded a mean hydrodynamic diameter (D_H) = 100±1 nm and D_H = 87.9±4.5 nm for the UCNPs@PS with TEM ⦸ = 88 nm and ⦸ = 70 nm, respectively.

As a first strategy, the volume of the monomer used for miniemulsion polymerization was reduced from 1.2 to 0.6 or 0.3 mL (Figure 36P4, P5, and P6). As a result, the mean diameter of the UCNPs@PS decreased from 88±4 to 70±5 and to 60 nm±5 nm, respectively. Interestingly, when we increased the SDS/monomer ratio after decreasing the amount of monomer, we observed that the lower volume tested (0.3 mL of St, Figure 36P6) was accompanied by an increase in multinucleated UCNPs@PS (23.8%), compared with only ≈4.8% of multinucleated NPs in Figure 36P5 (0.6 mL of St). This can be explained by the increase in UCNPs/monomer ratio with the decrease in monomer volume, resulting in an effective increase in UCNPs concentration.

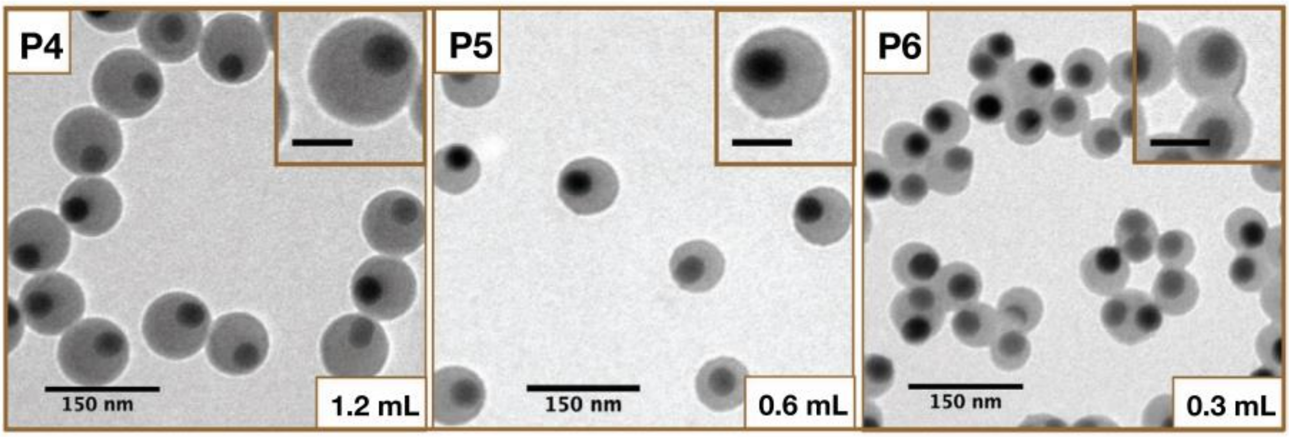

Figure 36. UCNPs@PS produced after adjusting the initial amount of monomer (St) from **P4)** 1.2 mL, **P5)** 0.6 mL and **P6)** 0.3 mL, respectively. All main image scale bars = 150 nm; All inset scale bars = 50 nm.

5.2.6.2.3. ***Reaction time:*** after selecting 0.6 mL as the optimal amount of monomer, we tested the effect of polymerization reaction time to adjust the thickness of the PS shell (Figure 37P7$_{15}$-P7$_{60}$). The polymerization was stopped by quenching the flask in an ice bath 15, 30, and 60 minutes after the start. This method allowed further control of the size of the UCNPs@ PS from 48±5, to 63±4 and 70± 5nm (Figure 37P7$_{15}$, Figure 37P7$_{45}$ and Figure 37P7$_{60}$ respectively). Longer reaction times did not increase the final diameter of the UCNP@PS significantly under the conditions tested. The smallest size obtained tended to aggregate, attributed to the incomplete coating of the UCNPs with PS, which resulted in hydrophobic regions leading to interparticle interactions and aggregation in aqueous media.

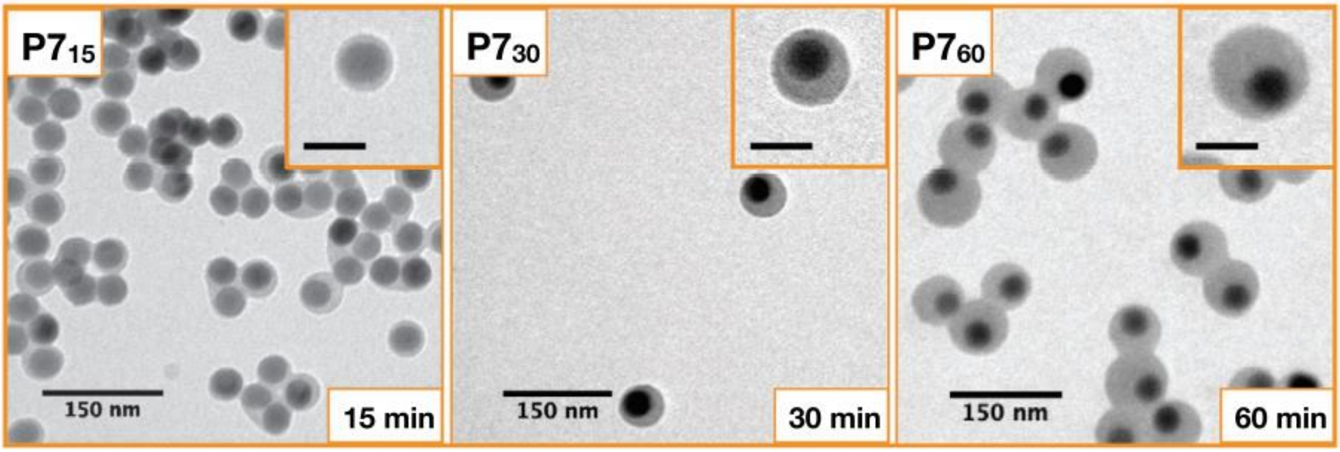

Figure 37. UCNPs@ PS produced after quenching the polymerization reaction at **P7$_{15}$)** 15 minutes, **P7$_{30}$)** 30 minutes and **P7$_{60}$)** 60 minutes after initiation, respectively. All main image scale bars = 150 nm; All inset scale bars = 50 nm.

Based on the previous experiments we chose the following conditions as optimal (coating, protection and relatively small size, see Figure 35C and E) to obtain single-core@shell UCNPs@PS: ultrasonication of the sample, 11 mg of UCNPs-MDP, 0.6 mL of St, and 60 min of polymerization reaction time.

5.2.6.2.4. ***Modification of shell composition:*** Finally, modification of the shell composition was explored by varying the monomer concentration added to the reaction from 100 vol% St to 50/50 vol% St/MMA (see Figure 38). We found that the resulting polymer shells tended to become thinner when the %MMA content was increased. In fact, a final diameter of 58 nm was obtained for P75%, while we obtained the same diameter, 58 nm, for P50% after increasing the initial amount of monomer by 1.5 times (see Table 4). Further increase in MMA volume fraction (i.e., St/MMA 25%/75%, Synth. P25%) resulted in poorer control over polymer shell thickness, morphology, and polymerization under the conditions we tested (Figure 39).

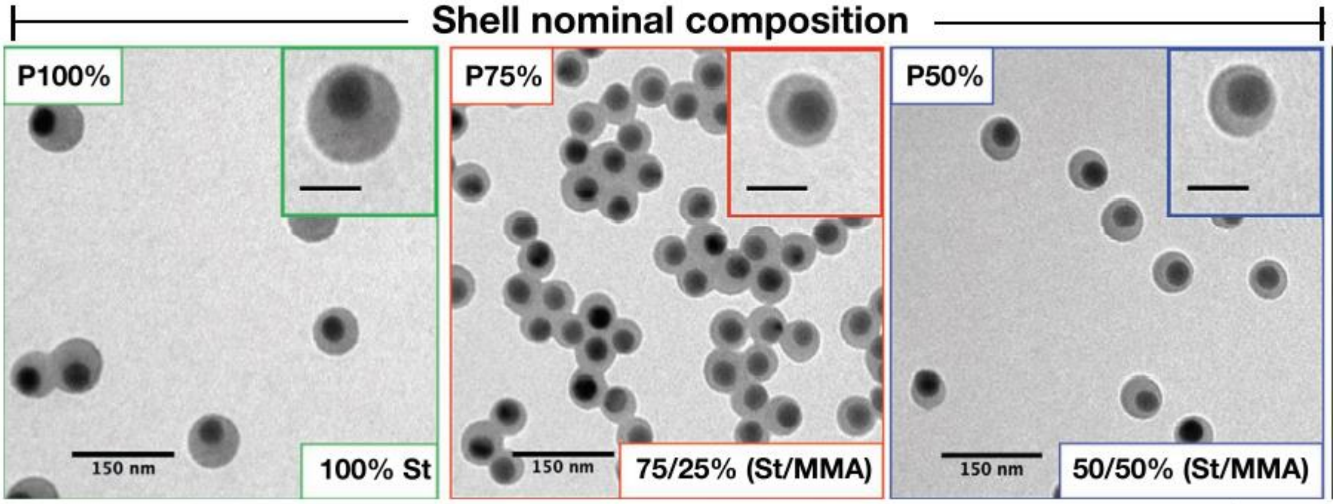

Figure 38. P100%–P50%) TEM images of UCNPs-MDP coated with HPSs with nominal compositions of 100% PS, 75%/25% PS/PMMA, and 50%/50% PS/PMMA, respectively.

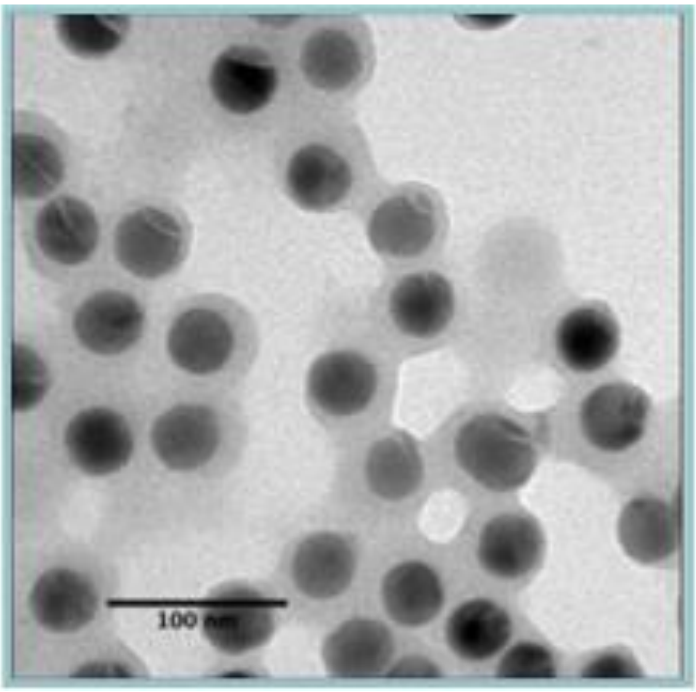

Figure 39. UCNPs coated with a HPS containing 25%/75% St/MMA nominal composition (synthesis P25%). As observed by the TEM image, the increase of MMA beyond 50% yielded thinner shells, and poorer control on the polymerization process and the overall HPS homogeneity.

This can be explained by the increased nucleation and growth of PMMA particles in the aqueous phase, which can be attributed to the higher polarity of MMA compared to St.[207] Nevertheless, the incorporation of PMMA into the protective shell was confirmed by FT-IR analyses (see Figure 40), proving that it is possible to easily incorporate different monomers during the polymerization process to vary the shell properties of the resulting UCNPs. The peaks at 2923 and 2848 cm^{-1} correspond to the asymmetric and symmetric vibrations of $-CH_2$ typical of PS, while the bands at 2997, 2953, 1465, and 987 cm^{-1} correspond to the vibrations of $(O)CH_3$, the band of the carbonyl group (C=O) appears in 1732 cm^{-1}, and the vibrations from 1250 to 1150 cm^{-1} are from the ester group of PMMA.

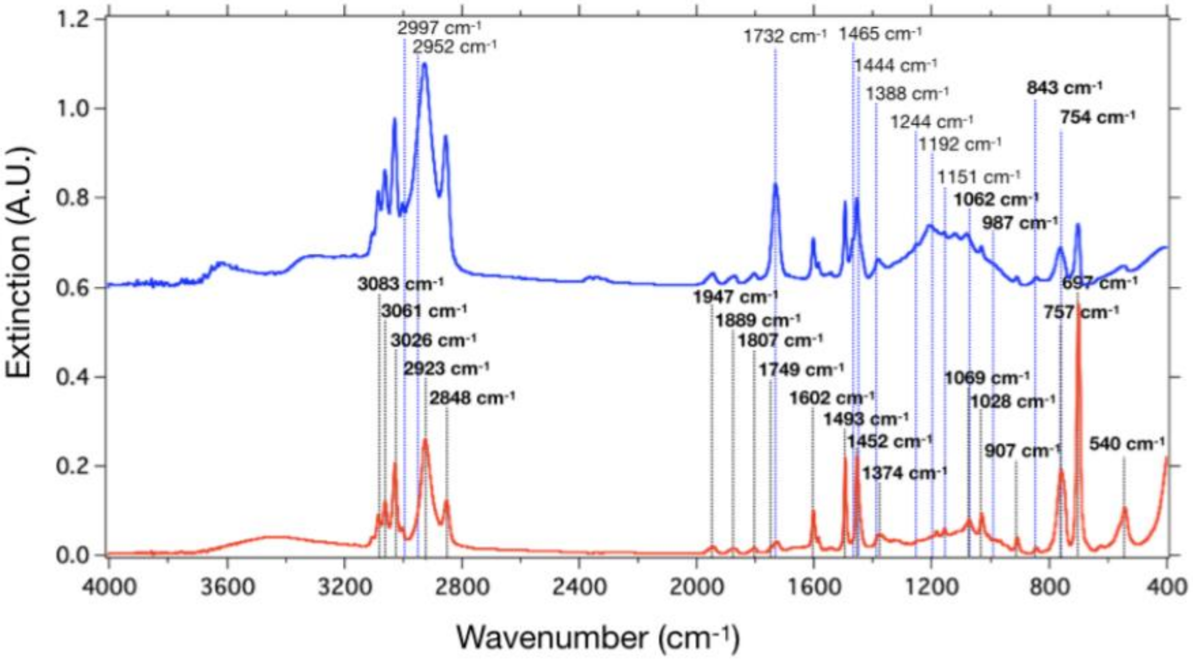

Figure 40. FT-IR spectra of UCNPs@PS, red line; and UCNPs@PS/PMMA (50%/50% St/MMA), blue line.

5.2.6.3 Comparison of Protective HPS with a Standard Poly-Acrylic Acid Coating

Given the polar nature of the chemicals responsible for degrading UCNPs during water transfer, the most effective way to protect them may be to maintain a robust hydrophobic environment near the surface of the UCNPs to prevent diffusion of these polar species toward the surface. This should result in reducing all the adverse effects associated with the water transfer of UCNPs with a single strategy. In this sense, miniemulsion polymerization has the advantage of isolating UCNPs in hydrophobic nanoreactors (i.e., monomer droplets) until a thick hydrophobic polymer layer is formed that provides protection from the aqueous environment, while being only slightly affected by the ligand equilibrium due to its solid-state-like state, unlike other strategies.[208] The surface of the resulting shell is simultaneously decorated with sulfate groups originating both from chain terminations with sulfate radicals generated by the initiator (KPS) and from SDS surfactant molecules that remain adsorbed after polymerization.[209–211]

To test the effectiveness of our coating shell, we compared the stability of our HPS-coated UCNPs with that of poliacrylic acid (PAA)-coated UCNPS in aqueous solution. PAA is a widely used polydentate ligand for water transfer of UCNPs and confers colloidal stability, surface passivation, relative protection in aqueous media, and carboxyl groups that can be used for further bioconjugation. [180,212] For these reasons, we will compare both coatings in terms of optical properties and chemical resistance using PAA-coated UCNPs as a control, as this system has been extensively studied in previous work and we will henceforth call it "UCNPs-PAA" [186,189,195]. The $NaYF_4$:Yb^{3+},Er^{3+} nanoparticles were subsequently coated with PAA. They were synthesized exactly as described above and have a size of 35±1 nm. They were subsequently coated with PAA using the method described in sec. 4.3.4. Figure 41 shows the images of TEM of HPS-UCNPs with different shell composition and UCNPs-PAA. which in all cases show homogeneous and dispersed nanoparticles in aqueous solution.

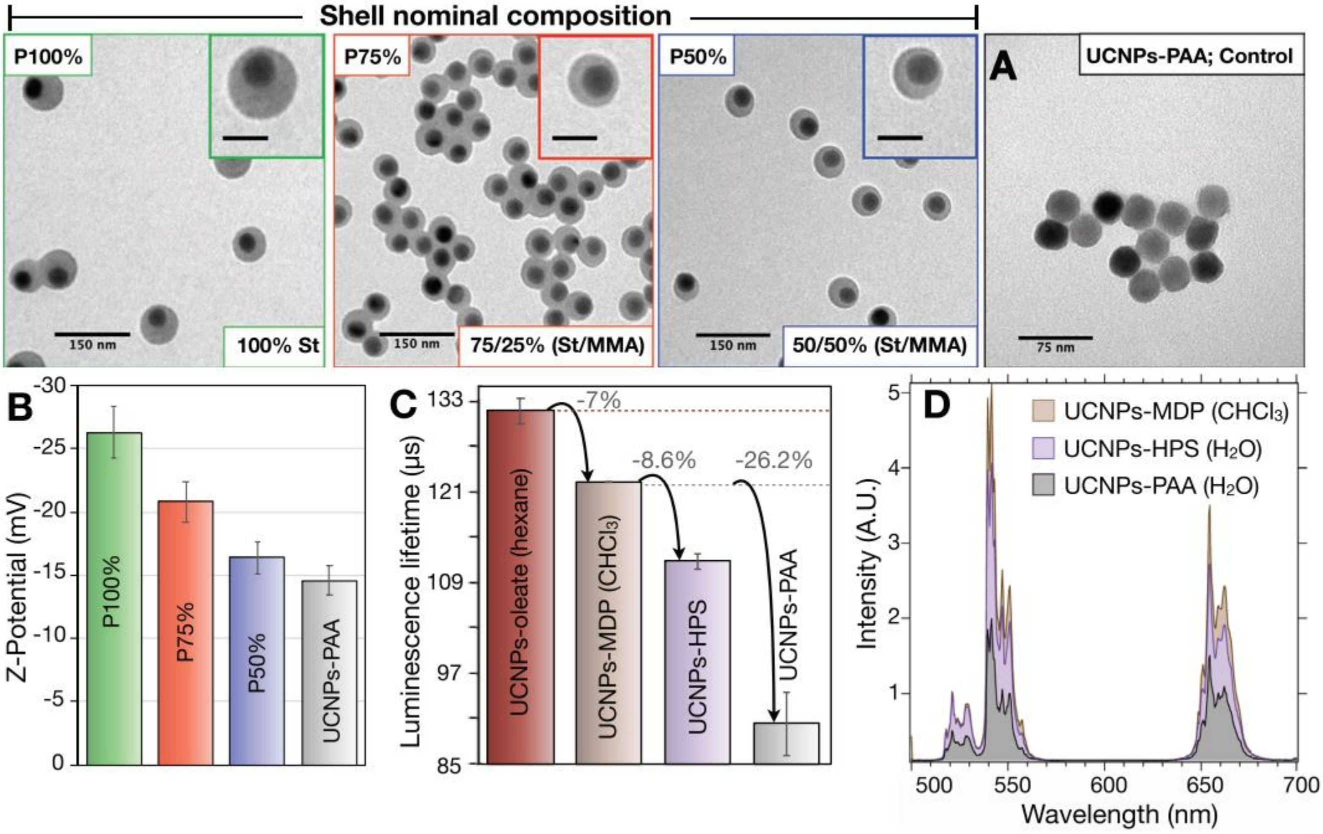

Figure 41. **P100%–P50%)** TEM images of UCNPs-MDP coated with HPSs with nominal compositions of 100% PS, 75%/25% PS/PMMA, and 50%/50% PS/PMMA, respectively. **A)** TEM image of UCNPs coated with PAA (control sample). All inset scale bars = 50 nm. **B)** Z-potential values of P100%, P75%, P50%, and UCNPs-PAA. C) Green emission lifetime values at 540 nm ($^4S_{3/2}\rightarrow{}^4I_{15/2}$) of UCNPs-Oleate (hexane), UCNPs-MDP ($CHCl_3$), UCNPs-HPS (H_2O), and UCNPs-PAA (H_2O). **D)** Upconversion emission spectra of UCNPs-MDP, UCNPs-HPS, and UCNPs-PAA at 525 nm ($^2H_{11/2}\rightarrow{}^4I_{15/2}$; green), 540 nm ($^4S_{3/2}\rightarrow{}^4I_{15/2}$; green), and 655 nm ($^4F_{9/2}\rightarrow{}^4I_{15/2}$; red). UCNPs-HPS, and UCNPs-PAA was 100 µg mL^{-1} for the **C)** lifetime and the **D)** steady-state luminescence measurements.

Sulfate groups deprotonate within a wide range of pHs (pKa<2), providing colloidal stability in water. The presence of these highly stabilizing surface charges is demonstrated for all HPSs by Z-potential measurements, as seen in Figure 41B. It is noteworthy that the colloidal stability offered by those surface charges is, in principle, higher than that provided to UCNPs-PAA.

Replacement of oleate with MDP as a capping agent is associated with a 7% reduction in the lifetime of UCNPs (see. Figure 41C), which is due to the change of solvent (from hexane to $CHCl_3$) and to a slight quenching effect caused by the phosphate component present in the MDP structure. (see Figure 30A). The subsequent water transfer of the UCNPs by miniemulsion polymerization leads to a further decrease in lifetime (8.6%), which is probably due to the adsorption of a small number of water molecules on the surface of the UCNPs. Interestingly, different HPS compositions yielded almost the same exact lifetime (Figure 42) indicating that the coating process is not substantially affected by changing the hydrophobic monomer, at least within the tested range of compositions. This indicates that the tested range of shell compositions offer similar protection against the luminescence quenching caused by water molecules.

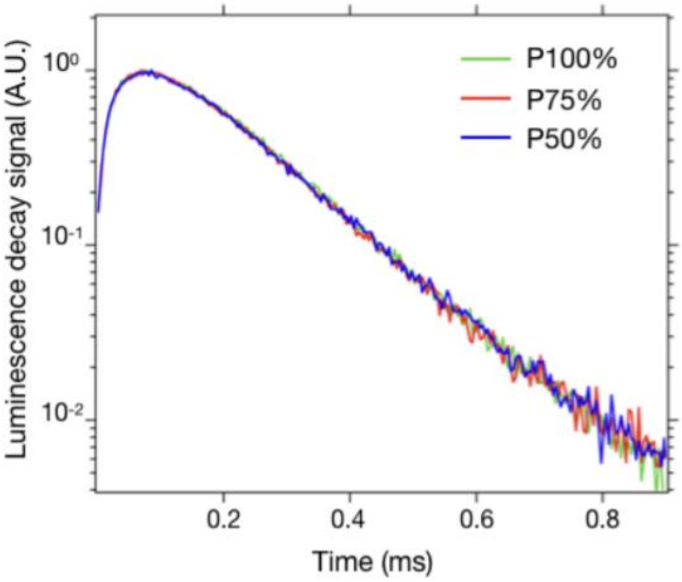

Figure 42. Decay curves of the lifetime of UCNPs coated with different HPS compositions at 0.1 mg/mL, namely 100% St (green, P100%), 75% St: 25% MMA (red, P75%), 50% St: 50% MMA (blue, P50%).

In contrast, water transfer of UCNPs with the conventional PAA ligand results in a significant reduction in lifetime (26.2%) compared with UCNPs-MDP. This is explained by the high permeability of this polydentate ligand to water molecules, which easily reach the surface of UCNPs and cause a strong quenching of their luminescence. The effect of lifetime shortening on the luminescence properties of these UCNPs was also confirmed by steady-state luminescence measurements, as shown in Figure 41D. Indeed, the use of HPSs resulted in UCNPs with about 2-fold more intense upconversion luminescence than the same UCNPs coated with PAA (see Figure 43), further confirming the effectiveness of our strategy to reduce luminescence quenching in aqueous media.

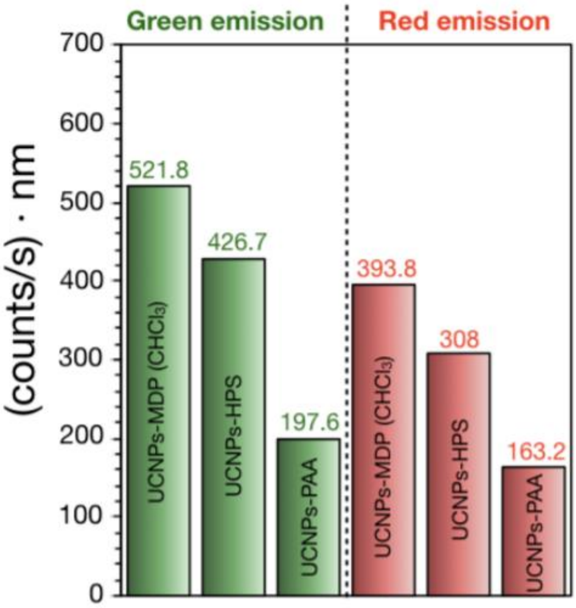

Figure 43. Steady state luminescence [(counts/s) nm] corresponding to the integration of the green ($^2H_{11/2}\rightarrow^4I_{15/2}$ and $^4S_{3/2}\rightarrow$ $^4I_{15/2}$) and red ($^4F_{9/2}\rightarrow$ $^4I_{15/2}$) emission bands of UCNPs with different coatings under CW 976 nm excitation (~100 W/cm^2). In all cases the UCNPs core concentration =0.1mg/mL. Left-green and left-red columns correspond to UCNPs-MDP in chloroform. Center-green and centerred columns correspond to UCNPs protected with HPS in water. Right-green and right-red columns correspond to UCNPs coated with PAA in water. The coating of UCNPs with HPS translates in a ~2.2- fold and a 1.9-fold improvement in their green and red emissions, respectively, in comparison with UCNP coated with PAA, highlighting the protective role of HPS from the quenching produced by water vibrational modes.

To further evaluate the protective role of HPS and compare it with the PAA shell, we performed long-term stability studies at RT with aqueous dispersions of UCNPs-HPS at very low concentrations (5 µg/mL), which is well below the concentration at which noticeable degradation of UCNPs occurs (≈50 µg/mL).[170] This low concentration allowed us to study the effect of UCNPs dissolution on their optical and structural/morphological properties. (Figure 44).

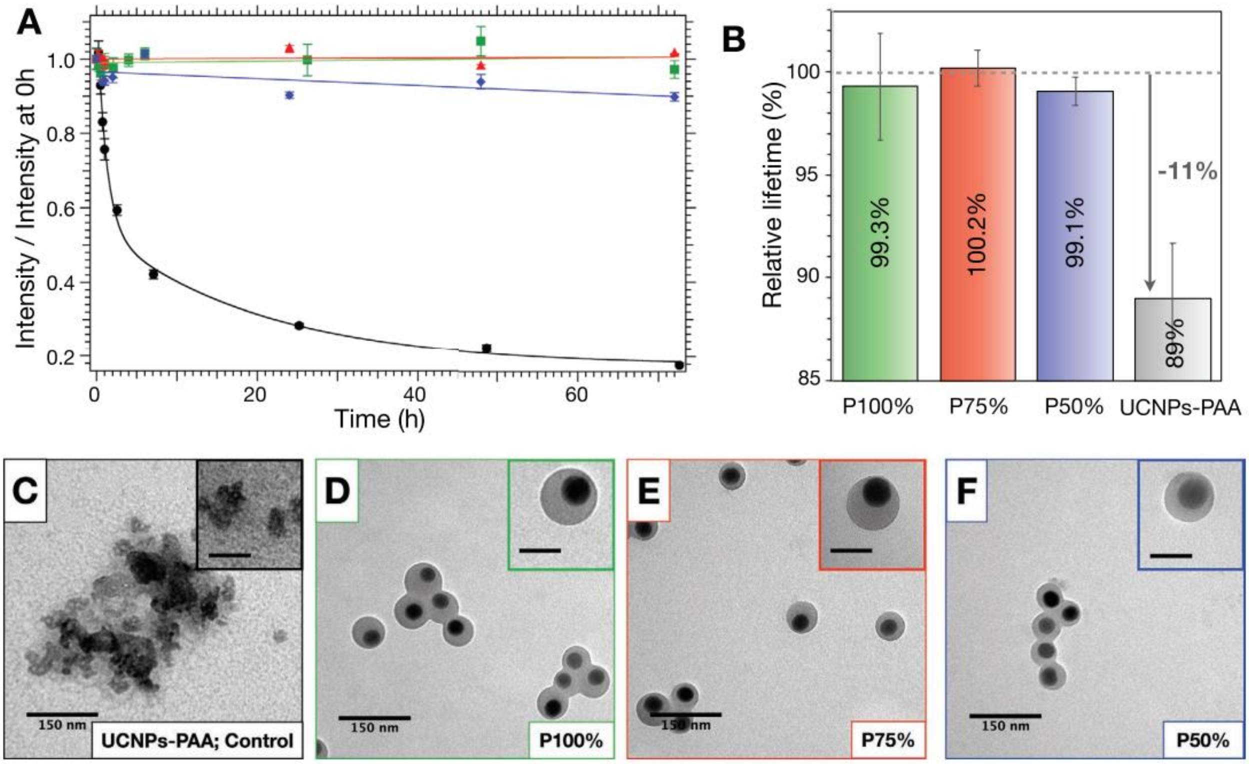

Figure 44. **A)** Time evolution (0–72 h) of the green upconversion luminescence intensity after dilution of the samples at a core concentration of 5 µg mL . P100% (green), P75% (red), P50% (blue), and UCNPs-PAA (black). **B)** Relative lifetime change of the green upconversion emission after 72 h, compared with the original lifetime at 0 h. P100% (green bar), P75% (red bar), P50% (blue bar), and UCNPs-PAA (gray bar). **C–F)** TEM images of UCNPs-PAA, P100%, P75%, and P50%, after 72 h in water at a core concentration of 5 µg/mL , respectively. All inset scale bars = 50 nm.

The degradation of the samples was monitored by following their luminescence intensity for 72 h. Figure 44A shows their luminescence intensity normalized to their initial intensity, as a function of time. Samples P100% and P75% did not exhibit any sign of degradation, since their luminescence intensity did not change during the 72 h (see green and red lines, respectively). On the other hand, P50% sample (blue line) showed a slight decrease in luminescence intensity of ≈10%, which may be ascribed either to a slightly worse colloidal stability, or a less effective protection compared with P100% and P75%. The luminescence from the UCNPs-PAA sample was highly compromised (see black line in Figure 44A) especially during the first 3–4 h, with a reduction of 50% in their luminescence intensity, and after that, a slower decrease continued over time up to 80%. Figure 44B shows the relative luminescence lifetime change of the samples after 72 h, in comparison with the lifetime value yielded by the original non-aged UCNPs samples. These measurements can be used to confirm structural degradation of UCNPs, as reported by other authors.[178,198] Our results confirm once again the degradation of UCNPs-PAA (Figure 44B, gray bar), as the 72 h aged NPs are accompanied by a ≈11% decrease compared with their original lifetime. Interestingly, the relative lifetime measurements obtained for P100%, P75%, and P50% after 72 h (see Figure 44B; green, red, and blue bars, respectively) show negligible changes (less than 1%). These results clearly highlight the remarkable protection exhibited by the HPS against UCNPs dissolution. This was also corroborated by TEM, where no damage or structural/morphological changes could be found for the UCNPs-HPS (see Figure 44D–F), whereas the UCNPs-PAA were strongly affected, as shown in Figure 44C. Interestingly, the latter NPs presented a significant reduction of their diameter, from the initial value of 36 nm to a final value of 27 nm. This would mean that the degradation took place at the outer part of the nanoparticle, maintaining the spherical symmetry. After these results, it may seem counterintuitive how the huge relative intensity drops shown by the UCNPs@PAA (≈80%) was accompanied by only a modest relative lifetime decrease (≈11%). However, this can be explained by the fact that UCNPs-PAA's surface is already highly quenched by water, so further lifetime reductions should be mainly due to an increase in UCNPs' surface-to-volume (S/V) ratio as dissolution progresses. On the contrary, the same dissolution process has a more relevant deleterious effect on the UCNPs intensity, as the physical separation and diffusion of Ln^{3+} from the host matrix implies the reduction of the number of sensitizers (Yb^{3+}) and activators (Er^{3+}) that can produce efficient energy transfer, and ultimately photon upconversion. As a direct consequence, the intensity of upconversion luminescence is highly reduced.

To test this hypothesis, we theoretically estimated the decrease in UCNPs-PAA luminescence intensity by considering the experimentally observed decrease in UCNP diameter. In doing so, we considered two main contributions. First, the reduction of the number of ions presents in the UCNP, which is related to the UCNP volume. Second, the decrease in the emission efficiency (quantum yield or lifetime) of the UCNP-PAA due to surface quenching effects as the S/V ratio of the nanoparticles increases. Then, we theoretically calculated the luminescence intensity when the degradation of UCNPs-PAA occurs in water at RT (control sample). The luminescence intensity was calculated by considering the effects of the decrease in nanoparticle size (shown by TEM images) on both the number of active ions and the emission efficiency (or lifetime). First, the decrease in nanoparticle radius r_{UC} leads to a decrease in the number of active ions, which is proportional to the UCNP volume:

$$N_{Er} = \rho_{Er} \frac{4\pi}{3} r_{UC}^{3}$$

Equation 14

where N_{Er} and ρ_{Er} are the number and the concentration of Er^{3+} ions in the nanoparticle, respectively. Second, the decrease of the nanoparticle radius increases the surface area to volume ratio (S/V) which is well known to reduce the emission efficiency (or lifetime) due to surface quenching effects. We use the relationship between the luminescence lifetime and the S/V given by other works[213,214] to characterize the emission efficiency of the transitions involved in the upconversion mechanism, $\eta = \tau_f / \tau_{rad}$, where τ_{rad} is the corresponding radiative decay time. This relation is given by:

$$\frac{1}{\tau_f} = 1600 s^{-1} + 19000 nm s^{-1} \frac{S}{V} \ (nm^{-1})$$

Equation 15

Assuming that the red and green emission involved a two-step absorption process, the luminescence intensity is expected to depend on η quadratically. As expected, the luminescence intensity, calculated as $N_{Er}\eta^2$, properly reproduced the intensity drop when decreasing the UCNP diameter. We also plotted in the same figure the contribution of the number of active ions

N_{Er} (dashed line) to show that this intensity drop is mainly due to the ion dissolution so that the decrease in η with particle diameter only represents a small correction. Moreover, Figure 45 allowed us to predict that the variation of the UCNP size had a logarithmic relationship with time and that half of the reduction of the UCNP diameter took place during the first two-three hours. As stated before, the emission efficiency η exhibited a smaller variation with particle diameter (see dotted line in Figure 45).

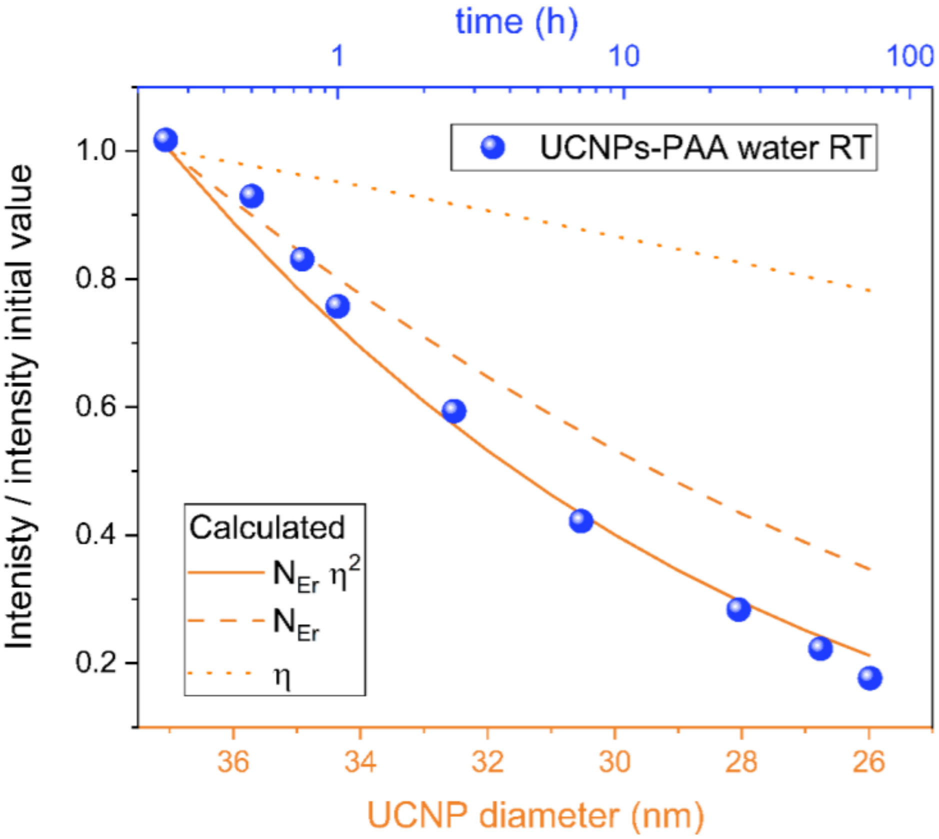

Figure 45. Experimental luminescence intensity normalized to its initial value as a function of time (circles). Theoretical luminescence intensity calculated from $N_{Er}\eta^2$ (solid line) or from N_{Er} (dashed line) normalized to its initial value as a function of particle diameter. We also plotted the variation of η (dotted line) as a function of particle diameter which gives the behavior of the luminescence decay time.

This allowed us to confirm that the main contribution came from the ion dissolution, since more than 50% of ions were estimated to be lost. This result helps to explain why the degradation of the UCNPs showed a smaller decrease in the lifetime than in the luminescence intensity. Furthermore, the reduction in UCNP size during dissolution was predicted to follow a logarithmic relationship with time, matching quite accurately the experimental data. We also estimated the solubility product $K_{sp} = [Na^{+}][RE^{3+}][F^{-}]^{4}$, where RE^{3+} represents the rare-earth ions Y^{3+}, Yb^{3+}, and Er^{3+}. For this, we assumed that ions dissolved stoichiometrically. Here we assumed that the ions dissolve stoichiometrically. Experimental results (TEM images) showed a mean final diameter of less than 27 nm, consistent with a RE^{3+} ion dissolution near to 70%. Therefore, the equilibrium RE^{3+} ion concentration was 0.7 times the RE^{3+} ion concentration in the sample, being 0.0266 mM for 5 µg/mL of UCNPS. the computed solubility product was K_{sp} = 1×10^{-26} which roughly agrees with previous values.[186]

We also studied the stability of very diluted samples of UCNPs (5 µg/ mL) with different protective shells in potassium phosphate buffer (K^{+}PB) at a concentration of 100 mm, which is ten times higher than common phosphate buffer saline. This buffer quickly and completely degraded the control sample UCNPs-PAA, as can be observed by the 50% luminescence reduction after 1 h and the almost complete disappearance of upconversion luminescence after 72 h (Figure 46A, black line). The reduction in luminescence was such that it was impossible for us to measure the resulting lifetime of the sample (Figure 46B), indicating a profound degradation of the UCNP host matrix and its structure.

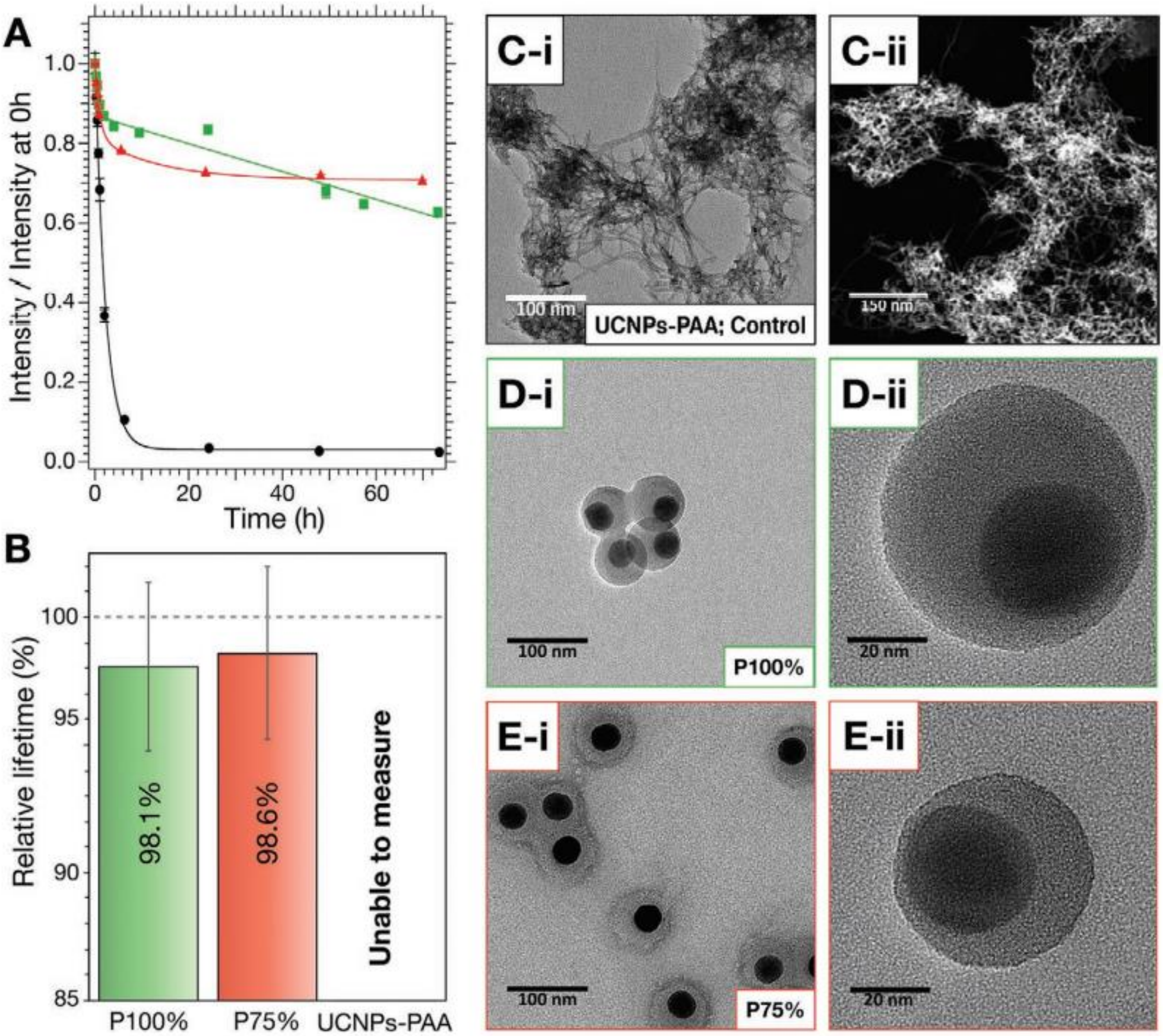

Figure 46. **A)** Time evolution (0–72 h) of the green upconversion luminescence intensity after dilution of the samples to a core concentration of 5 μg/mL in concentrated K^+PB (100 mm). P100% (green), P75% (red), and UCNPs-PAA (black). **B)** Relative lifetime change of the green upconversion emission after 72 h at 5 μg/mL in concentrated K^+PB (100 mm), compared with the original lifetime at 0 h. P100% (green bar), P75% (red bar), and UCNPs-PAA (gray bar). HR-TEM images of **C[i])** UCNPs-PAA, **D[i,ii])** P100%, and **E[i,ii])** P75% after 72 h in K^+PB (100 mm) at a core concentration of 5 μg/ mL, respectively. **C[ii])** HAADF-STEM image of UCNPs-PAA, where the brightest regions within the material are likely to contain atoms of higher atomic number.

HR-TEM characterization further confirmed the complete degradation of UCNPs-PAA by K^+PB, yielding a new inorganic phase with an acicular and entangled morphology (see Figure 46C [i]). Characterization of the sample by HAADF-TEM indicates the presence of clusters containing atoms of high atomic number (brighter regions), probably traces of aggregated UCNPs-PAA, from which the acicular structures seem to originate.

On the other hand, EDX elemental mapping analyses confirm the presence of phosphorus (P), ytterbium (Yb), and yttrium (Y) in these structures, (see Figure 47A[i], A[ii], and A[iii], respectively). Noteworthy, the merged image in Figure 47A[iv] shows a spatial correlation between these elements, suggesting that the new phase formed during the degradation of UCNPs consists of a complex mixture of RE phosphates. Interestingly, we did not detect fluorine (F) in this sample, suggesting the complete degradation of UCNPs-PAA upon reaction with phosphate and the release of all fluoride ions (F-) to the medium in the form of soluble species (e.g. NaF and/or KF). These observations are consistent with the results reported in previous work.[178,198] The multiple centrifugations performed prior to HR-TEM characterization, aiming to remove excess K^+PB, may have washed away these water-soluble F species, which explains the total absence of fluorine signal during EDX elemental mapping analyze.

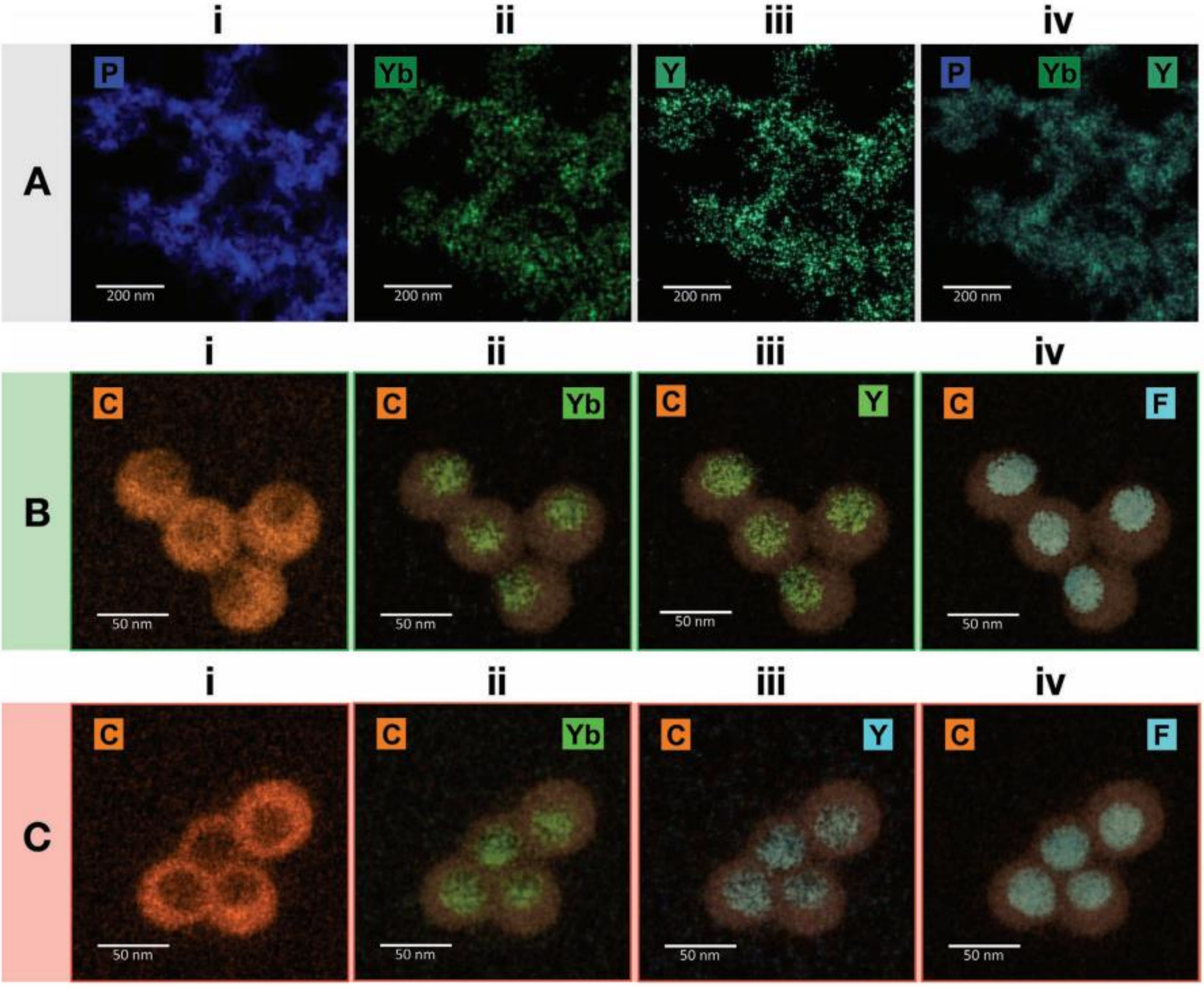

Figure 47. EDX elemental mapping analyses of **A)** UCNPs-PAA, **B)** P100%, and **C)** P75%. **(A[i-iv])** corresponds to the signals of the elements in UCNPsPAA: **A[i])** Phosphorus, **A[ii])** ytterbium, **A[iii])** yttrium, **A[iv])** Merged image of phosphorus, ytterbium and yttrium. The scale in (A[i-iv]) is 200 nm. **(B[i-iv])** corresponds to the elements in P100%: **B[i])** carbon, **B[ii])** ytterbium, **B[iii])** yttrium and **B[iv])** Fluorine**. (C[i-iv])** corresponds to the elements in P75%: **C[i])** carbon, **C[ii])** ytterbium, **C[iii])** yttrium, and **C[iv])** Fluorine. The scale in B[i-iv] and in C[i-iv] is 50 nm.

In contrast to UCNPs-PAA, the long-term study of the luminescence intensity of P100% and P75% presented a much lower, but still moderate decrease in their upconversion luminescence after 72 h (37% and 29% reduction, see Figure 46A, green and red symbols, respectively). However, when measuring their relative lifetime change, an almost negligible decrease of 1.9% and 1.4% was observed (Figure 46B green and red bars, respectively). This indicates that most UCNPs are well protected and preserve their luminescence properties in K^+PB. Nevertheless,

K^+PB forms less soluble potassium salts SDS and is used at similar high concentrations in biochemical protocols to reduce the solubility of SDS, which in our case acts as a colloidal stabilizer at the surface of the HPS.[215,216] This could indeed explain the almost negligible change in the lifetime, but a moderate reduction in luminescence intensity. To further test this hypothesis, we confirmed by DLS that the hydrodynamic diameter (D_H) of P100% and P75% increased in K^+PB compared with the results obtained in DI-H_2O, which can be ascribed to a reduction of the interparticle distance due to a decrease in colloidal stability, see Figure 48.

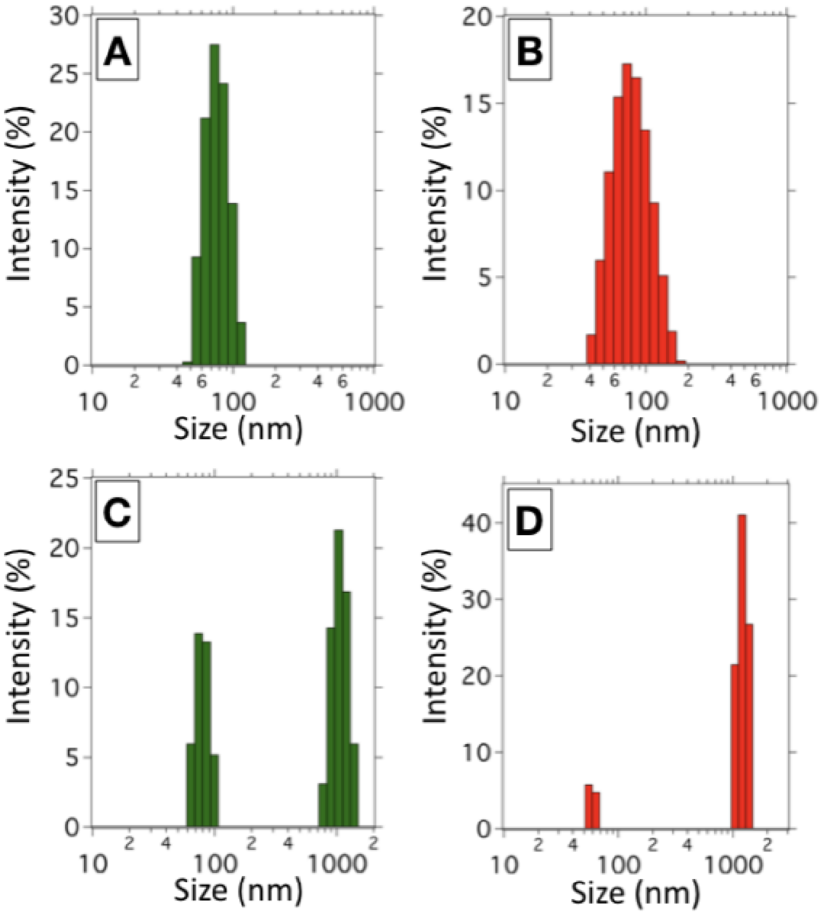

Figure 48. DLS analyses of P100% (green bars) and P75% (red bars). **A)** P100% in DI-H_2O; **B)** P75% in DI-H_2O; **C)** P100% in K^+PB; and **D)** P75% in K^+PB.

The results of UCNPs-HPS in K^+PB represent a vast improvement over more traditional coating such as UCNPs-PAA. To fully confirm the morphological and structural integrity of P100% and P75%, we performed HR-TEM characterizations of the samples after 72 hours of aging in K^+PB. Figure 46D[i,ii],E[i,ii] confirms that the morphology of P100% and P75% was not affected after 72 hours in K^+PB. The quasi-spherical shape of the UCNP cores is preserved, while no signs of the acicular structures formed by the reaction between phosphate and RE^{3+} are visible (see Figure 46C[i,ii] for comparison). A closer look at P100% and P75% (Figure 46 [ii],E[ii]) confirms that no degradation of the UCNP cores is visible even in the areas with thinner HPS coating. A higher magnification of these images showing the conserved crystallinity of the NPs can be seen Figure 49, where the lattice planes can be seen. These images provide the first evidence that an HPS shell thickness of only 3-4 nm can be sufficient to fully protect UCNPs from chemical degradation in aqueous media.

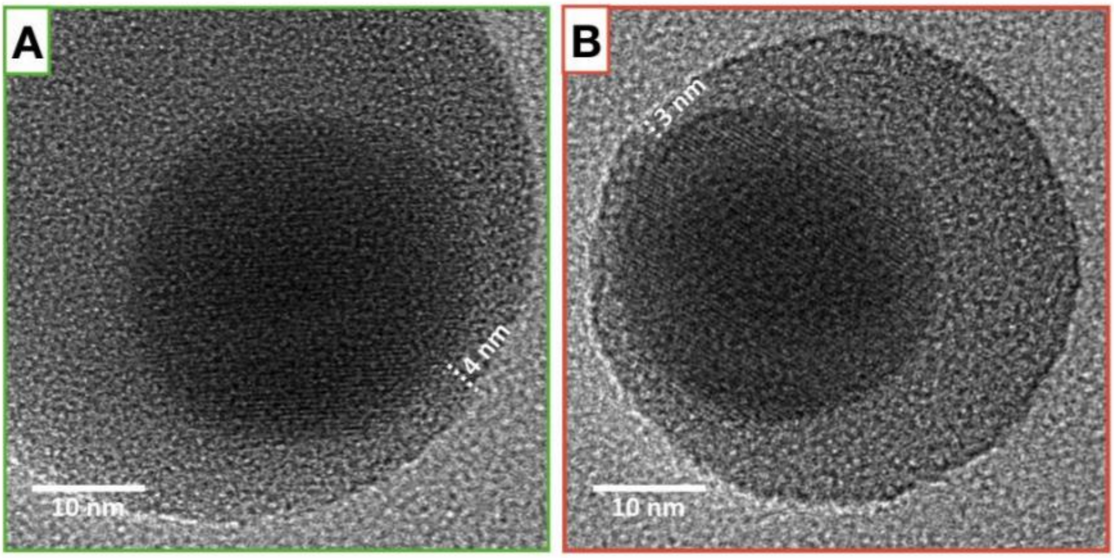

Figure 49. HR-TEM Magnification of the UCNP core of **A)** P100%; and **B)** P75%; showing the β-$NaYF_4$:Yb,Er lattice planes after 72 h incubation in K^+PB. The thinnest side of the HPS of P100% and P75% has 4 nm and 3 nm, respectively.

For final chemical and structural characterization, we performed EDX elemental mapping of P100% and P75% (see Figure 47B and C, respectively). A strong carbon signal was observed in the region corresponding to the HPS, while it was not detectable in its core due to the presence of the inorganic UCNP (Figure 47B[i],C[i]). Within this region, ytterbium, yttrium and fluorine could be identified, very consistent with the region corresponding to the UCNP core in both samples, see images of Yb, Y, and F merged with carbon in Figure 47B[ii], [iii] and [iv] (for P100%) and (Figure 47C[ii], [iii] and [iv] (for P75%), respectively. The high signal of these elements in the UCNP core region is strong evidence that the HPS prevents the leakage of ions from the UCNP into solution and their subsequent reaction with phosphate. Indeed, the case of fluorine is particularly revealing, as its high abundance in the core of P100% and P75% contrasts strongly with the complete absence of this signal in UCNPs-PAA, where all fluoride was replaced by phosphate after 72 hours in K^+PB (see Figure 47A[i,iv]). Interestingly, we were able to detect the presence of MDP ligands at the surface of UCNP cores within the HPS, as this is the only possible source of phosphorus that can be present at the UCNP core surface before they come into contact with K^+PB (see Figure 50).

To further verify that MDP was detected, we also confirmed that the phosphor signal in UCNPs-PAA was not present in K^+PB before ageing (data not shown). The detection of MDP suggests that the growth of HPS not only forms a robust hydrophobic barrier, but also ensures long-term passivation of the surface by keeping the phosphate moieties of MDP molecules in place. Further analysis of the composition of P100% and P75% after 72-hour incubation in K^+PB can be found in Figure 51 and Figure 52. Overall, our results indicate that HPS provides great protection against water quenching, ion leakage and dissolution, and chemically harmful species such as phosphate.

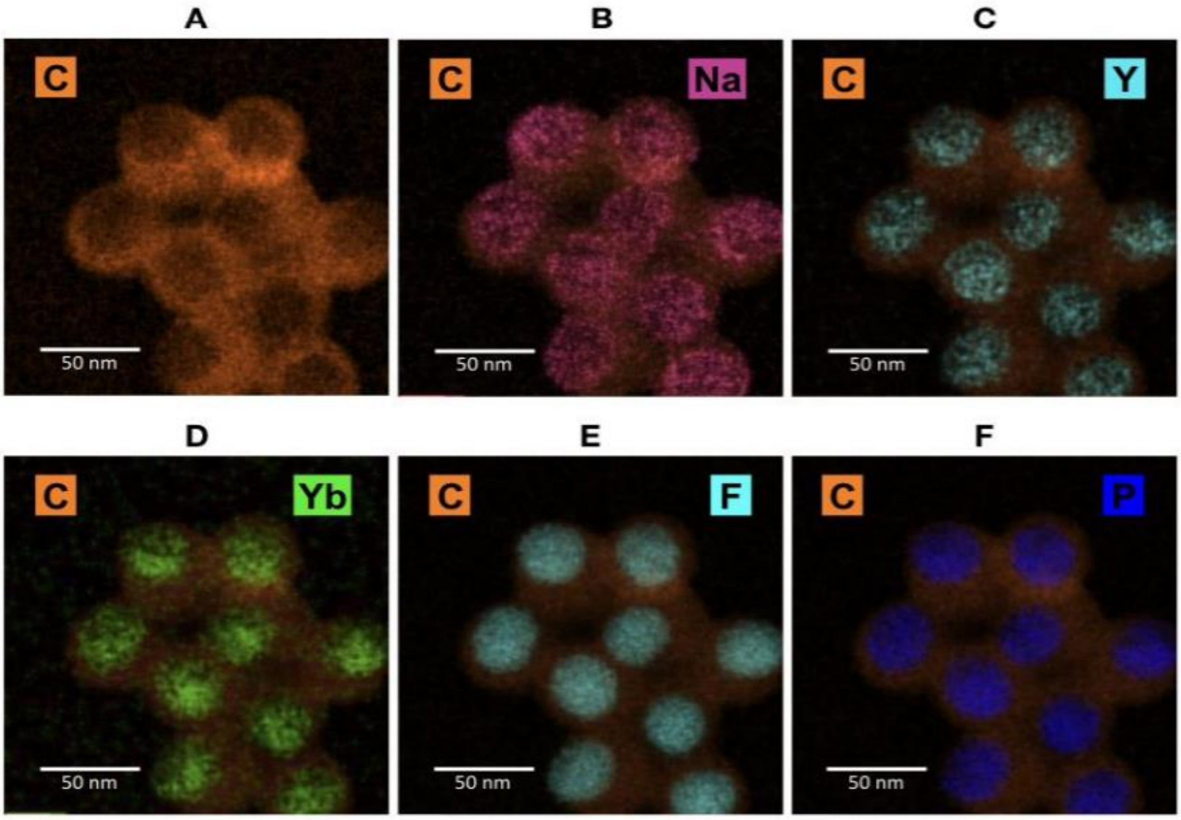

Figure 50. Elemental mapping analyses of P75% before incubation in K⁺PB showing signals from **A)** carbon "C"; **B)** "C" and sodium "Na"; **C)** "C" and yttrium "Y"; **D)** "C" and ytterbium; **E)** "C" and fluoride "F"; **F)** "C" and phosphorus "P".

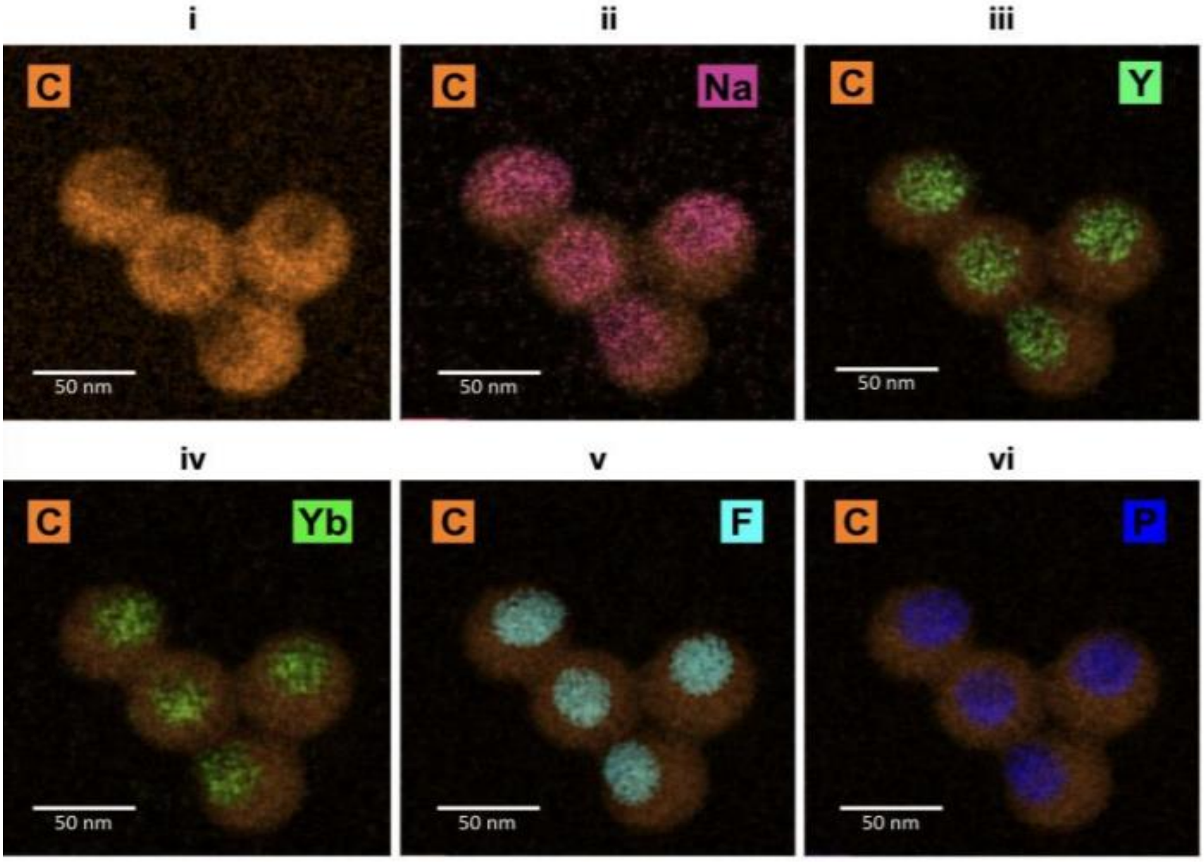

Figure 51. Elemental mapping analyses of P100% after 72 h incubation in K⁺PB. **i)** carbon "C"; **ii)** "C" and sodium "Na"; **iii)** "C" and yttrium "Y"; **iv)** "C" and ytterbium; **v)** "C" and fluoride "F"; **vi)** "C" and phosphorus "P".

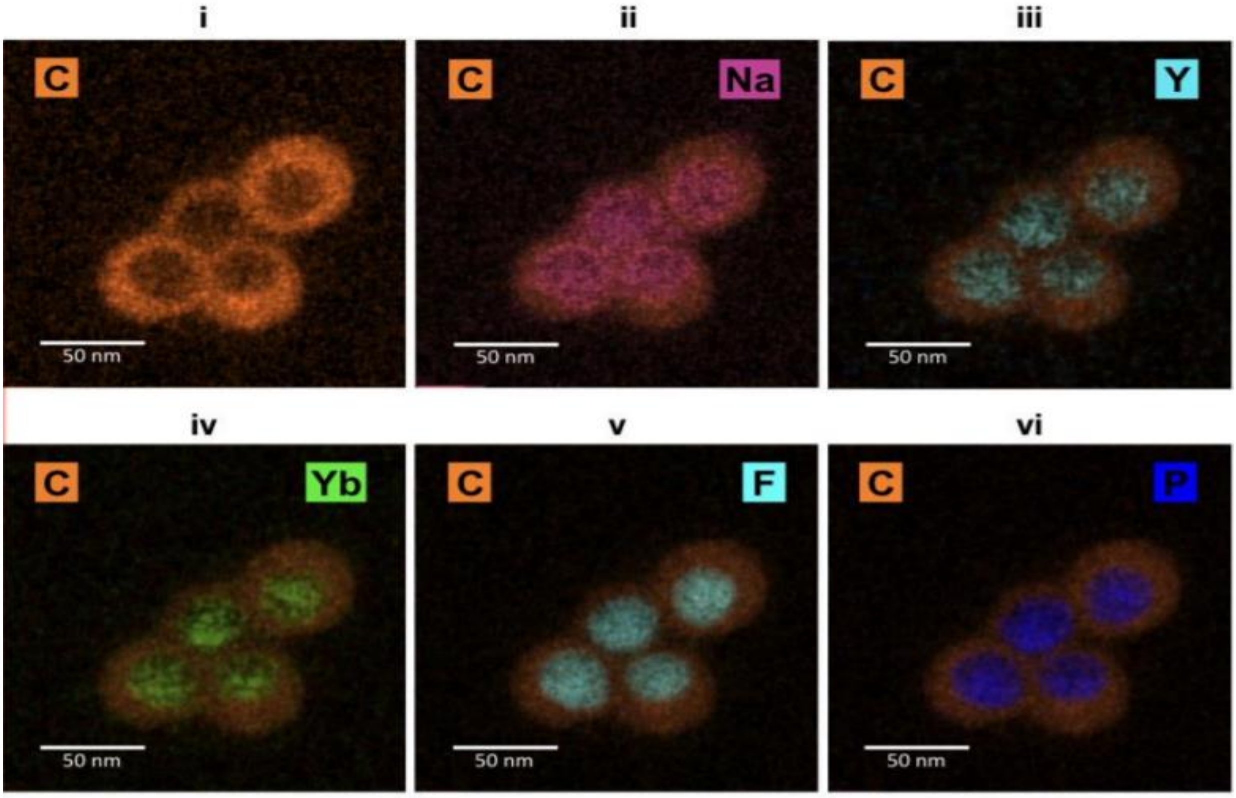

Figure 52. Elemental mapping analyses of P75% after 72 h incubation in K^+PB. **i)** carbon "C"; **ii)** "C" and sodium "Na"; **iii)** "C" and yttrium "Y"; **iv)** "C" and ytterbium; **v)** "C" and fluoride "F"; **vi)** "C" and phosphorus "P".

With the aim of reliably extending the current applications of UCNPs, we have explored the potential of HPS as a protective layer under high temperature conditions in aqueous media. Thus, we studied the stability of UCNPs in DI-H_2O at 70°C and high dilution (5µg/mL). Again, the HPS provided much higher protection against degradation than the PAA shell. Indeed, UCNPs-PAA are completely degraded in the first 3 hours, dropping their luminescence intensity by 90% (see Figure 53A, black). In contrast, P75%, which gave the best results in the previous experiments, shows only a 20% decrease (red in Figure 53A). Although this is not a negligible decrease, it is important to emphasize that the intensity of P75% after 7 hours at 70°C is still higher than that of undegraded (unaged) UCNPs-PAA at the same concentration. The undetectable luminescence signal obtained for the UCNP-PAA sample after 7 hours at 70°C made it impossible to determine the lifetime. In contrast, the lifetime for P75% (drop≈3%) remains almost unchanged, see red bar in Figure 53B. This could indicate that the reduction in their luminescence is due to a very small, but not negligible, quenching or degradation of a small portion of P75%. We hypothesize that when the temperature is increased to 70°C, the thinnest shell regions become partially permeable, and some H_2O molecules can reach the surface of UCNPs in a small population of UCNPs-HPS. Nevertheless, TEM characterization showed that UCNPs-PAA were completely degraded and aggregated due to dissolution reprecipitation processes (Figure 53C), whereas P75% showed that the HPS effectively protected the UCNPs cores even under these extreme conditions (see Figure 53D). In fact, no evidence sign of degradation of the particles by TEM was observed, which may indicate that only a very small fraction of the UCNPs HPS is partially compromised. These results are very exciting as they open the possibility of using UCNPs-HPS more reliably in novel applications such as high temperature nanothermy, nucleic acid amplification techniques such as PCR or isothermal approaches. In search of these new applications, we have conducted an in-depth study of the thermometric properties of UCNPs-HPs, which is presented in the next section (5.2.6.4).

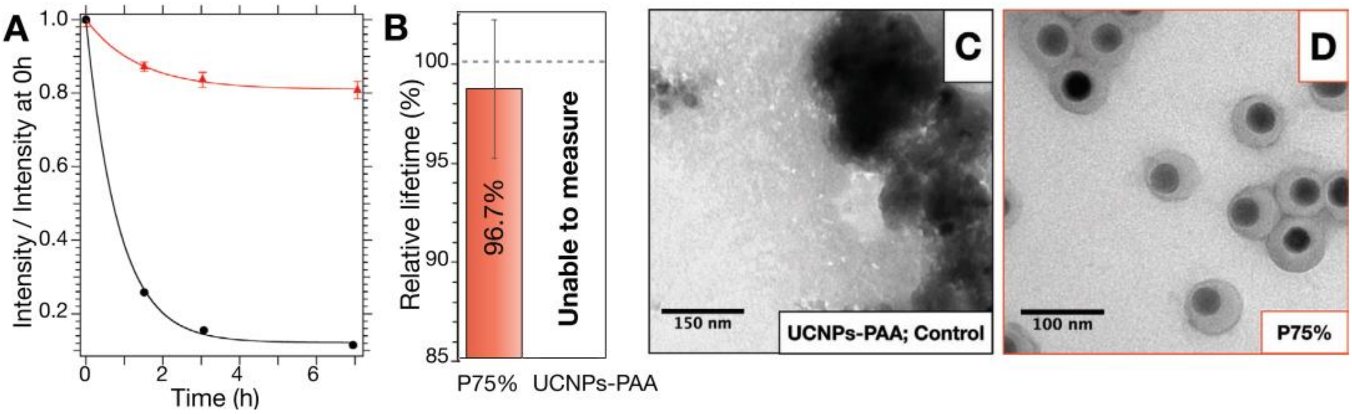

Figure 53. **A)** Time evolution (0–7 h) of the green upconversion luminescence intensity of the samples with a core concentration of 5 µg/mL in DI-H_2O at 70 °C. P75% (red) and UCNPs-PAA (black). **B)** Relative lifetime change of the green upconversion emission after 72 h at 5 µg/mL in DI-H_2O at 70°C, compared with the original lifetime at 0 h. P75% (red bar) and UCNPs-PAA (gray bar). **C,D)** HR-TEM images of UCNPs-PAA, and P75% after 7 h in DI-H_2O at 70 °C.

5.2.6.4. Thermometric properties of UCNPs-HPs

We tested the ability of the UCNPs-HPS to be used as nanothermometers by analyzing the green upconversion emission of the thermally coupled energy levels $^2H_{11/2}$ (525 nm from $^2H_{11/2}\rightarrow{}^4I_{15/2}$) and $^2S_{3/2}$ (545 nm from $^2S_{3/2}\rightarrow{}^4I_{15/2}$) of the Er^{3+} ions. The small energy separation between these two levels (several hundred of wavenumbers) provides efficient thermalization of their populations. Then, the integrated luminescence intensities of both bands, I_{525} and I_{545}, follow the Boltzmann distribution and the luminescence intensity ratio (LIR) depends on temperature as follows:

$$LIR = \frac{I_{525}}{I_{545}} = Ae^{-\frac{\Delta E}{k_B T}}$$

Equation 16

Where ΔE is the energy gap between both levels k_B is the Boltzmann constant, T is the absolute temperature and A is a constant, which includes dependencies on the level degeneracy, spontaneous emission rates and energies of the emitting states in the host. We measured the green upconversion luminescence spectra of highly diluted UCNPs-P75% samples in water at 5 µg/mL as a function of temperature from 20 °C (293.15 K) to 50°C (323.15 K). After determining the integrated intensity area of both bands, we calculate the corresponding ratio at each measured temperature. The natural logarithm of the luminescence intensity ratio shows a linear trend with the inverse of temperature following the population ratio of the Boltzmann distribution, as shown in the right panel of Figure 54. The linear fit yielded an energy gap ΔE = 710 cm^{-1}.

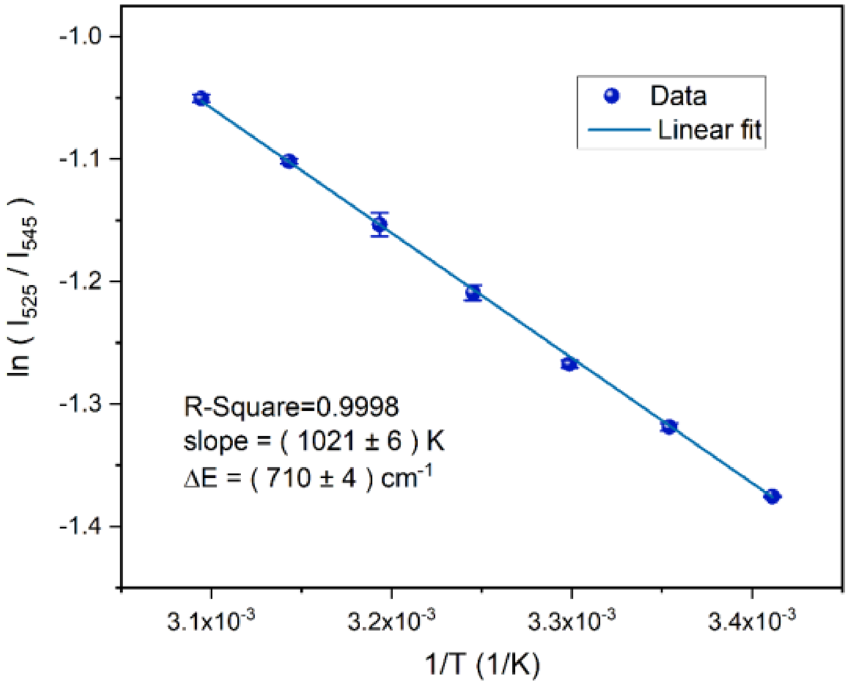

Figure 54. Thermometric calibration of P75% in water at 5 µg/mL. The plot depicts the variation of the logarithm of the green luminescence intensity ratio (I_{525}/I_{545}) with the inverse of temperature (K^{-1}).

Using the above equation, we calculatede the absolute sensitive $\boldsymbol{S_a}$ and the relative sensitivity $\boldsymbol{S_r}$:

$$\boldsymbol{S_a = \left|\frac{\partial LIR}{\partial T}\right| = LIR\ \frac{\Delta E}{k_B T^2}} \qquad\qquad \boldsymbol{S_r = \frac{1}{LIR}\left|\frac{\partial LIR}{\partial T}\right| = \frac{\Delta E}{k_B T^2}}$$

Equation 17

The results are shown in Figure 55 the sensitivity values obtained are similar to the values found in literature for β-$NaYF_4$:Yb, Er nanothermometers.[217]

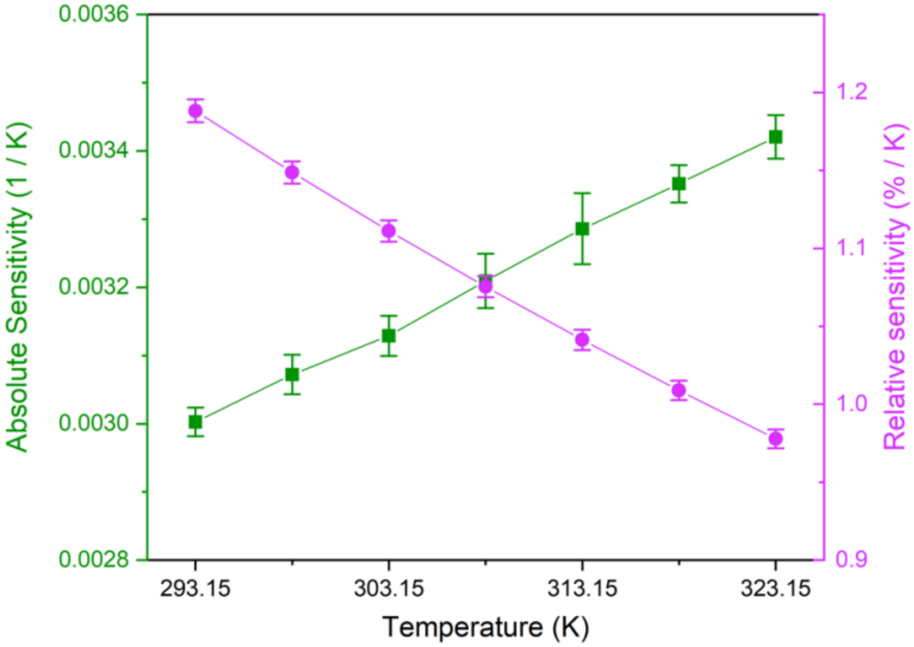

Figure 55. Absolute sensitivity (green squares) and relative sensitivity (pink circles) of highly diluted P75% in water (5 µg/mL) at different temperatures.

Furthermore, we calculated the temperature resolution (or temperature uncertainty) as:

$$\delta T = \frac{1}{S_r}\frac{\delta(LIR)}{LIR}$$

Equation 18

Where $\frac{\delta(LIR)}{LIR}$ is the relative uncertainty in the determination of the luminescence intensity ratio. The mean value in our temperature range was 0.3 K. These results show that UCNPsHPS are rising as robust nanothermometers at temperatures of biological interest because they have clean emissions due to the photon upconversion process, allow temperature measurements over longer periods of time because they do not dissolve, and provide more reliable measurements because their fluorescence is not altered by chemical environmental changes thanks to the protective polymer shell.

As mentioned above, most of the proposed strategies aim to avoid degradation by using capping agents or polydentate ligands with high binding affinity, sometimes in the form of multiple layers, to passivate their surface and limit the diffusion of ions.[186,195,212,218,219] Nevertheless, it is important to emphasise that these ligands inherently have a hydrophilic character (e.g., PEG-phosphate, poly-phosphates, poly-phosphonates, PAA, and polysulfonates), which is necessary to impart the desired water dispersibility to UCNPs. This means that they can typically be associated with some degree of water permeability and unprotected surface areas due to incomplete coating.[183,189,220] Although these strategies effectively delay the deleterious effects associated to water-transfer, they are expected to eventually allow diffusion of water and other small polar molecules to the surface of UCNPs and to the inner regions of their host matrix when degradation begins, especially at high dilution and under unstable conditions.[170] A shocking example of this permeability is the dissolution of UCNPs coated with silica shells, even when these shells are thick and robust, which can be explained by a certain porosity of these hydrophilic coatings. Only superthick silica shells have recently been shown to protect UCNPs at concentrations of 50 µg mL^{-1} over a 72h period in aqueous media, including phosphates, representing a significant advance over previous attempts, albeit at the expense of their ultimate size (≈166 nm in diameter).[180]

Based on our results, the best way to solve these problems may be to maintain a protective hydrophobic environment around the UCNPs, as this will simultaneously abolish all these deleterious mechanisms. Indeed, a very recent work by Märkl et al. also points in this direction by isolating UCNPs with phospholipid bilayers and showing very promising results in various media, including phosphate buffers.[221] In this regard, our strategy proved remarkably effective: all experiments were performed at very low concentrations (5 µg mL^{-1}; similar to ultrasensitive bioassays), and on top of that, under extremely aggressive conditions such as highly concentrated K^{+}PB (100 mm) and high temperatures (70°C). In-depth characterizations provided strong evidence that HPS provide a simultaneous solution to all problems associated with water transfer of UCNPs, namely water quenching, dissolution/leaking, and degradation by reaction with chemically aggressive species such as phosphates. Although further bioconjugation of UCNPs-HPS is beyond the scope of the present work, several chemical approaches can be used to address this problem. These include layer-by-layer deposition,[222] growing a thin organosilane layer,[223,224] or adding functional monomers during polymerization (e.g., acrylic acid).[225] The miniemulsion polymerization approach developed here is characterised by its versatility and cost-effectiveness, and also allows easy TEM characterization of the quality and thickness of the resulting HPS coating. We therefore believe that the proven advantages of this strategy, combined with the possibility of creating exciting new optical and multifunctional systems by embedding additional NPs or moieties into the HPS, will drive the development of a new wave of lanthanide-doped materials with novel functionalities and improved properties and reliability.

5.2.7 Conclusions

In this work, we have developed a new methodology to resolve all detrimental effects associated with the transfer of UCNPs into aqueous media. We successfully combined two strategies: 1) substituting oleate by MDP as capping agent, to achieve higher binding affinity, hydrophobic surface properties, and polymerizable groups; and 2) growing a robust HPS around the UCNPs to ensure long-term and effective environmental protection. Fine tuning of the number of encapsulated UCNPs, the thickness of the shell, and the composition (PS and PS /PMMA HPS) was demonstrated. There is clear evidence of the high level of protection that this HPS provides against water quenching, dissolution, and degradation by phosphates, even at the atomic level. This was demonstrated under extremely aggressive conditions for UCNPs (high dilution combined with high phosphate concentration or high temperature) and was even more remarkable compared to the very strong degradation of UCNPs coated with PAA used as control sample.

The results of the UCNPs-PAA dissolution study allowed us to theoretically estimate and understand the causes of the decrease in luminescence. We attributed this effect largely to the release of Ln^{3+} from the host matrix into the environment, while a smaller part was due to the loss of quantum efficiency as the S/V ratio of UCNPs increases during dissolution, this last effect being responsible for the decrease in the lifetime of luminescence. This also allowed us to roughly calculate the solubility Ksp of β-$NaYF_4$. Finally, we successfully confirmed the protective role of HPS in aqueous media at 70°C.

This lays the foundation to reliably extend the use of UCNPs, or more generally HPS-coated lanthanide-doped NPs, as reporters in applications requiring high temperatures, such as sensing platforms based on real-time PCR and isothermal amplification strategies. In addition, their use as luminescent nanothermometers that can provide reliable thermal feedback in these techniques could prove to be a valuable tool, especially when integrated into microfluidic platforms or during hyperthermal and photothermal ablation therapies. Overall, the proposed strategy proves to be a promising and versatile solution, not only for UCNPs, but potentially also for other NPs where similar water transfer issues may arise. More interestingly, it offers room for a new generation of multifunctional materials by exploiting the possibilities associated with embedding additional components into the HPS.

5.3 Rational Design of Rare-Earth Nanothermometers with Complex Core@Shell @Architceture

"There's Plenty of Room at the Bottom."

Richard Feynman

5.3.1 Abstract

The emission efficiency of rare-earth doped nanoparticles is intrinsically related with the chemical composition but also with their structural architecture. In this work, we have studied the role of the structure in the emission and thermal sensitivity of $NaYF_4$@$NaYF_4$:Nd_{60},Yb_{20}@CaF_2 nanoparticles, which are one of the most efficient rare-earth nanothermometers working in the near-infrared region. In particular, we have studied the effect of the active shell thickness, the presence of a protective shell as well as the influence of having an active or inactive core in the overall spectroscopic properties. For that, we have synthesized a set of core, core@shell and core@shell@shell nanoparticles and evaluated the emission intensity, luminescent decay time curves, absolute quantum yield, and thermal sensitivity as a function of the core nature, active shell thickness and presence of a protective CaF_2 outer shell. The results reveal the great importance of the active shell thickness in the photoluminescence properties as well as in the thermal sensitivity. In fact, nanocrystals with a 2-nm thick active shell exhibit the longest lifetime and the highest quantum yield. In addition, we have observed a linear relationship between absolute quantum yield and thermal sensitivity. These features are conspicuously enhanced when the CaF_2 protective shell is grown. This information is used to develop a simple theoretical model accounting for the different de-excitation pathways of the emissive ions that allows a deep understanding of the thermal sensitivity and emission efficiency of the nanocrystals and that could be used for the design of new and more efficient thermal probes.

Keywords: Rare Earth-based nanoparticles, nanothermometry, influence of the active layer.

5.3.2 Resumen

La eficiencia de emisión de las nanopartículas dopadas con tierras raras está intrínsecamente relacionada con la composición química, pero también con su arquitectura estructural. En este trabajo, hemos estudiado el papel de la estructura en la emisión y la sensibilidad térmica de las nanopartículas de $NaYF_4$@$NaYF_4$:Nd_{60},Yb_{20}@CaF_2, que son uno de los nanotermómetros de tierras raras más eficientes en la región del infrarrojo cercano (NIR). En particular, hemos estudiado el efecto del grosor de la capa activa, la presencia de una capa protectora y la influencia de tener un núcleo activo o inactivo en las propiedades espectroscópicas generales. Por lo tanto, hemos sintetizado un conjunto de nanopartículas core, core@shell y core@shell@shell y evaluando la intensidad de la emisión, las curvas del tiempo de decaimiento luminiscente, el rendimiento cuántico absoluto y la sensibilidad térmica en función de la naturaleza del núcleo, el espesor de la capa activa. y presencia de una capa exterior protectora de CaF_2. Los resultados revelan la gran importancia del espesor de capa activa en las propiedades fotoluminiscentes así como en la sensibilidad térmica. De hecho, los nanocristales con una capa activa de 2 nm de espesor exhiben el tiempo de vida y el rendimiento cuántico más alto. Además, hemos observado una relación lineal entre el rendimiento cuántico absoluto y la sensibilidad térmica. Estas características se mejoran notablemente cuando se crece la capa protectora de CaF_2. Esta información se usa para desarrollar un modelo teórico simple que explica las diferentes vías de desexcitación de los iones emisivos que permite una comprensión profunda de la sensibilidad térmica y la eficiencia de emisión de los nanocristales y que podría usarse para el diseño de nuevos y más eficientes sondas térmicas.

Palabras clave: *Nanopartículas basadas en lantánidos, nanotermometría, influencia de la capa activa.*

5.3.3 Introduction

Rare earth nanoparticles (NPs) have become one of the most interesting systems as photoluminescent probes due to their superb optical properties, such as photochemical stability, long luminescence lifetime, no photobleaching, and large Stokes shifts.[226–228] In addition, their multiband emission from the ultraviolet-visible range to the near infrared (NIR) has opened a way for illumination applications such as sensors,[166,229] solar cells,[230] photoresponsive drug delivery systems[231] or imaging applications.[232–235] Moreover, these NPs exhibit temperature-dependent emission, which can be used to reveal fundamental properties of living tissues in a noninvasive way by remote reading. This ability of rare earth NPs to change the intensity of light emission as a function of temperature has made them ideal candidates for nanothermometric applications and paved the way for noninvasive temperature measurements in vivo.[236–239]

However, designing these NPs with optimal and reliable properties requires a deep understanding of how composition, structure, and architecture affect their spectroscopic properties.[240–242] One of the best-known strategies for tuning the luminescence properties of rare earth nanoparticles is the design of core-shell structures.[243] On the one hand, previous work has built a protective outer shell around the optically active region to reduce surface defects and quenching of ligand vibrations.[233,234] On the other hand, confining the optically active ions in different layers can increase the versatility and efficiency of the system compared to structures with a core. For example, forming a migration energy shell between the absorbing layer and the emitting layer can lead to longer decay times;[244] or isolating two different absorbing ions in separate layers can allow excitation at two combinable wavelengths.[245]

The inert-core@active-shell@inert-shell structure has also been selected as the ideal architecture for nanothermometry in living mammals.[241] Consequently, our goal in this work is to evaluate how the architecture of complex core@shell@shell structures affects the photoluminescent properties and thermal response of rare-earth probes. To this end, we varied the thickness (from 1.1 to 2.8 nm) of an optically active shell doped with Nd^{3+} and Yb^{3+} ions and confined between an inert core and a protective CaF_2 shell on the $NaYF_4$ matrix. In this way, we explored the advantages of an inert core over an active core, as well as the optimal thickness of the active shell and the optimal core size on which to grow the shell structure. All of this resulted in a very fine architecture that exhibits excellent fluorescence efficiency, absolute photoluminescence quantum yield (~15%), and high thermal sensitivity (1.1%-$^{\circ}C^{-1}$). This is the result of a competition between the thermally activated energy transfer from Nd^{3+} to Yb^{3+} ions and the non-radiative processes at the surface. Based on a simple theoretical model that accounts for the competition between the excitation processes, the best optical performance is associated with the highest thermal sensitivity.

5.3.4 *Objectives*

5.3.4.1 Overall Objective

Study the influence of the thickness of the active shell on the photoluminescence properties and thermal sensitivity of $NaYF_4@Nd^{3+},Yb^{3+}@CaF_2$ nanoparticles.

5.3.4.2 Specific Objectives

- Synthesis and morphological characterization of the cores of $NaYF_4$.
- Synthesis, morphological and optical characterization of $NaYF_4@Nd^{3+},Yb^{3+}$ core/shell nanoparticles with different core/shell ratios.
- Synthesis, morphological and optical characterization of core/shell/shell $NaYF_4@Nd^{3+},Yb^{3+}@CaF_2$ nanoparticles with different ratios between the $Nd^{3+}{}_{60\%},Yb^{3+}{}_{20\%}$ shell and the CaF_2 shell.
- Perform thermal sensitivity studies by measuring infrared photoluminescence and lifetimes as a function of temperature in a range of 20-50°C for both core/shell and core/shell/shell structures.
- Measure the quantum yield of core/shell and core/shell/shell structures.

5.3.5 *Experimental section*

5.3.5.1 Synthesis of $NaYF_4@Nd^{3+}{}_{60\%},Yb^{3+}{}_{20\%}@CaF_2$

The methodology carried out in this chapter was to prepare core/Shell/Shell structures by varying the thickness of the Shell through the modification of the ratios between the α-$NaYF_4$ cores and the $Re(TFA)_3$ precursors. To achieve this purpose, the methodology described in sections 4.3.6 for the α-$NaYF_4$ core, 4.3.7 for the $NaYF_4@Nd^{3+},Yb^{3+}$ core/Shell, and 4.3.8 for the $NaYF_4@Nd^{3+},Yb^{3+}@CaF_2$ core/Shell/Shell was used.

5.3.5.2 Characterization

Dynamic light scattering (DLS) was performed using a Malvern Nano ZS. Images in High-angle annular dark field (HAADF), transmission electron microscopy (TEM), and energy dispersive X-ray spectroscopy (EDS) mappings were acquired using a FEI Talos F200X (FEI, USA) at 80 kV and a EDS detector. Samples for TEM were prepared by pouring a 10 µL drop of each dispersion onto a Cu grid with a carbon support membrane and then drying. X-ray diffraction (XRD) patterns were recorded using a Philips X'pert diffractometer (Cu Kα-radiation, 45 kV and 40 mA). Data were recorded in the range of 20-90° 2θ with a step size of 0.02° and a normalized count time of 1 $s\text{-}step^{-1}$. Emission spectra were collected after samples were illuminated with an 800-nm CW laser using an Andor iDus InGaAs 491 cooled to -90°C. Luminescence decay curves were obtained by exciting the dispersions of nanoparticles (NPs) with an OPO oscillator (Lotis) tuned to 800 nm, providing 8 ns pulses at a repetition rate of 10 Hz. Fluorescence intensity was measured using a Peltier-cooled photomultiplier tube with enhanced sensitivity in the NIR region (Hamamatsu R5509-73). The contribution of scattered laser radiation was removed by using two bandpass filters (FEL850 from Thorlabs) and a high-brightness monochromator (Shamrock 320 from Andor). Finally, the time evolution of the fluorescence signal was recorded and averaged using a digital oscilloscope (LeCroy WaveRunner 6000). The absolute photoluminescence quantum yield (PLQY) of the NPs was measured using a 6-inch diameter integrating sphere (Labsphere, 4P- GPS -060- SF). The sample cuvette (5 mm path length) was mounted at the center of the sphere. Light from a pigtailed 808nm laser (Omicrom, BrixX808-2500- HP-FC) was collimated onto the sample with a beam diameter of 2.5 mm. The collected signal was sent to a monochromator (Horiba, iHR320) for wavelength selection and detected with a NIR InGaAs photodetector (Horiba, DSS-IGA020TC).

5.3.6 Results and analysis

The synthesis of the core@shell@shell structures $NaYF_4$@$NaYF_4$:Nd,Yb@CaF_2 was carried out by the thermal decomposition of trifluoroacetates starting from the core and subsequent epitaxial growth of the shells. Synthesis of α-$NaYF_4$ cores leads to NPs with an average diameter of 7±1 nm as measured by TEM, Figure 56A. In HAADF and element mapping images (Figure 56G and Figure 56J, respectively), we can observe that each nucleus has a homogeneous electron density and a ubiquitous distribution of Y^{3+} and F^- within the NPs. The epitaxial growth of the shell around the nucleus leads to an enlargement of the NPs, as shown in Figure 56B. This enlargement is the result of the growth of an optically active shell heavily doped with Nd^{3+} (60%) and Yb^{3+} (20%). This composition was selected as optimal for use as a nanothermometer based on previous studies.[241] This difference in composition between the core and shell is confirmed by HAADF, where an increase in electron density can be observed in the outer part of the NPs, which may be associated with an enhancement of the Z contrast by the Nd^{3+} ions (Figure 56H). Moreover, elemental mapping reveals the presence of $Nd3^+$, which is preferentially located in the outer part of the NPs (Figure 56K). Finally, the incorporation of an inert and protective shell based on CaF_2 is clearly evident in Figure 56F. Here we observe an increase in the size of the NPs corresponding to a CaF_2 shell thickness of about 2 nm, as well as a change in the shape of the NPs from spherical to cubic after the incorporation of CaF_2. Moreover, we can observe a change in the electron density of the NPs with HAADF (Figure 56I), while elemental mapping shows the presence of Ca^{2+} ions distributed around the outer shell (Figure 56L). The change in shape from spherical to cubic observed after encapsulation with CaF_2 could be due to kinetically dominated shell growth due to the lower decomposition temperature of Ca-trifluoroacetate compared to the other alkaline earth metal trifluoroacetates, which can produce a more crystalline structure.[246,247]

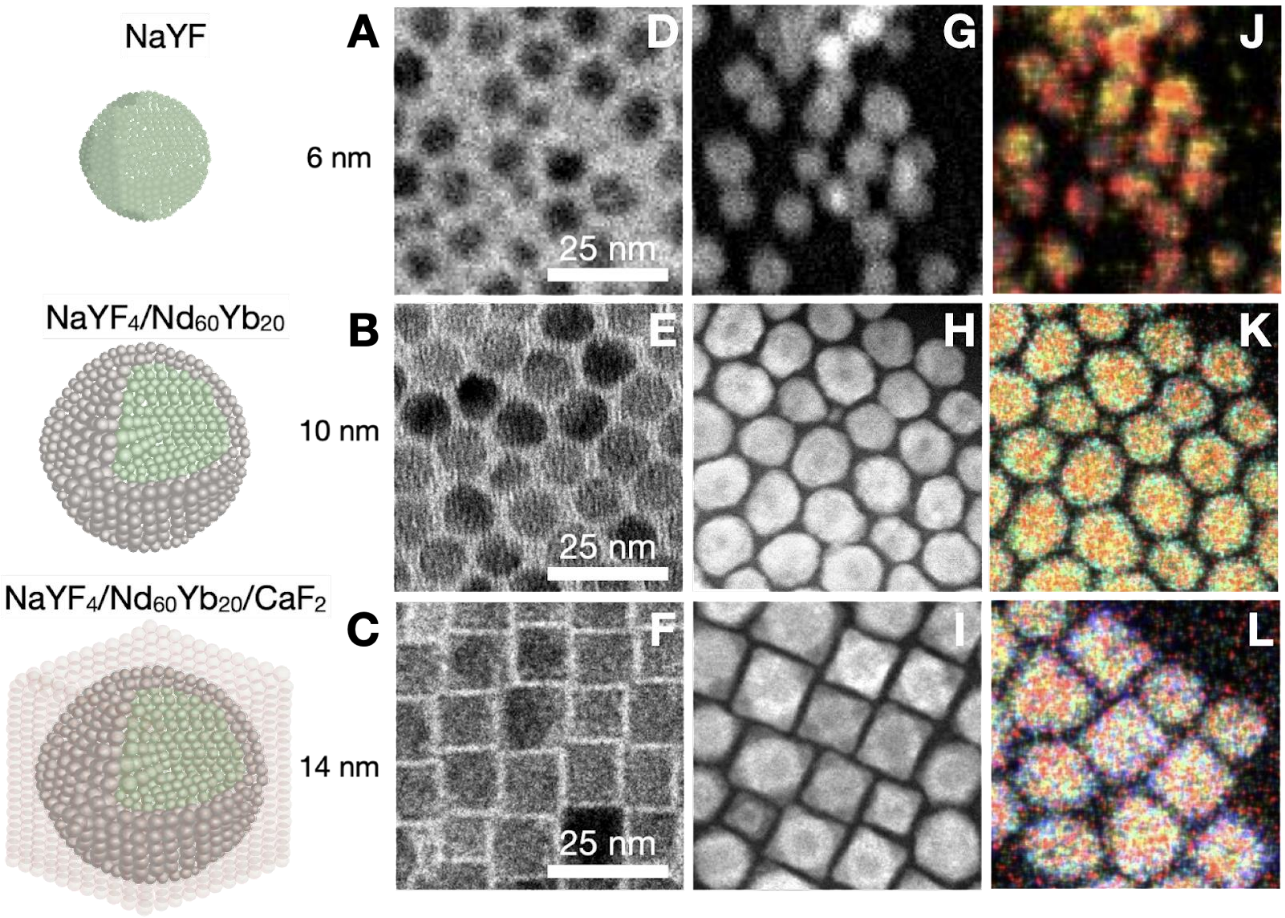

Figure 56. Schematic representation of an inert core (A), a core@shell (B) and core@shells@shell NP (C) with their representative mean size and composition. The inset D, E and F represent the TEM of the core, core@shell and core@shell@shell at the different synthetic steps. The insets G, H, I and J, K, L depict the HAADF-STEM and elemental mapping images of the nanoparticles obtained at the different steps.

To gain insight into the ion composition, EDS and HAXPES (Figure 57) analyses of the different NPs were performed. All these experiments provide valuable information about the concentration of Nd^{3+} and Yb^{3+} within the matrix and the hierarchical architecture of the core@shell@shell structure. In this context, HAXPES analysis performed with a focused X-ray beam at two different energies (7 and 9 keV) probes the depth-dependent chemical composition of the NPs near the surface of the material, where the signals originating from the Ca^{2+} ions predominate (Figure 57C and Figure 57D). Moreover, XRD analyses of the cores, core@shell, and core@shell@shell NPs reveal their crystalline structure, which can be assigned to the α-cubic phase of $NaYF_4$ and CaF_2, respectively (Figure 57B).

Figure 58A shows a schematic energy level diagram of Nd^{3+} and Yb^{3+} ions within the active shell layer. The figure shows the absorption of the excitation beam at 800 nm by Nd^{3+} ions, the energy transfer process from Nd^{3+} to Yb^{3+} (and vice versa, the back transfer), and finally the PL emission at 980 nm from the excited state $^2F_{5/2}$ of Yb^{3+} ions. The energy gap of 1000 cm^{-1} between the metastable excited states $^4F_{3/2}$ (Nd^{3+}) and $^2F_{5/2}$ (Yb^{3+}) hinders a direct resonant energy transfer and forces the energy transfer between $^4F_{3/2}$ (Nd^{3+}) and $^2F_{5/2}$ (Yb^{3+}) through a phonon-assisted process.[248,249]

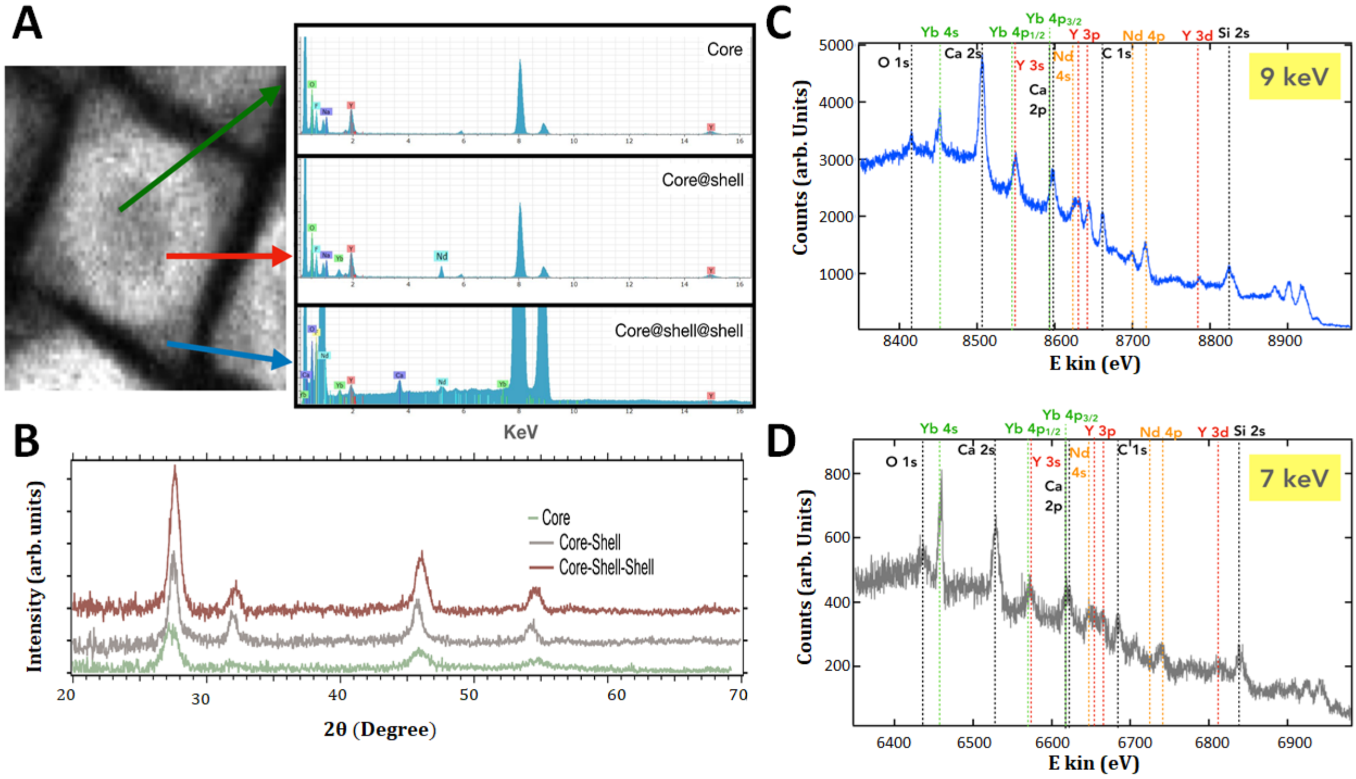

Figure 57. **A.** EDS analysis of Core, core@shell and core@shell@shell Nps. **B**. XRD diffraction peaks of the core, core@shell and core@shell@shell NPs. All samples show crystalline peaks corresponding to a $NaYF_4$ and CaF_2 cubic phase structure. HAXPES analyses at two different energies, 9 keV (**C**) and 7 keV (**D**).

On the other hand, thermally activated back energy transfer from $^2F_{5/2}$ (Yb^{3+}) to $^4F_{3/2}$ (Nd^{3+}) reduces the $^2F_{5/2}$ of Yb^{3+} steady state population and increases the $^4F_{3/2}$ metastable state of Nd^{3+} ions that due to its low quantum efficiency decays non-radiatively,[250] rendering a reduction in the emission intensity of the NPs and shortening the PL emission lifetime at 980 nm. This phenomenon makes the NPs emission strongly dependent on the environmental temperature and therefore can be used for nanothermometry applications.

Furthermore, the outer shell of inert CaF_2 has been chosen as protective layer due to its biocompatibility, stability, and lattice match with α-rare earth NPs. Upon excitation with 800 nm light source, the core@shell@shell NPs exhibit a much more intense PL emission than the core@shell NPs, as shown in Figure 58B, highlighting the importance of the inert outer shell to protect the ions from the large vibrational energies of the solvent and surface-associated ligands.[233,234]

5.3.6.1 Optimization of the optically active shell thickness

Based on the structure $NaYF_4@NaYF_4$:Nd,Yb@CaF_2 analyzed in the previous section, we have studied the influence of the optically active shell thickness on the spectroscopic and thermometric properties of the nanosystem, varying the size of this layer from 1.1 nm to 2.8 nm. One of the most interesting results after analyzing the luminescence properties of NPs is the fact that the emission intensity, PL quantum yield, and PL decay time increase when the thickness of the active shell is increased. The increment of the thickness of the active shell decreases the surface-to-volume ratio and minimizes the likelihood of unwanted energy loss through surface quenchers, such as vibrational modes coupled with capping agents or solvent molecules.[234] However, increasing the active volume enhances energy migration and increases the number of host defects that can quench emission,[251] so an optimal shell thickness is expected.

Figure 58C and Figure 58D show the PL decay curves of NaYF$_4$@Nd,Yb and NaYF$_4$@Nd,Yb@CaF$_2$ NPs, respectively, for active shell thicknesses from 1.1 to 2.0 nm, in which an increment of the PL decay time with the active shell thickness is observed. This behavior can be clearly seen in Figure 58E where it can be observed how NaYF$_4$@Nd,Yb and NaYF$_4$@Nd,Yb@CaF$_2$ show a progressive increment of the decay time when the active shell thickness is increased until a value of 2 nm, after which the decay time starts to decrease. The quantum yield of NaYF$_4$@Nd,Yb and NaYF$_4$@Nd,Yb@CaF$_2$ NPs versus the active shell thickness is also plotted in Figure 58E, showing the same trend as decay times. Therefore, an optimum active shell thickness close to 2 nm has been found.

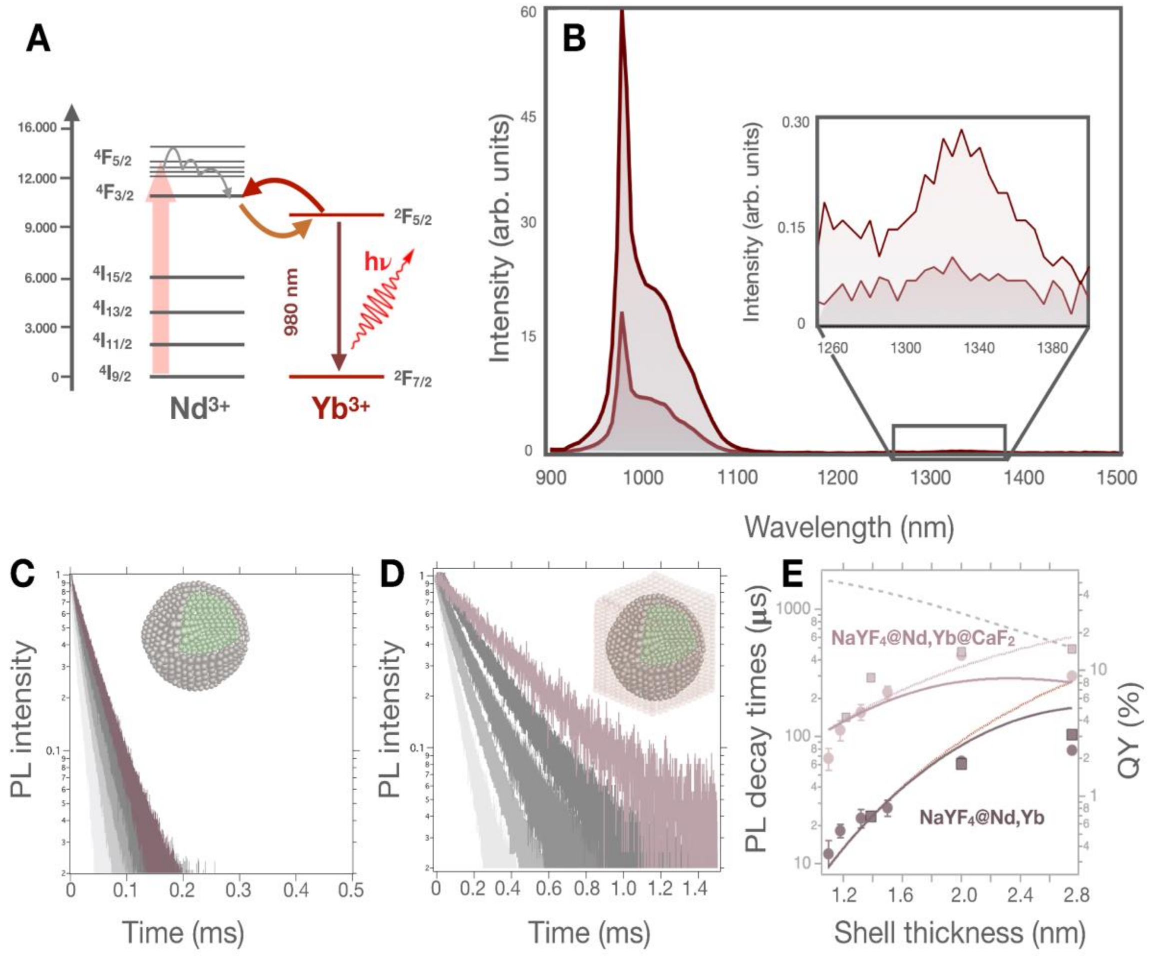

Figure 58. **A.** Energy transfer scheme for populating the Yb^{3+} 980 nm emission level $^2F_{5/2}$ upon excitation of Nd^{3+} ions by a 800 nm laser. **B.** Emission spectra of NaYF$_4$@Nd,Yb and NaYF$_4$@Nd,Yb@CaF$_2$ NPs, showing an increment in the PL emission when de CaF$_2$ is incorporated. **C.** and **D.** PL decay curves of NaYF$_4$@Nd,Yb and NaYF$_4$@Nd,Yb@CaF$_2$ NPs, respectively, when increasing the active shell thickness. **E.** Representation of the experimental PL decay time (circle symbols) and absolute PL quantum yield (square symbols) as a function of the active shell thickness for NaYF$_4$@Nd,Yb and NaYF$_4$@Nd,Yb@CaF$_2$. The dashed gray line represents the theoretical decay time of the NPs considering solely host matrix defects as the origin of the emission quenching. The brown and pink dotted lines represent the theoretical decay time considering only surface quenching defects, while solid lines represent the theoretical decay time when both quenching processes take place.

To get a deeper understanding of the role played by the different layers of the heterostructure, we developed a simple theoretical model describing the total de-excitation rate of each excited Yb^{3+} ion inside the NP as a sum of a radiative decay rate Γ_R and two non-radiative decay rates attributed to surface effects Γ_{SQ} and defects in the active region Γ_{DQ}:

$$\Gamma^{ion} = \Gamma_R + \Gamma_{SQ} + \Gamma_{DQ}$$

Equation 19

Then, the excited Yb^{3+} ion can radiatively decay by emitting a photon with a typical 2-ms radiative decay time $\tau_R = 1/\Gamma_R$. On the other hand, emission quenching mechanisms can occur which non radiatively de-excite the Yb^{3+} ion, being the most important the surface-related quenching processes (Γ_{SQ}). Surface quenching effects can be described as a dipole-surface type energy transfer from each Yb^{3+} active ion (donor) to a film of acceptors around the NP which follows the $1/d^4$ distance dependence, being the non-radiative energy transfer rate:

$$\Gamma_{SQ} = \frac{1}{\tau_R}\left(\frac{d_0}{d}\right)^4$$

Equation 20

where d_0 is the Förster distance, and d is the distance from the Yb^{3+} ion under consideration to the external NP surface. This strong surface quenching is alleviated by the presence of the external inert shell of CaF_2. Another non-radiative pathway is the energy transfer process between the Nd^{3+}/Yb^{3+} ions and defects present in the active region of the NP (Γ_{DQ}) which is favored by the energy migration between ions. By confining the active ions in a thin layer, the deactivation from the host defects is strongly minimized, as was shown in previous.[76,241,252] Then, we simulated this quenching mechanism by increasing the non-radiative decay rate Γ_{DQ} with the volume of the active shell following the expression $\Gamma_{DQ}/\Gamma_R = 3\cdot(D_{shell}/2.8)$[228], where D_{shell} is the active shell thickness. Then, Γ_{DQ} reaches a value close to three times the radiative value at the largest thickness used (~2.8 nm).

The decay time of each Yb^{3+} ion depends on its position inside the NP following:

$$\tau^{ion} = \frac{1}{\Gamma^{ion}} = \frac{\tau_R}{1 + \tau_R\Gamma_{DQ} + \left(\frac{d_0}{d}\right)^4}$$

Equation 21

and also the quantum yield of the ion:

$$QY^{ion} = \frac{\Gamma_R}{\Gamma^{ion}} = \frac{1}{1 + \tau_R\Gamma_{DQ} + \left(\frac{d_0}{d}\right)^4}$$

Equation 22

To calculate the decay time of the NP, τ, we averaged the decay time of all the Yb^{3+} ions, τ^{ion}, by weighting each value by the quantum yield of the ion, QY^{ion}, which measures its emission intensity. To compute the weighted average decay time, we distributed the Yb^{3+} ions into imaginary thin shells inside the active shell. The ions inside each thin shell are expected to have the same interaction with the surface quenchers.

$$\tau = \frac{\sum_{shell} \nu_{shell}\, QY^{ion}\, \tau^{ion}}{\sum_{shell} \nu_{shell}\, QY^{ion}}$$

Equation 23

Where ν_{shell} is the volume of each imaginary thin shell which measures the number of ions inside the shell. In our calculations, the Förster distance d_0 was used as a control parameter to fit the experimental data, being its value 3.6 nm. We calculated the decay time τ for a 7 nm-core NP by varying the active shell thickness from 1.1 to 2.8 nm for the cases with and without an external inert shell. For the sake of simplicity, we considered a spherical external inert shell with a 1 nm thickness. The simulated curves are plotted in solid lines in Figure 58E, showing a rough agreement with the experimental data. To analyze the contribution of both non-radiative mechanisms we also plotted in the same figure the decay time computed when only the surface quenching is present (dotted lines) and when only the quenching due to defects in the active region participates (dashed line). This clearly shows how the competition between these two non-radiative pathways leads to an optimum active shell thickness close to 2 nm, in agreement with the experiments.

5.3.6.2 Inert core versus active core

As we mentioned above, the active ions were confined in a thin layer to minimize the deactivation from the host defects, in accordance with previous works.[76,241,252] However, we decided here to analyze more in detail to what extent this point depends on the NP structure. To answer this question, we synthesized NPs with active cores but following the same synthetic procedure as for the inert core NPs. As expected, we experimentally found that core@shell@shell NPs with inert core presented a larger decay time and quantum yield than the active core NPs (Figure 59). However, the situation changes in the case without the protective outer shell, the core@shell NPs with inert core presented almost the same optical performance than the active core NPs (Figure 59). That is, the confinement of active ions in a thin shell is not advantageous without a protective outer shell. This can be ascribed to the strong quenching suffered by the active ions placed in the active shell when no external protective shell is present. Once again, this result highlights the importance of covering the NP with a protective CaF_2 shell.

in Figure 59A (light colors). The same happens with the quantum yield, as shown in Figure 59B (light colors) where a small increase takes place by doping the cores. Therefore, in the case of core@shell NPs, without the external inert shell, the confinement of the ions in a thin layer does not work which is due to the strong surface quenching suffered by the active ions placed in the active shell. So, although the excitation migration in the case of an active core will produce an overall increase of the non-radiative quenching due to host defects, the Yb^{3+} ions in the core will compensate for the strong surface quenching suffered by the ions placed in the active shell. We corroborated this statement by using our model to compare the decay time τ of a NP with an active shell of 2 nm and an inert core of 7 nm with the same NP with an active core. For the active core NP we took a non-radiative decay rate due to deactivation from host defects equal to $\Gamma_{DQ} = 13\ \Gamma_R$ which leads to a value of τ similar to the case with an inert core. Figure 59C shows the radial distribution inside the NP of the decay time of Yb^{3+} ions for both architectures. Here we see how the strong surface quenching suffered by the Yb^{3+} ions placed in the active shell avoids that confined ions show a better performance than the ions placed in the core

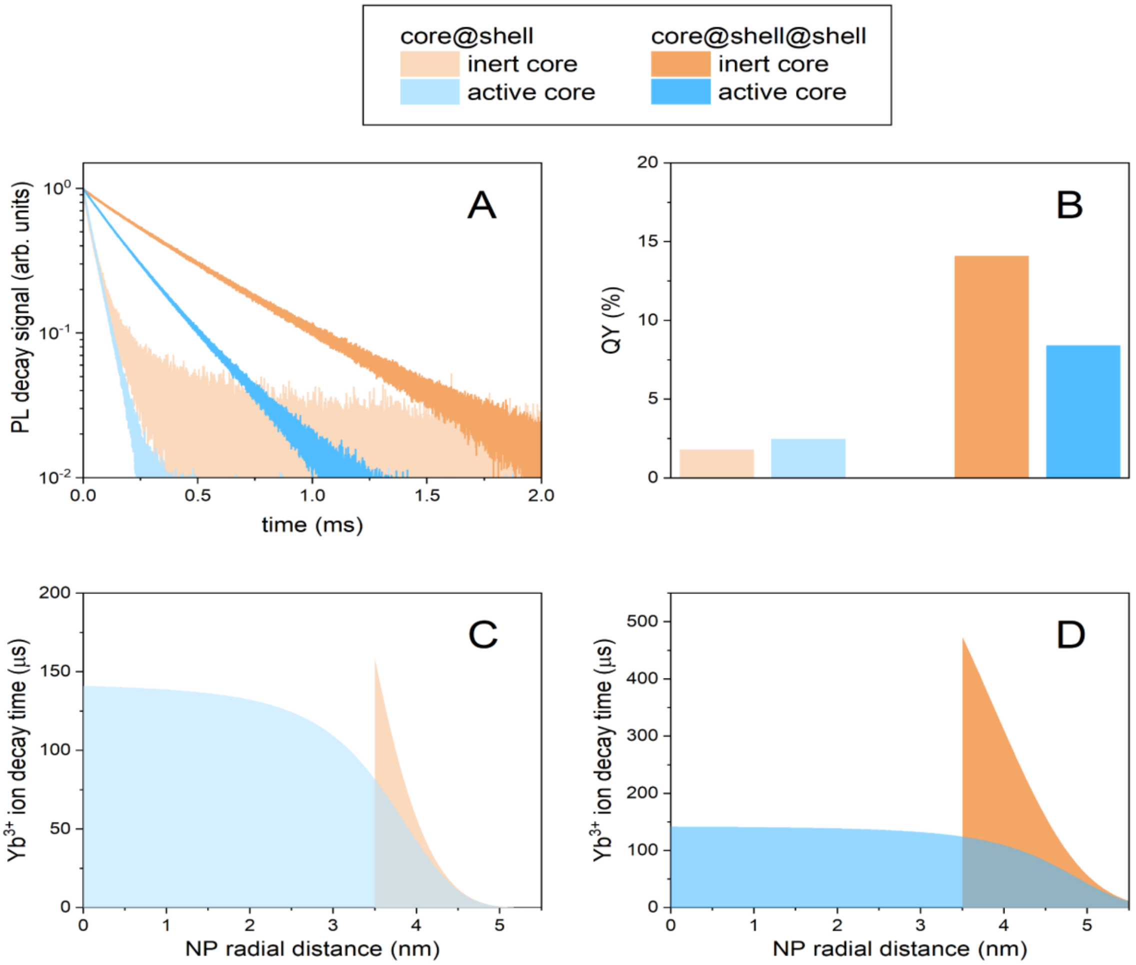

Figure 59. **A.** Experimental PL decay curves and **B.** PL quantum yield comparing inert core (core/shell and core/shell/shell) and active core (active core/shell and active core/shell/shell) NPs. Simulated decay time of each Yb^{3+} ion as a function of radial distance within the NP for the case of **C.** NPs with inert core@shell (light orange) and NPs with active core@shell (light blue) and **D.** NPs with inert core@shell@shell (dark orange) and NPs with active core@shell@shell (dark blue).

We found that the active core NPs have the same decay time than the inert core NPs, as shown

5.3.6.3 Inert Core Size

One of the most interesting applications of these NPs is their use as nanothermometers for in vitro and in vivo studies. In this field, the size of the NPs is of paramount importance because it can determine the NP pharmacokinetics and, consequently, their use.[253] In general, smaller NPs show better biodistribution properties than larger ones when both are similarly functionalized.[254,255] In this sense, the preparation of the smallest NPs while maintaining their spectroscopic properties could be considered the holy grail. With this goal in mind, we have theoretically evaluated the effects of nuclear reduction on the spectroscopic properties of NPs. However, it should be kept in mind that core reduction is accompanied by an increase in the surface-to-volume ratio and, consequently, an increase in the surface deactivation rate.[256–258]

To answer this question, we used the previous model and calculated the NP decay time τ by varying the size of the inert core for a NP with an active shell thickness of 2 nm and an outer inert shell of 1 nm. The result is shown in Figure 60, which shows how the NP decay time increases with increasing core size until a plateau is reached at values close to 7 nm, the value used in our experiments. This was a surprising result since changing the size of the inert core had no effect on the non-radiative decay rates in the active shell, i.e., the decay time of each Yb^{3+} ion should remain unchanged.

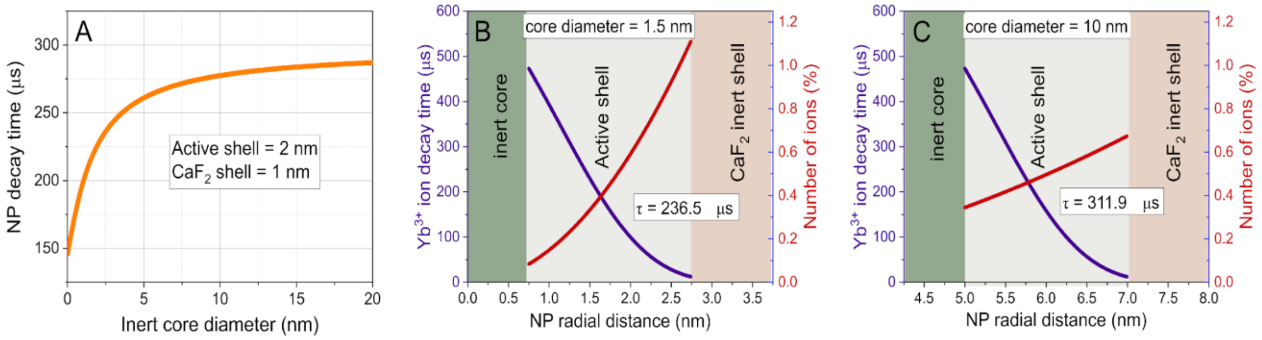

Figure 60. A. Simulated plot of NP lifetime as a function of inert core size. **B.** and **C.** Simulated decay time of each Yb^{3+} ion (left axis) and the number of Yb3+ ions (right axis) as a function of radial distance within the active shell for the case of an inert core diameter of 1.5 nm (**plot B**) and 10 nm (**plot C**). It can be clearly seen that the lifetime of each Yb^{3+} ion is identical for the 1.5-nm core and the 10-nm core (purple lines), while the distribution of Yb^{3+} ions changes as a function of core size (red lines).

This can be seen in Figure 60B and Figure 60C (purple lines), where the distribution of τ^{ion} is plotted along the radial distance NP for a small and a large inert core, respectively. On the other hand, the relative radial distribution of Yb^{3+} ions in the active shell depends on the size of the inert core. Indeed, in a NP with a small core, there are many more Yb^{3+} ions in the outer part of the active shell, where the ions are strongly quenched, than in the inner part, where the ions have longer decay times (see red line in Figure 60B). In contrast, in a NP with a larger core, there is a much more even distribution of ions with distance and comparatively more ions with longer decay times, as shown in Figure 60C (red line). Thus, we can conclude that for a more efficient NP the core@shell@shell ternary structure should have a core size large enough to achieve a nearly uniform distribution of active ions along the radial distance of the NP.

5.3.6.4 Photoluminescence emission temperature dependence

The PL emission of $NaYF_4$@Nd,Yb NPs hardly varies in the range between 15 and 50°C, (Figure 61A). In stark contrast, the same experiment with $NaYF_4$@Nd,Yb@CaF_2 NPs shows that the PL emission decreases sharply with increasing temperature, as shown in Figure 61B. The same trend is observed when the PL decay curves of the $NaYF_4$@Nd,Yb NPs and $NaYF_4$@Nd,Yb@CaF_2 NPs are analyzed, see Figure 61C through Figure 61F. The thickness of the active shell seems to influence the thermal quenching effect. The thicker the active shell, the higher the thermal sensitivity by up to 2 nm. As a result, the $NaYF_4$@Nd,Yb NPs reach a maximum relative sensitivity Sr of 0.25 %-°C^{-1}. Such an effect is maximized when the NPs are additionally covered with an inert shell layer of CaF_2, resulting in a Sr of 1.11 %-°C^{-1}. Analysis of these data clearly shows that thermal sensitivity occurs only when the NPs are protected with the outer CaF_2 layer, with lifetimes following a sigmoidal curve and maximum thermal sensitivity being reached when the NPs have a maximum lifetime.

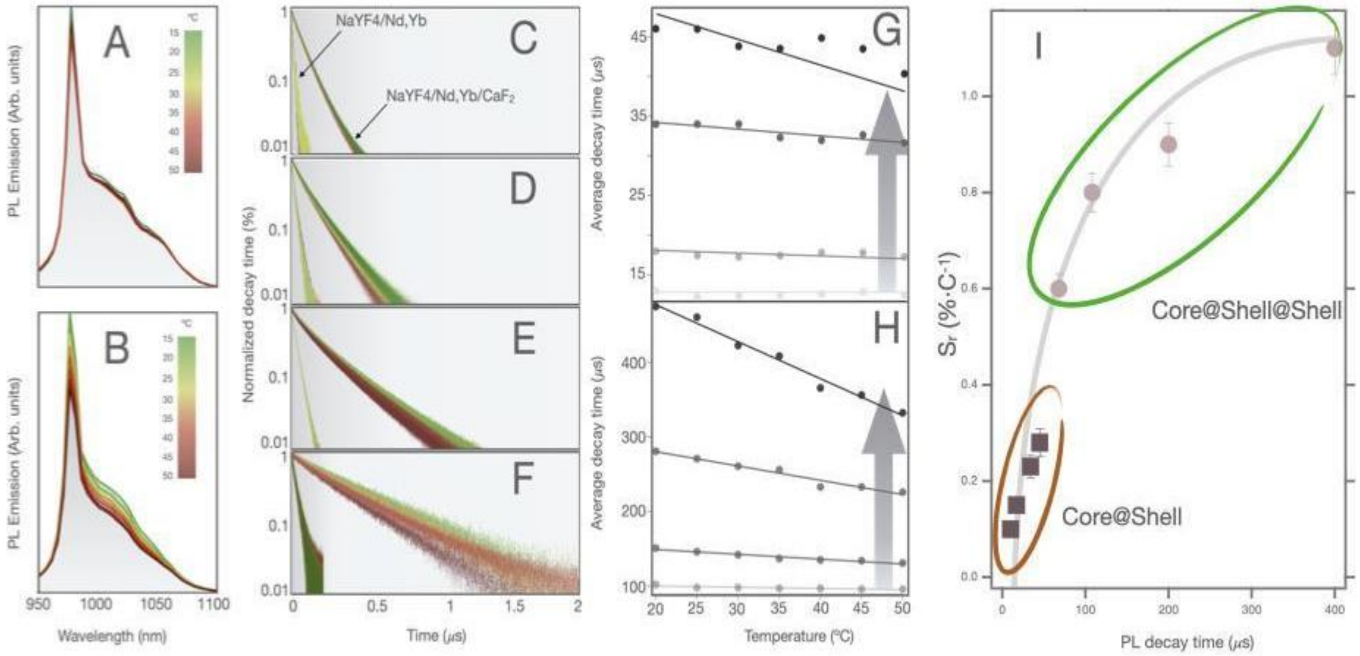

Figure 61. A. PL emission spectra of $NaYF_4@NaYF_4$:Nd,Yb NPs and B) $NaYF_4@NaYF_4$:Nd,Yb@CaF_2 NPs with an active shell thickness of 2 nm recorded at different temperatures. From **C** to **F** PL decay curves of $NaYF_4@NaYF_4$:Nd,Yb and $NaYF_4@NaYF_4$:Nd,Yb@CaF_2 NPs with increasing active shell thickness. **G** Lifetimes of $NaYF_4@NaYF_4$:Nd,Yb and **H.** $NaYF_4@NaYF_4$:Nd,Yb@CaF_2 NPs with varying active shell thickness as a function of temperature. **I.** Relative thermal sensitivity at 15°C as a function of lifetime of core@shell (squares) and core@shell@shell (circles) NPs. The gray line serves as a guide for viewing the trend.

These results let us hypothesize that the action mechanism that rules the thermal sensitivity of these NPs is based on a competitive process between emission, surface quenching effect and a thermally dependent back energy transfer (BET). Basically, once the NPs are irradiated with a 800 nm laser, Nd^{3+} ions absorb the energy and transfer the quanta to Yb^{3+} ions via a phonon assisted process, which populates the excited state $^2F_{5/2}$. This state can be depopulated through different ways: 1) by radiative emission of a photon at 980 nm, 2) through surface quenching which is related to defects, solvents and capping agent vibrational couplings and 3) through a back energy transfer from Yb^{3+} to Nd^{3+} ions, which is thermally dependent and enhanced when high doping level of Nd^{3+} ions are present in the NPs[11]. Quenching effect through surface energy transfer seems to be dominant when CaF_2 shell is not present, that can be due to its faster non-radiative rate when comparing with the radiative rate of Yb^{3+} ($1/\tau \approx 1/2000\ s^{-1}$). When this non-radiative pathway is predominant, the thermal sensitivity is scarce (Figure 62A). In stark contrast, the presence of the CaF_2 outer shell significantly reduces the non-radiative pathways due to surface quenching, increasing the NPs lifetime and favoring back energy transfer from Yb^{3+} to Nd^{3+} which renders an increment of the thermal sensitivity of the NPs (Figure 62B). Taking into consideration the competition between surface quenching and BET, we have modelized the lifetime of each Yb^{3+} ion within the structure, τ^{ion}, by adding a new non-radiative decay rate Γ_{TQ} to the total de-excitation rate, Γ^{ion}, which accounts for the quenching produced by the thermally activated BET. To theoretically reproduce the measured relative sensitivity values the non-radiative decay rate Γ_{TQ} was linearly increased with temperature starting from $\Gamma_{TQ}=0$ at T=20 ºC and reaching a value of $\Gamma_{TQ}=2\cdot\Gamma_R$ at 50 ºC. Figure 62C and Figure 62D show the τ^{ion} as a function of the radial position inside the active shell for NPs without (Figure 62C) and with (Figure 62D) the CaF_2 protective shell at two different temperatures, 20 and 50°C. In the case without the outer shell, the lifetime of the ion's decays steeply with radial distance, due to their proximity to the surface, which facilitates the energy transfer to the surface quenching defects. As a result, only few Yb^{3+} ions located in the inner part of the shell are less quenched and can participate in the BET processes yielding NPs with scarce temperature sensitivity (Figure 62C). This scenario changes significantly when the protective inert shell is grown. In this case, the proportion of Yb^{3+} ions quenched is drastically reduced due to the distance enlargement to the surface quenchers. Therefore, those Yb^{3+} ions located in the inner part of the shell are highly shielded from quenching effects, exhibiting longer lifetimes and higher thermal sensitivity (Figure 62D).

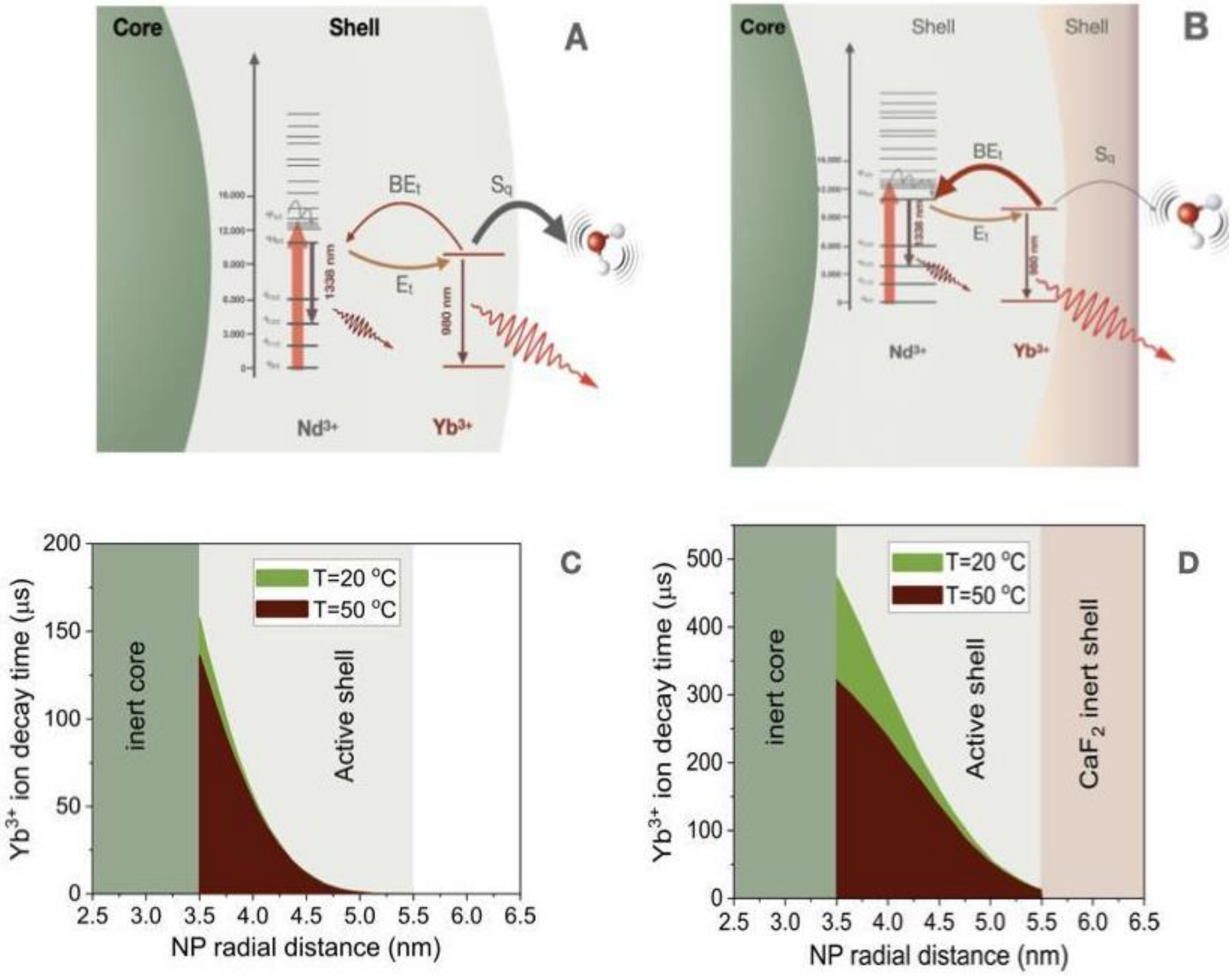

Figure 62. Proposed mechanism of the radiative and non-radiative de-excitation of the Yb^{3+} ions in the absence (**A**) and in the presence (**B**) of an inert shell based on CaF_2. Simulation of the radial distribution of the Yb^{3+} ion decay time for NPs without (**C**) and with (**D**) an outer inert shell at 20 and 50°C.

5.3.7 Conclusions

In this work, we have synthesized different types of NPs based on a α-$NaYF_4$@$NaYF_4$:Nd,Yb structure covered with an outer inert shell of CaF_2. These NPs were parametrically characterized to determine the influence of the architecture of the NPs on their spectroscopic properties. Thus, we evaluated the influence of the absence or presence of the outer inert shell, the thickness of the active middle shell, and the effect of core size and composition. This information was used to develop a model describing the radiative and non-radiative dynamics of Yb^{3+} ions as a function of their localization in the host matrix and the architecture of the NPs.

In this model, the thermally dependent BET is understood as a non-radiative process with a slower rate than other competing non-radiative processes such as surface or host matrix defects. For this reason, any change that leads to a decrease in the nonradiative processes, such as surface- or host-dependent quenching, will also increase the BET probability and thus the thermal sensitivity of the NPs, in addition to increasing the QY. In this sense, we experimentally found that the reduction of surface quenching can be achieved by the growth of a protective and thick outer shell that prevents the energy transfer from Yb^{3+} ions to solvent molecules, capping agents, and so on. On the other hand, the reduction of non-radiative processes associated with host defects can be achieved by using NPs in which the Nd^{3+} and Yb^{3+} ions are enclosed in an active shell. This architecture has been shown to be more efficient (QY =14.1%) than NPs with active cores (QY =8.4%). Overall, the most efficient rare earth NPs can be considered for NIR imaging and nanothermometry.

5.4 Stabilization of Vascular Endothelial Growth Factor (VEGF) using $NaYF_4@Nd^{3+},Yb^{3+}@CaF_2$ Nanoparticles to Increase the Endothelial Cells Proliferation to Enhance The Angiogenesis Process

"La sapienza è figliola dell'esperienza."

Leonardo da Vinci

5.4.1 Abstract

Vascular endothelial Growth Factor (VEGF) works as a signaling protein for endothelial cell recognition that, at the same time, helps to regulate cellular angiogenesis, either by increasing its expression in tissues after cardiovascular accidents or decreasing it in presence of tumors. However, there is a major challenge with VEGF linked to its low stability in biological systems, i.e. it has a short lifetimes effect on organisms. Based on this constraint, the project discussed in this section proposes a nanostructure that stabilizes VEGF-A using lanthanide-based nanoparticles to promote the angiogenesis process in tissues. The strategy to create this nanostructure is based on binding VEGF-A to a $NaYF_4@Nd^{3+},Yb^{3+}@CaF_2$ nanoparticles through a "coupling reaction". In vitro studies were then performed using HUVEC cells, where the VEGF-A-$NaYF_4@Nd^{3+},Yb^{3+}@CaF_2@PAA$ nanocomplex is found, in order to increase endothelial cells' survival and proliferation by 20% compared to the same VEGF-A concentration. Ex vivo experiments were performed in mice that were explicitly genetically engineered to express endothelial cells by changing the color of the fluorophore. The results indicated that the number of endothelial cells increases by 30% when the nanoplatform is used compared to free VEGF. Moreover, the formation of tubular structures was observed, showing the growth of new blood vessels, typically expressed in a successful angiogenesis process.

Keywords: *Lanthanide-Based Nanoparticles, VEGF-A, Angiogenesis, Cardiovascular biology.*

5.4.2 Resumen

El factor de crecimiento endotelial VEGF es un sistema de interés ya que es una proteína señalizadora que juega un papel crucial en el proceso de angiogénesis. Debido a que es un factor para el reconocimiento de células endoteliales y sirve también como como terapia para regular la angiogénesis celular aumentando su expresión en tejidos después de accidentes cardiovasculares o disminuyéndola en tumores. Uno de los principales desafíos con la VEGF es su baja estabilidad en los sistemas biológicos. Es decir, tiene un efecto de corta duración en los organismos. Por esta razón, el objetivo de este proyecto fue desarrollar una nanoestructura que pudiera estabilizar VEGF-A utilizando nanopartículas basadas en lantánidos para promover el proceso de angiogénesis en los tejidos. La estrategia para crear esta nanoestructura fue unir VEGF-A a nanopartículas de $NaYF_4@Nd^{3+},Yb^{3+}@CaF_2$ a través de una "reacción de acoplamiento". Luego se realizaron estudios in vitro usando células HUVEC, donde se encontró que el nanocomplejo VEGF-A-$NaYF_4@Nd^{3+},Yb^{3+}@CaF_2@PAA$ aumenta la supervivencia y proliferación de células endoteliales en un 20 % en comparación con la misma concentración de VEGF-A libre. Se realizaron experimentos ex vivo en ratones manipulados genéticamente para expresar células endoteliales cambiando el color del fluoróforo. Los resultados indican que el número de células endoteliales aumenta un 30% cuando se utiliza la nanoplataforma en comparación con VEGF libre. Además, se observa la formación de estructuras tubulares, mostrando el crecimiento de nuevos vasos sanguíneos, propios de un proceso de angiogénesis exitoso.

Palabras clave: *Nanopartículas basadas en lantánidos, VEGF-A, Angiogénesis, Biología cardiovascular.*

5.4.3 Introduction

Blood vessels are responsible for the proper transport of nutrients and oxygen through the blood, as well as for the proper elimination of waste and CO_2 from the organism. The formation of blood vessels in the embryo is generated as a result of the differentiation *in situ* of angioblasts (undifferentiated cells) into endothelial cells, which then form a network of tubular structrures; this process is called vasculogenesis.[259] In contrast, blood vessels in adult tissues mainly emerge from existing ones. This process is called angiogenesis and occurs mainly during the growth of a tissue, where the sprouting of new blood vessel branches is necessary for the enlargement of the circulatory system.[260] This type of sprouting also appears during development, inflammation, wound healing, or cancer growth.[261]

Figure 63 presents a schematic representation of the angiogenesis, starting with the sprouting of new capillaries from pre-existing vessels and ending with the maturation and stabilization of the newly formed vessels, as a result of a physiological or a pathological process.[262] Several pathologies can be associated with imbalances along the process.

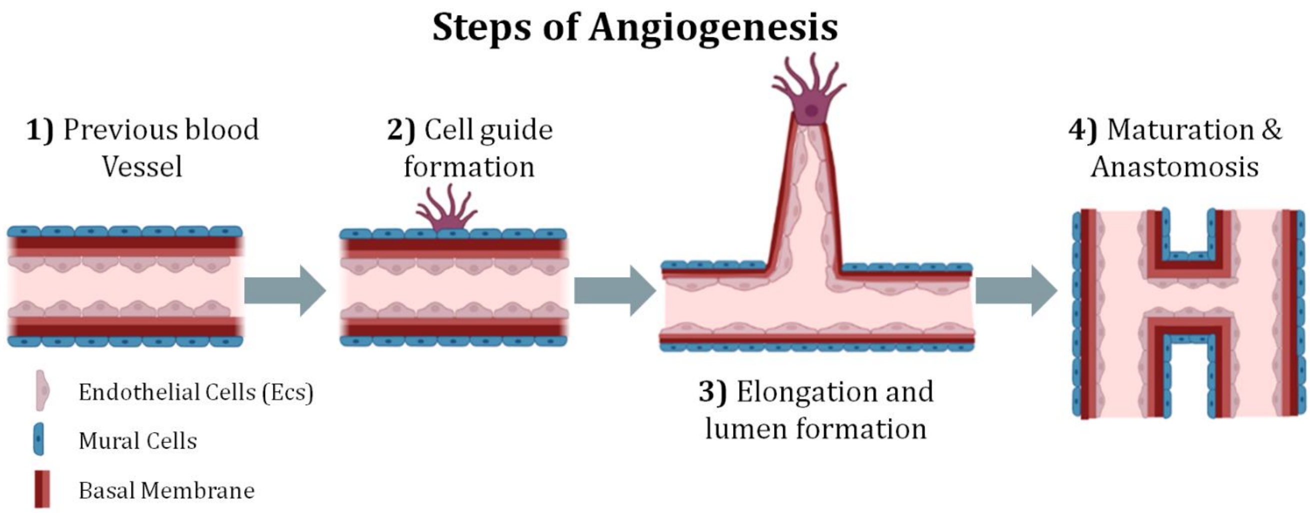

Figure 63. Steps of Angiogenesis. Sprouting represents the first phase of angiogenesis. Subsequent steps include the recruitment of mural cells and the return of ECs to a quiescent state.

An excess of angiogenesis could be associated with solid tumor growth considering that the abnormal enlargement of these tissues, and the vascular network that supports it, have slow and inefficient blood flow that does not meet metabolic demands. [259,263] Currently, most efforts are focused on finding an antiangiogenic therapy that may support treatment for cancerous tumors. In 2005, the FDA approved Avastin, an antiangiogenic therapy consisting of a specific antibody against VEGF.[264] Nevertheless, a comprehensive analysis of the angiogenesis is not only important for cancer treatment. In some tissues, such as the heart, the process of angiogenesis is inefficient, especially after a cardiovascular accident when the damaged tissues are less likely to regenerate.[265] The role of angiogenesis in cardiovascular diseases is still not fully understood, but it is known that the VEGF plays a crucial role in this process.

VEGF is a signaling protein that appears in muscle tissue after a long period of cellular hypoxia. During these phases, HIF factor (hypoxia-inducible factor-1) is overstimulated and produces pro-angiogenic factors such as VEGF. There are several different isoforms of this growth factor (VEGF A [isoforms 165, 121, 189], B, C, D, and E) which are produced by different gene splicing and have different biological functions.[266] VEGF-C and VEGF-D are primarily implicated in regulation of lymphangiogenesis[267], given the dominant role of VEGF-A in the regulation of the angiogenesis.[268] VEGF-A are secreted mitogens with high specificity for endothelial cells and promote proliferation, migration, and survival of these cells, and their vascular permeability.[269]

Several studies show that expression of VEGF in muscle increases the number of blood vessels by stimulating proliferation of endothelial cells, migration and smooth muscle recruitment.[262,270] *In vivo* studies, such as the one of Feng *et al.* in rats have shown that the administration of VEGF-A, after a few minutes of reoxygenation, leads to a significant reduction in brain lesions after stroke.[271], or Hendel *et al.*, also demonstrated the efficacy of VEGF in humans by showing a significant improvement in exercise capacity with VEGF.[272] These studies suggest that this protein is a therapeutic target with great potential for the treatment of cardiovascular diseases. However, the results of clinical trials of VEGF delivery to the myocardium have generally been discouraging, and research studies have failed to demonstrate substantial improvements in patients compared to placebo control groups.

Many of these studies were based on intravenous infusion or intracoronary administration of the recombinant protein.[273] Some of the negative results were attributed, at least in part, to the short-lived effect and high instability of the protein when it is injected. Intravenous administration of VEGF is limited by its short in vivo lifetime (~30 minutes) and total dose by off-target toxicity issues.[274] In the case of myocardial ischemia, the amount of VEGF after systemic administration found within the ischemic region is minimal and does not last longer than one day.[275] To solve this problem, different types of systems have been tested, i.e., scaffolds,[276–278] gels,[279,280] fibers,[281] PLGA nanoparticles[282,283] and hyaluronic acid/chitosan nanoparticles,[284,285] etc. In the case of nanoparticles, a strong enhancement of the therapeutic angiogenic effect of VEGF *in vivo* was observed. To promote endothelial cell proliferation and angiogenesis, we developed a nanosystem based on lanthanide-based nanoparticles linked to VEGF-A to improve stability and increase the lifetime of the VEGF in endothelial cell and in vivo too.

5.4.4 Objectives

5.4.4.1 Overall Objective

Enhance endothelial cell proliferation using VEGF-A-$NaYF_4$@$NaYF_4$:$Nd^{3+}_{60\%}$,$Yb^{3+}_{20\%}$@CaF_2@PAA nanostructure in HUVEC cell and in animal model.

5.4.4.2 Specific Objective

- Synthesize and characterize $NaYF_4$@ $NaYF_{4:}Nd^{3+}{}_{60\%}$,$Yb^{3+}{}_{20\%}$@$CaF_2$ nanoparticles
- Functionalize the surface of $NaYF_4$@ $NaYF_{4:}Nd^{3+}{}_{60\%}$,$Yb^{3+}{}_{20\%}$@$CaF_2$ nanoparticles with polyacrylic acid.
- Link the $NaYF_4$@$Nd^{3+}{}_{60\%}$,$Yb^{3+}{}_{20\%}$@CaF_2@PAA with the VEGF-A
- Perform cytotoxicity test of VEGF-A-$NaYF_4$@ $NaYF_{4:}Nd^{3+}{}_{60\%}$,$Yb^{3+}{}_{20\%}$@$CaF_2$@PAA nanostructure in human umbilical vein endothelial cells
- *In-vitro* studies of cell proliferation using VEGF-A-$NaYF_4$@ $NaYF_{4:}Nd^{3+}{}_{60\%}$, $Yb^{3+}{}_{20\%}$@CaF_2@PAA nanostructure in human umbilical vein endothelial cells
- *In vivo* studies of VEGF-A-$NaYF_4$@ $NaYF_{4:}Nd^{3+}{}_{60\%}$,$Yb^{3+}{}_{20\%}$@$CaF_2$@PAA nanostructure in AplnCreER mice.

5.4.5 Experimental Section

5.4.5.1 Synthesis of VEGF-A-$NaYF_4$@$Nd^{3+}{}_{60\%}$,$Yb^{3+}{}_{20\%}$@CaF_2@PAA nanostructure

As first step, the synthesis of the nanoparticles with the core/shell/shell $NaYF_4$@Nd^{3+}60%,$Yb^{3+}{}_{20\%}$@CaF_2 structure was performed. These are the same nanoparticles described in the previous chapter (5.3). The α-$NaYF_4$ core was synthesized according to the methodology described in Section 4.3.6, the $NaYF_4$@$Nd^{3+}{}_{60\%}$,$Yb^{3+}{}_{20\%}$ core/shell according to Section 2.3.7, and the $NaYF_4$@$Nd^{3+}{}_{60\%}$,$Yb^{3+}{}_{20\%}$@CaF_2 core/shell/shell according to Section 4.3.8. Once the nanoparticles were characterized, their surface was functionalized with polyacrylic acid to achieve two goals: a) to impart hydrophilic properties to the nanoparticles and allow their dissolution in aqueous media, and b) to promote that OH^- serves as a platform for protein binding. The procedure is described in the section 4.3.9. Finally, the recombinant human VEGF-A 165 protein was linked to the nanoparticles by a two-step coupling reaction (see section 4.3.10).

5.4.5.2 Characterization Methods

Transmission electron microscopy (TEM) was performed using a JEM 1010 microscope (JEOL, Japan; 80 kV) equipped with a digital camera (Olympus, Megaview II). A Malvern Nano-ZS instrument was used to measure the ζ-potential. To determine the crystalline phase, a powder X-ray was acquired using a PANalytical Model X'Pert PRO MPD Multi-Purpose Diffractometer, and the measurement was made from 10° to 70°. FT-IR spectrums were carried out using a Nicolet IR 200 spectrometer. We used a TGA/DSC-1 820 from Mettler Toledo for the thermogravimetry analysis, working under an air atmosphere. The determination of the actual concentration of VEGF-A bound to the surface of the nanoparticles was performed by a Western blot method described in section 4.4.3 Fluorescence images were acquired with Leica inverted fluorescent microscope equipped with Leica DFC450 C camera using LAS V4.4 software (Leica Microsystems), Nikon Eclipse Ti-E inverted fluorescent microscope equipped with DC-152Q-C00-FI using NIS V4.30 software (Nikon) and Zeiss Laser Scanning microscope. Images were acquired at 4x or 20x magnification. Individual 4x magnification fields were stitched together using Image Composite Editor software (Microsoft Research).

5.4.5.3 *In-vitro* studies of Cell Proliferation in Human Umbilical Vein Endothelial Cells

After the isolation of endothelial cells from the umbilical cord of newborns, the cytotoxicity tests of nanoparticles in these cells were performed. The procedure for the cytotoxicity tests is described in section 4.4.1 of the Materials & Methods chapter. Once the ideal concentration of the nanosystem VEGF-A-$NaYF_4@Nd^{3+}_{60\%},Yb^{3+}_{20\%}@CaF_2@PAA$ was determined, we examined its effect on endothelial cell proliferation compared to free VEGF. The procedure is described in Sect. 4.4.1. Cell proliferation experiments were performed 24, 36, 48, and 120 hours after addition of the nanocomplex. In all cases, nanoparticle concentrations of 10 ug/mL and 200 ug/mL were used. As a positive control, 10 ng of free VEGF-A was used. To monitor cell proliferation at the time of addition of the nanosystem, 10 uL (1:100) of ethynyl-labelled deoxyuridine (5-EdU) was also added. At the end of the cell proliferation experiments, cells were fixed according to the method described in section 4.4.2. and the images were acquired using a fluorescence inverted microscope. Images were processed (contrast enhancement by brightness/contrast regulation) and analyzed using Fiji software (NIH, Bethesda). Three or more experiments per condition were analyzed, with at least 15 images acquired per sample.

Statistical analysis was performed using Excel and GraphPad Prism 7.0. Mean and standard error were calculated for all the datasets. Unpaired student's T-test and One-Way ANOVA with Student-Newman-Keuls correction were used to determine statistical significance for the normally distributed datasets, whereas non-normally distributed datasets were analyzed by ANOVA on ranks and Mann-Whitney U test. A p-value <0.05 was considered significant.

To determine the actual concentration of VEGF on the surface of VEGF-A-$NaYF_4@Nd^{3+}_{60\%},Yb^{3+}_{20\%}@CaF_2@PAA$ NPs, a western blot was performed to generate a calibration curve with known VEGF concentrations. Samples were prepared by first lysing the proteins according to the protocol described in section 4.4.3. Electrophoresis was then performed in 10% polyacrylamide gels with a SDS/MOPS 10X running buffer at 180 V for 20 minutes. The transfer buffer was prepared with 25 mM Tris, 192 mM glycine and 20% MtOH. Proteins were transferred to a PVDF membrane (GE Healthcare, #10600015) at 350 mA for 30 minutes. After transfer, the membranes were incubated with Immobilion® Solution 1X for 1 hour at RT. Membranes were then incubated overnight at 4°C with the anti-VEGFR2 antibody, followed by a 1-hour incubation at room temperature with the secondary antibody, polyclonal goat anti-rabbit IgG (H+L) HRP (1:2000; Invitrogen, #31460). Western blots were developed using the SuperSignal West Dura kit (Thermoscientific, #34577). Images were acquired using Biorad Chemidoc Touch and quantified using Biorad software.

5.4.5.4 In vivo studies using AplnCreER mice

Animal studies were conducted in accordance with the guidelines described in the section 4.4.4. Adult AplnCreER6 mice were crossed with Rosa26-mT/mG mice to obtain AplnCreER; Rosa26-mT/mG animals. To activate Cre-mediated recombination, 4-hydroxytamoxifen was dissolved in corn oil and injected intraperitoneally. To label proliferating cells, 5-ethynyl-20-deoxyuridine (EdU) was administered intraperitoneally. Mice were anaesthetized with 1% isoflurane for intramuscular injections. The nanocomplex was injected into the tibia of the mice under different conditions. Tamoxifen was then administered for 7 days. The health of the mice was monitored daily, and at the end of the experiment, the mice were anaesthetized with 5%

isoflurane and euthanized by cervical dislocation. After extracting the muscle, it was fixed according to the procedure in section 4.4.5. Images were acquired using an inverted fluorescence microscope. Images were processed (contrast enhancement by brightness/contrast adjustment) and analyzed using Fiji software (NIH, Bethesda). A minimum of three experiments per condition were analyzed, with at least 5 images taken per sample. Statistical analysis was performed using Excel and GraphPad Prism 7.0. Mean and standard error were calculated for all data sets. Unpaired Student's T-tests and one-way ANOVA with Student-Newman-Keuls correction were used to determine statistical significance for the normally distributed datasets, while non-normally distributed datasets were analyzed using ANOVA on ranks and Mann-Whitney U-test. A p-value < 0.05 was considered significant.

5.4.6 Results

5.4.6.1 Morphology and Characterization of VEGF-$NaYF_4@Nd^{3+}_{60\%},Yb^{3+}_{20\%}@CaF_2@PAA$

Based on the results of the chapter 5.3, nanoparticles with a core-shell-shell structure in the ratio 0.5/1/0.5 were synthesized, as they have the best optical and morphological properties. Figure 64 shows the images obtained from the synthesized nanoparticles by TEM. The core of α-$NaYF_4$ has an average size of 7.5± 0.1 nm, whereas the core/shell $NaYF_4@Nd^{3+}_{60\%},Yb^{3+}_{20\%}$ structure increases to 11.2±0.1 nm, reaching an active shell thickness of 1.9 nm. Finally, when the CaF_2 layer grew, nanoparticles with a diameter of 14±0.3 nm were obtained. As shown in Figure 64A, all the structures are monodisperse, without any aggregates, which is consistent with the reports from Tan *et al.*[241]. Figure 64C shows the measured X-ray diffraction patterns of the core $NaYF_4$, core/shell $NaYF_4$@ $NaYF_4:Nd^{3+}$, Yb^{3+} and core/shell/shell $NaYF_4$@ $NaYF_4:Nd^{3+}$, $Yb^{3+}@CaF_2$ nanoparticles, the results demonstrate that the core, the core/shell, and the core/shell/shell nanoparticles all have a cubic phase corresponding to the typical fluorite structure. As the shell grow in the nanoparticles, an increase in the crystallinity of the structure is also observed. The Figure 64B shows the emission spectrum corresponding to $NaYF_4$@ $NaYF_4:Nd^{3+}$, Yb^{3+} and $NaYF_4$@ $NaYF_4:Nd^{3+}$, $Yb^{3+}@CaF_2$ NPs under 808 nm continuous wave (CW) optical excitation. The emission spectrum is mainly constituted by the broadband emission of Yb^{3+} ions expanding from 950 up to 1100 nm.[286]

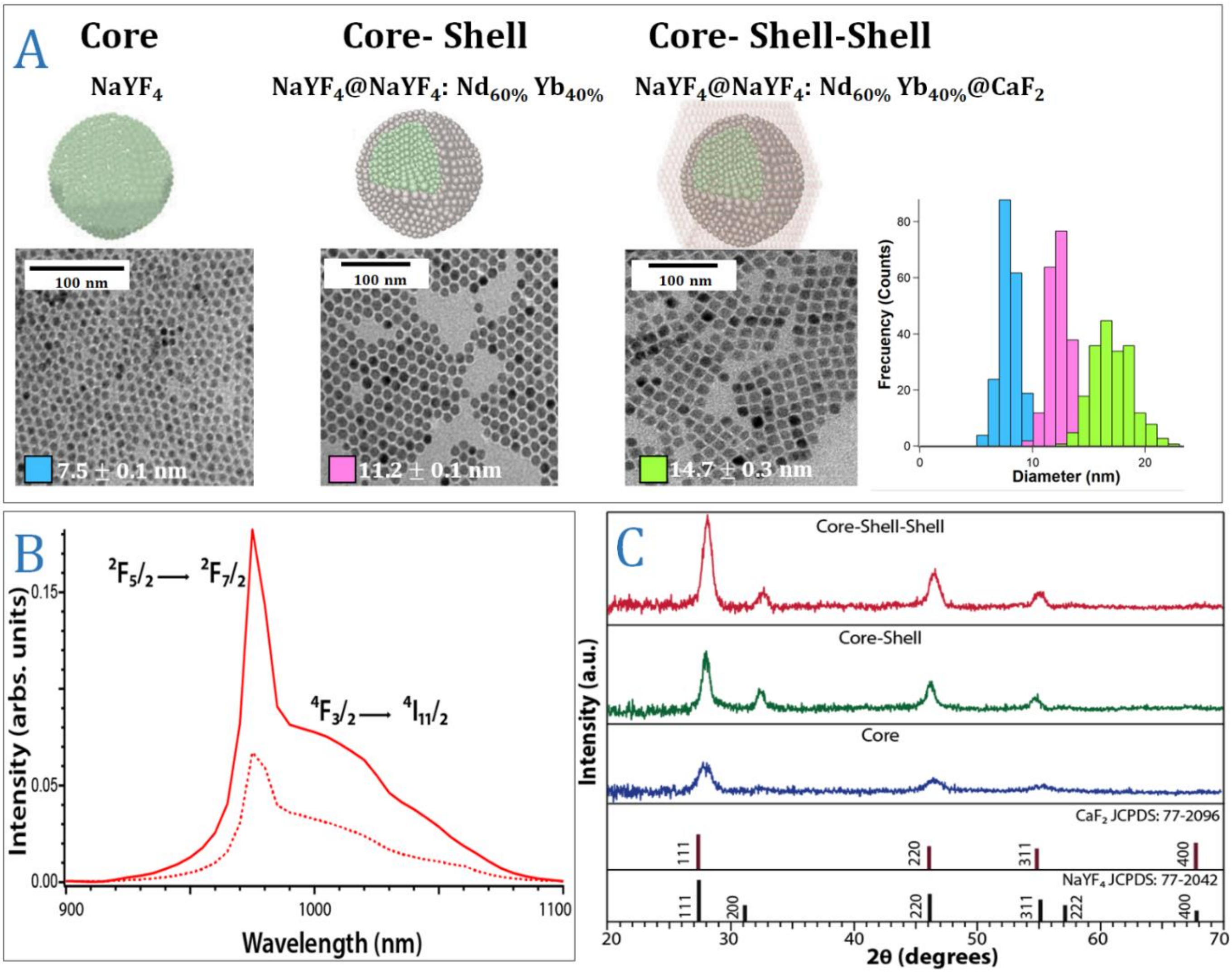

Figure 64. **A)** Schematic representation of the nanoparticles used, accompanied by TEM images of the core, core-shell, and core-shell shell. The distribution of sizes is shown in the histogram. Cyan for core, pink for core/shell/shell, and light green for core/shell/shell. **B)** Emission spectra at 800 nm, red dots correspond to the core/shell structure and the red line belongs to the core/shell/shell nanoparticles. **C)** Measured XRD patterns of core (blue line), core/shell (green line) and core/shell/shell (red line). The standard diffraction patterns of the two cubic phases $NaYF_4$ (JCPDS:77-2042) and CaF_2 (JCPDS 77-2096) are included for refrerence.

To impart hydrophilic behavior to the nanoparticles and enable their dispersion in aqueous media, as well as to serve as a functional platform for their subsequent functionalization with the VEGF-A. (Figure 65A). A full characterization of $NaYF_4$@ $NaYF_4$:Nd^{3+}, Yb^{3+}@CaF_2 NPs PAA can be found in Figure 65. The FTIR spectrum (Figure 65D) The stronger peak at 1720 cm^{-1}, corresponding to the stretching mode of the C=O group in the PAA-functionalized nanoparticles compared to the untreated nanoparticles, confirms the successful ligand exchange. The bands at 3420, 1450 and 1560 cm^{-1} originate from the asymmetric and symmetric vibrations of the C-O-H in the carboxyl group. The peak at 1415 cm^{-1} may be present from the carboxyl groups of the PAA, which do not coordinate with the metal ions on the surface of the nanoparticles.[241] The absorption bands at 2960 and 2928 cm^{-1} are from the asymmetric and symmetric stretching modes of the $-CH_2$ group. These bands decrease after PAA modification, indicating that the number of $-CH_2$ groups on the nanoparticle surface was reduced, which complements the evidence for an appropriate surface modification. When the PAA shell covers the NPS surface, the overall charge of the solution must be negative due to the COO^- ions, as shown by the ζ-potential with a value of -25mV for a solution in water. Figure 65B shows the TEM images where monodisperse nanoparticles with a size of 17±1nm can be seen, i.e., the average size of the PAA layer is about 3±1nm.

Thermogravimetric analyses were performed to determine the amount of PAA on the surface of $NaYF_4$@$NaYF_4$:Nd^{3+}, Yb^{3+}@CaF_2 NPs. The results (Figure 65C) show that 15% corresponds to the total mass of the polyacrylic acid layer. To confirm the binding between the protein and the nanoparticles, the z-potential (+15 mV) was determined by changing the surface charge for the amino acids present in VEGF-A from negative to positive.

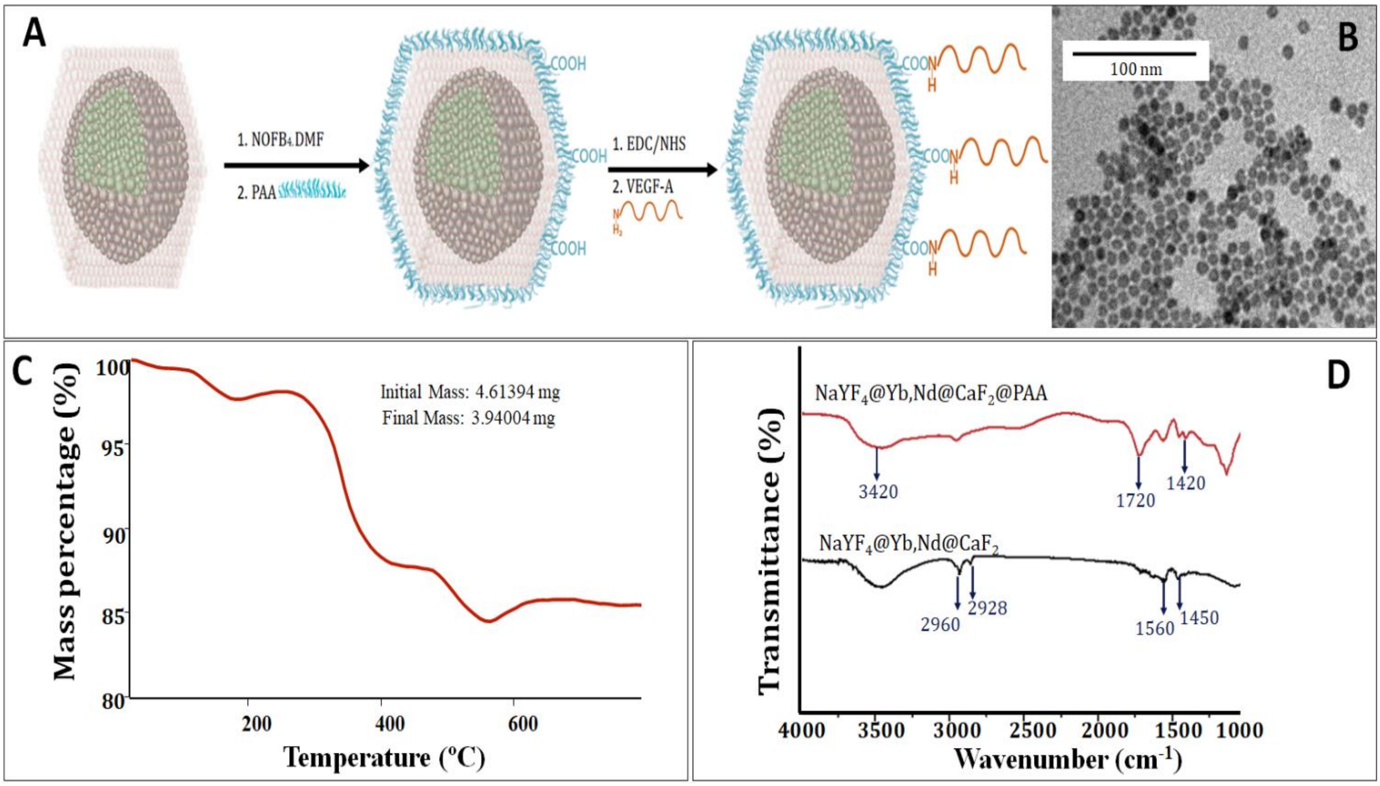

Figure 65. **A)** Schematic representation of functionalization of nanoparticles with VEGF. **B)** TEM image of NPS functionalized with polyacrylic acid, average size 17±1 nm. **C)** Spectro-TGA, 85% inorganics and 15% organics. **D)** FTIR spectra of representative nanoparticles before and after PAA modification.

5.4.6.2 *In-vitro* studies of Cell Proliferation in Human Umbilical Vein Endothelial Cells

To test the potential application of the $NaYF_4$@$NaYF_4$:Nd^{3+},Yb^{3+}@CaF_2 NPs, *in vitro* cytotoxicity assessment was studied in HUVEC cells, which were incubated the $NaYF_4$@$NaYF_4$:Nd^{3+},Yb^{3+}@CaF_2@PAA Nps in different concentrations between 0.1-5 mg/mL for 24 h at 37°C, according with similar previous works reported.[287,288] The viability of the untreated HUVEC cells was set as 100%, and the viability of the NPs-treated HUVEC cells was calculated. Cell viability is greater than 80% when the concentration of below to 1000 μg/mL Figure 66A. At higher concentrations it is observed that the viability of the cells decreases, on the images, it is seen that the cells look sick. It is concluded that the proper range for in vitro experiments is between 100 and 500 ug/ml. Figure 66B.

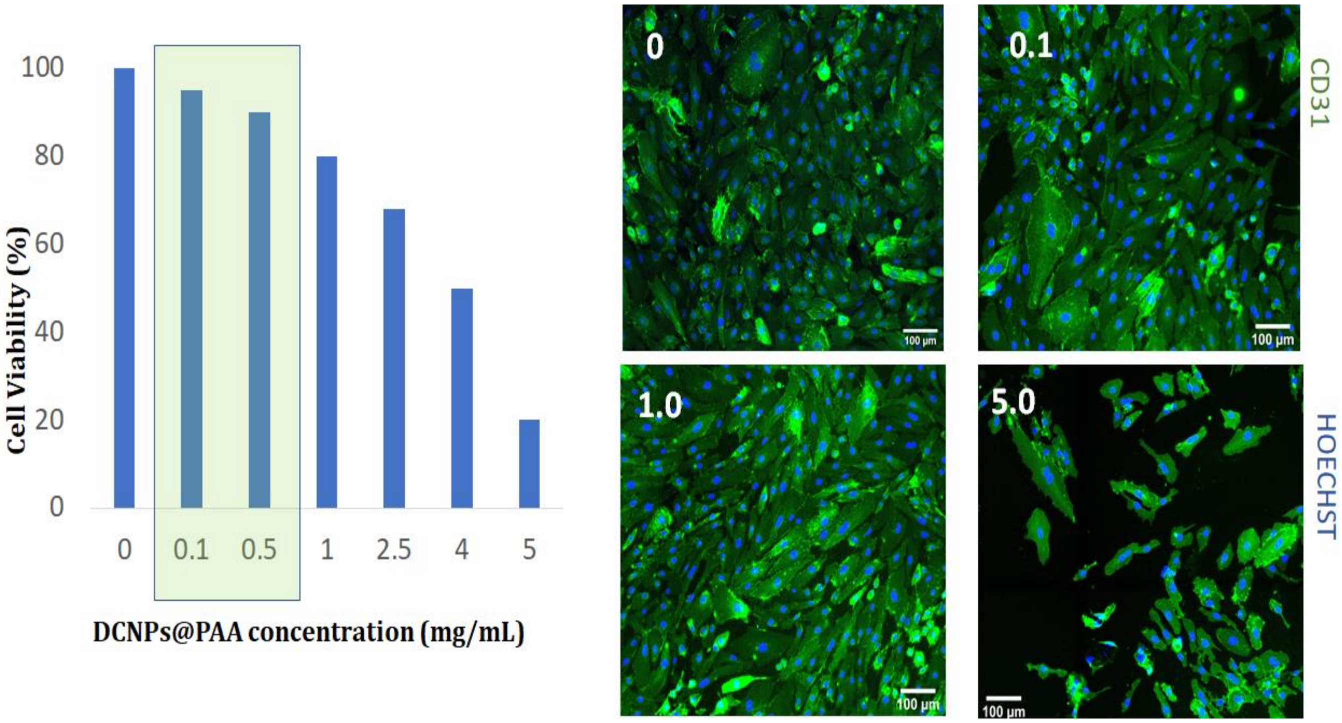

Figure 66. **A)** *In vitro* cell viability of HUVEC cells incubated with different concentrations of NaYF$_4$@NaYF$_4$:Nd^{3+},Yb^{3+}@CaF$_2$ NPs for 24 hours. **B)** Immunofluorescence staining of endothelial cells with CD31 (green) for endothelial cells and HOECHST (blue) for nuclei.

The results of cell proliferation of HUVEC cells after 24 hours of incubation and without additional factors promoting survival and proliferation are shown in Figure 67*.* Endothelial cells without treatment showed a survival rate of 55% and proliferation of 35% (Figure 67A), whereas cells with free VEGF showed a survival rate of only 60% and proliferation of 45% (Figure 67B). Addition of nanoparticles without VEGF decreased the survival rate to 50% and proliferation was much lower at about 30%. (Figure 67C). In contrast, the cells incubated with the nanocomplex showed increased survival and proliferation rates. The cells added with 10 µg/ml of the nanocomplex survived 70% and proliferated 55% (Figure 67D), and the cells added with 50 µg/ml of nanocomplex survived 78% and proliferated 60% (Figure 67E). When the concentration of nanocomplex was increased to 200 µg/ml, cell survival increased to 88% and proliferation increased to 66% (Figure 67F), resulting in a 30% increase in proliferation of endothelial cells compared with VEGF-free cells. (Figure 67G). The results on cell viability in HUVEC cells are consistent with previous reports in the literature on metallic VEGF-NPs systems, in which cell viability ranges from 85 to 100% at a range of similar concentrations and always below 1000 µg/mL.[289,290] Regarding the increase in cell proliferation, no similar studies were found with metal- or rare earth-based nanoparticles. However, studies with PLGA nanoparticles and hyaluronic acid/chitosan nanoparticles showed an increase in cell proliferation of HUVEC cells due to the stabilization of VEGF by the nanoparticles compared with free VEGF, increasing the lifetime from 30 minutes to hours and even days.[282–285]These results may suggest that the 30% increase in cell proliferation with our nanosystem is due to the stabilization of VEGF induced by the nanoparticles, which increases the lifetime within the cell culture and consequently leading to higher survival, proliferation, and migration.

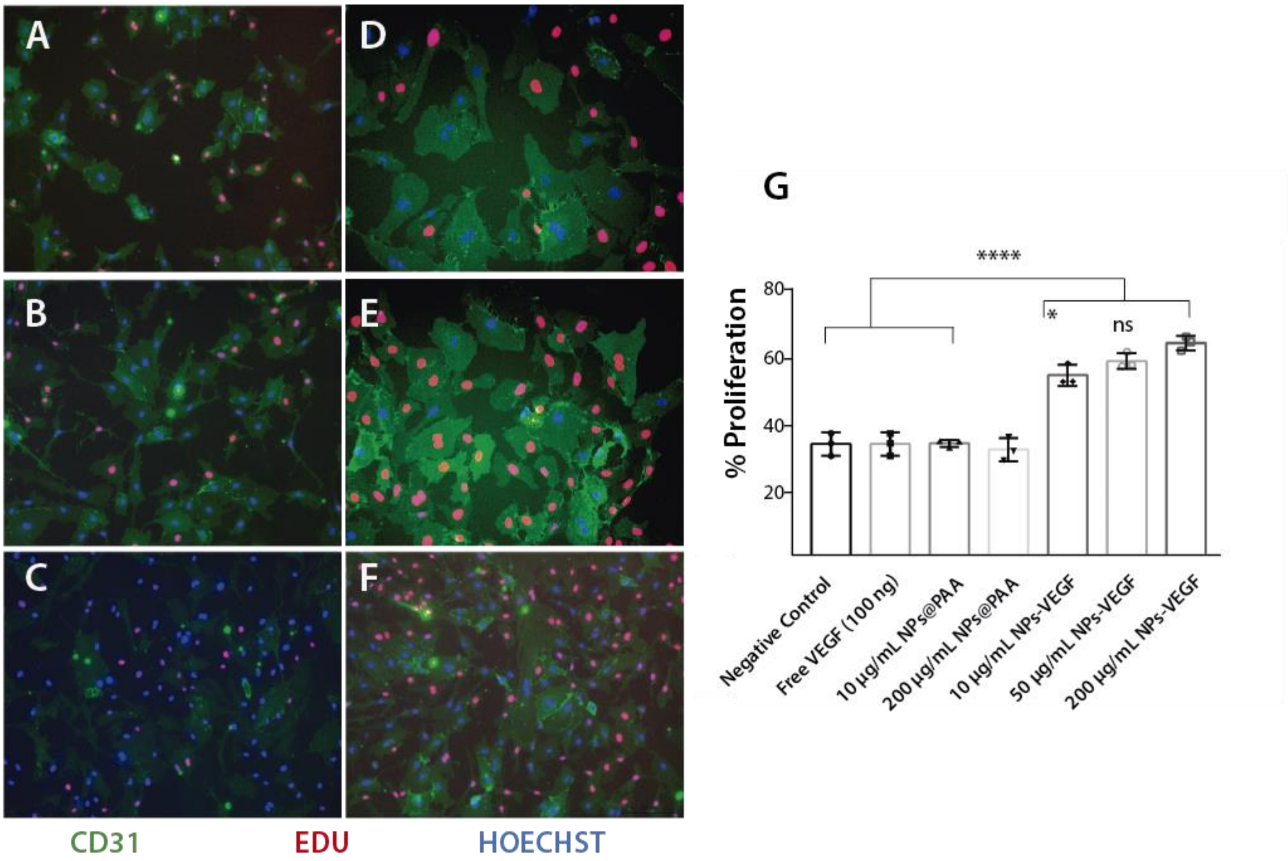

Figure 67. **A-F** Representative immunofluorescence analysis of HUVEC cells treated with the nanocomplex and kept in culture for 24 h and stained for CD31 (green), EdU (red), and with the nuclear dye Hoechst (blue). **A)** Negative Control **B)** positive control, free VEGF (100 ng) **C)** 200 μg/mL of $NaYF_4@NaYF_4:Nd^{3+},Yb^{3+}@CaF_2@PAA$ Nanoparticles **D)** 10 μg/mL of VEGF-nanocomplex **E)** 50 μg/mL of VEGF-nanocomplex **F)** 200 μg/mL of VEGF-nanocomplex. **G)** Quantification of proliferating cells at different conditions. All data are shown as mean ± S.E.M. Statistical significance was determined using a one-wayANOVA followed by Dunnett's multiple comparison test, $*P < 0.05$, $****P < 0.0001$.

To determine the therapeutic effect of the nanocomplex on cell proliferation during the time, HUVEC cells were cultured with 200 μg/ml of the nanocomplex for different times (24 h, 36, 72, 120 h) as the same conditions showed above. The results of proliferation of HUVEC cells after different times of incubation and without additional factors promoting survival and proliferation are shown in Figure 68. In all cases, cells were analyzed by confocal fluorescence microscopy. Morphology served as an indicator of their health status during the experiments, and survival (blue areas) and proliferation (red areas) rates were calculated based on the quantification of the number of cells and the results are shown in the Figure 69.

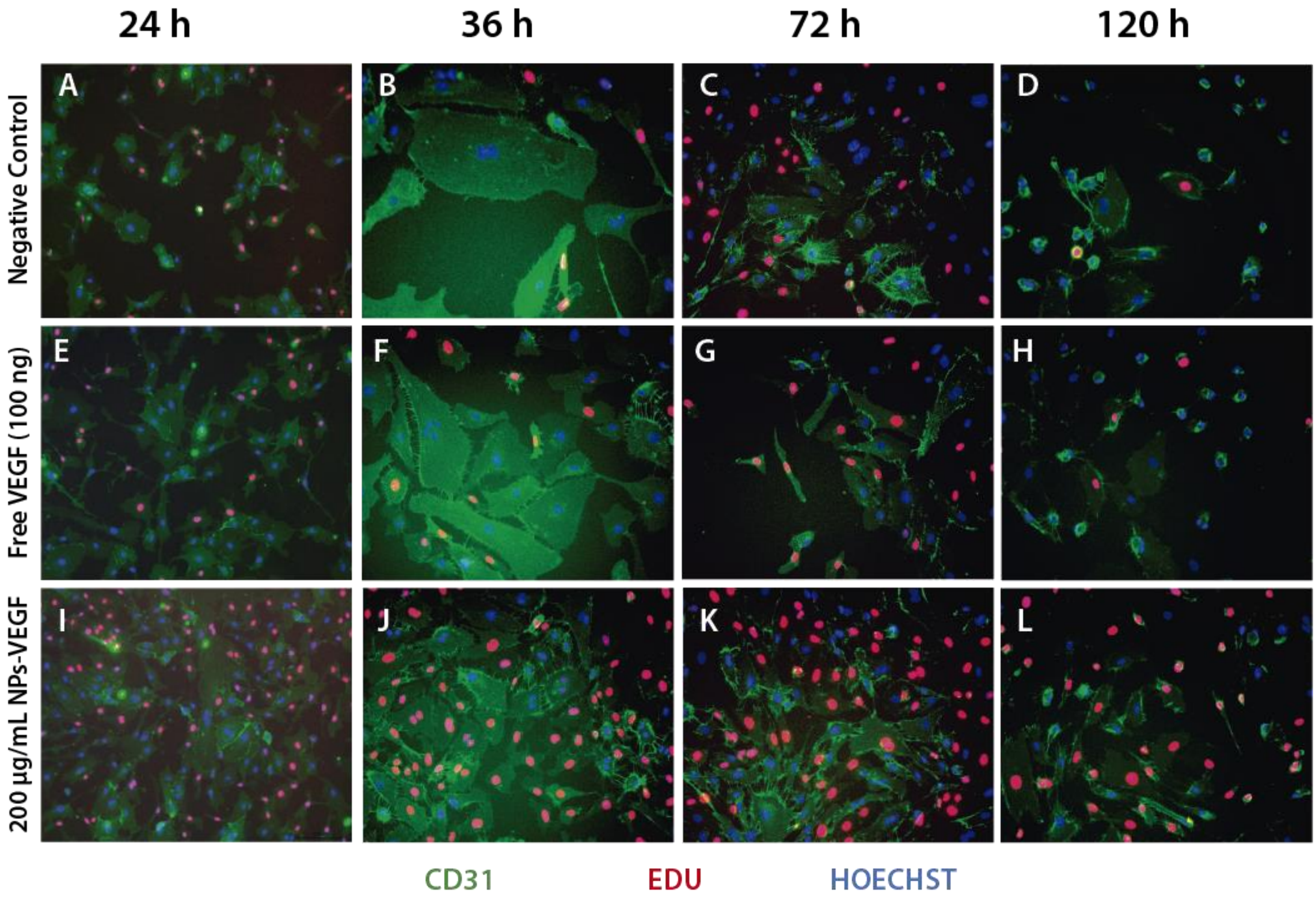

Figure 68. **A-L** Representative immunofluorescence analysis of HUVEC cells treated with the nanocomplex and kept in culture for different times and stained for CD31 (green), EdU (red), and with the nuclear dye Hoechst (blue). **A-D** Negative control (untreated cells), **E-H** positive control, free VEGF (100 ng), **I-L** 200 µg/mL of VEGF-nanocomplex (VEGF-$NaYF_4@NaYF_4:Nd^{3+},Yb^{3+}@CaF_2@PAA$). **A,E,I,** corresponding to experiments into 24h. **B,F,J** 36h. **C,G,K** 72h, **D,H,L** 120 h.

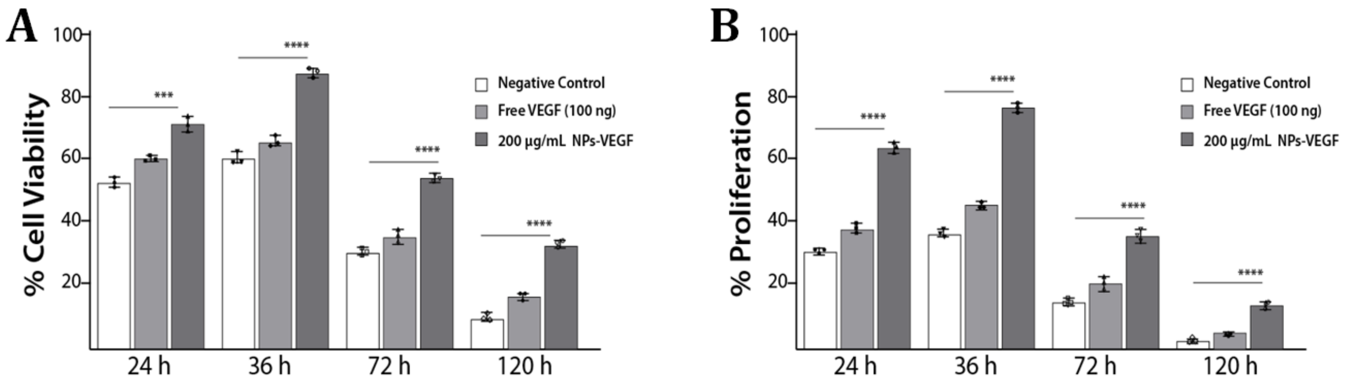

Figure 69*.* Quantification of cell viability and proliferating cells at different times. White bars negative control (untreated cells), light gray corresponds to Free VEGF 100 ng, dark gray corresponds to 200 µg/ml of VEGF-$NaYF_4@NaYF_4:Nd^{3+}$, $Yb^{3+}@CaF_2@PAA$. **A). %** Cell Viability at different times. **B).** % Cell Proliferation at different times. All data are shown as mean ± S.E.M. Statistical significance was determined using a one-way ANOVA followed by Dunnett's multiple comparison test, *P < 0.05, ****P < 0.0001.

These results suggest that all cases reach the maximum viability and proliferation of cells after 36 hours of incubation (88% and 75%, respectively), after that time it decreases significantly. (Figure 68B,F,J). Cell viability continues be higher over time when the nanocomplex is present in the cell culture, even after 120 hours when viability is about 30%, compared to the effect of free VEGF, which is 18%, corresponding to an improvement of 60% (Figure 69). In cell proliferation, an increase of 57% is observed in the presence of the nanocomplex compared to the effect of free VEGF. These results indicate that the stabilizing effect of the nanoparticles is not only an immediate effect, but also lasts for a longer period and their effects are noticeable.

To verify whether the effect on the improvement of viability and proliferation is an effect of stabilization of VEGF due to the nanoparticles and not an effect of the increase of VEGF concentration, the concentration of VEGF bound to the surface of the 200 μg nanoparticles was determined, the results are shown in Figure 70.

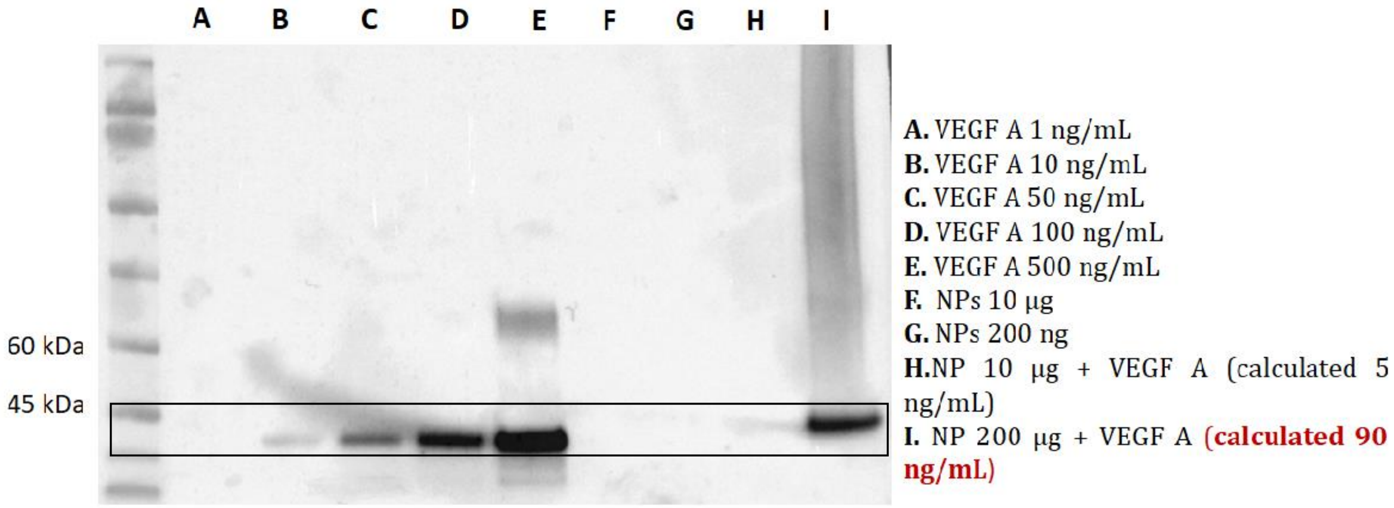

Figure 70. Western blotting showing the concentration of the VEGF (≃45 kDa) on the surface, Channels A-E belongs to the calibration curve. . Free-VEGF at 1 ng/mL. **B.** Free-VEGF at 10 ng/mL. **C.** Free-VEGF at 50 ng/mL. **D.** Free-VEGF at 100 ng/mL. **E.** Free-VEGF at 500 ng/mL. Channels **F,G** negative control $NaYF_4@NaYF_4:Nd^{3+},Yb^{3+}@CaF_2@PAA$ without VEGF. **F.** 10 μg of nanoparticles. **G.** 200 μg of nanoparticles. Channels. **8,9** concentrations of nanoparticles using in the HUVEC cells experiments. **8.** 10 μg VEGF-$NaYF_4@NaYF_4:Nd^{3+},Yb^{3+}@CaF_2@PAA$. **9.** 200 μg VEGF- $NaYF_4@NaYF_4:Nd^{3+},Yb^{3+}@CaF_2@PAA$.

According to the results in Figure 70, it was found that the concentration of VEGF in 200 ug of the surface was 90 ng. This means that even though 10% less VEGF is present in the cell culture, its activity increases cell viability by 20% and cell proliferation by 30% due to the presence of nanoparticles. A prolongation of therapeutic time stimulated by the nanoparticles, which confirms the stabilizing effect of the nanocomplex.

5.4.6.3 In vivo studies using AplnCreER mice

Following the results obtained in HUVEC cells with the enhancement of cell proliferation, we decided to study how the nanocomplex could affect the angiogenesis process in vivo. The stimulation of angiogenesis in mice was investigated using the documented ability of Apln-CreER; R26mT/mG mice to label sprouting endothelial cells, we implanted our nanocomplex into their tibialis anterior. The mechanism providing foundations to the endothelial cell labelling is shown in Figure 71.

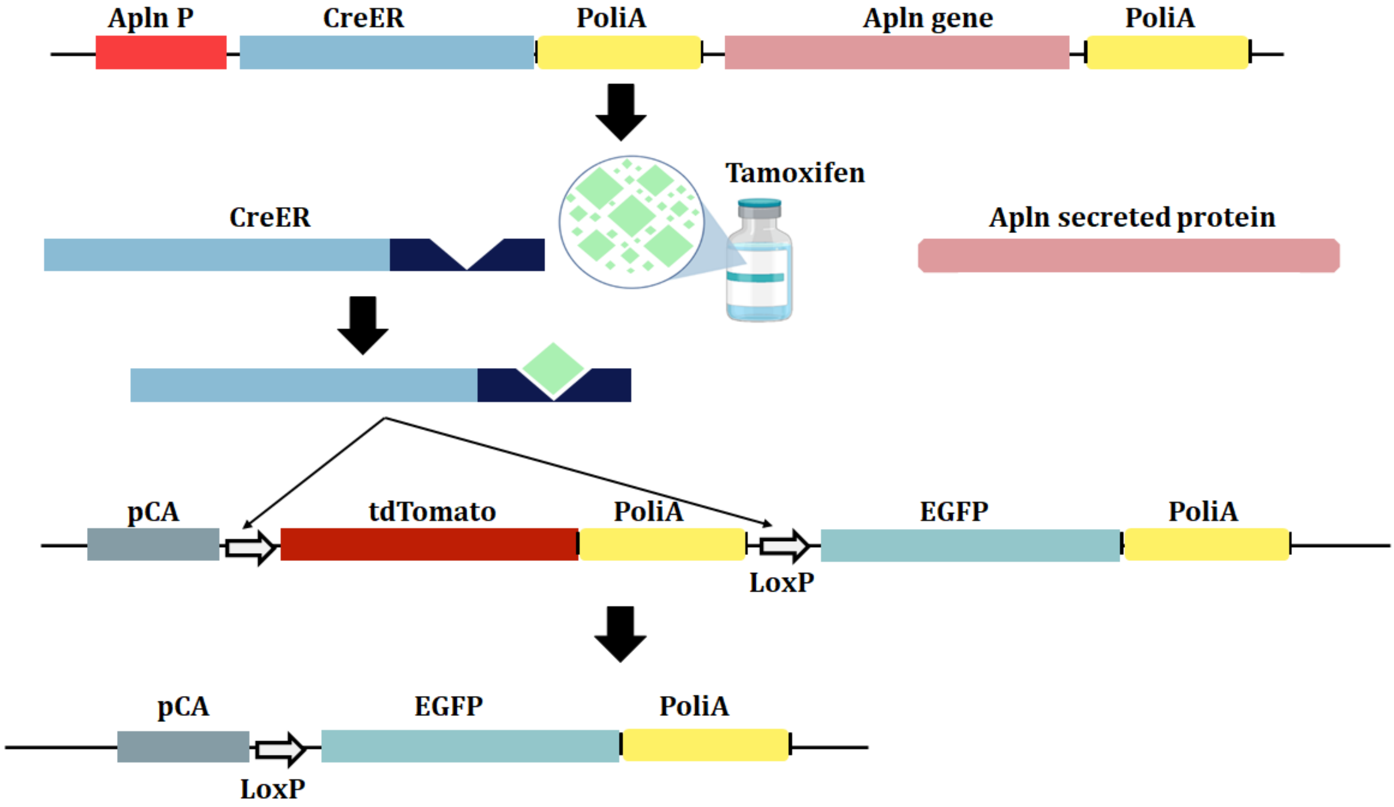

Figure 71. Genomic organization and functional explanation of the operation of the genetic tool (AplnCre:mT/mG). First, activation of the Apln promoter (Apln P) is required. Downstream of the Apln promoter, the inducible Cre recombinase (CreER) is expressed together with the Apln protein. Only in the presence of hydroxytamoxifen (Tam.), Cre recombinase is activated and acts on LoxP target sequences (LoxP). In the Rosa26 locus, a membrane-tagged tdTomato protein is continuously expressed under the control of a pCA promoter. The tdTomato coding sequence is flanked by two LoxP sequences. Cre-mediated recombination generates a recombinant cell in which only EGFP is expressed in the Rosa26 locus after excision of the tdTomato sequence. The Apln promoter and the following construct are located on the X chromosome and are derived from AplnCreER:Rosa26-tdTomato, while the second sequence on chromosome 6 is inserted into the Rosa26 locus of the reporter mouse.

Apelin (Apln) is a secreted protein abundantly expressed by vascular ECs during embryonic development. During the adult life, Apln expression is significantly reduced, but during sprouting angiogenesis, triggered by hypoxia, Apln expression is reactivated. The Apln gene encodes for 77 amino acid peptides, which binds Apelin receptor (AplnR or APJ), a G-coupled protein receptor with seven transmembrane domains. The Apln-APJ signaling acts downstream of VEGFR2 activation, particularly in hypoxic conditions, and is highly expressed by capillary of endothelial cells. Studies in the mouse retina and zebrafish showed that EC proliferation is reduced in the absence of either Apln or APJ, indicating that Apln on the tip cells interacts with APJ receptor to regulate vessel growth in a paracrine fashion.[291] Apln-APJ signaling in stalk cells induce proliferation through mTOR activation, which is essential for EC proliferation.[291]

On the other hand, Cre is a 38kDa bacteriophageP1 recombinase that mediates site-specific recombination between LoxP sites consisting of a short asymmetric sequence.[292] The Cre-LoxP system is widely used to study cellular and molecular functions *in vivo*. This recombination results in loss of function or gain of function of the gene depending on the LoxP-flanked sequence.[293–295] Loss of function is achieved by placing two LoxP sites to disrupt the coding sequence of the gene of interest, while gain of function can be achieved by removing a LoxP-flanked STOP sequence that normally blocks expression of a construct downstream. [293–295] In addition, it is possible to act on a reporter gene by removing the coding sequence for a fluorescent protein, thereby blocking its expression by the recombinant cells, or allowing expression of a different sequence downstream,[294,295] as in the system used in this project.

Tissue-specific expression of Cre can be achieved by placing the sequence encoding Cre recombinase under the control of a tissue-specific promoter. [293–295] In this way, Cre is expressed whenever the promoter is active. However, Cre recombinase activity is not always necessary or may be undesirable (e.g., during morphogenesis) because it could affect the viability of the transgenic animal or render the reporter useless for studying a relevant biological process in adulthood. To overcome this limitation, an inducible form of Cre (CreER or CreERT) is usually used. This form of Cre recombinase must bind tamoxifen to enter the nucleus and act on its targets. Therefore, CreER induces genetic recombination only after administration of tamoxifen (or 4-hydroxytamoxifen for in vivo applications).[295]

In our case, we injected AplnCreER mice with our nanocomplex under the conditions indicated in Table 5. Tamixofen was then administered between days 1 and 4. Mice were sacrificed on days 7 and 21 after injection, and angiogenesis was examined by cofocal fluorescence microscopy.

Table 5. Different conditions used in in vivo experiments. In all conditions, tests were performed in triplicate.

Name	Conditions	Free VEGF (ng/g)	VEGF-NPs (μg/g)	NPs (μg/g)
Negative Control	NPs without VEGF	--	--	200
Positive Control	Free VEGF	100	--	--
NPs+ non conjugated VEGF-A	NPs without VEGF+ Free VEGF	100	--	200
NPs+VEGF (Conjugated)	VEGF-NPs	--	200	--

As mentioned earlier, active endothelial cells express abundant apelin, implying that apelin expression is activated in response to an angiogenic stimulus (as expected from the nanocomplex). To analyze the effect of our compound on the angiogenesis process, a genetic lineage model was used. In this model, the tamoxifen-inducible form of CreER is expressed under the control of the Apln promoter (Figure 71). When these mice are crossed with mTmG reporter mice, activation of Cre leads to a switch from red to green fluorescence specifically in budding endothelial cells. Under different conditions, the angiogenic response is followed by quantification of the endothelial cells present in the tissue. The results obtained under each condition studied are shown in Figure 72, and their quantification is shown in Figure 73.

The results show that the angiogenic response with the nanocomplex (VEGF-NPs) after a 7-day injection increases cell proliferation by 37% compared to the response of tissue cells injected with VEGF alone and by 62% compared with the endothelial cells of the tissue injected with the nanoparticles without VEGF on the surface (13%). The therapeutic effect of the nanocomplex on angiogenesis is also confirmed when the results are compared with the addition of nanoparticles and VEGF, free in solution and not bound to the surface. In this case, the increase in cell proliferation thanks to the nanocomplex is about 40%.

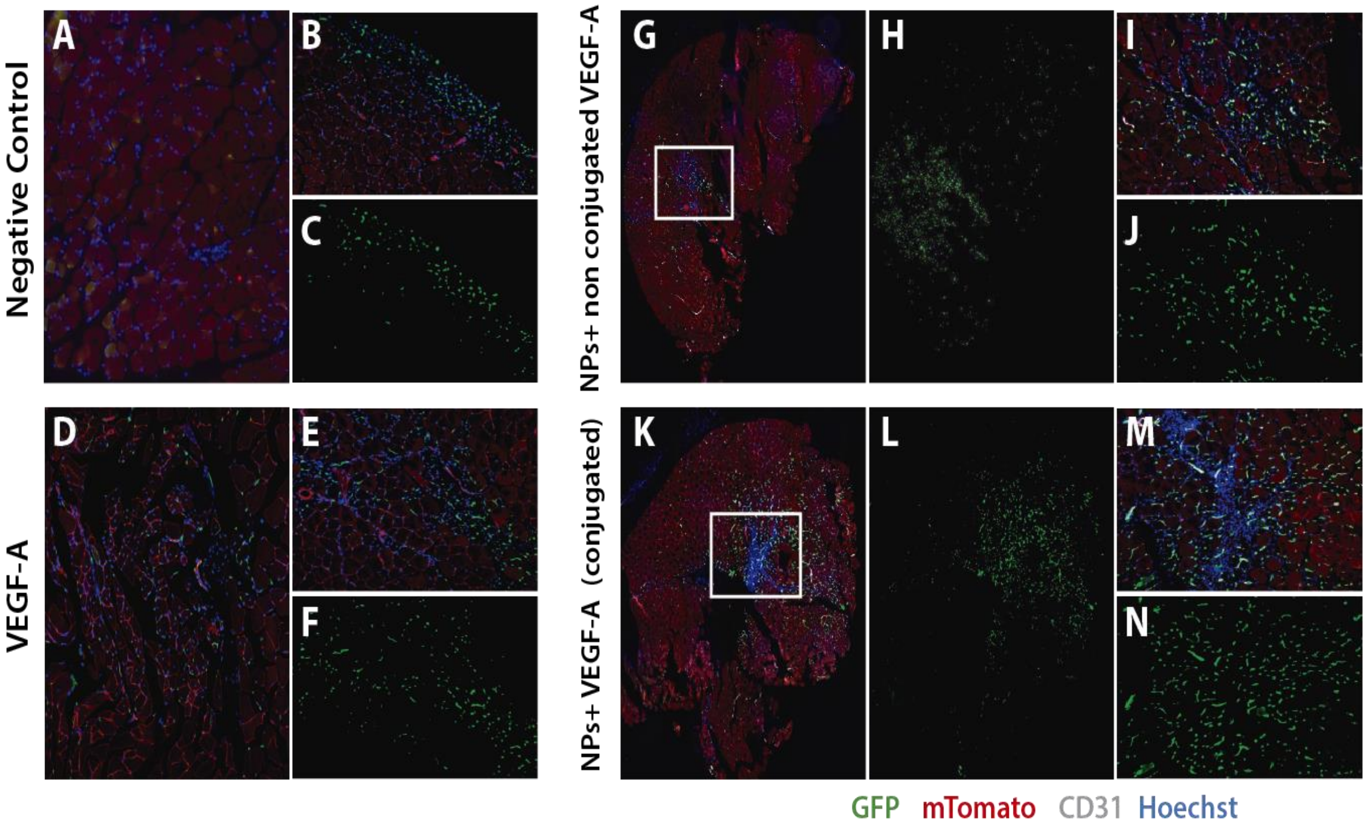

Figure 72. Representative inmunofluorescence images of angiogenesis sprouting *in vivo* after 7 days. **A-C.** Negative control (tibials injected with just NaYF$_4$@NaYF$_4$:Nd^{3+},Yb^{3+}@CaF$_2$@PAA NPs without VEGF). **D-F** Positive control (10 ng/g of Free VEGF). **G-J.** NaYF$_4$@NaYF$_4$:Nd^{3+},Yb^{3+}@CaF$_2$@PAA NPs+ non conjugated VEGF (200µg/g & 10 ng/g respectively). **K-N**. 200 µg/g of VEGF-NaYF$_4$@NaYF$_4$:Nd^{3+},Yb^{3+}@CaF$_2$@PAA. **B,E,I,M** are zoom of the images. **C,F,L,N** images taken to express the Apln. Apln-EdU (green), dTomato (red), CD31 (white) and nuclei were stained with nuclear marker dye Hoechst (blue).

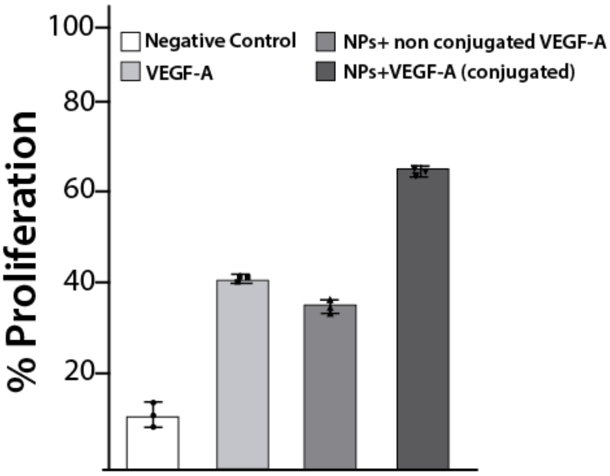

Figure 73. Quantification of cells expressing Apln-EdU was performed. All data are shown as mean ± S.E.M. Statistical significance was determined using a one-way ANOVA followed by Dunnett's multiple comparison test, $^*P < 0.05$, $^{****}P < 0.0001$

The process of angiogenesis not only involves the formation of new vessels by proliferation of endothelial cells at an early stage after exposure to VEGF, but these new vessels must also mature and be functional. For successful pro-angiogenic therapy, it is necessary that the effect of cell proliferation of ECs remains constant for some time. For this reason, another study following the same mechanisms followed before was performed, but the mice were sacrificed after 21 days to observe the efficacy of the therapy over a longer period. The results are shown in Figure 74, and the quantification is presented in Figure 75.

The results showed that the long-term effect of VEGF stabilized by nanoparticles is slightly higher compared to the one of VEGF alone. These two show a slight increase (10%) in the proliferation of endothelial cells compared to negative controls, which may indicate an effective therapeutic effect.

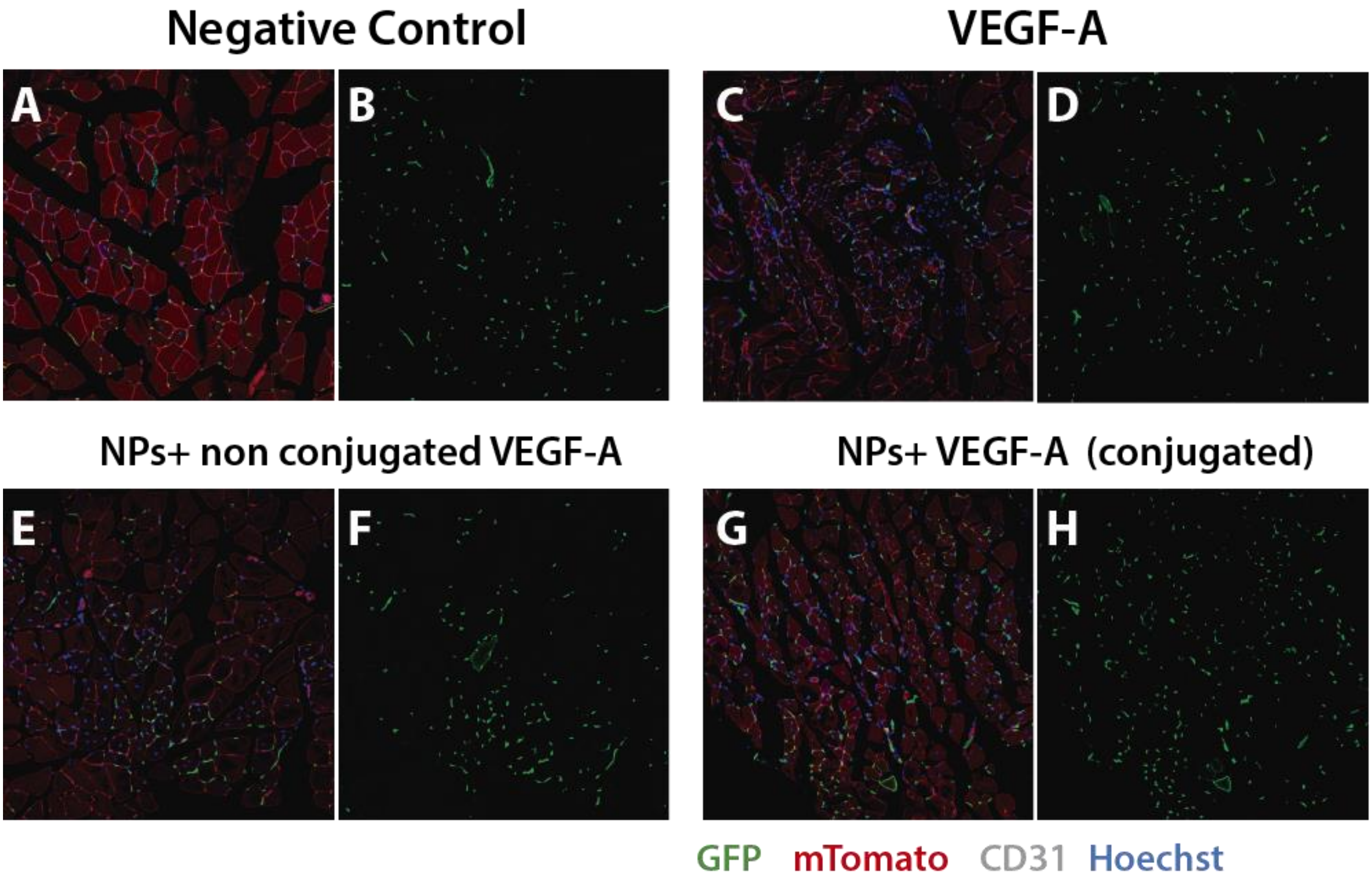

Figure 74. Representative inmunofluorescence images of angiogenesis sprouting *in vivo* after 21 days. **A-B.** Negative control (tibials injected with just $NaYF_4@NaYF_4:Nd^{3+},Yb^{3+}@CaF_2@PAA$ NPs without VEGF). **C-D** Positive control (10 ng/g of Free VEGF). **E-F.** $NaYF_4@NaYF_4:Nd^{3+},Yb^{3+}@CaF_2@PAA$ NPs+ non conjugated VEGF (200µg/g & 10 ng/g respectively). **G-H** 200 µg/g of VEGF-$NaYF_4@NaYF_4:Nd^{3+},Yb^{3+}@CaF_2@PAA$. **B,D,F,H** images taken to express the Apln. Apln-EdU (green), dTomato (red), CD31 (white) and nuclei were stained with nuclear marker dye Hoechst (blue).

This 10% increase in cell proliferation at 21 days is like previous studies with other systems (ref, ref), but the VEGF concentration used is two and three times higher in each case. Our nanosystem has the advantage of achieving the same results with a lower VEGF concentration. A future perspective is to study the same effects by increasing the concentration of the nanosystem and to perform studies trying to inject the nanosystem regularly to develop a therapy to improve the angiogenesis process in vivo.

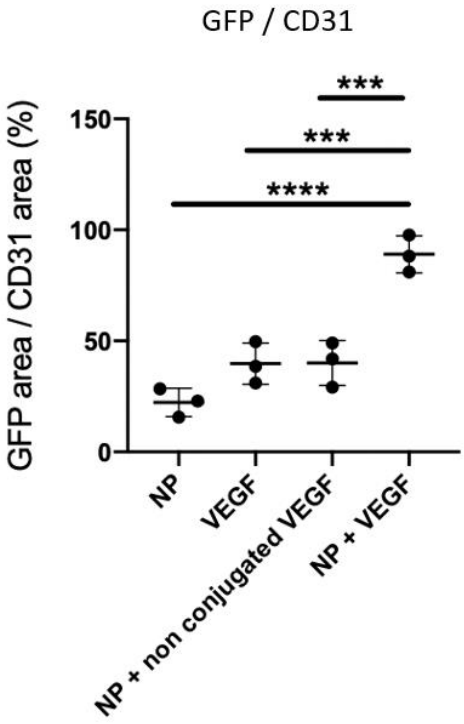

Figure 75. Quantification of cells expressing GFP/CD31 was performed. All data are shown as mean ± S.E.M. Statistical significance was determined using a one-way ANOVA followed by Dunnett's multiple comparison test, $*P < 0.05$, $****P < 0.0001$

5.4.7 Conclusions

The effect of using rare earth nanoparticles on stabilizing VEGF and enhancing endothelial cell proliferation in vitro in HUVEC cells and in vivo in AplnCreER mice. For this purpose, a nanosystem consisting of $NaYF_4@NaYF_4:Nd^{3+}, Yb^{3+}@CaF_2@PAA$ nanoparticles surface-bound with VEGF was designed. In vivo, it is observed that the influence of the nanosystem increases cell survival at 40-60% compared with the cells with free VEGF and cell proliferation between 15-30%, depending on the concentration of the nanoparticles. These increases are due to the stabilization of VEGF thanks to the action of the nanoparticles and a possible controlled release of VEGF in the cells, increasing the viability of VEGF compared to the tests performed with free VEGF. It was also confirmed that this effect is achieved by the nanosystem and not by an increase in protein concentration, since the concentration of VEGF bound to the surface of the nanoparticles is 10% lower than that used as a control in this study.

As for in vivo studies, we were performed with genetically modified mice expressing proliferation of endothelial cells by changing the cell color from red for endothelial cells that do not proliferate to green for cells that are in the process of proliferation. After injection of our nanosystem, it was observed that after 7 days, there was an increase 37% in cell proliferation in the mice injected with the nanosystem compared with the mice injected with VEGF alone. This again suggests that the use of rare earth nanoparticles increases the stabilization of VEGF and enhances its effect over a longer period. It was also observed that greater cell proliferation persisted after 21 days thanks to the nanosystem, but this was not higher than in other studies using other types of carriers for VEGF. Finally, as an outlook for the future, it is proposed to systematically study how an injection of the nanosystem for several days affects cell proliferation to observe the effect of angiogenic therapy over time.

6. General Conclusions

GENERAL CONCLUSIONS

The following is a summary of the main conclusions that can be drawn from this work:

1. The influence of dopant concentration on the UCL and DCL properties of rare earth nanoparticles at different excitation intensities has been studied experimentally and theoretically. In particular, the luminescence emissions of β-NaYF$_4$:Yb^{3+}/Er^{3+} nanoparticles were investigated, varying the ratio of Yb^{3+}/Er^{3+} dopants (22% in total) between 0 and 10. In both cases (UCL and DCL), the light intensity increases exponentially when the ratio of Yb^{3+}/Er^{3+} increases from 0 to 2. Thereafter, the increase is not as significant, with the highest light intensity being reached at a ratio of 4. The influence of Yb^{3+}/Er^{3+} ratios on the emission processes UC was also studied. It was found that at low ratios, between 0 and 1, the dominant process is ESA, while at higher ratios the dominant process is ETU.
2. A new method was developed to address the adverse effects on optical properties associated with the transfer of rare earth nanoparticles into aqueous or biological media for biomedical applications. A dual strategy was designed to coat β-NaYF$_4$:Yb^{3+}/Er^{3+} nanoparticles with a hydrophobic polymer such as polystyrene and/or methyl methacrylate, first replacing the oleates on the surface of the nanoparticles with MPD and then growing a robust HPS layer around the surface of the NPs. Effective and durable protection was achieved in aqueous media under extreme conditions, such as: low concentrations of NPs, high temperatures, dilutions in media with high concentrations of phosphates.
3. The influence of rare earth nanoparticle architecture on spectroscopic properties was determined. Different types of α-NaYF$_4$@NaYF$_4$:Nd,Yb@CaF$_2$ nanoparticles were synthesized and the influence of the presence of a protective layer, the thickness of the active layer, and the effect of the core composition were evaluated. The results showed that the CaF$_2$ protective layer increased the light intensity, quantum yield, lifetime, and thermal sensitivity compared to NPs without this protection. In addition, it was found that the most efficient NPs are those with all Yb^{3+}, Nd^{3+} ions inside the active layer with a thickness of about 2 nm, since there is a better distribution of ions, which improves all spectroscopic properties.
4. A new rare earth nanoparticle-based complex that can increase endothelial cell proliferation in vivo and in vitro has been synthesized and could be used as a potential pro-angiogenic therapy. A nanosystem was developed in which VEGF was linked to nanoparticles of NaYF$_4$@ NaYF$_4$: Nd,Yb@CaF$_2$. The results showed a higher cell survival rate of 20-30% compared to free VEGF and an increase in HUVEC cell proliferation by 15%. In addition, a 37% increase in cell proliferation was observed in mouse models after 7 days of injection.

7. Conclusiones Generales

CONCLUSIONES GENERALES

A continuación, se presenta un resumen de las conclusiones más importantes que pueden ser extraídas de este trabajo de tesis:

1. Se estudió experimental y teóricamente la influencia de la concentración de dopantes en las propiedades de UCL y DCL de nanopartículas de tierras raras a diferentes intensidades de excitación. En particular se estudió las emisiones luminiscentes de nanopartículas de β-NaYF$_4$:Yb^{3+}/Er^{3+} variando el ratio de los dopantes Yb^{3+}/Er^{3+} (22% en total) entre ratios de 0 a 10. En los dos casos (UCL Y DCL) la intensidad lumínica crece exponencialmente al aumentar el ratio entre Yb^{3+}/Er^{3+} desde 0 hasta 2, posteriormente el incremento no es tan significativo registrando la mayor intensidad lumínica en ratios de 4. También se estudió la influencia de los ratios de Yb^{3+}/Er^{3+} en los procesos de emisión UC y se observó que a ratios bajos, entre 0 y 1, el proceso que predomina es el ESA mientras que a ratios mayores el proceso dominante es el ETU.

2. Se desarrolló una nueva metodología para resolver los efectos adversos, en las propiedades ópticas, asociados con la transferencia de las nanopartículas de tierras raras en medios acuosos o biológicos, para ser utilizadas en aplicaciones biomédicas. Se diseñó una estrategia dual para recubrir nanopartículas de β-NaYF$_4$:Yb^{3+}/Er^{3+} con un polímero hidrofóbico de poliestireno y/o metilmetacrilato, primero sustituyendo los oleatos de la superficie de las nanopartículas con MPD y posteriormente creciendo una capa robusta de HPS que rodee la nanopartícula. Se logró una protección efectiva y duradera en medios acuosos bajo condiciones extremas como: bajas concentraciones de NPs, altas temperaturas, diluciones en medios con altas concentraciones de fosfatos.

3. Se determinó la influencia de la arquitectura de las nanopartículas de tierras raras en las propiedades espectroscópicas. Se sintetizaron diferentes tipos de nanopartículas α-NaYF$_4$@ NaYF$_4$: Nd,Yb@CaF$_2$ y se evaluó la influencia de la presencia de una capa protectora, el grosor de la capa activa y el efecto de la composición del núcleo. Los resultados mostraron que la capa protectora de CaF$_2$ incrementa la intensidad lumínica, el rendimiento cuántico, los tiempos de vida y la sensibilidad térmica frente a las NPs que no tienen está protección. Adicionalmente se observó que las NPs más eficientes son las que poseen todos los iones de Yb^{3+}, Nd^{3+} dentro de la capa activa con un grosor de 2 nm aproximadamente ya que hay una mejor distribución de los iones mejorando así todas las propiedades espectroscópicas.

4. Se sintetizó un nuevo complejo basado en nanopartículas de tierras raras capaz de aumentar la proliferación de células endoteliales *in vivo* e *in vitro* y que puede ser utilizado como posible terapia pro-angiogénica. Se diseñó un nanosistema anclando la VEGF a nanopartículas de NaYF$_4$@ NaYF$_4$: Nd,Yb@CaF$_2$ que reporta una tasa de supervivencia celular mayor entre el 20-30% comparado con la VEGF libre, también los resultados muestran un aumento de la proliferación de células HUVEC en un 15% y un aumento de la proliferación celular del 37% en modelos de ratón luego de 7 días de inyección.

8. Publications & Congress

PUBLICATIONS & CONGRESS PUBLICATIONS

8.1 Peer-view Articles

8.1.1 Publications derived from this work.

- Diego Mendez-Gonzalez, Vivian Torres Vera, Irene Zabala Gutierrez, Concepción Cascales-Sedano, Enrique López-Cabarcos, Jorge Rubio-Retama, Óscar G. Calderón, Sonia Melle, Marco Laurenti. "*Upconverting nanoparticles in aqueous media: not a dead-end road. Avoiding degradation by using hydrophobic polymer shells*". Small, **2022**, (18), 2105652.
- Vivian Torres Vera, Diego Mendez-Gonzalez, Diego J. Ramos, Asmae Igalla, Marco Laurenti, Rafael Contreras-Caceres, Enrique Lopez-Cabarcos, Elena Díaz, Jorge Rubio-Retama, Sonia Melle, and Oscar G. Calderón. "*Effect of dopant concentration and excitation intensity on the upconversion and downconversion emission of β-*$NaYF_4$*:*Yb^{3+}*,*Er^{3+} *nanoparticles*". J. Mater. Chem. C, **2021** (9), 8902-8911.
- Hamraoui Khouloud, Torres Vera Vivian, Zabala Gutierrez Irene, Casilllas-Rubio Alejandro, Benayas Antonio, Marin Riccardo, Natile Martha, Manso Silvan Miguel, Rubio-Zuazo Juan, Melle Sonia, Jaque Daniel, Caledron G. Oscar, Rubio-Retama Jorge. "*Rational Design of Rare-Earth Nanothermometers with Complex Core@Shell@Shell Architecture*" **Submitted article**.
- Torres Vera Vivian, Vuerich Roman, Cauteruccio Matteo, López-Cabarcos Enrique, Zacchigna Serena, Rubio-Retama Jorge. *"Stabilization of Vascular Endothelial Growth Factor (VEGF) using* $NaYF_4$*@*Nd^{3+}*,*Yb^{3+}*@*CaF_2 *Nanoparticles to Increase the Endothelial Cells Proliferation to Enhance The Angiogenesis Process*". **Article in writing process**

8.1.2 Other Publications

- Alicia Ortega-Rodríguez, Yingli Shen, Irene Zabala Gutierrez, Harrison D. A. Santos, Vivian Torres Vera, Erving Ximendes, Gonzalo Villaverde, José Lifante, Christoph Gerke, Nuria Fernández, Oscar G. Calderón, Sonia Melle, José Marques-Hueso, Diego Mendez-Gonzalez, Marco Laurenti, Callum M. S. Jones, Juan Manuel López-Romero, Rafael Contreras-Cáceres, Daniel Jaque, and Jorge Rubio-Retama. "*10-Fold Quantum Yield Improvement of Ag2S Nanoparticles by Fine Compositional Tuning*". ACS Applied Materials & Interfaces **2020** 12 (11), 12500-12509.
- Yingli Shen, José Lifante, Erving Ximendes, Harrison D.A. Santos, Diego Ruiz, Beatriz H. Juárez, Irene Zabala Gutiérrez, Vivian Torres Vera, Jorge Rubio Retama, Emma Martín Rodríguez, Dirk H. Ortgies, Daniel Jaque, Antonio Benayas and Blanca del Rosal. "*Perspectives for Ag2S NIR-II nanoparticles in biomedicine: from imaging to multifunctionality*". Nanoscale, **2019** 11, 19251-19264.

8.2 Congress presentation

- “Stabilization of VEGF to enhance the angiogenesis process in Cardiac Tissue" **NALS 2022**. (26-29 April 2022) Santander, Spain. **Oral presentation.**
- "Detection of Brain Tumors by Exploiting the Thermal Sensitivity Using Nanoparticles" **NALS 2022.** (26-29 April 2022) Santander, Spain. **Poster presentation.**
- "Avoiding degradation of upconverting nanoparticles in aqueous media by using hydrophobic polymer shells" **Upcon 2020**. (6-9 April 2021) Compiègne, France. **Oral presentation.**
- "Effect of dopant concentration and excitation intensity of UC and DC emission of ß-$NaYF_4$:Yb^{3+},Er^{3+} NPs" **Upcon 2020.** (6-9 April 2021) Compiègne,France. **Poster presentation.**
- “Avoiding degradation of upconverting nanoparticles in aqueous media by using hydrophobic polymer shells”. **ECIS 2019** 33rd Conference of The European Colloid and Interface Society (8-13 Sep 2019). Leuven, Belgium. **Oral presentation.**
- “UCNPS of $NaYF_4$: Yb^{3+}/Er^{3+}: The relationship between the ratio of the dopants and the size, luminescence and lifetimes.” **ECIS 2019** 33rd Conference of The EuropeanColloid and Interface Society (8-13 Sep 2019). Leuven, Belgium. **Poster presentation.**

9. Bibliography

BIBLIOGRAPHY

(1) Cohen, I. B. A History of Luminescence From the Earliest Times Until 1900. By E. Newton Harvey. [Memoirs of the American Philosophical Society, Volume 44]. (Philadelphia: The Society. 1957. Pp. Xxiv, 692. $6.00.). *Am. Hist. Rev.* **1958**, *63* (4), 937–939. https://doi.org/10.1086/ahr/63.4.937.

(2) Ronda, C. R. Emission and Excitation Mechanisms of Phosphors. *Luminescence*. October 24, 2007, pp 1–34. https://doi.org/https://doi.org/10.1002/9783527621064.ch1.

(3) Valeur, B.; Ario, M.; Berberan-Santos, N. A Brief History of Fluorescence and Phosphorescence before the Emergence of Quantum Theory. *J. Chem. Educ* **2011**, *88*, 731–738. https://doi.org/10.1021/ed100182h.

(4) María Ibarra-Ruiz, A.; Rodríguez Burbano, D. C.; Capobianco, J. A. Photoluminescent Nanoplatforms in Biomedical Applications. **2016**, *1* (2), 194–225. https://doi.org/10.1080/23746149.2016.1165629.

(5) Della Rocca, J.; Lin, W. Nanoscale Metal-Organic Frameworks: Magnetic Resonance Imaging Contrast Agents and Beyond. **2010**. https://doi.org/10.1002/ejic.201000496.

(6) Vetrone, F.; Naccache, R.; Zamarrón, A.; De La Fuente, A. J.; Sanz-Rodríguez, F.; Maestro, L. M.; Rodriguez, E. M.; Jaque, D.; Sole, J. G.; Capobianco, J. A. Temperature Sensing Using Fluorescent Nanothermometers. *ACS Nano* **2010**, *4* (6), 3254–3258. https://doi.org/10.1021/nn100244a.

(7) Li, B.; Yu, Q.; Duan, Y. Fluorescent Labels in Biosensors for Pathogen Detection. *Critical Reviews in Biotechnology*. Informa Healthcare March 1, 2015, pp 82–93. https://doi.org/10.3109/07388551.2013.804487.

(8) Dobrucki, J. W.; Kubitscheck, U. Fluorescence Microscopy. *Fluorescence Microscopy*. May 8, 2017, pp 85–132. https://doi.org/https://doi.org/10.1002/9783527687732.ch3.

(9) Xu, J.; Tanabe, S. Persistent Luminescence Instead of Phosphorescence : History , Mechanism , and Perspective. *J. Lumin.* **2019**, *205* (September 2018), 581–620. https://doi.org/10.1016/j.jlumin.2018.09.047.

(10) Peter Atkins, Julio de Paula, J. K. *Physical Chemistry*, 11th ed.; Press, O. U., Ed.; London, England, 2017.

(11) Albrecht, C. Joseph R. Lakowicz: Principles of Fluorescence Spectroscopy, 3rd Edition. *Anal. Bioanal. Chem.* **2008**, *390* (5), 1223–1224. https://doi.org/10.1007/s00216-007-1822-x.

(12) Dickinson Mary E., D. M. http://zeiss-campus.magnet.fsu.edu/articles/spectralimaging/introduction.html (accessed Nov 19, 2022).

(13) Würth, C.; Grabolle, M.; Pauli, J.; Spieles, M.; Resch-Genger, U. Relative and Absolute Determination of Fluorescence Quantum Yields of Transparent Samples. *Nat. Protoc.* **2013**, *8* (8), 1535–1550. https://doi.org/10.1038/nprot.2013.087.

(14) Heinrichs, A. Stains and Fluorescent Dyes. *Nat. Cell Biol.* **2009**, *11* (S1), S7–S7. https://doi.org/10.1038/ncb1939.

(15) Fu, Y.; Finney, N. S. Small-Molecule Fluorescent Probes and Their Design. *RSC Advances*. Royal Society of Chemistry 2018, pp 29051–29061. https://doi.org/10.1039/c8ra02297f.

(16) Zimmer, M. Green Fluorescent Protein (GFP): Applications, Structure, and Related Photophysical Behavior. *Chem. Rev.* **2002**, *102* (3), 759–781. https://doi.org/10.1021/CR010142R/ASSET/IMAGES/LARGE/CR010142RF00016.JPEG.

(17) Klonis, N.; Rug, M.; Harper, I.; Wickham, M.; Cowman, A.; Tilley, L. Fluorescence Photobleaching Analysis for the Study of Cellular Dynamics. *Eur. Biophys. J.* **2002**, *31* (1), 36–51. https://doi.org/10.1007/s00249-001-0202-2.

(18) He, H.; Lin, Y.; Tian, Z. Q.; Zhu, D. L.; Zhang, Z. L.; Pang, D. W. Ultrasmall Pb:Ag2S Quantum Dots with Uniform Particle Size and Bright Tunable Fluorescence in the NIR-II Window. *Small* **2018**, *14* (11), 1–7. https://doi.org/10.1002/smll.201703296.

(19) Surre, J.; Saint-Ruf, C.; Collin, V.; Orenga, S.; Ramjeet, M.; Matic, I. Strong Increase in the Autofluorescence of Cells Signals Struggle for Survival. *Sci. Rep.* **2018**, *8* (1), 1–14. https://doi.org/10.1038/s41598-018-

30623-2.

(20) Santra, S.; Xu, J.; Wang, K.; Tan, W. Luminescent Nanoparticle Probes for Bioimaging. **2004**, *4* (6), 590–599. https://doi.org/10.1166/jnn.2004.017.

(21) Wolfbeis, O. S. An Overview of Nanoparticles Commonly Used in Fluorescent Bioimaging †. *Chem. Soc. Rev* **2015**, *44*, 4743. https://doi.org/10.1039/c4cs00392f.

(22) Gubala, V.; Giovannini, G.; Kunc, F.; Monopoli, M. P.; Moore, C. J. *Dye-Doped Silica Nanoparticles: Synthesis, Surface Chemistry and Bioapplications*; Springer Vienna, 2020; Vol. 11. https://doi.org/10.1186/s12645-019-0056-x.

(23) Moore, C. J.; Giovannini, G.; Kunc, F.; Hall, A. J.; Gubala, V. "Overloading" Fluorescent Silica Nanoparticles with Dyes to Improve Biosensor Performance. *J. Mater. Chem. B* **2017**, *5* (28), 5564–5572. https://doi.org/10.1039/c7tb01284e.

(24) Nooney, R. I.; McCormack, E.; McDonagh, C. Optimization of Size, Morphology and Colloidal Stability of Fluorescein Dye-Doped Silica NPs for Application in Immunoassays. *Anal. Bioanal. Chem.* **2012**, *404* (10), 2807–2818. https://doi.org/10.1007/s00216-012-6224-z.

(25) Dhir, A.; Datta, A. FRET on Surface of Silica Nanoparticle: Effect of Chromophore Concentration on Dynamics and Efficiency. *J. Phys. Chem. C* **2016**, *120* (36), 20125–20131. https://doi.org/10.1021/acs.jpcc.6b05242.

(26) Nooney, R.; O'Connell, C.; Roy, S.; Boland, K.; Keegan, G.; Kelleher, S.; Daniels, S.; McDonagh, C. Synthesis and Characterisation of Far-Red Fluorescent Cyanine Dye Doped Silica Nanoparticles Using a Modified Microemulsion Method for Application in Bioassays. *Sensors and Actuators, B: Chemical*. 2015, pp 470–479. https://doi.org/10.1016/j.snb.2015.06.117.

(27) Sardesai, N.; Pan, S.; Rusling, J. Electrochemiluminescent Immunosensor for Detection of Protein Cancer Biomarkers Using Carbon Nanotube Forests and [Ru-(Bpy)3] 2+-Doped Silica Nanoparticles. *Chem. Commun.* **2009**, No. 33, 4968–4970. https://doi.org/10.1039/b909220j.

(28) Kadimisetty, K.; Malla, S.; Sardesai, N. P.; Joshi, A. A.; Faria, R. C.; Lee, N. H.; Rusling, J. F. Automated Multiplexed Ecl Immunoarrays for Cancer Biomarker Proteins. *Anal. Chem.* **2015**, *87* (8), 4472–4478. https://doi.org/10.1021/acs.analchem.5b00421.

(29) Li, Y.; Xu, W. Highly Sensitive Detection of Shigella Flexneri Using Fluorescent Silica Nanoparticles. *New Microbiol.* **2009**, *32* (4), 377–383.

(30) Yao, J.; Li, P.; Li, L.; Yang, M. Biochemistry and Biomedicine of Quantum Dots: From Biodetection to Bioimaging, Drug Discovery, Diagnostics, and Therapy. *Acta Biomater.* **2018**, *74*, 36–55. https://doi.org/10.1016/j.actbio.2018.05.004.

(31) Farzin, M. A.; Abdoos, H. A Critical Review on Quantum Dots: From Synthesis toward Applications in Electrochemical Biosensors for Determination of Disease-Related Biomolecules. *Talanta* **2021**, *224* (November 2020), 121828. https://doi.org/10.1016/j.talanta.2020.121828.

(32) Ortega-Rodríguez, A.; Shen, Y.; Zabala Gutierrez, I.; Santos, H. D. A.; Torres Vera, V.; Ximendes, E.; Villaverde, G.; Lifante, J.; Gerke, C.; Fernández, N.; Calderón, O. G.; Melle, S.; Marques-Hueso, J.; Mendez-Gonzalez, D.; Laurenti, M.; Jones, C. M. S.; López-Romero, J. M.; Contreras-Cáceres, R.; Jaque, D.; Rubio-Retama, J. 10-Fold Quantum Yield Improvement of Ag2S Nanoparticles by Fine Compositional Tuning. *ACS Appl. Mater. Interfaces* **2020**, *12* (11), 12500–12509. https://doi.org/10.1021/acsami.9b22827.

(33) Schultz, S.; Smith, D. R.; Mock, J. J.; Schultz, D. A. Single-Target Molecule Detection with Nonbleaching Multicolor Optical Immunolabels. *Proc. Natl. Acad. Sci. U. S. A.* **2000**, *97* (3), 996–1001. https://doi.org/10.1073/pnas.97.3.996.

(34) Kim, H. S.; Lee, D. Y. Near-Infrared-Responsive Cancer Photothermal and Photodynamic Therapy Using Gold Nanoparticles. *Polymers (Basel).* **2018**, *10* (9), 1–14. https://doi.org/10.3390/polym10090961.

(35) Lu, X.; Dong, X.; Zhang, K.; Han, X.; Fang, X.; Zhang, Y. A Gold Nanorods-Based Fluorescent Biosensor for the Detection of Hepatitis B Virus DNA Based on Fluorescence Resonance Energy Transfer. *Analyst* **2013**, *138* (2), 642–650. https://doi.org/10.1039/c2an36099c.

(36) Lohse, S. E.; Murphy, C. J. The Quest for Shape Control: A History of Gold Nanorod Synthesis. *Chem. Mater.* **2013**, *25* (8), 1250–1261. https://doi.org/10.1021/cm303708p.

(37) Love, A. J.; Makarov, V. V.; Sinitsyna, O. V.; Shaw, J.; Yaminsky, I. V.; Kalinina, N. O.; Taliansky, M. E. A Genetically Modified Tobacco Mosaic Virus That Can Produce Gold Nanoparticles from a Metal Salt Precursor. *Front. Plant Sci.* **2015**, *6* (NOVEMBER), 1–10. https://doi.org/10.3389/fpls.2015.00984.

(38) Elahi, N.; Kamali, M.; Baghersad, M. H. Recent Biomedical Applications of Gold Nanoparticles: A Review. *Talanta* **2018**, *184* (February), 537–556. https://doi.org/10.1016/j.talanta.2018.02.088.

(39) Zhang, Z.; Wang, J.; Nie, X.; Wen, T.; Ji, Y.; Wu, X.; Zhao, Y.; Chen, C. Near Infrared Laser-Induced Targeted Cancer Therapy Using Thermoresponsive Polymer Encapsulated Gold Nanorods. *J. Am. Chem. Soc.* **2014**, *136* (20), 7317–7326. https://doi.org/10.1021/ja412735p.

(40) Lin, J.; Wang, S.; Huang, P.; Wang, Z.; Chen, S.; Niu, G.; Li, W.; He, J.; Cui, D.; Lu, G.; Chen, X.; Nie, Z. Photosensitizer-Loaded Gold Vesicles with Strong Plasmonic Coupling Effect for Imaging-Guided Photothermal/Photodynamic Therapy. *ACS Nano* **2013**, *7* (6), 5320–5329. https://doi.org/10.1021/nn4011686.

(41) Ye, X.; Gao, Y.; Chen, J.; Reifsnyder, D. C.; Zheng, C.; Murray, C. B. Seeded Growth of Monodisperse Gold Nanorods Using Bromide-Free Surfactant Mixtures. *Nano Lett.* **2013**, *13* (5), 2163–2171. https://doi.org/10.1021/nl400653s.

(42) Lin, D. Z.; Chuang, P. C.; Liao, P. C.; Chen, J. P.; Chen, Y. F. Increasing the Spectral Shifts in LSPR Biosensing Using DNA-Functionalized Gold Nanorods in a Competitive Assay Format for the Detection of Interferon-γ. *Biosens. Bioelectron.* **2016**, *81*, 221–228. https://doi.org/10.1016/j.bios.2016.02.071.

(43) Zepf, V. Chapter 1 - An Overview of the Usefulness and Strategic Value of Rare Earth Metals. In *Rare Earths Industry*; Borges De Lima, I., Leal Filho, W., Eds.; Elsevier: Boston, 2016; pp 3–17. https://doi.org/https://doi.org/10.1016/B978-0-12-802328-0.00001-2.

(44) Loo, J. F. C.; Chien, Y. H.; Yin, F.; Kong, S. K.; Ho, H. P.; Yong, K. T. Upconversion and Downconversion Nanoparticles for Biophotonics and Nanomedicine. *Coord. Chem. Rev.* **2019**, *400*, 213042. https://doi.org/10.1016/j.ccr.2019.213042.

(45) Zhang, H.; Zhang, H. Special Issue: Rare Earth Luminescent Materials. *Light Sci. Appl.* **2022**, *11* (1), 10–12. https://doi.org/10.1038/s41377-022-00956-9.

(46) Qin, X.; Liu, X.; Huang, W.; Bettinelli, M.; Liu, X. Lanthanide-Activated Phosphors Based on 4f-5d Optical Transitions: Theoretical and Experimental Aspects. *Chem. Rev.* **2017**, *117* (5), 4488–4527. https://doi.org/10.1021/acs.chemrev.6b00691.

(47) Wei, Y.; Cheng, Z.; Lin, J. An Overview on Enhancing the Stability of Lead Halide Perovskite Quantum Dots and Their Applications in Phosphor-Converted LEDs. *Chem. Soc. Rev.* **2019**, *48* (1), 310–350. https://doi.org/10.1039/c8cs00740c.

(48) Deng, R.; Qin, F.; Chen, R.; Huang, W.; Hong, M.; Liu, X. Temporal Full-Colour Tuning through Non-Steady-State Upconversion. *Nat. Nanotechnol.* **2015**, *10* (3), 237–242. https://doi.org/10.1038/nnano.2014.317.

(49) Wang, L.; Fang, P.; Zhao, Z.; Huang, Y.; Liu, Z.; Bian, Z. Rare Earth Complexes with 5d-4f Transition: New Emitters in Organic Light-Emitting Diodes. *J. Phys. Chem. Lett.* **2022**, *13* (12), 2686–2694. https://doi.org/10.1021/acs.jpclett.2c00400.

(50) Zheng, W.; Huang, P.; Tu, D.; Ma, E.; Zhu, H.; Chen, X. Lanthanide-Doped Upconversion Nano-Bioprobes: Electronic Structures, Optical Properties, and Biodetection. *Chem. Soc. Rev.* **2015**, *44* (6), 1379–1415. https://doi.org/10.1039/c4cs00178h.

(51) Dong, H.; Du, S. R.; Zheng, X. Y.; Lyu, G. M.; Sun, L. D.; Li, L. D.; Zhang, P. Z.; Zhang, C.; Yan, C. H. Lanthanide Nanoparticles: From Design toward Bioimaging and Therapy. *Chem. Rev.* **2015**, *115* (19), 10725–10815. https://doi.org/10.1021/acs.chemrev.5b00091.

(52) Carnall, W. T.; Goodman, G. L.; Rajnak, K.; Rana, R. S. A Systematic Analysis of the Spectra of the Lanthanides Doped into Single Crystal LaF3. *J. Chem. Phys.* **1989**, *90* (7), 3443–3457. https://doi.org/10.1063/1.455853.

(53) Ungur, L. 1 - Introduction to the Electronic Structure, Luminescence, and Magnetism of Lanthanides. In *Advanced Nanomaterials*; Martín-Ramos, P., Ramos Silva, M. B. T.-L.-B. M. M., Eds.; Elsevier, 2018; pp 1–58. https://doi.org/https://doi.org/10.1016/B978-0-12-813840-3.00001-6.

(54) Blasse, G.; Grabmaier, B. C. *Luminescent Materials*; Springer: Berlin, 1994.

(55) Wen, H.; Wang, F. *Synthesis , Property , and Application*, Second Edi.; Elsevier Ltd, 2014. https://doi.org/10.1016/B978-0-12-407796-6.00004-X.

(56) Shen, J.; Sun, L. D.; Yan, C. H. Luminescent Rare Earth Nanomaterials for Bioprobe Applications. *Dalt. Trans.* **2008**, *9226* (42), 5687–5697. https://doi.org/10.1039/b805306e.

(57) Liu, Y.; Zhou, S.; Tu, D.; Chen, Z.; Huang, M.; Zhu, H.; Ma, E.; Chen, X. Amine-Functionalized Lanthanide-Doped Zirconia Nanoparticles: Optical Spectroscopy, Time-Resolved Fluorescence Resonance Energy Transfer Biodetection, and Targeted Imaging. *J. Am. Chem. Soc.* **2012**, *134* (36), 15083–15090. https://doi.org/10.1021/JA306066A/SUPPL_FILE/JA306066A_SI_001.PDF.

(58) Cheng, L.; Wang, C.; Liu, Z. Upconversion Nanoparticles and Their Composite Nanostructures for Biomedical Imaging and Cancer Therapy. *Nanoscale* **2012**, *5* (1), 23–37. https://doi.org/10.1039/C2NR32311G.

(59) Yang, D.; Ma, P.; Hou, Z.; Cheng, Z.; Li, C.; Lin, J. Current Advances in Lanthanide Ion (Ln3+)-Based Upconversion Nanomaterials for Drug Delivery. *Chem. Soc. Rev.* **2015**, *44* (6), 1416–1448. https://doi.org/10.1039/C4CS00155A.

(60) Idris, N. M.; Jayakumar, M. K. G.; Bansal, A.; Zhang, Y. Upconversion Nanoparticles as Versatile Light Nanotransducers for Photoactivation Applications. *Chem. Soc. Rev.* **2015**, *44* (6), 1449–1478. https://doi.org/10.1039/C4CS00158C.

(61) Hinklin, T. R.; Rand, S. C.; Laine, R. M. Transparent, Polycrystalline Upconverting Nanoceramics: Towards 3-D Displays**. https://doi.org/10.1002/adma.200701235.

(62) Huang, X.; Han, S.; Huang, W.; Liu, X. Enhancing Solar Cell Efficiency: The Search for Luminescent Materials as Spectral Converters. *Chem. Soc. Rev.* **2012**, *42* (1), 173–201. https://doi.org/10.1039/C2CS35288E.

(63) Chen, G.; Yang, C.; Prasad, P. N. Nanophotonics and Nanochemistry: Controlling the Excitation Dynamics for Frequency up- and down-Conversion in Lanthanide-Doped Nanoparticles. *Acc. Chem. Res.* **2013**, *46* (7), 1474–1486. https://doi.org/10.1021/ar300270y.

(64) Cooke, A. H. *Spectroscopic Properties of Rare Earths*; Springer Berlin Heidelberg: Berlin, Heidelberg, 1965; Vol. 280. https://doi.org/10.1016/0016-0032(65)90540-5.

(65) Lauffer, R. B. Paramagnetic Metal Complexes as Water Proton Relaxation Agents for NMR Imaging: Theory and Design. *Chem. Rev.* **1987**, *87* (5), 901–927. https://doi.org/10.1021/cr00081a003.

(66) Xia, A.; Chen, M.; Gao, Y.; Wu, D.; Feng, W.; Li, F. Gd 3+ Complex-Modified NaLuF 4-Based Upconversion Nanophosphors for Trimodality Imaging of NIR-to-NIR Upconversion Luminescence, X-Ray Computed Tomography and Magnetic Resonance. *Biomaterials* **2012**, *33* (21), 5394–5405. https://doi.org/10.1016/j.biomaterials.2012.04.025.

(67) Estelrich, J.; Sánchez-Martín, M. J.; Busquets, M. A. Nanoparticles in Magnetic Resonance Imaging: From Simple to Dual Contrast Agents. *Int. J. Nanomedicine* **2015**, *10*, 1727–1741. https://doi.org/10.2147/IJN.S76501.

(68) Gong, F.-M.; Zhang, Z.-Q.; Chen, X.-D.; Zhang, L.; Yu, X.-S.; Yang, Q.-H.; Shuai, X.-T.; Liang, B.-L.; Cheng, D. A Dual Ligand Targeted Nanoprobe with High MRI Sensitivity for Diagnosis of Breast Cancer *. *Chinese J. Polym. Sci.* **2014**, *32* (3). https://doi.org/10.1007/s10118-014-1399-8.

(69) Zhong, Y.; Ma, Z.; Zhu, S.; Yue, J.; Zhang, M.; Antaris, A. L.; Yuan, J.; Cui, R.; Wan, H.; Zhou, Y.; Wang, W.; Huang, N. F.; Luo, J.; Hu, Z.; Dai, H. Boosting the Down-Shifting Luminescence of Rare-Earth Nanocrystals for Biological Imaging beyond 1500 Nm. *Nat. Commun.* **2017**, *8* (1), 1–7. https://doi.org/10.1038/s41467-017-00917-6.

(70) Escudero, A.; Becerro, A. I.; Carrillo-Carrión, C.; Núñez, N. O.; Zyuzin, M. V.; Laguna, M.; González-Mancebo, D.; Ocanã, M.; Parak, W. J. Rare Earth Based Nanostructured Materials: Synthesis, Functionalization, Properties and Bioimaging and Biosensing Applications. *Nanophotonics* **2017**, *6* (5), 881–921. https://doi.org/10.1515/nanoph-2017-0007.

(71) Altinoğlu, E. I.; Russin, T. J.; Kaiser, J. M.; Barth, B. M.; Eklund, P. C.; Kester, M.; Adair, J. H. Near-Infrared Emitting Fluorophore-Doped Calcium Phosphate Nanoparticles for in Vivo Imaging of Human Breast Cancer. *ACS Nano* **2008**, *2* (10), 2075–2084. https://doi.org/10.1021/NN800448R/ASSET/IMAGES/MEDIUM/NN-2008-00448R_0007.GIF.

(72) Chen, D.; Wang, Y. Impurity Doping: A Novel Strategy for Controllable Synthesis of Functional Lanthanide Nanomaterials. *Nanoscale* **2013**, *5* (11), 4621–4637. https://doi.org/10.1039/c3nr00368j.

(73) Haase, M.; Schäfer, H. Upconverting Nanoparticles. *Angewandte Chemie - International Edition*. June 20, 2011, pp 5808–5829. https://doi.org/10.1002/anie.201005159.

(74) Auzel, F. Upconversion and Anti-Stokes Processes with f and d Ions in Solids. *Chemical Reviews*. 2004, pp 139–173. https://doi.org/10.1021/cr020357g.

(75) Chen, G.; Qiu, H.; Prasad, P. N.; Chen, X. Upconversion Nanoparticles: Design, Nanochemistry, and Applications in Theranostics. *Chemical Reviews*. American Chemical Society May 28, 2014, pp 5161–5214. https://doi.org/10.1021/cr400425h.

(76) Chen, G.; Qiu, H.; Prasad, P. N.; Chen, X. Upconversion Nanoparticles: Design, Nanochemistry, and Applications in Theranostics. *Chem. Rev.* **2014**, *114* (10), 5161–5214. https://doi.org/10.1021/cr400425h.

(77) Suyver, J. F.; Grimm, J.; Van Veen, M. K.; Biner, D.; Krämer, K. W.; Güdel, H. U. Upconversion Spectroscopy and Properties of NaYF4 Doped with Er3+, Tm3+ and/or Yb3+. *J. Lumin.* **2006**, *117* (1), 1–12. https://doi.org/10.1016/j.jlumin.2005.03.011.

(78) Diamente, P. R.; Raudsepp, M.; Van Veggel, F. C. J. M. Dispersible Tm3+-Doped Nanoparticles That Exhibit Strong 1.47 Mm Photoluminescence. *Adv. Funct. Mater.* **2007**, *17* (3), 363–368. https://doi.org/10.1002/adfm.200600142.

(79) Wen, H.; Wang, F. 4 - Lanthanide-Doped Nanoparticles: Synthesis, Property, and Application; Tjong, S.-C. B. T.-N. M. (Second E., Ed.; Elsevier: Oxford, 2014; pp 121–160. https://doi.org/https://doi.org/10.1016/B978-0-12-407796-6.00004-X.

(80) Saha, S.; Pala, R. G. S.; Sivakumar, S. Catalyzing Cubic-to-Hexagonal Phase Transition in NaYF4 via Ligand Enhanced Surface Ordering. *Cryst. Growth Des.* **2018**, *18* (9), 5080–5088. https://doi.org/10.1021/acs.cgd.8b00535.

(81) Eliseeva, S. V.; Bünzli, J. C. G. Lanthanide Luminescence for Functional Materials and Bio-Sciences. *Chem. Soc. Rev.* **2010**, *39* (1), 189–227. https://doi.org/10.1039/b905604c.

(82) Hong, G.; Antaris, A. L.; Dai, H. Near-Infrared Fluorophores for Biomedical Imaging. *Nat. Biomed. Eng.* **2017**, *1* (1). https://doi.org/10.1038/s41551-016-0010.

(83) Zhong, Y.; Dai, H. A Mini-Review on Rare-Earth down-Conversion Nanoparticles for NIR-II Imaging of Biological Systems. *Nano Research*. 2020, pp 1281–1294. https://doi.org/10.1007/s12274-020-2721-0.

(84) Antaris, A. L.; Chen, H.; Cheng, K.; Sun, Y.; Hong, G.; Qu, C.; Diao, S.; Deng, Z.; Hu, X.; Zhang, B.; Zhang, X.; Yaghi, O. K.; Alamparambil, Z. R.; Hong, X.; Cheng, Z.; Dai, H. A Small-Molecule Dye for NIR-II Imaging. *Nat. Mater.* **2016**, *15* (2), 235–242. https://doi.org/10.1038/nmat4476.

(85) Li, B.; Lu, L.; Zhao, M.; Lei, Z.; Zhang, F. An Efficient 1064 Nm NIR-II Excitation Fluorescent Molecular Dye for Deep-Tissue High-Resolution Dynamic Bioimaging. *Angew. Chemie - Int. Ed.* **2018**, *57* (25), 7483–7487. https://doi.org/10.1002/anie.201801226.

(86) Wan, H.; Yue, J.; Zhu, S.; Uno, T.; Zhang, X.; Yang, Q.; Yu, K.; Hong, G.; Wang, J.; Li, L.; Ma, Z.; Gao, H.; Zhong, Y.; Su, J.; Antaris, A. L.; Xia, Y.; Luo, J.; Liang, Y.; Dai, H. A Bright Organic NIR-II Nanofluorophore for Three-Dimensional Imaging into Biological Tissues. *Nat. Commun.* **2018**, *9* (1), 1–9. https://doi.org/10.1038/s41467-018-03505-4.

(87) Tao, Z.; Hong, G.; Shinji, C.; Chen, C.; Diao, S.; Antaris, A. L.; Zhang, B.; Zou, Y.; Dai, H. Biological Imaging Using Nanoparticles of Small Organic Molecules with Fluorescence Emission at Wavelengths Longer than 1000 Nm. *Angew. Chemie - Int. Ed.* **2013**, *52* (49), 13002–13006. https://doi.org/10.1002/anie.201307346.

(88) Bruns, O. T.; Bischof, T. S.; Harris, D. K.; Franke, D.; Shi, Y.; Riedemann, L.; Bartelt, A.; Jaworski, F. B.; Carr, J. A.; Rowlands, C. J.; Wilson, M. W. B.; Chen, O.; Wei, H.; Hwang, G. W.; Montana, D. M.; Coropceanu, I.; Achorn, O. B.; Kloepper, J.; Heeren, J.; So, P. T. C.; Fukumura, D.; Jensen, K. F.; Jain, R. K.; Bawendi, M. G. Next-Generation in Vivo Optical Imaging with Short-Wave Infrared Quantum Dots. *Nat. Biomed. Eng.* **2017**, *1* (4). https://doi.org/10.1038/s41551-017-0056.

(89) Naczynski, D. J.; Tan, M. C.; Zevon, M.; Wall, B.; Kohl, J.; Kulesa, A.; Chen, S.; Roth, C. M.; Riman, R. E.; Moghe, P. V. Rare-Earth-Doped Biological Composites as in Vivo Shortwave Infrared Reporters. *Nat. Commun.* **2013**, *4* (1), 1–10. https://doi.org/10.1038/ncomms3199.

(90) Liang, L.; Chen, N.; Jia, Y.; Ma, Q.; Wang, J.; Yuan, Q.; Tan, W. Recent Progress in Engineering Near-Infrared Persistent Luminescence Nanoprobes for Time-Resolved Biosensing/Bioimaging. *Nano Res.* **2019**, *12* (6), 1279–1292. https://doi.org/10.1007/s12274-019-2343-6.

(91) Singh, R.; Dumlupinar, G.; Andersson-Engels, S.; Melgar, S. Emerging Applications of Upconverting Nanoparticles in Intestinal Infection and Colorectal Cancer. *Int. J. Nanomedicine* **2019**, 14–1027. https://doi.org/10.2147/IJN.S188887.

(92) Xie, X.; Li, Z.; Zhang, Y.; Guo, S.; Pendharkar, A. I.; Lu, M.; Huang, L.; Huang, W.; Han, G. Emerging ≈800 Nm Excited Lanthanide-Doped Upconversion Nanoparticles. *Small* **2017**, *13* (6). https://doi.org/10.1002/smll.201602843.

(93) Van Dijk, J. M. F.; Schuurmans, M. F. H. On the Nonradiative and Radiative Decay Rates and a Modified Exponential Energy Gap Law for 4f-4f Transitions in Rare-Earth Ions. *J. Chem. Phys.* **1983**, *78* (9), 5317–5323. https://doi.org/10.1063/1.445485.

(94) Zou, W.; Visser, C.; Maduro, J. A.; Pshenichnikov, M. S.; Hummelen, J. C. Broadband Dye-Sensitized Upconversion of near-Infrared Light. *Nat. Photonics* **2012**, *6* (8), 560–564. https://doi.org/10.1038/nphoton.2012.158.

(95) Zhang, Q.; Meijerink, A.; Rabouw, F. T.; Yu, D.; Martı, R. Multi-Photon Quantum Cutting in Gd 2 O 2 S : Tm 3 1 to Enhance the Photo-Response of Solar Cells. **2015**, No. March, 1–8. https://doi.org/10.1038/lsa.2015.117.

(96) *Rare Earth Nanotechnology*; Pan Stanford: Singapore, 2012.

(97) Bünzli, J. C. G.; Eliseeva, S. V. Lanthanide NIR Luminescence for Telecommunications, Bioanalyses and Solar Energy Conversion. *J. Rare Earths* **2010**, *28* (6), 824–842. https://doi.org/10.1016/S1002-0721(09)60208-8.

(98) Wang, R.; Zhang, F. *Infrared Nanomaterials for Bioimaging*; The Royal Society of Chemistry, 2016.

(99) Diao, S.; Blackburn, J. L.; Hong, G.; Antaris, A. L.; Chang, J.; Wu, J. Z.; Zhang, B.; Cheng, K.; Kuo, C. J.; Dai, H. Fluorescence Imaging in Vivo at Wavelengths beyond 1500 Nm. *Angew. Chemie - Int. Ed.* **2015**, *54* (49), 14758–14762. https://doi.org/10.1002/anie.201507473.

(100) Diao, S.; Hong, G.; Antaris, A. L.; Blackburn, J. L.; Cheng, K.; Cheng, Z.; Dai, H. Biological Imaging without Autofluorescence in the Second Near-Infrared Region. *Nano Res.* **2015**, *8* (9), 3027–3034. https://doi.org/10.1007/s12274-015-0808-9.

(101) Mcdonald, S. A.; Konstantatos, G.; Zhang, S.; Cyr, P. W.; Klem, E. J. D.; Levina, L.; Sargent, E. H. Solution-Processed PbS Quantum Dot Infrared Photodetectors and Photovoltaics. *Nat. Mater.* **2005**, *4* (2), 138–142. https://doi.org/10.1038/nmat1299.

(102) Dang, X.; Gu, L.; Qi, J.; Correa, S.; Zhang, G.; Belcher, A. M.; Hammond, P. T. Layer-by-Layer Assembled Fluorescent Probes in the Second near-Infrared Window for Systemic Delivery and Detection of Ovarian Cancer. *Proc. Natl. Acad. Sci. U. S. A.* **2016**, *113* (19), 5179–5184. https://doi.org/10.1073/pnas.1521175113.

(103) Chatterjee, D. K.; Rufaihah, A. J.; Zhang, Y. Upconversion Fluorescence Imaging of Cells and Small Animals Using Lanthanide Doped Nanocrystals. *Biomaterials* **2008**, *29* (7), 937–943. https://doi.org/10.1016/j.biomaterials.2007.10.051.

(104) Gu, Y.; Guo, Z.; Yuan, W.; Kong, M.; Liu, Y.; Liu, Y.; Gao, Y.; Feng, W.; Wang, F.; Zhou, J.; Jin, D.; Li, F. High-Sensitivity Imaging of Time-Domain near-Infrared Light Transducer. *Nat. Photonics* **2019**, *13* (8), 525–531. https://doi.org/10.1038/s41566-019-0437-z.

(105) Geschwind, D. H.; Konopka, G. Neuroscience in the Era of Functional Genomics and Systems Biology. *Nature* **2009**, *461* (7266), 908–915. https://doi.org/10.1038/nature08537.

(106) McDonald, M. A.; Watkin, K. L. Small Particulate Gadolinium Oxide and Gadolinium Oxide Albumin Microspheres as Multimodal Contrast and Therapeutic Agents. *Invest. Radiol.* **2003**, *38* (6), 305–310. https://doi.org/10.1097/01.rli.0000067487.84243.91.

(107) Mignot, A.; Truillet, C.; Lux, F.; Sancey, L.; Louis, C.; Denat, F.; Boschetti, F.; Bocher, L.; Gloter, A.; Stéphan, O.; Antoine, R.; Dugourd, P.; Luneau, D.; Novitchi, G.; Figueiredo, L. C.; De Morais, P. C.; Bonneviot, L.; Albela, B.; Ribot, F.; Van Lokeren, L.; Déchamps-Olivier, I.; Chuburu, F.; Lemercier, G.; Villiers, C.; Marche, P. N.; Le Duc,

G.; Roux, S.; Tillement, O.; Perriat, P. A Top-down Synthesis Route to Ultrasmall Multifunctional Gd-Based Silica Nanoparticles for Theranostic Applications. *Chem. - A Eur. J.* **2013**, *19* (19), 6122–6136. https://doi.org/10.1002/chem.201203003.

(108) Sancey, L.; Motto-Ros, V.; Busser, B.; Kotb, S.; Benoit, J. M.; Piednoir, A.; Lux, F.; Tillement, O.; Panczer, G.; Yu, J. Laser Spectrometry for Multi-Elemental Imaging of Biological Tissues. *Sci. Rep.* **2014**, *4*, 1–8. https://doi.org/10.1038/srep06065.

(109) Li, L.; Tong, R.; Li, M.; Kohane, D. S. Self-Assembled Gemcitabine-Gadolinium Nanoparticles for Magnetic Resonance Imaging and Cancer Therapy. *Acta Biomater.* **2016**, *33*, 34–39. https://doi.org/10.1016/j.actbio.2016.01.039.

(110) Xu, W.; Bony, B. A.; Kim, C. R.; Baeck, J. S.; Chang, Y.; Bae, J. E.; Chae, K. S.; Kim, T. J.; Lee, G. H. Mixed Lanthanide Oxide Nanoparticles as Dual Imaging Agent in Biomedicine. *Sci. Rep.* **2013**, *3*, 1–10. https://doi.org/10.1038/srep03210.

(111) Estelrich, J.; Sánchez-Martín, M. J.; Busquets, M. A. Nanoparticles in Magnetic Resonance Imaging: From Simple to Dual Contrast Agents. *Int. J. Nanomedicine* **2015**, *10*, 1727–1741. https://doi.org/10.2147/IJN.S76501.

(112) Ma, Q.; Wang, J.; Li, Z.; Lv, X.; Liang, L.; Yuan, Q. Recent Progress in Time-Resolved Biosensing and Bioimaging Based on Lanthanide-Doped Nanoparticles. *Small* **2019**, *15* (32), 1–22. https://doi.org/10.1002/smll.201804969.

(113) Shukla, A. K. *Nanoparticles and Their Biomedical Applications*; 2020. https://doi.org/10.1007/978-981-15-0391-7.

(114) Stipić, F.; Pletikapić, G.; Jakšić, Ž.; Frkanec, L.; Zgrablić, G.; Burić, P.; Lyons, D. M. Application of Functionalized Lanthanide-Based Nanoparticles for the Detection of Okadaic Acid-Specific Immunoglobulin G. *J. Phys. Chem. B* **2015**, *119* (4), 1259–1264. https://doi.org/10.1021/jp506382w.

(115) Lu, Y.; Zhao, J.; Zhang, R.; Liu, Y.; Liu, D.; Goldys, E. M.; Yang, X.; Xi, P.; Sunna, A.; Lu, J.; Shi, Y.; Leif, R. C.; Huo, Y.; Shen, J.; Piper, J. A.; Robinson, J. P.; Jin, D. Tunable Lifetime Multiplexing Using Luminescent Nanocrystals. *Nat. Photonics* **2014**, *8* (1), 32–36. https://doi.org/10.1038/nphoton.2013.322.

(116) Mendez-Gonzalez, D.; Laurenti, M.; Latorre, A.; Somoza, A.; Vazquez, A.; Negredo, A. I.; Lópezlópez-Cabarcos, E.; Calderóncalderón, O. G.; Melle, S.; Rubio-Retama, J. Oligonucleotide Sensor Based on Selective Capture of Upconversion Nanoparticles Triggered by Target-Induced DNA Interstrand Ligand Reaction. **2017**. https://doi.org/10.1021/acsami.7b00575.

(117) Kobayashi, H.; Ogawa, M.; Alford, R.; Choyke, P. L.; Urano, Y. New Strategies for Fluorescent Probe Design in Medical Diagnostic Imaging. *Chem. Rev.* **2010**, *110* (5), 2620–2640.

(118) Abdukayum, A.; Chen, J. T.; Zhao, Q.; Yan, X. P. Functional near Infrared-Emitting Cr3+/Pr3+ Co-Doped Zinc Gallogermanate Persistent Luminescent Nanoparticles with Superlong Afterglow for in Vivo Targeted Bioimaging. *J. Am. Chem. Soc.* **2013**, *135* (38), 14125–14133. https://doi.org/10.1021/ja404243v.

(119) Dong, C.; Van Veggel, F. C. J. M. Cation Exchange in Lanthanide Fluoride Nanoparticles. *ACS Nano* **2009**, *3* (1), 123–130. https://doi.org/10.1021/nn8004747.

(120) Mangaiyarkarasi, R.; Chinnathambi, S.; Aruna, P.; Ganesan, S. Synthesis and Formulation of Methotrexate (MTX) Conjugated LaF3: TB3+/Chitosan Nanoparticles for Targeted Drug Delivery Applications. *Biomed. Pharmacother.* **2015**, *69*, 170–178. https://doi.org/10.1016/j.biopha.2014.11.023.

(121) Yang, D.; Dai, Y.; Ma, P.; Kang, X.; Cheng, Z.; Li, C.; Lin, J. One-Step Synthesis of Small-Sized and Water-Soluble NaREF4 Upconversion Nanoparticles for in Vitro Cell Imaging and Drug Delivery. *Chem. - A Eur. J.* **2013**, *19* (8), 2685–2694. https://doi.org/10.1002/chem.201203634.

(122) Wu, Y.; Yang, D.; Kang, X.; Ma, P.; Huang, S.; Zhang, Y.; Li, C.; Lin, J. Core–Shell Structured Luminescent and Mesoporous β-NaYF4:Ce3+/Tb3+@mSiO2-PEG Nanospheres for Anti-Cancer Drug Delivery. *J. Chem. Soc. Dalt. Trans.* **2013**, *42* (27), 9852–9861. https://doi.org/10.1039/c3dt50658d.

(123) Chai, W. J.; Li, W. X.; Sun, X. J.; Ren, T.; Shi, X. Y. Fluorescence Enhancement of Lanthanide(III) Perchlorate by 1,10-Phenanthroline in Bis(Benzoylmethyl) Sulfoxide Complexes and Luminescence Mechanism. *J. Lumin.* **2011**, *131* (2), 225–230. https://doi.org/10.1016/j.jlumin.2010.10.002.

(124) Hagan, A. K.; Zuchner, T. Lanthanide-Based Time-Resolved Luminescence Immunoassays. *Anal. Bioanal.*

Chem. **2011**, *400* (9), 2847–2864. https://doi.org/10.1007/s00216-011-5047-7.

(125) Victor, S. P.; Paul, W.; Vineeth, V. M.; Komeri, R.; Jayabalan, M.; Sharma, C. P. Neodymium Doped Hydroxyapatite Theranostic Nanoplatforms for Colon Specific Drug Delivery Applications. *Colloids Surfaces B Biointerfaces* **2016**, *145*, 539–547. https://doi.org/10.1016/j.colsurfb.2016.05.067.

(126) Rocha, U.; Kumar, K. U.; Jacinto, C.; Villa, I.; Sanz-Rodríguez, F.; Del Carmen Iglesias De La Cruz, M.; Juarranz, A.; Carrasco, E.; Van Veggel, F. C. J. M.; Bovero, E.; Solé, J. G.; Jaque, D. Neodymium-Doped LaF3 Nanoparticles for Fluorescence Bioimaging in the Second Biological Window. *Small* **2014**, *10* (6), 1141–1154. https://doi.org/10.1002/smll.201301716.

(127) Singh, L. P.; Singh, N. P.; Srivastava, S. K. Terbium Doped SnO2 Nanoparticles as White Emitters and SnO2:5Tb/Fe3O4 Magnetic Luminescent Nanohybrids for Hyperthermia Application and Biocompatibility with HeLa Cancer Cells. *Dalt. Trans.* **2015**, *44* (14), 6457–6465. https://doi.org/10.1039/c4dt03000a.

(128) Liu, Z.; Yun, B.; Han, Y.; Jiang, Z.; Zhu, H.; Ren, F.; Li, Z. Dye-Sensitized Rare Earth Nanoparticles with Up/Down Conversion Luminescence for On-Demand Gas Therapy of Glioblastoma Guided by NIR-II Fluorescence Imaging. *Adv. Healthc. Mater.* **2022**, *11* (3), 1–16. https://doi.org/10.1002/adhm.202102042.

(129) Augustine, R.; Nethi, S. K.; Kalarikkal, N.; Thomas, S.; Patra, C. R. Electrospun Polycaprolactone (PCL) Scaffolds Embedded with Europium Hydroxide Nanorods (EHNs) with Enhanced Vascularization and Cell Proliferation for Tissue Engineering Applications. *J. Mater. Chem. B* **2017**, *5* (24), 4660–4672. https://doi.org/10.1039/C7TB00518K.

(130) Zhao, H.; Osborne, O. J.; Lin, S.; Ji, Z.; Damoiseux, R.; Wang, Y.; Nel, A. E.; Lin, S. Lanthanide Hydroxide Nanoparticles Induce Angiogenesis via ROS-Sensitive Signaling. *Small* **2016**, *12* (32), 4404–4411. https://doi.org/10.1002/smll.201600291.

(131) Dhall, A.; Self, W. Cerium Oxide Nanoparticles: A Brief Review of Their Synthesis Methods and Biomedical Applications. *Antioxidants* **2018**, *7* (8), 1–13. https://doi.org/10.3390/antiox7080097.

(132) Lai, B. H.; Chen, D. H. LaB6 Nanoparticles with Carbon-Doped Silica Coating for Fluorescence Imaging and near-IR Photothermal Therapy of Cancer Cells. *Acta Biomater.* **2013**, *9* (7), 7556–7563. https://doi.org/10.1016/j.actbio.2013.03.034.

(133) Bakht, M. K.; Sadeghi, M.; Ahmadi, S. J.; Sadjadi, S. S.; Tenreiro, C. Preparation of Radioactive Praseodymium Oxide as a Multifunctional Agent in Nuclear Medicine: Expanding the Horizons of Cancer Therapy Using Nanosized Neodymium Oxide. *Nucl. Med. Commun.* **2013**, *34* (1), 5–12. https://doi.org/10.1097/MNM.0b013e32835aa7bd.

(134) Cisterna, B. A.; Kamaly, N.; Choi, W. Il; Tavakkoli, A.; Farokhzad, O. C.; Vilos, C. Targeted Nanoparticles for Colorectal Cancer. *Nanomedicine* **2016**, *11* (18), 2443–2456. https://doi.org/10.2217/nnm-2016-0194.

(135) Ismail, A. A.; van de Voort, F. R.; Sedman, J. Chapter 4 Fourier Transform Infrared Spectroscopy: Principles and Applications. *Tech. Instrum. Anal. Chem.* **1997**, *18* (C), 93–139. https://doi.org/10.1016/S0167-9244(97)80013-3.

(136) Cho, T. J.; Hackley, V. A. Fractionation and Characterization of Gold Nanoparticles in Aqueous Solution: Asymmetric-Flow Field Flow Fractionation with MALS, DLS, and UV-Vis Detection. *Anal. Bioanal. Chem.* **2010**, *398* (5), 2003–2018. https://doi.org/10.1007/s00216-010-4133-6.

(137) Grumezescu, A. M. *Nanomaterials for Drug Delivery and Therapy*; Elsevier, 2019. https://doi.org/10.1016/C2017-0-04478-6.

(138) Melle, S.; Calderóncalderón, O. G.; Laurenti, M.; Mendez-Gonzalez, D.; Egatz-Gómezgómez, A.; Lópezlópez-Cabarcos, E.; Cabrera-Granado, E.; Díaz, E.; Rubio-Retama, J. Fö Rster Resonance Energy Transfer Distance Dependence from Upconverting Nanoparticles to Quantum Dots A Fundamental Study of FRET between NaYF 4 :Er 3+ /Yb 3+ Nanoparticles and CdSe QDs Was Reported by Bednarkiewicz Et. *J. Phys. Chem. C* **2018**, *122*, 2020. https://doi.org/10.1021/acs.jpcc.8b04908.

(139) Gu, Z.; Yan, L.; Tian, G.; Li, S.; Chai, Z.; Zhao, Y. Recent Advances in Design and Fabrication of Upconversion Nanoparticles and Their Safe Theranostic Applications. *Adv. Mater.* **2013**, *25* (28), 3758–3779. https://doi.org/10.1002/adma.201301197.

(140) Dong, A.; Ye, X.; Chen, J.; Kang, Y.; Gordon, T.; Kikkawa, J. M.; Murray, C. B. A Generalized Ligand-Exchange Strategy Enabling Sequential Surface Functionalization of Colloidal Nanocrystals. *J. Am. Chem. Soc.* **2011**,

133 (4), 998–1006. https://doi.org/10.1021/jal08948z.

(141) Muhr, V.; Würth, C.; Kraft, M.; Buchner, M.; Baeumner, A. J.; Resch-Genger, U.; Hirsch, T. Particle-Size-Dependent Förster Resonance Energy Transfer from Upconversion Nanoparticles to Organic Dyes. *Anal. Chem.* **2017**, *89* (9), 4868–4874. https://doi.org/10.1021/acs.analchem.6b04662.

(142) Sirkka, N.; Lyytikäinen, A.; Savukoski, T.; Soukka, T. Upconverting Nanophosphors as Reporters in a Highly Sensitive Heterogeneous Immunoassay for Cardiac Troponin I. *Anal. Chim. Acta* **2016**, *925*, 82–87. https://doi.org/10.1016/J.ACA.2016.04.027.

(143) Wang, F.; Deng, R.; Wang, J.; Wang, Q.; Han, Y.; Zhu, H.; Chen, X.; Liu, X. Tuning Upconversion through Energy Migration in Core–Shell Nanoparticles. *Nat. Mater.* **2011**, *10* (12), 968–973. https://doi.org/10.1038/nmat3149.

(144) Mendez-Gonzalez, D.; Laurenti, M.; Latorre, A.; Somoza, A.; Vazquez, A.; Negredo, A. I.; López-Cabarcos, E.; Calderón, O. G.; Melle, S.; Rubio-Retama, J. Oligonucleotide Sensor Based on Selective Capture of Upconversion Nanoparticles Triggered by Target-Induced DNA Interstrand Ligand Reaction. *ACS Appl. Mater. Interfaces* **2017**, *9* (14), 12272–12281. https://doi.org/10.1021/acsami.7b00575.

(145) You, M.; Zhong, J.; Hong, Y.; Duan, Z.; Lin, M.; Xu, F. Inkjet Printing of Upconversion Nanoparticles for Anti-Counterfeit Applications. *Nanoscale* **2015**, *7* (10), 4423–4431. https://doi.org/10.1039/c4nr06944g.

(146) Schoenauer Sebag, M.; Hu, Z.; De Oliveira Lima, K.; Xiang, H.; Gredin, P.; Mortier, M.; Billot, L.; Aigouy, L.; Chen, Z. Microscopic Evidence of Upconversion-Induced Near-Infrared Light Harvest in Hybrid Perovskite Solar Cells. *ACS Appl. Energy Mater.* **2018**, *1* (8), 3537–3543. https://doi.org/10.1021/acsaem.8b00518.

(147) Alonso-Cristobal, P.; Oton-Fernandez, O.; Mendez-Gonzalez, D.; Díaz, J. F.; Lopez-Cabarcos, E.; Barasoain, I.; Rubio-Retama, J. Synthesis, Characterization, and Application in HeLa Cells of an NIR Light Responsive Doxorubicin Delivery System Based on NaYF4:Yb,Tm@SiO2-PEG Nanoparticles. *ACS Appl. Mater. Interfaces* **2015**, *7* (27), 14992–14999. https://doi.org/10.1021/acsami.5b03881.

(148) Lage, M. M.; Moreira, R. L.; Matinaga, F. M.; Gesland, J. Y. Raman and Infrared Reflectivity Determination of Phonon Modes and Crystal Structure of Czochralski-Grown NaLnF4 (Ln = La, Ce, Pr, Sm, Eu, and Gd) Single Crystals. *Chem. Mater.* **2005**, *17* (17), 4523–4529. https://doi.org/10.1021/cm050860k.

(149) Schietinger, S.; De S. Menezes, L.; Lauritzen, B.; Benson, O. Observation of Size Dependence in Multicolor Upconversion in Single Yb 3+, Er3+ Codoped NaYF4 Nanocrystals. *Nano Lett.* **2009**, *9* (6), 2477–2481. https://doi.org/10.1021/nl901253t.

(150) Klier, D. T.; Kumke, M. U. Analysing the Effect of the Crystal Structure on Upconversion Luminescence in Yb3+,Er3+-Co-Doped NaYF4 Nanomaterials. *J. Mater. Chem. C* **2015**, *3* (42), 11228–11238. https://doi.org/10.1039/c5tc02218e.

(151) Wilhelm, S. Perspectives for Upconverting Nanoparticles. *ACS Nano* **2017**, *11* (11), 10644–10653. https://doi.org/10.1021/acsnano.7b07120.

(152) Xu, C. T.; Zhan, Q.; Liu, H.; Somesfalean, G.; Qian, J.; He, S.; Andersson-Engels, S. Upconverting Nanoparticles for Pre-Clinical Diffuse Optical Imaging, Microscopy and Sensing: Current Trends and Future Challenges. *Laser Photonics Rev.* **2013**, *7* (5), 663–697. https://doi.org/10.1002/lpor.201200052.

(153) Kaiser, M.; Würth, C.; Kraft, M.; Soukka, T.; Resch-Genger, U. Explaining the Influence of Dopant Concentration and Excitation Power Density on the Luminescence and Brightness of β-NaYF4:Yb3+,Er3+ Nanoparticles: Measurements and Simulations. *Nano Res.* **2019**, *12* (8), 1871–1879. https://doi.org/10.1007/s12274-019-2450-4.

(154) Wen, S.; Zhou, J.; Zheng, K.; Bednarkiewicz, A.; Liu, X.; Jin, D. Advances in Highly Doped Upconversion Nanoparticles. *Nat. Commun.* **2018**, *9* (1). https://doi.org/10.1038/s41467-018-04813-5.

(155) Cao, B. S.; He, Y. Y.; Zhang, L.; Dong, B. Upconversion Properties of Er3+-Yb3+:NaYF4 Phosphors with a Wide Range of Yb3+ Concentration. *J. Lumin.* **2013**, *135* (18), 128–132. https://doi.org/10.1016/j.jlumin.2012.10.031.

(156) Shen, B.; Cheng, S.; Gu, Y.; Ni, D.; Gao, Y.; Su, Q.; Feng, W.; Li, F. Revisiting the Optimized Doping Ratio in Core/Shell Nanostructured Upconversion Particles. *Nanoscale* **2017**, *9* (5), 1964–1971. https://doi.org/10.1039/C6NR07687D.

(157) Ma, C.; Xu, X.; Wang, F.; Zhou, Z.; Liu, D.; Zhao, J.; Guan, M.; Lang, C. I.; Jin, D. Optimal Sensitizer Concentration

in Single Upconversion Nanocrystals. *Nano Lett.* **2017**, *17* (5), 2858–2864. https://doi.org/10.1021/acs.nanolett.6b05331.

(158) Chen, X.; Zhu, Y.; Zhou, D.; Xu, W.; Zhu, J.; Pan, G.; Yin, Z.; Wang, H.; Cui, S.; Song, H. Size-Dependent Downconversion near-Infrared Emission of NaYF 4 :Yb 3+ ,Er 3+ Nanoparticles. *J. Mater. Chem. C* **2017**, *5* (9), 2451–2458. https://doi.org/10.1039/c7tc00267j.

(159) The International Centre for Diffraction Data https://www.icdd.com/ (accessed Oct 11, 2020).

(160) Shi, R.; Ling, X.; Li, X.; Zhang, L.; Lu, M.; Xie, X.; Huang, L.; Huang, W. Tuning Hexagonal NaYbF4 Nanocrystals down to Sub-10 Nm for Enhanced Photon Upconversion. *Nanoscale* **2017**, *9* (36), 13739–13746. https://doi.org/10.1039/c7nr04877g.

(161) Anderson, R. B.; Smith, S. J.; May, P. S.; Berry, M. T. Revisiting the NIR-to-Visible Upconversion Mechanism in β-NaYF 4:Yb3+,Er3+. *J. Phys. Chem. Lett.* **2014**, *5* (1), 36–42. https://doi.org/10.1021/jz402366r.

(162) Wetter, N. U.; Deana, A. M.; Ranieri, I. M.; Gomes, L.; Baldochi, S. L. Influence of Excited-State-Energy Upconversion on Pulse Shape in Quasi-Continuous-Wave Diode-Pumped Er:LiYF4 Lasers. *IEEE J. Quantum Electron.* **2010**, *46* (1), 99–104. https://doi.org/10.1109/JQE.2009.2028305.

(163) Fischer, S.; Steinkemper, H.; Löper, P.; Hermle, M.; Goldschmidt, J. C. Modeling Upconversion of Erbium Doped Microcrystals Based on Experimentally Determined Einstein Coefficients. *J. Appl. Phys.* **2012**, *111* (1). https://doi.org/10.1063/1.3674319.

(164) Mackenzie, L. E.; Goode, J. A.; Vakurov, A.; Nampi, P. P.; Saha, S.; Jose, G.; Millner, P. A. The Theoretical Molecular Weight of NaYF 4 :RE Upconversion Nanoparticles. *Sci. Rep.* **2018**, *8* (1), 1–11. https://doi.org/10.1038/s41598-018-19415-w.

(165) Dormand, J. R.; Prince, P. J. A Reconsideration of Some Embedded Runge-Kutta Formulae. *J. Comput. Appl. Math.* **1986**, *15* (2), 203–211. https://doi.org/10.1016/0377-0427(86)90027-0.

(166) Mendez-Gonzalez, D.; Lahtinen, S.; Laurenti, M.; López-Cabarcos, E.; Rubio-Retama, J.; Soukka, T. Photochemical Ligation to Ultrasensitive DNA Detection with Upconverting Nanoparticles. *Anal. Chem.* **2018**, *90* (22), 13385–13392. https://doi.org/10.1021/acs.analchem.8b03106.

(167) Ortiz-Rivero, E.; Labrador-Páez, L.; Rodríguez-Sevilla, P.; Haro-González, P. Optical Manipulation of Lanthanide-Doped Nanoparticles: How to Overcome Their Limitations. *Frontiers in Chemistry*. 2020, p 593398. https://doi.org/10.3389/fchem.2020.593398.

(168) Wilhelm, S.; Kaiser, M.; Würth, C.; Heiland, J.; Carrillo-Carrion, C.; Muhr, V.; Wolfbeis, O. S.; Parak, W. J.; Resch-Genger, U.; Hirsch, T. Water Dispersible Upconverting Nanoparticles: Effects of Surface Modification on Their Luminescence and Colloidal Stability. *Nanoscale* **2015**, *7* (4), 1403–1410. https://doi.org/10.1039/c4nr05954a.

(169) Arppe, R.; Hyppänen, I.; Perälä, N.; Peltomaa, R.; Kaiser, M.; Würth, C.; Christ, S.; Resch-Genger, U.; Schäferling, M.; Soukka, T. Quenching of the Upconversion Luminescence of NaYF4:Yb3+,Er3+ and NaYF4:Yb3+,Tm3+ Nanophosphors by Water: The Role of the Sensitizer Yb3+ in Non-Radiative Relaxation. *Nanoscale* **2015**, *7* (27), 11746–11757. https://doi.org/10.1039/c5nr02100f.

(170) Lahtinen, S.; Lyytikäinen, A.; Päkkilä, H.; Hömppi, E.; Perälä, N.; Lastusaari, M.; Soukka, T. Disintegration of Hexagonal NaYF4:Yb3+,Er3+ Upconverting Nanoparticles in Aqueous Media: The Role of Fluoride in Solubility Equilibrium. *J. Phys. Chem. C* **2017**, *121* (1), 656–665. https://doi.org/10.1021/acs.jpcc.6b09301.

(171) Lisjak, D.; Plohl, O.; Ponikvar-Svet, M.; Majaron, B. Dissolution of Upconverting Fluoride Nanoparticles in Aqueous Suspensions. *RSC Adv.* **2015**, *5* (35), 27393–27397. https://doi.org/10.1039/c5ra00902b.

(172) Dukhno, O.; Przybilla, F.; Muhr, V.; Buchner, M.; Hirsch, T.; Mély, Y. Time-Dependent Luminescence Loss for Individual Upconversion Nanoparticles upon Dilution in Aqueous Solution. *Nanoscale* **2018**, *10* (34), 15904–15910. https://doi.org/10.1039/c8nr03892a.

(173) Gargas, D. J.; Chan, E. M.; Ostrowski, A. D.; Aloni, S.; Altoe, M. V. P.; Barnard, E. S.; Sanii, B.; Urban, J. J.; Milliron, D. J.; Cohen, B. E.; Schuck, P. J. Engineering Bright Sub-10-Nm Upconverting Nanocrystals for Single-Molecule Imaging. *Nat. Nanotechnol.* **2014**, *9* (4), 300–305. https://doi.org/10.1038/nnano.2014.29.

(174) Halimi, I.; Rodrigues, E. M.; Maurizio, S. L.; Sun, H. Q. T.; Grewal, M.; Boase, E. M.; Liu, N.; Marin, R.; Hemmer, E. Pick Your Precursor! Tailoring the Size and Crystal Phase of Microwave-Synthesized Sub-10 Nm Upconverting Nanoparticles. *J. Mater. Chem. C* **2019**, *7* (48), 15364–15374.

https://doi.org/10.1039/c9tc04817k.

(175) Chen, G.; Ohulchanskyy, T. Y.; Kumar, R.; Ågren, H.; Prasad, P. N. Ultrasmall Monodisperse NaYF4:Yb3+/Tm3+ Nanocrystals with Enhanced near-Infrared to near-Infrared Upconversion Photoluminescence. *ACS Nano* **2010**, *4* (6), 3163–3168. https://doi.org/10.1021/nn100457j.

(176) Chen, B.; Kong, W.; Wang, N.; Zhu, G.; Wang, F. Oleylamine-Mediated Synthesis of Small NaYbF4 Nanoparticles with Tunable Size. *Chem. Mater.* **2019**, *31* (13), 4779–4786. https://doi.org/10.1021/acs.chemmater.9b01050.

(177) Würth, C.; Fischer, S.; Grauel, B.; Alivisatos, A. P.; Resch-Genger, U. Quantum Yields, Surface Quenching, and Passivation Efficiency for Ultrasmall Core/Shell Upconverting Nanoparticles. *J. Am. Chem. Soc.* **2018**, *140* (14), 4922–4928. https://doi.org/10.1021/jacs.8b01458.

(178) Plohl, O.; Kraft, M.; Kovač, J.; Belec, B.; Ponikvar-Svet, M.; Würth, C.; Lisjak, D.; Resch-Genger, U. Optically Detected Degradation of NaYF4:Yb,Tm-Based Upconversion Nanoparticles in Phosphate Buffered Saline Solution. *Langmuir* **2017**, *33* (2), 553–560. https://doi.org/10.1021/acs.langmuir.6b03907.

(179) Zhao, G.; Tong, L.; Cao, P.; Nitz, M.; Winnik, M. A. Functional PEG-PAMAM-Tetraphosphonate Capped NaLnF4 Nanoparticles and Their Colloidal Stability in Phosphate Buffer. *Langmuir* **2014**, *30* (23), 6980–6989. https://doi.org/10.1021/la501142v.

(180) Saleh, M. I.; Rühle, B.; Wang, S.; Radnik, J.; You, Y.; Resch-Genger, U. Assessing the Protective Effects of Different Surface Coatings on NaYF4:Yb3+, Er3+ Upconverting Nanoparticles in Buffer and DMEM. *Sci. Rep.* **2020**, *10* (1). https://doi.org/10.1038/s41598-020-76116-z.

(181) Verma, A.; Ali, D.; Pathak, A. K. Fluoride Induces DNA Damage and Cytotoxicity in Human Hepatocellular Carcinoma Cells. *Toxicol. Environ. Chem.* **2017**, *99* (1), 148–159. https://doi.org/10.1080/02772248.2016.1155380.

(182) Goenka, S.; Simon, S. R. Effects of Fluoride Exposure on Primary Human Melanocytes from Dark and Light Skin. *Toxics* **2020**, *8* (4), 1–13. https://doi.org/10.3390/toxics8040114.

(183) Li, R.; Ji, Z.; Dong, J.; Chang, C. H.; Wang, X.; Sun, B.; Wang, M.; Liao, Y. P.; Zink, J. I.; Nel, A. E.; Xia, T. Enhancing the Imaging and Biosafety of Upconversion Nanoparticles through Phosphonate Coating. *ACS Nano* **2015**, *9* (3), 3293–3306. https://doi.org/10.1021/acsnano.5b00439.

(184) Von Euw, S.; Wang, Y.; Laurent, G.; Drouet, C.; Babonneau, F.; Nassif, N.; Azaïs, T. Bone Mineral: New Insights into Its Chemical Composition. *Sci. Rep.* **2019**, *9* (1). https://doi.org/10.1038/S41598-019-44620-6.

(185) Palo, E.; Salomäki, M.; Lastusaari, M. Restraining Fluoride Loss from NaYF4:Yb3+,Er3+ Upconverting Nanoparticles in Aqueous Environments Using Crosslinked Poly(Acrylic Acid)/Poly(Allylamine Hydrochloride) Multilayers. *J. Colloid Interface Sci.* **2019**, *538*, 320–326. https://doi.org/10.1016/j.jcis.2018.11.094.

(186) Palo, E.; Lahtinen, S.; Päkkilä, H.; Salomäki, M.; Soukka, T.; Lastusaari, M. Effective Shielding of NaYF4:Yb3+,Er3+ Upconverting Nanoparticles in Aqueous Environments Using Layer-by-Layer Assembly. *Langmuir* **2018**, *34* (26), 7759–7766. https://doi.org/10.1021/acs.langmuir.8b00869.

(187) Zhang, Q.; Song, K.; Zhao, J.; Kong, X.; Sun, Y.; Liu, X.; Zhang, Y.; Zeng, Q.; Zhang, H. Hexanedioic Acid Mediated Surface-Ligand-Exchange Process for Transferring NaYF4:Yb/Er (or Yb/Tm) up-Converting Nanoparticles from Hydrophobic to Hydrophilic. *J. Colloid Interface Sci.* **2009**, *336* (1), 171–175. https://doi.org/10.1016/j.jcis.2009.04.024.

(188) Boyer, J. C.; Manseau, M. P.; Murray, J. I.; Van Veggel, F. C. J. M. Surface Modification of Upconverting NaYF4 Nanoparticles with PEG-Phosphate Ligands for NIR (800 Nm) Biolabeling within the Biological Window. *Langmuir* **2010**, *26* (2), 1157–1164. https://doi.org/10.1021/la902260j.

(189) Himmelstoß, S. F.; Hirsch, T. Long-Term Colloidal and Chemical Stability in Aqueous Media of NaYF4-Type Upconversion Nanoparticles Modified by Ligand-Exchange. *Part. Part. Syst. Charact.* **2019**, *36* (10), 1900235. https://doi.org/10.1002/ppsc.201900235.

(190) Kostiv, U.; Lobaz, V.; Kučka, J.; Švec, P.; Sedláček, O.; Hrubý, M.; Janoušková, O.; Francová, P.; Kolářová, V.; Šefc, L.; Horák, D. A Simple Neridronate-Based Surface Coating Strategy for Upconversion Nanoparticles: Highly Colloidally Stable 125I-Radiolabeled NaYF4:Yb3+/Er3+@PEG Nanoparticles for Multimodal in Vivo Tissue Imaging. *Nanoscale* **2017**, *9* (43), 16680–16688. https://doi.org/10.1039/c7nr05456d.

(191) Cao, P.; Tong, L.; Hou, Y.; Zhao, G.; Guerin, G.; Winnik, M. A.; Nitz, M. Improving Lanthanide Nanocrystal Colloidal Stability in Competitive Aqueous Buffer Solutions Using Multivalent Peg-Phosphonate Ligands. *Langmuir* **2012**, *28* (35), 12861–12870. https://doi.org/10.1021/la302690h.

(192) Jiang, G.; Pichaandi, J.; Johnson, N. J. J.; Burke, R. D.; Van Veggel, F. C. J. M. An Effective Polymer Cross-Linking Strategy to Obtain Stable Dispersions of Upconverting NaYF 4 Nanoparticles in Buffers and Biological Growth Media for Biolabeling Applications. *Langmuir* **2012**, *28* (6), 3239–3247. https://doi.org/10.1021/la204020m.

(193) Liras, M.; González-Béjar, M.; Peinado, E.; Francés-Soriano, L.; Pérez-Prieto, J.; Quijada-Garrido, I.; García, O. Thin Amphiphilic Polymer-Capped Upconversion Nanoparticles: Enhanced Emission and Thermoresponsive Properties. *Chem. Mater.* **2014**, *26* (13), 4014–4022. https://doi.org/10.1021/cm501663n.

(194) Zhang, W.; Peng, B.; Tian, F.; Qin, W.; Qian, X. Facile Preparation of Well-Defined Hydrophilic Core-Shell Upconversion Nanoparticles for Selective Cell Membrane Glycan Labeling and Cancer Cell Imaging. *Anal. Chem.* **2014**, *86* (1), 482–489. https://doi.org/10.1021/ac402389w.

(195) Estebanez, N.; González-Béjar, M.; Pérez-Prieto, J. Polysulfonate Cappings on Upconversion Nanoparticles Prevent Their Disintegration in Water and Provide Superior Stability in a Highly Acidic Medium. *ACS Omega* **2019**, *4* (2), 3012–3019. https://doi.org/10.1021/acsomega.8b03015.

(196) Chen, H.; Lang, Y.; Zhao, D.; He, C.; Qin, W. Enhanced High-Order Upconversion Luminescence of Hexagonal Phase NaYF4:Yb3+,Tm3+ Crystals Coated with Homogeneous Shell. *J. Fluor. Chem.* **2015**, *174*, 70–74. https://doi.org/10.1016/J.JFLUCHEM.2015.02.019.

(197) Blanco, M.; Coello, J.; Iturriaga, H.; Maspoch, S.; De La Pezuela, C. Near-Infrared Spectroscopy in the Pharmaceutical Industry. *Analyst*. Royal Society of Chemistry January 1, 1998, pp 135R-150R. https://doi.org/10.1039/a802531b.

(198) Andresen, E.; Würth, C.; Prinz, C.; Michaelis, M.; Resch-Genger, U. Time-Resolved Luminescence Spectroscopy for Monitoring the Stability and Dissolution Behaviour of Upconverting Nanocrystals with Different Surface Coatings. *Nanoscale* **2020**, *12* (23), 12589–12601. https://doi.org/10.1039/d0nr02931a.

(199) Autran, C.; De La Cal, J. C.; Asua, J. M. (Mini)Emulsion Polymerization Kinetics Using Oil-Soluble Initiators. *Macromolecules* **2007**, *40* (17), 6233–6238. https://doi.org/10.1021/ma070916r.

(200) Zhang, S.-W.; Zhou, S.-X.; Weng, Y.-M.; Wu, L.-M. Synthesis of SiO 2 /Polystyrene Nanocomposite Particles via Miniemulsion Polymerization. **2005**. https://doi.org/10.1021/la047652b.

(201) Board, E.; De Meijere, : A; Houk, K. N.; Hunter, C. A.; Lehn, J.-M.; Ley, S. V; Olivucci, M.; Thiem, J.; Trost, B. M.; Venturi, M.; Vogel, P.; Wong, C.-H.; Wong, H.; Yamamoto, H. *Topics in Current Chemistry*.

(202) Guangwei Jia, Yongshen Xu, Xiumin Tan, and N. C. Monomer Emulsification and Polymerization Kinetics in Styrene Miniemulsion. *Iran. Polym. J.* **2006**, *15* (12), 979–987.

(203) Wang, S.; Zhang, Y.; Li, Y.; Chen, K.; Dai, Y.; Zhou, D.; Ali, A.; Yang, S.; Xu, X.; Jiang, T.; Zhu, L. Au Nanostars@PDA@Fe3O4-Based Multifunctional Nanoprobe for Integrated Tumor Diagnosis and Photothermal Therapy. *Mater. Des.* **2021**, *205*, 109707. https://doi.org/10.1016/J.MATDES.2021.109707.

(204) Ge, J.; Hu, Y.; Zhang, T.; Yin, Y. Superparamagnetic Composite Colloids with Anisotropic Structures. *J. Am. Chem. Soc.* **2007**, *129* (29), 8974–8975. https://doi.org/10.1021/ja0736461.

(205) Hübner, C.; Fettkenhauer, C.; Voges, K.; Lupascu, D. C. Agglomeration-Free Preparation of Modified Silica Nanoparticles for Emulsion Polymerization - A Well Scalable Process. *Langmuir* **2018**, *34* (1), 376–383. https://doi.org/10.1021/acs.langmuir.7b03753.

(206) Li, Y.; Liu, B. Core-Shell SiO2-PS Colloids with Controlled Eccentric Ratio. *ACS Macro Lett.* **2017**, *6* (11), 1315–1319. https://doi.org/10.1021/acsmacrolett.7b00629.

(207) Chern, C. S.; Lin, C. H. Particle Nucleation Loci in Emulsion Polymerization of Methyl Methacrylate. *Polymer (Guildf).* **2000**, *41* (12), 4473–4481. https://doi.org/10.1016/S0032-3861(99)00667-9.

(208) Li, R.; Ji, Z.; Dong, J.; Chang, C. H.; Wang, X.; Sun, B.; Wang, M.; Liao, Y.-P.; Zink, J. I.; Nel, A. E.; Xia, T. Enhancing the Imaging and Biosafety of Upconversion Nanoparticles through Phosphonate Coating. *ACS Nano* **2015**, *9* (3), 3293–3306. https://doi.org/10.1021/acsnano.5b00439.

(209) Lundqvist, M.; Stigler, J.; Elia, G.; Lynch, I.; Cedervall, T.; Dawson, K. A. Nanoparticle Size and Surface Properties Determine the Protein Corona with Possible Implications for Biological Impacts. *Proc. Natl. Acad. Sci. U. S. A.* **2008**, *105* (38), 14265–14270. https://doi.org/10.1073/PNAS.0805135105.

(210) Bonham, J. A.; Waggett, F.; Faers, M. A.; van Duijneveldt, J. S. The Role of Initiator on the Dispersibility of Polystyrene Microgels in Non-Aqueous Solvents. *Colloid Polym. Sci.* **2017**, *295* (3), 479–486. https://doi.org/10.1007/S00396-017-4023-Y/FIGURES/5.

(211) Sefcik, J.; Verduyn, M.; Storti, G.; Morbidelli, M. Charging of Latex Particles Stabilized by Sulfate Surfactant. *Langmuir* **2003**, *19* (11), 4778–4783. https://doi.org/10.1021/LA026445D.

(212) Sedlmeier, A.; Gorris, H. H. Surface Modification and Characterization of Photon-Upconverting Nanoparticles for Bioanalytical Applications. *Chem. Soc. Rev.* **2015**, *44* (6), 1526–1560. https://doi.org/10.1039/C4CS00186A.

(213) Xue, X.; Uechi, S.; Tiwari, R. N.; Duan, Z.; Liao, M.; Yoshimura, M.; Suzuki, T.; Ohishi, Y. Size-Dependent Upconversion Luminescence and Quenching Mechanism of LiYF_4: Er^3+/Yb^3+ Nanocrystals with Oleate Ligand Adsorbed. *Opt. Mater. Express* **2013**, *3* (7), 989. https://doi.org/10.1364/ome.3.000989.

(214) Lim, S. F.; Ryu, W. S.; Austin, R. H. Particle Size Dependence of the Dynamic Photophysical Properties of NaYF_4:Yb, Er Nanocrystals. *Opt. Express* **2010**, *18* (3), 2309. https://doi.org/10.1364/oe.18.002309.

(215) Farrell, R. E. *An RNA Paradigm*; 2005. https://doi.org/10.1016/b978-012249696-7/50026-3.

(216) Zaman, Z.; Verwilghen, R. L. Quantitation of Proteins Solubilized in Sodium Dodecyl Sulfate-Mercaptoethanol-Tris Electrophoresis Buffer. *Anal. Biochem.* **1979**, *100* (1), 64–69. https://doi.org/10.1016/0003-2697(79)90110-6.

(217) Klier, D. T.; Kumke, M. U. Upconversion NaYF 4 :Yb:Er Nanoparticles Co-Doped with Gd 3+ and Nd 3+ for Thermometry on the Nanoscale †. **2015**. https://doi.org/10.1039/c5ra11502g.

(218) Vozlič, M.; Černič, T.; Gyergyek, S.; Majaron, B.; Ponikvar-Svet, M.; Kostiv, U.; Horák, D.; Lisjak, D. Formation of Phosphonate Coatings for Improved Chemical Stability of Upconverting Nanoparticles under Physiological Conditions. *Dalt. Trans.* **2021**, *50* (19), 6588–6597. https://doi.org/10.1039/d1dt00304f.

(219) Naccache, R.; Vetrone, F.; Mahalingam, V.; Cuccia, L. A.; Capobianco, J. A. Controlled Synthesis and Water Dispersibility of Hexagonal Phase NaGdF 4:Ho3+/Yb3+ Nanoparticles. *Chem. Mater.* **2009**, *21* (4), 717–723. https://doi.org/10.1021/CM803151Y/ASSET/IMAGES/MEDIUM/CM-2008-03151Y_0008.GIF.

(220) Estebanez, N.; González-Béjar, M.; Pérez-Prieto, J. Polysulfonate Cappings on Upconversion Nanoparticles Prevent Their Disintegration in Water and Provide Superior Stability in a Highly Acidic Medium. *ACS Omega* **2019**, *4* (2), 3012–3019. https://doi.org/10.1021/acsomega.8b03015.

(221) Mä, S.; Schroter, A.; Hirsch, T. Small and Bright Water-Protected Upconversion Nanoparticles with Long-Time Stability in Complex, Aqueous Media by Phospholipid Membrane Coating. **2020**. https://doi.org/10.1021/acs.nanolett.0c03327.

(222) Kang, E.; Kim, H.; Gray, L. A. G.; Christie, D.; Jonas, U.; Graczykowski, B.; Furst, E. M.; Priestley, R. D.; Fytas, G. Ultrathin Shell Layers Dramatically Influence Polymer Nanoparticle Surface Mobility. **2018**, *51*, 8529. https://doi.org/10.1021/acs.macromol.8b01804.

(223) Deng, T. S.; Bongard, H. J.; Marlow, F. A One-Step Method to Coat Polystyrene Particles with an Organo-Silica Shell and Their Functionalization. *Mater. Chem. Phys.* **2015**, *162*, 548–554. https://doi.org/10.1016/J.MATCHEMPHYS.2015.06.027.

(224) Sarma, D.; Carl, P.; Climent, E.; Schneider, R. J.; Rurack, K. Correction to "Multifunctional Polystyrene Core/Silica Shell Microparticles with Antifouling Properties for Bead-Based Multiplexed and Quantitative Analysis." *ACS Appl. Mater. Interfaces* **2019**, *2019* (1), 11028–11028. https://doi.org/10.1021/acsami.8b10306.

(225) Ramli, R. A.; Laftah, W. A.; Hashim, S. Core-Shell Polymers: A Review. *RSC Adv.* **2013**, *3* (36), 15543–15565. https://doi.org/10.1039/c3ra41296b.

(226) Fan, Y.; Zhang, F. A New Generation of NIR-II Probes: Lanthanide-Based Nanocrystals for Bioimaging and Biosensing. *Adv. Opt. Mater.* **2019**, *7* (7), 1801417. https://doi.org/10.1002/ADOM.201801417.

(227) Liu, B.; Li, C.; Yang, P.; Hou, Z.; Lin, J. 808-Nm-Light-Excited Lanthanide-Doped Nanoparticles: Rational

Design, Luminescence Control and Theranostic Applications. *Adv. Mater.* **2017**, *29* (18). https://doi.org/10.1002/ADMA.201605434.

(228) Qu, X.; Liu, Z.; Ma, B.; Li, N.; Zhao, H.; Yang, T.; Xue, Y.; Zhang, X.; Shao, Y.; Chang, Y.; Xu, J.; Lei, B.; Du, Y. All in One Theranostic Nanoplatform Enables Efficient Anti-Tumor Peptide Delivery for Triple-Modal Imaging Guided Cancer Therapy. *Nano Res. 2018 123* **2018**, *12* (3), 593–599. https://doi.org/10.1007/S12274-018-2261-Z.

(229) Alonso-Cristobal, P.; Vilela, P.; El-Sagheer, A.; Lopez-Cabarcos, E.; Brown, T.; Muskens, O. L.; Rubio-Retama, J.; Kanaras, A. G. Highly Sensitive DNA Sensor Based on Upconversion Nanoparticles and Graphene Oxide. *ACS Appl. Mater. Interfaces* **2015**, *7* (23), 12422–12429. https://doi.org/10.1021/AM507591U/SUPPL_FILE/AM507591U_SI_001.PDF.

(230) Huang, X.; Han, S.; Huang, W.; Liu, X. Enhancing Solar Cell Efficiency: The Search for Luminescent Materials as Spectral Converters. *Chem. Soc. Rev.* **2012**, *42* (1), 173–201. https://doi.org/10.1039/C2CS35288E.

(231) Zhang, X.; Ai, F.; Sun, T.; Wang, F.; Zhu, G. Multimodal Upconversion Nanoplatform with a Mitochondria-Targeted Property for Improved Photodynamic Therapy of Cancer Cells. *Inorg. Chem.* **2016**, *55* (8), 3872–3880. https://doi.org/10.1021/ACS.INORGCHEM.6B00020/ASSET/IMAGES/LARGE/IC-2016-00020X_0008.JPEG.

(232) Zhang, Z.; Suo, H.; Zhao, X.; Sun, D.; Fan, L.; Guo, C. NIR-to-NIR Deep Penetrating Nanoplatforms Y2O3:Nd3+/Yb3+@SiO2@Cu2S toward Highly Efficient Photothermal Ablation. *ACS Appl. Mater. Interfaces* **2018**, *10* (17), 14570–14576. https://doi.org/10.1021/ACSAMI.8B03239/ASSET/IMAGES/LARGE/AM-2018-03239N_0005.JPEG.

(233) Tan, M.; Del Rosal, B.; Zhang, Y.; Martín Rodríguez, E.; Hu, J.; Zhou, Z.; Fan, R.; Ortgies, D. H.; Fernández, N.; Chaves-Coira, I.; Núñez, Á.; Jaque, D.; Chen, G. Rare-Earth-Doped Fluoride Nanoparticles with Engineered Long Luminescence Lifetime for Time-Gated in Vivo Optical Imaging in the Second Biological Window. *Nanoscale* **2018**, *10* (37), 17771–17780. https://doi.org/10.1039/C8NR02382D.

(234) Ortgies, D. H.; Tan, M.; Ximendes, E. C.; Del Rosal, B.; Hu, J.; Xu, L.; Wang, X.; Martín Rodríguez, E.; Jacinto, C.; Fernandez, N.; Chen, G.; Jaque, D. Lifetime-Encoded Infrared-Emitting Nanoparticles for in Vivo Multiplexed Imaging. *ACS Nano* **2018**, *12* (5), 4362–4368. https://doi.org/10.1021/ACSNANO.7B09189/ASSET/IMAGES/LARGE/NN-2017-09189V_0004.JPEG.

(235) Rocha, U.; Kumar, K. U.; Jacinto, C.; Villa, I.; Sanz-Rodríguez, F.; Del Carmen Iglesias De La Cruz, M.; Juarranz, A.; Carrasco, E.; Van Veggel, F. C. J. M.; Bovero, E.; Solé, J. G.; Jaque, D. Neodymium-Doped LaF3 Nanoparticles for Fluorescence Bioimaging in the Second Biological Window. *Small* **2014**, *10* (6), 1141–1154. https://doi.org/10.1002/SMLL.201301716.

(236) Rocha, U.; Hu, J.; Rodríguez, E. M.; Vanetsev, A. S.; Rähn, M.; Sammelselg, V.; Orlovskii, Y. V.; Solé, J. G.; Jaque, D.; Ortgies, D. H. Subtissue Imaging and Thermal Monitoring of Gold Nanorods through Joined Encapsulation with Nd-Doped Infrared-Emitting Nanoparticles. *Small* **2016**, *12* (39), 5394–5400. https://doi.org/10.1002/smll.201600866.

(237) Skripka, A.; Benayas, A.; Marin, R.; Canton, P.; Hemmer, E.; Vetrone, F. Double Rare-Earth Nanothermometer in Aqueous Media: Opening the Third Optical Transparency Window to Temperature Sensing. *Nanoscale* **2017**, *9* (9), 3079–3085. https://doi.org/10.1039/c6nr08472a.

(238) Rocha, U.; Jacinto Da Silva, C.; Ferreira Silva, W.; Guedes, I.; Benayas, A.; Martínez Maestro, L.; Acosta Elias, M.; Bovero, E.; Van Veggel, F. C. J. M.; García Solé, J. A.; Jaque, D. Subtissue Thermal Sensing Based on Neodymium-Doped LaF3 Nanoparticles. *ACS Nano* **2013**, *7* (2), 1188–1199. https://doi.org/10.1021/nn304373q.

(239) Liang, L.; Chen, N.; Jia, Y.; Ma, Q.; Wang, J.; Yuan, Q.; Tan, W. Recent Progress in Engineering Near-Infrared Persistent Luminescence Nanoprobes for Time-Resolved Biosensing/Bioimaging. *Nano Research*. Springer May 29, 2019, pp 1279–1292. https://doi.org/10.1007/s12274-019-2343-6.

(240) Balabhadra, S.; Debasu, M. L.; Brites, C. D. S.; Nunes, L. A. O.; Malta, O. L.; Rocha, J.; Bettinelli, M.; Carlos, L. D. Boosting the Sensitivity of Nd3+-Based Luminescent Nanothermometers. *Nanoscale* **2015**, *7* (41), 17261–17267. https://doi.org/10.1039/c5nr05631d.

(241) Tan, M.; Li, F.; Cao, N.; Li, H.; Wang, X.; Zhang, C.; Jaque, D.; Chen, G. Accurate In Vivo Nanothermometry through NIR-II Lanthanide Luminescence Lifetime. *Small* **2020**, *16* (48), 1–10. https://doi.org/10.1002/smll.202004118.

(242) Fischer, S.; Mehlenbacher, R. D.; Lay, A.; Siefe, C.; Alivisatos, A. P.; Dionne, J. A. Small Alkaline-Earth-Based Core/Shell Nanoparticles for Efficient Upconversion. *Nano Lett.* **2019**, *19* (6), 3878–3885. https://doi.org/10.1021/acs.nanolett.9b01057.

(243) Labrador-Páez, L.; Ximendes, E. C.; Rodríguez-Sevilla, P.; Ortgies, D. H.; Rocha, U.; Jacinto, C.; Martín Rodríguez, E.; Haro-González, P.; Jaque, D. Core–Shell Rare-Earth-Doped Nanostructures in Biomedicine. *Nanoscale* **2018**, *10* (27), 12935–12956. https://doi.org/10.1039/C8NR02307G.

(244) Fan, Y.; Wang, P.; Lu, Y.; Wang, R.; Zhou, L.; Zheng, X.; Li, X.; Piper, J. A.; Zhang, F. Lifetime-Engineered NIR-II Nanoparticles Unlock Multiplexed in Vivo Imaging. *Nat. Nanotechnol. 2018 1310* **2018**, *13* (10), 941–946. https://doi.org/10.1038/s41565-018-0221-0.

(245) Dong, H.; Sun, L. D.; Feng, W.; Gu, Y.; Li, F.; Yan, C. H. Versatile Spectral and Lifetime Multiplexing Nanoplatform with Excitation Orthogonalized Upconversion Luminescence. *ACS Nano* **2017**, *11* (3), 3289–3297. https://doi.org/10.1021/acsnano.7b00559.

(246) Roberts, J. E. Lanthanum and Neodymium Salts of Trifluoroacetic Acid. *J. Am. Chem. Soc.* **1961**, *83* (5), 1087–1088. https://doi.org/10.1021/ja01466a020.

(247) Khristov, M.; Peshev, P.; Angelova, O.; Petrova, R.; Macicek, J. *Preparation, Thermal Behaviour, and Structure of Calcium Tri¯uoroacetate Monohydrate*; 1998; Vol. 129.

(248) Oliveira, S. L.; De Sousa, D. F.; Andrade, A. A.; Nunes, L. A. O.; Catunda, T. Upconversion in Nd3+ -Doped Glasses: Microscopic Theory and Spectroscopic Measurements. *J. Appl. Phys.* **2008**, *103* (2), 23103. https://doi.org/10.1063/1.2826908.

(249) Weber, M. J. Optical Properties of Yb3+ and Nd3+-Yb3+ Energy Transfer in YAlO3. *Phys. Rev. B* **1971**, *4* (9), 3153–3159. https://doi.org/10.1103/PhysRevB.4.3153.

(250) D Jaque,J A.Muñoz, F. C. and J. G. S.´e. *Quantum Efficiency of the YAl3(BO3/4:Ndself-Frequency-Doubling Laser Material*; 1998; Vol. 10.

(251) Narayan, J. Critical Size for Defects in Nanostructured Materials. *J. Appl. Phys.* **2006**, *100* (3), 34309. https://doi.org/10.1063/1.2220472.

(252) Li, Z.; Park, W.; Zorzetto, G.; Lemaire, J. S.; Summers, C. J. Synthesis Protocols for δ-Doped NaYF4:Yb,Er. *Chem. Mater.* **2014**, *26* (5), 1770–1778. https://doi.org/10.1021/cm4023425.

(253) Hoshyar, N.; Gray, S.; Han, H.; Bao, G. The Effect of Nanoparticle Size on in Vivo Pharmacokinetics and Cellular Interaction. *Nanomedicine*. 2016, pp 673–692. https://doi.org/10.2217/nnm.16.5.

(254) Wang, S.-H.; Lee, C.-W.; Chiou, A.; Wei, P.-K. *Size-Dependent Endocytosis of Gold Nanoparticles Studied by Three-Dimensional Mapping of Plasmonic Scattering Images*; 2010. https://doi.org/10.1186/1477-3155-8-33.

(255) Cruje, C.; Chithrani, B. D. Integration of Peptides for Enhanced Uptake of PEGylayed Gold Nanoparticles. *J. Nanosci. Nanotechnol.* **2015**, *15* (3), 2125–2131. https://doi.org/10.1166/JNN.2015.10321.

(256) Ma, C.; Xu, X.; Wang, F.; Zhou, Z.; Wen, S.; Liu, D.; Fang, J.; Lang, C. I.; Jin, D. Probing the Interior Crystal Quality in the Development of More Efficient and Smaller Upconversion Nanoparticles. *J. Phys. Chem. Lett* **2016**, *7*. https://doi.org/10.1021/acs.jpclett.6b01434.

(257) Chen, B.; Wang, F. Combating Concentration Quenching in Upconversion Nanoparticles. *Acc. Chem. Res.* **2019**. https://doi.org/10.1021/acs.accounts.9b00453.

(258) Würth, C.; Fischer, S.; Grauel, B.; Alivisatos, A. P.; Resch-Genger, U. Quantum Yields, Surface Quenching, and Passivation Efficiency for Ultrasmall Core/Shell Upconverting Nanoparticles. *J. Am. Chem. Soc.* **2018**, *140* (14), 4922–4928. https://doi.org/10.1021/jacs.8b01458.

(259) Carmeliet, P. Mechanisms of Angiogenesis and Lymphangiogenesis. *Nat. Med.* **2000**, *6* (3), 389–395.

(260) Arima, S.; Nishiyama, K.; Ko, T.; Arima, Y.; Hakozaki, Y.; Sugihara, K.; Koseki, H.; Uchijima, Y.; Kurihara, Y.; Kurihara, H. Angiogenic Morphogenesis Driven by Dynamic and Heterogeneous Collective Endothelial Cell Movement. *Development* **2011**, *138* (21), 4763–4776. https://doi.org/10.1242/dev.068023.

(261) Dang, L. T. H.; Aburatani, T.; Marsh, G. A.; Johnson, B. G.; Alimperti, S.; Yoon, C. J.; Huang, A.; Szak, S.; Nakagawa, N.; Gomez, I.; Ren, S.; Read, S. K.; Sparages, C.; Aplin, A. C.; Nicosia, R. F.; Chen, C.; Ligresti, G.; Duffield, J. S. Hyperactive FOXO1 Results in Lack of Tip Stalk Identity and Deficient Microvascular

Regeneration during Kidney Injury. *Biomaterials* **2017**, *141*, 314–329. https://doi.org/10.1016/J.BIOMATERIALS.2017.07.010.

(262) Zacchigna, S.; Papa, G.; Antonini, A.; Novati, F.; Moimas, S.; Carrer, A.; Arsic, N.; Zentilin, L.; Visintini, V.; Pascone, M.; Giacca, M. Improved Survival of Ischemic Cutaneous and Musculocutaneous Flaps after Vascular Endothelial Growth Factor Gene Transfer Using Adeno-Associated Virus Vectors. *Cell Cycle Mol.*

(263) Morikawa, S.; Baluk, P.; Kaidoh, T.; Haskell, A.; Jain, R. K.; McDonald, D. M. Abnormalities in Pericytes on Blood Vessels and Endothelial Sprouts in Tumors. *Am. J. Pathol.* **2002**, *160* (3), 985–1000. https://doi.org/10.1016/S0002-9440(10)64920-6.

(264) Khurana, R.; Simons, M.; Martin, J. F.; Zachary, I. C. Role of Angiogenesis in Cardiovascular Disease: A Critical Appraisal. *Circulation* **2005**, *112* (12), 1813–1824. https://doi.org/10.1161/CIRCULATIONAHA.105.535294.

(265) Kocijan, T.; Rehman, M.; Colliva, A.; Groppa, E.; Leban, M.; Vodret, S.; Volf, N.; Zucca, G.; Cappelletto, A.; Piperno, G. M.; Zentilin, L.; Giacca, M.; Benvenuti, F.; Bin, Z.; Adams, R.; Zacchigna, S. Genetic Lineage Tracing Reveals Poor Angiogenic Potential of Cardiac Endothelial Cells. *Cardiovasc. Res.* **2020**. https://doi.org/10.1093/cvr/cvaa012.

(266) Schaper, W.; Buschmann, I. VEGF and Therapeutic Opportunities in Cardiovascular Diseases. *Current Opinion in Biotechnology*. Current Biology Ltd December 1, 1999, pp 541–543. https://doi.org/10.1016/S0958-1669(99)00032-4.

(267) Alitalo, K.; Tammela, T.; Petrova, T. V. Lymphangiogenesis in Development and Human Disease. *Nat. 2005 4387070* **2005**, *438* (7070), 946–953. https://doi.org/10.1038/nature04480.

(268) Ferrara, N. Binding to the Extracellular Matrix and Proteolytic Processing: Two Key Mechanisms Regulating Vascular Endothelial Growth Factor Action. *Mol. Biol. Cell* **2010**, *21* (5), 687. https://doi.org/10.1091/MBC.E09-07-0590.

(269) Battegay, E. J. Angiogenesis: Mechanistic Insights, Neovascular Diseases, and Therapeutic Prospects. *J. Mol. Med.* **1995**, *73* (7), 333–346. https://doi.org/10.1007/BF00192885.

(270) Arsic, N.; Zentilin, L.; Zacchigna, S.; Santoro, D.; Stanta, G.; Salvi, A.; Sinagra, G.; Giacca, M. Induction of Functional Neovascularization by Combined VEGF and Angiopoietin-1 Gene Transfer Using AAV Vectors. *Mol. Ther.* **2003**, *7* (4), 450–459. https://doi.org/10.1016/S1525-0016(03)00034-0.

(271) Feng, Y.-M.; Verfaillie, C.; Yu, H. Editorial Vascular Diseases and Metabolic Disorders. **2016**. https://doi.org/10.1155/2016/5810358.

(272) Hendel, R. C.; Henry, T. D.; Rocha-Singh, K.; Isner, J. M.; Kereiakes, D. J.; Giordano, F. J.; Simons, M.; Bonow, R. O. Effect of Intracoronary Recombinant Human Vascular Endothelial Growth Factor on Myocardial Perfusion: Evidence for a Dose-Dependent Effect. *Circulation* **2000**, *101* (2), 118–121. https://doi.org/10.1161/01.CIR.101.2.118/FORMAT/EPUB.

(273) Sato, K.; Wu, T.; Laham, R. J.; Johnson, R. B.; Douglas, P.; Li, J.; Sellke, F. W.; Bunting, S.; Simons, M.; Post, M. J. Efficacy of Intracoronary or Intravenous VEGF165in a Pig Model of Chronic Myocardial Ischemia. *J. Am. Coll. Cardiol.* **2001**, *37* (2), 616–623. https://doi.org/10.1016/S0735-1097(00)01144-X.

(274) Eppler, S. M.; Combs, D. L.; Henry, T. D.; Lopez, J. J.; Ellis, S. G.; Yi, J. H.; Annex, B. H.; McCluskey, E. R.; Zioncheck, T. F. A Target-Mediated Model to Describe the Pharmacokinetics and Hemodynamic Effects of Recombinant Human Vascular Endothelial Growth Factor in Humans. *Clin. Pharmacol. Ther.* **2002**, *72* (1), 20–32. https://doi.org/10.1067/MCP.2002.126179.

(275) Simón-Yarza, T.; Formiga, F. R.; Tamayo, E.; Pelacho, B.; Prosper, F.; Blanco-Prieto, M. J.; Blanco-Prieto, M. J. Vascular Endothelial Growth Factor-Delivery Systems for Cardiac Repair: An Overview. *Theranostics* **2012**, *2012* (6), 541–552. https://doi.org/10.7150/thno.3682.

(276) Losi, P.; Briganti, E.; Magera, A.; Spiller, D.; Ristori, C.; Battolla, B.; Balderi, M.; Kull, S.; Balbarini, A.; Di Stefano, R.; Soldani, G. Tissue Response to Poly(Ether)Urethane-Polydimethylsiloxane-Fibrin Composite Scaffolds for Controlled Delivery of pro-Angiogenic Growth Factors. *Biomaterials* **2010**, *31* (20), 5336–5344. https://doi.org/10.1016/J.BIOMATERIALS.2010.03.033.

(277) Chapanian, R.; Amsden, B. G. Combined and Sequential Delivery of Bioactive VEGF165 and HGF from Poly(Trimethylene Carbonate) Based Photo-Cross-Linked Elastomers. *J. Control. Release* **2010**, *143* (1), 53–63. https://doi.org/10.1016/J.JCONREL.2009.11.025.

(278) Jay, S. M.; Shepherd, B. R.; Andrejecsk, J. W.; Kyriakides, T. R.; Pober, J. S.; Saltzman, W. M. Dual Delivery of VEGF and MCP-1 to Support Endothelial Cell Transplantation for Therapeutic Vascularization. *Biomaterials* **2010**, *31* (11), 3054–3062. https://doi.org/10.1016/J.BIOMATERIALS.2010.01.014.

(279) Wu, J.; Zeng, F.; Huang, X. P.; Chung, J. C. Y.; Konecny, F.; Weisel, R. D.; Li, R. K. Infarct Stabilization and Cardiac Repair with a VEGF-Conjugated, Injectable Hydrogel. *Biomaterials* **2011**, *32* (2), 579–586. https://doi.org/10.1016/J.BIOMATERIALS.2010.08.098.

(280) Silva, E. A.; Mooney, D. J. Effects of VEGF Temporal and Spatial Presentation on Angiogenesis. *Biomaterials* **2010**, *31* (6), 1235–1241. https://doi.org/10.1016/J.BIOMATERIALS.2009.10.052.

(281) Jia, X.; Zhao, C.; Li, P.; Zhang, H.; Huang, Y.; Li, H.; Fan, J.; Feng, W.; Yuan, X.; Fan, Y. Sustained Release of VEGF by Coaxial Electrospun Dextran/PLGA Fibrous Membranes in Vascular Tissue Engineering. *http://dx.doi.org/10.1163/092050610X528534* **2012**, *22* (13), 1811–1827. https://doi.org/10.1163/092050610X528534.

(282) Chung, Y. Il; Kim, S. K.; Lee, Y. K.; Park, S. J.; Cho, K. O.; Yuk, S. H.; Tae, G.; Kim, Y. H. Efficient Revascularization by VEGF Administration via Heparin-Functionalized Nanoparticle–Fibrin Complex. *J. Control. Release* **2010**, *143* (3), 282–289. https://doi.org/10.1016/J.JCONREL.2010.01.010.

(283) Golub, J. S.; Kim, Y. T.; Duvall, C. L.; Bellamkonda, R. V.; Gupta, D.; Lin, A. S.; Weiss, D.; Taylor, W. R.; Guldberg, R. E. Sustained VEGF Delivery via PLGA Nanoparticles Promotes Vascular Growth. *Am. J. Physiol. - Hear. Circ. Physiol.* **2010**, *298* (6). https://doi.org/10.1152/ajpheart.00199.2009.

(284) Des Rieux, A.; Ucakar, B.; Mupendwa, B. P. K.; Colau, D.; Feron, O.; Carmeliet, P.; Préat, V. 3D Systems Delivering VEGF to Promote Angiogenesis for Tissue Engineering. *J. Control. Release* **2011**, *150* (3), 272–278. https://doi.org/10.1016/J.JCONREL.2010.11.028.

(285) Parajó, Y.; D'Angelo, I.; Welle, A.; Garcia-Fuentes, M.; Alonso, M. J. Hyaluronic Acid/Chitosan Nanoparticles as Delivery Vehicles for VEGF and PDGF-BB. *Drug Deliv.* **2010**, *17* (8), 596–604. https://doi.org/10.3109/10717544.2010.509357.

(286) López-Peña, G.; Hamraoui, K.; Horchani-Naifer, K.; Gerke, C.; Ortgies, D. H.; Martín Rodríguez, E.; Chen, G.; Jaque, D.; Rubio Retama, J. Lanthanide Doped Nanoheaters with Reliable and Absolute Temperature Feedback. *Phys. B Condens. Matter* **2022**, *631*, 413652. https://doi.org/10.1016/J.PHYSB.2021.413652.

(287) Zhou, J. C.; Yang, Z. L.; Dong, W.; Tang, R. J.; Sun, L. D.; Yan, C. H. Bioimaging and Toxicity Assessments of Near-Infrared Upconversion Luminescent NaYF4:Yb,Tm Nanocrystals. *Biomaterials* **2011**, *32* (34), 9059–9067. https://doi.org/10.1016/J.BIOMATERIALS.2011.08.038.

(288) Lan, J.; Li, L.; Liu, Y.; Yan, L.; Li, C.; Chen, J.; Chen, & X. Upconversion Luminescence Assay for the Detection of the Vascular Endothelial Growth Factor, a Biomarker for Breast Cancer. *Microchim. Acta* **1965**. https://doi.org/10.1007/s00604-016-1965-6.

(289) Tse, W. H.; Yang, S.; Zhang, J. Cubic Upconversion Nanoparticles Used as the Theranostic System for the Treatment and Diagnosis of Angiogenesis-Related Diseases. *Mater. Today Adv.* **2022**, *16*. https://doi.org/10.1016/j.mtadv.2022.100285.

(290) Song, H.; Wang, W.; Zhao, P.; Qi, Z.; Zhao, S. Cuprous Oxide Nanoparticles Inhibit Angiogenesis via down Regulation of VEGFR2 Expression †. **2014**. https://doi.org/10.1039/c3nr04363k.

(291) Del Toro, R.; Prahst, C.; Mathivet, T.; Siegfried, G.; Kaminker, J. S.; Larrivee, B.; Breant, C.; Duarte, A.; Takakura, N.; Fukamizu, A.; Penninger, J.; Eichmann, A. Identification and Functional Analysis of Endothelial Tip Cell-Enriched Genes. *Blood* **2010**, *116* (19), 4025–4033. https://doi.org/10.1182/blood-2010-02-270819.

(292) Sauer, B. Functional Expression of the Cre-Lox Site-Specific Recombination System in the Yeast Saccharomyces Cerevisiae. *Mol. Cell. Biol.* **1987**, *7* (6), 2087–2096. https://doi.org/10.1128/mcb.7.6.2087-2096.1987.

(293) He, L.; Liu, Q.; Hu, T.; Huang, X.; Zhang, H.; Tian, X.; Yan, Y.; Wang, L.; Huang, Y.; Miquerol, L.; Wythe, J. D.; Zhou, B. Genetic Lineage Tracing Discloses Arteriogenesis as the Main Mechanism for Collateral Growth in the Mouse Heart. *Cardiovasc. Res.* **2016**, *109* (3), 419–430. https://doi.org/10.1093/cvr/cvw005.

(294) Liu, Q.; Hu, T.; He, L.; Huang, X.; Tian, X.; Zhang, H.; He, L.; Pu, W.; Zhang, L.; Sun, H.; Fang, J.; Yu, Y.; Duan, S.; Hu, C.; Hui, L.; Zhang, H.; Quertermous, T.; Xu, Q.; Red-Horse, K.; Wythe, J. D.; Zhou, B. Genetic Targeting of Sprouting Angiogenesis Using Apln-CreER. *Nat. Commun.* **2015**, *6*. https://doi.org/10.1038/ncomms7020.

(295) Pi, J.; Cheng, Y.; Sun, H.; Chen, X.; Zhuang, T.; Liu, J.; Li, Y.; Chang, H.; Zhang, L.; Zhang, Y.; Tao, T. Apln-CreERT:MT/MG Reporter Mice as a Tool for Sprouting Angiogenesis Study. *BMC Ophthalmol.* **2017**, *17* (1), 1–9. https://doi.org/10.1186/s12886-017-0556-6.